Galaxies through Cosmic Time Illuminated by Gamma-Ray Bursts and Quasars

Kasper Elm Heintz

Faculty of Physical Sciences
University of Iceland
2019

Galaxies through Cosmic Time Illuminated by Gamma-Ray Bursts and Quasars

Kasper Elm Heintz

Dissertation submitted in partial fulfillment of a
Philosophiae Doctor degree in Physics

PhD Committee
Prof. Páll Jakobsson (supervisor)
Assoc. Prof. Jesús Zavala
Prof. Emeritus Einar H. Guðmundsson

Opponents
Prof. J. Xavier Prochaska
Dr. Valentina D'Odorico

Faculty of Physical Sciences
School of Engineering and Natural Sciences
University of Iceland
Reykjavik, July 2019

Galaxies through Cosmic Time Illuminated by Gamma-Ray Bursts and Quasars
Dissertation submitted in partial fulfillment of a *Philosophiae Doctor* degree in Physics

Faculty of Physical Sciences
School of Engineering and Natural Sciences
University of Iceland
Dunhagi
107, Reykjavik
Iceland

Telephone: 525-4000

Bibliographic information:
Kasper Elm Heintz, 2019, *Galaxies through Cosmic Time Illuminated by Gamma-Ray Bursts and Quasars*, PhD dissertation, Faculty of Physical Sciences, University of Iceland, 262 pp.

ISBN 978-9935-9473-3-8

Printing: Háskólaprent
Reykjavik, Iceland, July 2019

Contents

Abstract

In the early Universe, most of the cold neutral gas that will later form into individual stars and galaxies is practically invisible to us. These neutral gas reservoirs can, however, be illuminated by bright cosmic lightsources such as gamma-ray bursts (GRBs) and quasars. The aim of this thesis is to use these luminous objects as tools to study the environments of intervening or host galaxy absorption systems through cosmic time.

Part I of this thesis is dedicated to examining the gas, dust and metals in the immediate region surrounding GRBs. In Chapter 2, a comprehensive analysis of the host galaxy of GRB 140506A is presented. The optical afterglow spectrum of this GRB showed a very peculiar shape, likely related to an unusual dust reddening curve that extinguished the intrinsic afterglow spectrum. We were able to better characterize this unusual afterglow extinction by subtracting the host galaxy spectrum from the first epoch afterglow spectrum and showed that it can be modelled by a very steep reddening law (but not a 2175 Å dust bump as previously proposed). Since no such extinction component was observed for the average host galaxy spectral energy distribution (SED), we concluded that it was produced local to the GRB, and likely related to the interaction of the GRB with the surrounding circumburst dust. In Chapter 3, the high-ionization metal lines in a sample of GRB afterglows observed with the VLT/X-shooter are examined. We argue that in particular the N v absorption line feature is produced by the surrounding gas that has been highly ionized by the GRB. This argument is also based on the observed tentative corelation with the X-ray derived equivalent hydrogen column density, $N_{\rm H,X}$, that is also believed to originate from gas within ~ 10 pc from the GRB. The highly-ionized N v line transition therefore likely probes gas and metals in the circumburst environment of the GRB.

Part II presents a search for and the study of cold and molecular gas in high-z GRB host galaxy absorption systems. Chapter 4 introduces a survey for neutral atomic-carbon (C I), which is used as a tracer for molecular hydrogen (H_2) in the GRB host absorbers. Here, we also characterize the basic properties of the GRB C I absorbers in terms of their gas, dust and metal content and compare them to C I-bearing absorbers in quasar sightlines. We find that a higher H I column density and metallicity is required for GRB host galaxies to contain cold and molecular gas. In Chapter 5, we specifically examine the dust properties of the GRB C I absorbers and demonstrate that the characteristic 2175 Å dust extinction feature is likely produced by dust particles associated with the C I-bearing molecular cloud. Chapter 6 provides a detailed analysis of the presence of different probes of the molecular gas-phase in the ISM of GRB host galaxies such as C I

and vibrationally-excited H_2. Here, the typical physical conditions of the H_2-bearing molecular clouds in GRB host galaxies are also derived.

Part III focuses on using quasars to examine gas-rich intervening galaxies in the line of sight, with specific focus on absorption systems rich in dust and metals. It is now clear that several dust-reddened quasars have evaded identification in e.g. the extensive Sloan Digital Sky Survey (SDSS). To alleviate this dust bias we designed the new optical to near/mid-infrared selection criteria presented in Chapter 7, specifically tailored to select dust-reddened quasars at $z > 2$. In Chapter 8, one of the dusty quasar absorption systems identified in this survey is presented. Here, we also characterize the properties of this absorber and compare the few cases of dusty and metal-rich absorption systems to the general population of absorbers observed in quasar sightlines. Finally, in Chapter 9 we demonstrate that it is possible to define a complete and unbiased quasar selection using the astrometric data from the space-based *Gaia* mission.

This thesis demonstrates the importance of observing large samples of GRB afterglows to 1) allow for statistical studies of the GRB phenomena itself and the associated host galaxy environments and 2) to obtain spectra of peculiar or unusual GRB afterglows, that is only observed rarely. In addition, it highlights that defining a complete and unbiased sample of quasars is vital to fully exploit the potential of quasars as probes of cosmic chemical evolution. In Chapter 10, the general work of this thesis is concluded and some future prospects are provided.

Útdráttur

Megnið af hinu kalda, ójónaða efni í ungum alheimi, sem síðar myndar stjörnur og vetrarbrautir, er nánast ósýnilegt okkur. Þó geta björt fyrirbæri eins og gammablossar og dulstirni lýst upp þetta dimma efni. Markmið ritgerðarinnar er að nota þessi fyrirbæri sem nokkurs konar verkfæri til að fræðast um útgeimsefnið.

Í fyrsta hluta ritgerðarinnar er gas, ryk og þungefni í nánasta nágrenni gammablossa kannað til hlítar. Í kafla 2 er kynnt yfirgripsmikil greining á hýsilvetrarbraut blossans GRB 140506A. Litróf sýnilegra glæða blossans var mjög óvenjulegt, líklega tengt sérstæðri geimroðnun. Okkur tókst að sýna fram á að þessi sérkennilega ljósdeyfing ætti upptök nálægt blossanum og væri afleiðing af víxlverkun blossans við sitt nánasta umhverfi. Í kafla 3 er safn blossa skoðað sem rannsakað var með nýlegum litrófsmæli á Very Large Telescope (VLT). Hér var áhersla lögð á gleypilínur frá mikið jónuðu gasi. Við sýndum fram á að þessar línur eru afleiðing blossans og notuðum auk þess röntgenmælingar til að styrkja þær niðurstöður.

Í öðrum hluta er lögð áhersla á rannsóknir á sameindagasi við hátt rauðvik. Í 4. kafla er hlutlaust kolefni (C I) kortlagt en það má nota sem nokkurs konar sporefni fyrir vetnissameindina H_2. Grunneiginleikar viðkomandi gass voru rannsakaðir og meginniðurstaðan var sú að hýsilvetrarbrautir gammablossa verða að hafa hátt hlutfall þungefna til að geta innihaldið kalt sameindagas. Í 5. kafla er athyglinni beint að eiginleikum ryks í C I kerfum og í 6. kafla er nákvæm greining á tilvist sporefna sameindagass í miðgeimsefni hýsilvetrarbrauta gammablossa.

Í þriðja og síðasta hluta eru dulstirnin í aðalhlutverki. Þau eru hér notuð til að rannsaka kerfi sem eru rykrík og hafa hátt hlutfall þungefna. Kynnt er ný aðferð til að finna slík kerfi við hátt rauðvik sem fyrri athuganir hafa hingað til misst af. Fjallað er um slíka valforsendu, sem byggir á sýnilegum og innrauðum mælingum, í kafla 7. Eitt slíkt kerfi er svo rannsakað gaumgæfilega í kafla 8. Að lokum eru gögn frá *Gaia* geimsjónaukanum notuð í kafla 9 til að sýna fram á að hægt er að skilgreina óhlutdrægt safn dulstirna.

Þessi ritgerð sýnir fram á mikilvægi þess að skoða stór söfn gammablossa til að 1) gera tölfræðilegar rannsóknir á þeim og hýsilvetrarbrautum þeirra sem og að 2) auka möguleikana á því að uppgötva sérkennilegt umhverfi sumra þeirra. Að auki þá undirstrika þessar rannsóknir brýna þörf á að skilgreina óhlutdrægt safn dulstirna. Þannig má nýta þau til að kortleggja aukningu þungefnis sem fall af tíma í alheiminum.

Acknowledgments

"If I have seen further, it is by
standing on the shoulders of Giants"
- Isaac Newton, 1675[1]

I think this quote is excellent in realizing the importance of the previously laid out groundwork any future advances in science relies on. For me personally, it also refers to my supervisors and mentors throughout my time as a PhD student, without whom the work done in this thesis would not have been possible.

First of all, I would like to thank my main supervisor Palli. You accepted me as a PhD student even though I had to spend the first half of my studies abroad in Copenhagen. You allowed me to pursue my childhood dream of studying astrophysics and for that I am deeply grateful. Then I would also like to thank Johan for accepting to be my unofficial supervisor in Copenhagen, and for always being there to discuss any problems I might have, scientific or otherwise. I am sure that I would not be where I am today without your help and guidance. I greatly appreciate the amount of freedom both of you have given me during my PhD studies. I am also thankful to both of you for including me in the GRB afterglow follow-up team as part of the XS-GRB/Stargate collaboration, which have been, and continue to be, very exciting. Related to this, I also owe a special thanks to Daniele for preparing me for the intense work that follows a GRB trigger and for inviting me to the ePESSTO team, which resulted in a great trip to the La Silla observatory in Chile together. Finally, I would also like to thank Palle for acting as a scientific mentor for me and for first showing me how astronomy is done outside of Copenhagen.

It has been a great privilege to be included in the GRB collaboration and the mature field of GRBs in general, guided by the foremost experts, and to work on this unique data set that has been collected throughout almost a decade as part of my PhD project. As part of this collaboration, I have had numerous experts on GRBs evaluate my work, whose knowledge has greatly expanded my own. Specifically, I would like to thank Darach for our great discussions on about almost everything, but in particular on the work done as part of our high-ion project and all of our ongoing projects. I would also like to thank Cédric and Pasquier for enlightening discussions during our work on cold and molecular gas and in general eminent scientific guidance.

[1] Modifications of this saying have been traced back to the 12th century, but the familiar English expression is from a letter to Robert Hooke from Isaac Newton, sent in 1675.

I probably owe my greatest thanks to my now wife, Julie, for her endless support throughout my PhD studies and for agreeing (though reluctantly in the beginning) to move to Iceland with me so that I could pursue my dream. It has been quite an adventure with you and our son, Oliver. Finally, I would like to thank my mom and dad for always believing in me and supporting me through my entire life. You sparked my interest for physics and astronomy in the first place.

Chapter 1

Introduction

The topics covered in this thesis are roughly divided into three parts. The first part (Chapters 2 and 3) is devoted to the study of the very local environment in which gamma-ray burst (GRB) progenitors reside. Chapters 4 to 6 constitute the second part, focusing on the cold and molecular gas-phase of the interstellar medium (ISM) in GRB host galaxies. The work in these first two parts is based on a combination of understanding a single, extraordinary burst and the resulting implications for the global GRB population in addition to a detailed characterization of a larger sample of GRB afterglows allowing for statistical analyses of a more homogenous selected sample. Both approaches are valuable to gauge the true underlying characteristics of the GRB host galaxy population and emphasizes the need for continuous follow-up of GRBs to identify single, peculiar cases and building large samples to draw general conclusions about the GRB host galaxy environments.

The last part (Chapters 7 through 9) is devoted to the study of quasars and intervening absorption systems, and in particular how current quasar selection techniques are subject to severe biases. Specifically, quasars with foreground dusty and metal-rich absorbers are evasive to classical quasar surveys, so in this part it is demonstrated how the selection of these bright cosmic sources can be modified to alleviate this bias. Below follows a brief, general introduction to the nature of GRBs and quasars, with particular focus on their use as cosmic probes. In Sect. 1.2, a more comprehensive introduction will be given to the study of absorption-line systems in GRB and quasar spectra.

1.1 The nature of GRBs and quasars

The central engine powering the light emitted from GRBs and quasars are believed to be produced by roughly the same mechanism, though on vastly different scales. Both phenomena are related to the accretion of gas onto black holes, extracting angular momentum and potential energy into electromagnetic radiation via the Blandford-Znajek mechanism (Blandford & Znajek, 1977). In this process, the strong induced magnetic fields will also form relativistic jets launched along the rotation axis of the accreting gas. In the case of (long-duration) GRBs, a stellar-mass black hole is formed by the core collapse of a single massive star, whereas the super-massive black holes observed

to reside in the centre of most galaxies can reach masses of $M = 10^5 - 10^9\,M_\odot$ via merging of smaller black holes and accretion of matter, and are able to explain the basic properties of quasars (Salpeter, 1964).

While the story of how GRBs were first discovered and the following attempts to piece together the puzzle of these cosmic explosions is interesting on its own (see every PhD theses on GRBs ever), I will in the following sections only outline the basic nature and properties of these energetic γ-ray flashes and subsequent emission components. I will also only briefly introduce the phenomenom of quasars as well, but still include a short description on how these were first discovered and subsequently identified in Sect. 1.1.3, since it is important for the later topics of this thesis. The overview provided in this section thus only highlights the relevant characteristics of GRBs and quasars and their application as cosmic tools and is not meant as a comprehensive introduction to either of the two phenomena.

1.1.1 GRB optical afterglows

With the first collection of GRBs observed by the Burst And Transient Source Experiment (BATSE) onboard the Compton Gamma Ray Observatory (CGRO), it was possible to constrain two fundamental properties of the overall GRB population. First, the angular distribution was observed to be isotropic on the sky, favoring a cosmological, instead of the previously proposed Galactic, origin (Meegan et al., 1992). Second, the burst durations appeared to follow an apparent bimodal distribution (typically quantified as t_{90}, the time in which 90% of the source photons are collected), with a division around 2 seconds (Kouveliotou et al., 1993). While not being clear at the time, it is now believed that the 'short' ($t_{90} < 2\,\mathrm{s}$) and 'long' ($t_{90} > 2\,\mathrm{s}$) GRBs are actually produced by two distinct physical phenomena. Later, several more characteristics have been used to divide the two sub-populations since the typically used observables show a large degree of overlap (e.g. Lien et al., 2016). For instance, short GRBs typically have a higher fraction of the radiation emitted at higher energies, which is often referred to as having 'harder' spectra. On the other hand, the total output energies are typically lower than observed for long GRBs resulting in significantly fainter X-ray and optical afterglows (Berger, 2014; D'Avanzo, 2015).

The canonical prescription for long GRBs is the so-called 'collapsar' model (Woosley, 1993; MacFadyen & Woosley, 1999), where a black hole is formed by the core collapse of a massive ($M_\star \gtrsim 40\,M_\odot$) Wolf-Rayet star. Short GRBs are instead believed to be produced by the merger of binary neutron stars or a neutron star and a stellar-mass black hole (e.g. Narayan et al., 1992). While the two GRB progenitor systems are physically distinct, the initial emission mechanisms are expected to be roughly the same. The energy output of both types of GRBs are separated into two phases, the prompt and afterglow emission. The prompt emission is characterized by an intense γ-ray flux and is produced by ultrarelativistic flows that gets dissipated in internal collisions along the jet direction. When the jet of γ-rays then collides with the surrounding medium it gets slowed down by external shocks and emits synchrotron radiation which is observed as the X-ray to optical and radio afterglow (Piran, 2004). The spectral shape of the afterglow typically follows a simple, temporally varying power-law as $F_\lambda = \lambda^{-\beta} t^{-\alpha}$ (Sari et al., 1998).

The still on-going *Swift* mission (Gehrels et al., 2004) has in the more recent years significantly contributed to our current understanding of GRBs (see e.g. Zhang, 2007; Gehrels et al., 2009). The typical precision of the on-sky localization of the X-ray afterglow is confined within an error circle of around 5 arcsec, which has substantially increased the number of detected optical afterglows. This allows for a better understanding of the afterglow itself, but also of the associated transients that provide imperative clues to the GRB progenitors.

1.1.2 Late-stage emission components associated with GRBs

Shortly after the discovery of the first afterglow from a long GRB, conclusive evidence for the stellar origin came from the detection of an associated broad-lined type Ic supernova (SN Ic-BL; Galama et al., 1998; Woosley et al., 1999). This particular type of SN show highly broadened spectral features with an apperent deficit of hydrogen and helium. These features suggests that the progenitor stars have been stripped and suffered significant mass-losses before exploding, in addition to revealing large ejecta velocities. Since then, several similar associated events have been observed and the GRB-SN connection is now firmly established (Stanek et al., 2003; Hjorth et al., 2003; Woosley & Bloom, 2006; Cano et al., 2017). A typical spectral evolution of a long GRB transitioning into a SN type Ic-BL is shown in Fig. 1.1.1 for the recent GRB 180728A (Rossi et al., in preparation). There are, however, also examples of long GRBs with apparently no associated SNe (e.g. Fynbo et al., 2006a; Della Valle et al., 2006; Gehrels et al., 2006). Conversely, several SN Ic-BLs have also been detected without being associated with GRBs (Soderberg et al., 2010; Modjaz et al., 2016). While the jet-structured geometry of the GRB output certainly plays a role in the detection of the prompt γ-ray emission in these cases, some jets are also expected to be 'choked' in the interior of the progenitor star before breaking out. In this process, a significant fraction of the energy from the jet is dissipated into a hot 'cocoon'. The first evidence for this was only observed recently for GRB 171205A (Izzo et al., 2019), demonstrating that at least some GRB-less SNe could be explained by a choked jet scenario.

In the scenario where short GRBs are produced by the merger of two neutron stars, the expected associated transient is a kilonova (e.g. Metzger & Berger, 2012). The first tentative detection of a kilonova following a short GRB was observed as an excess in the late-time near-infrared light curve of GRB 130603B (Tanvir et al., 2013; Berger et al., 2013). The smoking gun to the origin of short GRBs came from the kilonova AT 2017gfo accompanying the gravitational wave (GW)-detected neutron star merger GW 170817 (Abbott et al., 2017a). Only 1.7 seconds after the GW observations of the coalescence of the binary neutron star system, the *Fermi* satellite detected a new short GRB (Goldstein et al., 2017) spatially consistent with the GW event. The optical counterpart was identified less than 11 hours after the merger (Abbott et al., 2017b), and the first spectroscopic observations started after roughly 35 hours (Smartt et al., 2017; Pian et al., 2017). The first four epoch spectra observed with the X-shooter spectrograph mounted on the ESO-VLT are shown in Fig. 1.1.1, kindly provided by the ENGRAVE collaboration[1]. The spectral evolution reveals a rapidly-fading blue transient that quickly becomes significantly reddened, showing line features that are consistent

[1] `www.engrave-eso.org`

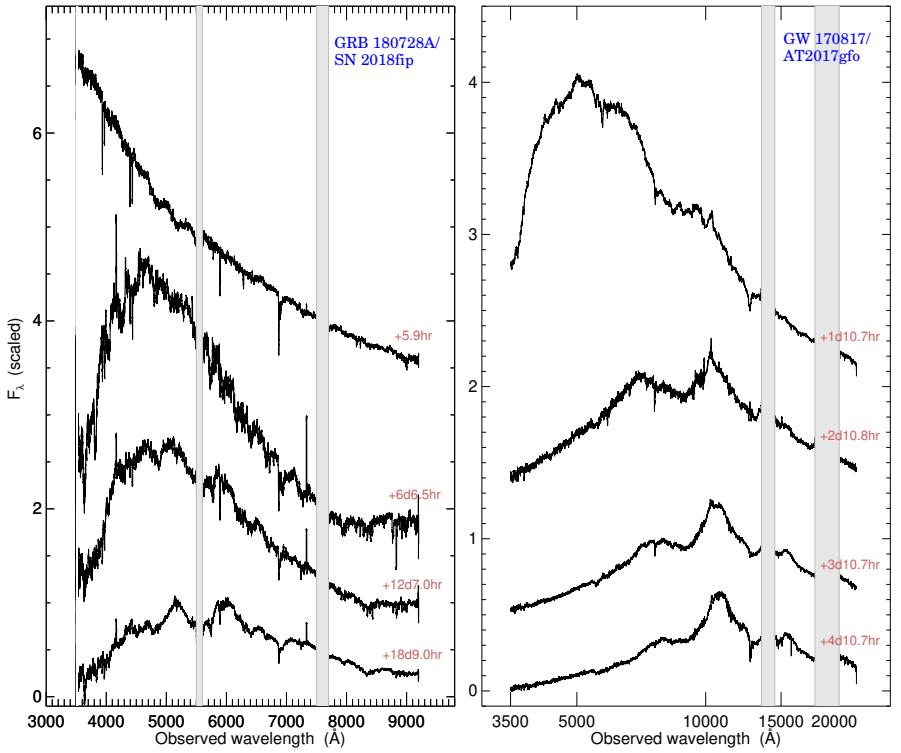

Figure 1.1.1. Spectral evolution of the long-duration GRB 180728A (left panel) and the short-duration GRB and gravitational wave counterpart GW 170817/AT 2017gfo (right panel). The left panel shows the evolution of typical long-duration GRBs that transitions into broad-lined type Ic supernova over the course of a few weeks. The right panel shows the first four VLT/X-shooter spectra obtained of the kilonova AT 2017gfo accompanying the gravitational wave-detected neutron star merger GW 170817, that first shows thermal emission from a $T \approx 5000$ K plasma that quickly cools and transitions into being dominated by wide spectral features in the near-infrared. The temporal evolution happens on much shorter time-scales compared to typical long-duration GRB-SNe. Both spectral sequences have been artifically offset along the y-axis for a more clear comparison.

with light r-process elements. This benchmark case provided conclusice evidence that binary neutron star mergers produce gravitational waves, in addition to electromagnetic radiation in the form of short GRBs and radioactively powered kilonovae.

1.1.3 Quasar classification and selection

Intrinsically, the emitting spectra of quasars follow a similar spectral power-law slope as observed for GRB afterglows and is also believed to be produced by synchrotron radiation. Quasars are typically observed with very strong energy output, ranging from X-ray to radio wavelengths, and characteristic broad (Type I) or narrow (Type

II) emission lines. They were first detected as radio sources with a seemingly star-like optical counterpart, hence the name quasi-stellar radio source or quasar (Schmidt, 1963; Matthews & Sandage, 1963). Because of their distinct spectral shape, they were also found to appear more 'blue' than typical main-sequence stars and could therefore be selected in greater numbers without relying on radio detections based on their ultraviolet excess (UVX; Sandage, 1965; Schmidt & Green, 1983). This approach has been used to build extensive quasar surveys such as the Sloan Digital Sky Survey (SDSS; York et al., 2000) or the 2dF QSO redshift survey (2QZ; Croom et al., 2004) and the number of spectroscopically-confirmed quasars now counts more than 500,000 individual sources (e.g. Pâris et al., 2018).

However, the UVX selection technique has two major disadvantages. First, for quasars located at redshifts above $z \gtrsim 2.2$, the Lyman-α (Lyα) forest starts to enter the optical u-band, effectively removing the observed u-band excess. Reddening from dust located either in the quasar host or in an intervening system (see also Sect. 1.2.2) will also extinguish most of the emitted light, especially in the bluest part of the spectrum, again diminishing the UV excess. To circumvent these two disadvantages, more efficient quasar selection techniques based on near-infrared (Warren et al., 2000) and mid-infrared (Stern et al., 2012) photometry were introduced.

In general, to gauge the true underlying population of quasars it is important to study a well-defined sample, free of selection bias. One approach is to target the specific sub-population of quasars that are missed in most current optical surveys, by defining a set of tailored selection criteria based on optical to near/mid-infrared photometry (see e.g. Fynbo et al., 2013a; Krogager et al., 2015, 2016b). This type of selection forms the basis of Chapter 7. Another approach is to redefine the selection criteria and build a complete and unbiased sample of quasars that is not based on any intrinsic properties. Chapter 9 presents such a novel selection, where we identify quasars solely as sources with zero proper motion on the sky using the astrometric measurements from the on-going *Gaia* mission.

1.1.4 GRBs and quasars as cosmic probes

Due to their immense intrinsic brightness, GRBs and quasars offer a viable approach to study the faintest galaxy population and the high-redshift Universe. The most distant observable structures (except for the CMB) are the population of galaxies and quasars at $z \sim 7-10$, at which point the reionization epoch and the formation of the first stars and galaxies initiated. To date, only two quasars have been identified at $z > 7$ (Mortlock et al., 2011; Bañados et al., 2018). The most distant GRBs found have been GRBs 090423 and 120923A, with spectroscopic redshifts of $z = 8.2$ (Salvaterra et al., 2009; Tanvir et al., 2009) and $z = 7.8$ (Tanvir et al., 2018), respectively. Two GRBs have also been found to have photometric redshifts of approximately $z = 9.4$ (Cucchiara et al., 2011) and $z = 7.9$ (Bolmer et al., 2018), although with larger uncertainties associated with placing the exact location of the Lyα break. While the number of GRBs and quasars at the epoch of first star formation is still scarce, the fact that they can in principle be observed at this time makes them valuable tools to study galaxies through most of cosmic time.

Due to their transient nature, it is important to have efficient selection criteria for GRBs to optimize the follow-up effort. Extensive samples of quasars are in that

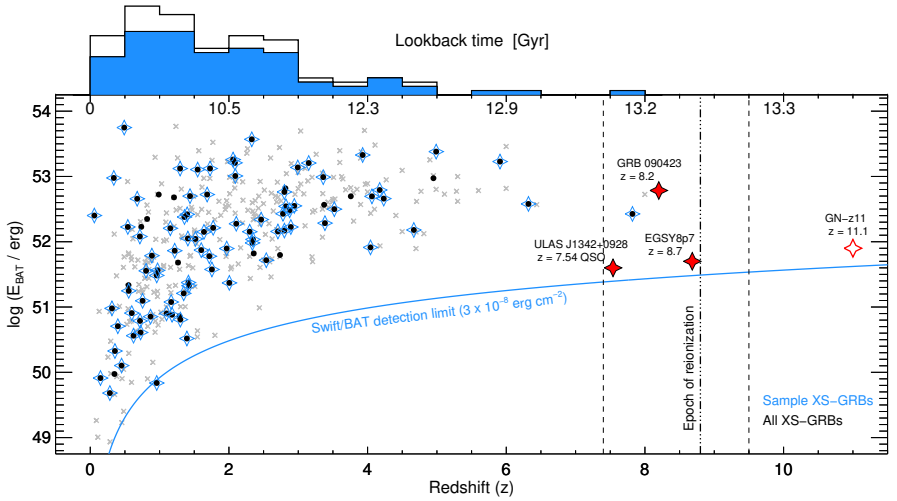

Figure 1.1.2. Redshift distribution of all *Swift* GRBs with measured redshifts (grey) as a function of intrinsic BAT γ-ray energy, $E_{\rm BAT}$. Bursts that are part of the statistical XS-GRB sample are marked by the blue stars, whereas black dots represent all GRBs observed with X-shooter. GRBs have been detected spectroscopically up to $z \approx 8$. Overplotted as the red stars are the GRB (Tanvir et al., 2009; Salvaterra et al., 2009), quasar (Bañados et al., 2018), and galaxies (Zitrin et al., 2015; Oesch et al., 2016) with the highest spectroscopically confirmed redshifts, the latter three shown at arbitrary $E_{\rm BAT}$. The blue solid line represents approximately the BAT sensitivity limit and it is clear that only a fraction of the most energetic GRBs are detected at high redshift. The estimated epoch of reionization is shown by the black dot-dashed line, with the uncertainty shown as the black dashed lines. Both GRBs and quasars have the potential to probe the first stars and galaxies formed, even as early as during the reionization epoch. This figure was produced for and first presented by Selsing et al. (2019).

regard more easily constructed, whereas GRBs offer the advantage of being much less susceptible to dust obscuration. To maximize the scientific yield from GRB samples it is therefore important to define an unbiased selection of bursts that are still broad enough to include the majority of the underlying GRB population. Most GRB afterglow surveys have therefore been defined in such a way that only exclude bursts based on conditions local to the Milky Way but independent of intrinsic GRB properties (e.g. Jakobsson et al., 2006a; Fynbo et al., 2009). Building on this, the X-shooter GRB (XS-GRB) afterglow legacy survey was defined (Selsing et al., 2019), that now counts more than 100 optical/near-infrared GRB afterglows, which a large fraction of the work done in this thesis is based on. The redshift distribution as a function of energy, $E_{\rm BAT}$ (defined as $E_{\rm BAT} = F_\gamma 4\pi d_L^2 (1+z)^{-1}$; Lien et al., 2016), of the full sample of XS-GRBs are shown in Fig. 1.1.2. It is clear that at large redshifts, only a fraction of the brighest GRBs can be detected by *Swift* but that the XS-GRB follow-up campaign targets the underlying *Swift*-detected GRB population homogeneously. Before drawing any conclusions related to the characteristics of the underlying population of GRB hosts it is, however, important to understand how the physical properties such as star-formation rate (SFR), stellar

mass and metallicity might also influence the GRB production rate. It was initially believed that GRB hosts should follow the general star formation history (Wijers et al., 1998). However, specifically at low redshifts ($z < 1.5$), GRBs have been shown to occur preferentially in low-metallicity environments (Krühler et al., 2015; Schulze et al., 2015; Japelj et al., 2016; Vergani et al., 2017), translating into generally lower stellar masses and fainter luminosities for their host galaxies (Sollerman et al., 2005; Wolf & Podsiadlowski, 2007; Vergani et al., 2015; Perley et al., 2013, 2016b). It is now evident, however, that luminous, massive and hence metal-rich GRB host galaxies do exist but they are often associated with dusty or 'dark' (e.g. Jakobsson et al., 2004) GRB afterglows (Krühler et al., 2011; Rossi et al., 2012; Perley et al., 2013; Hunt et al., 2014) and are therefore as a consequence underrepresented in samples selected by optical afterglow identification.

Material along the line of sight to both GRBs and quasars might also influence the detection probability. Even the faintest intervening or host galaxies are for example discovered by their associated absorption signatures imprinted on the background emission spectrum. These absorption systems are the main focus of this thesis, and a more detailed introduction to the phenomena are given below.

1.2 Damped Lyman-α absorbers

Previously, the study of the high-redshift galaxy population was limited to the study of intervening absorption systems observed toward background quasars (Weymann et al., 1981). While the capabilities of direct imaging of high-z galaxies has recently undergone a revolution (Madau & Dickinson, 2014; Stark, 2016), the use of first quasars (and later GRBs; Kulkarni et al., 1998) as cosmic tools to illuminate even the faintest high-z foreground or host galaxy absorption systems still provide the most detailed information about this galaxy population (Wolfe et al., 2005). This approach is also extremely powerful, since it can easily be extended out to the epoch of reionization (as mentioned above) and is not biased towards the brightest or most massive galaxies as is the case for the typical UV-selected galaxy surveys.

Detailed absorption-line analyses in GRB host galaxies have been possible for systems as far as $z \approx 6$ (Kawai et al., 2006; Hartoog et al., 2015). Currently, nine GRB host absorption systems within the first Gyr after the Big Bang ($z \gtrsim 4.7$) have measured gas-phase abundance, where in the same redshift range, slightly fewer than 20 quasar absorption systems have been identified (Rafelski et al., 2014; Poudel et al., 2018). Identifying galaxies in absorption is typically based on the strong Lyα line transition from neutral hydrogen (H I) in the line of sight, which implies a large amount of neutral gas. However, in sightlines towards very high-z quasars ($z \gtrsim 5.7$), this approach becomes increasingly more difficult due to the large increase in the Gunn-Peterson optical depth (Fan et al., 2006). Combined with significant blending with the Lyα forest whose line density per unit redshift increases with redshift, the flux bluewards of the quasar Lyα emission line will be completely suppressed, thus concealing any traces of neutral hydrogen absorbers (though identifying the associated metal line transitions at longer rest-frame wavelengths is still possible; Cooper et al., 2019). Identifying the host galaxy counterparts of GRB absorption systems is not affected by this effect though, since the

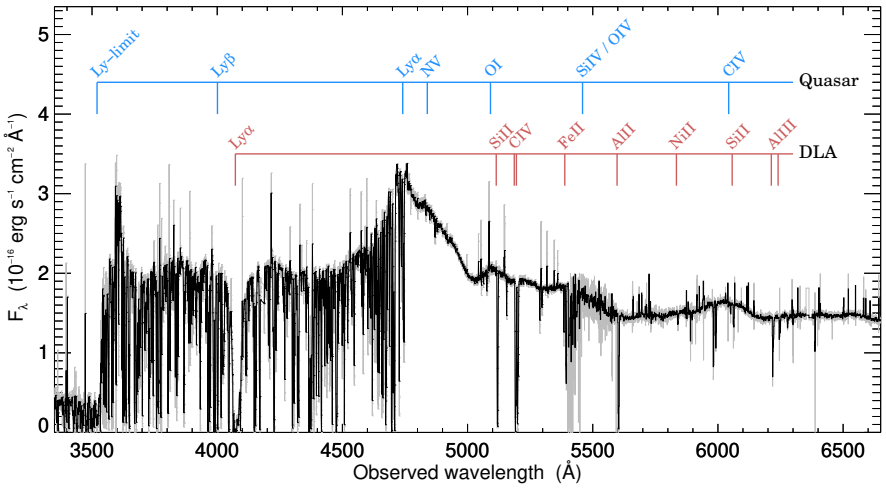

Figure 1.2.1. Spectrum of the quasar Q 2222-0946 at $z_{\rm em} = 2.93$ with an intervening DLA at $z_{\rm DLA} = 2.35$ (from Fynbo et al., 2010). The most prominent emission lines from the quasar and absorption lines from the DLA are marked in blue and red, respectively. The strong Lyα feature is clearly identified in the Lyα forest.

Lyα line is at the same redshift as the afterglow emission component so the Lyα forest will only appear bluewards of Lyα at the redshift of the GRB host galaxy. On the other end, the Lyα line transition at $\lambda_{\rm rest} = 1215.67$ Å is only observable from the ground when located at redshifts above $z \gtrsim 1.7$ due to the atmospheric cut-off. The detailed information that can be obtained from absorption-selected galaxies are therefore mainly limited to galaxies in the redshift range $z \sim 2-6$.

The strongest of the neutral hydrogen absorbers are called damped Lyα absorbers (DLAs) and are defined by having $N(\mathrm{H\,I}) > 2\times10^{20}$ cm^{-2}. An example of an intervening DLA in a typical quasar spectrum is shown in Fig. 1.2.1. The broad Lyα absorption trough can be identified even in low-resolution spectra and are easily distinguished from the typical narrow Lyα forest lines. With the goal of identifying the neutral-gas disks of high-redshift galaxies, Wolfe et al. (1986) carried out the first survey for this particular type of absorbers in quasar spectra. These systems dominate the cosmic reservoir of neutral gas from $z \approx 0-5$ (Noterdaeme et al., 2009b; Sánchez-Ramírez et al., 2016) and contain sufficient mass at $z > 3$ to account for most of the visible stellar mass in present day galaxies (Storrie-Lombardi & Wolfe, 2000). While the defined H I column density threshold for DLAs appear arbitrary, it ensures that a large fraction of the gas is neutral and thus completely self-shielding (see e.g. Wolfe et al., 2005). This means that ionization corrections are negligible, such that the singly-ionized metal lines with ionisation potentials below 13.6 eV trace the total metal abundance [i.e. $N(\mathrm{Zn\,II}) / N(\mathrm{H\,I}) = N(\mathrm{Zn}) / N(\mathrm{H})$]. The high neutrality of the gas is a vital precursor for the formation of molecular clouds and subsequent star formation. Other Lyα absorbers include sub-DLAs ($10^{19} < N(\mathrm{H\,I}) < 2\times10^{20}$ cm^{-2}), Lyman-limit systems (LLS; $10^{17} < N(\mathrm{H\,I}) < 10^{19}$ cm^{-2}), and Lyα forest absorbers ($N(\mathrm{H\,I}) < 10^{17}$ cm^{-2}), which all contain hydrogen mainly in

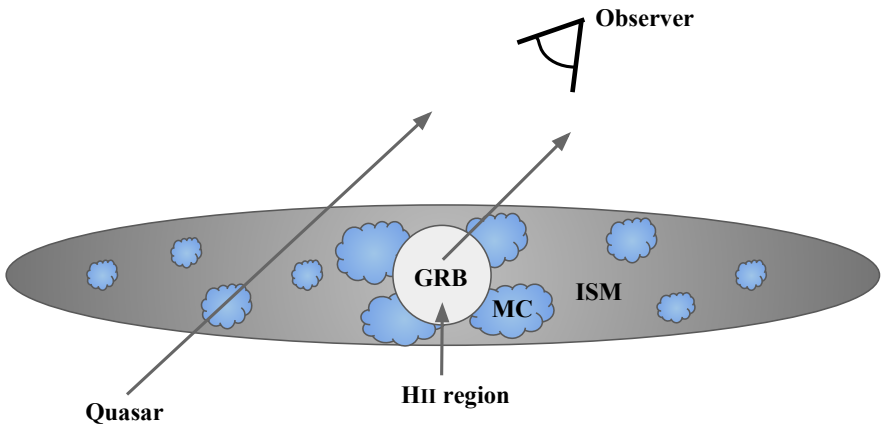

Figure 1.2.2. A simplistic cartoon illustration of the typical impact parameters for GRB and quasar sightlines (similar to fig. 1 from Prochaska et al., 2007). The extent of the galactic disc is roughly on a scale of 10 kpc. GRB absorption systems are expected to originate close to the center of the host, whereas quasar sightlines are more likely to probe the outer regions of the ISM. The typically observed larger abundance of H I in GRB absorbers is purely a selection effect. The blue bubbles represent cold molecular clouds distributed throughout the host galaxy environment. The 'clumpiness' increases closer to the center such that the detection probability of H_2 and C I decreases as a function of impact parameter.

ionized form (Rauch, 1998; Prochaska, 1999; Wolfe et al., 2005). DLAs therefore provide one of the most accurate probes of the chemical enrichment of the neutral gas-phase of the ISM in galaxies through most of cosmic time.

Since their first discovery, multiple surveys for DLAs in quasar sightlines have been carried out (Lanzetta et al., 1991, 1995; Wolfe et al., 1995; Boisse et al., 1998; Storrie-Lombardi & Wolfe, 2000; Rao & Turnshek, 2000; Ellison et al., 2001; Péroux et al., 2003; Rao et al., 2006). With the contribution of the extensive spectroscopic database from the SDSS, several thousand DLAs have been identified in quasar sightlines to date (Prochaska & Herbert-Fort, 2004; Prochaska et al., 2005; Noterdaeme et al., 2009b, 2012a), with a few hundred observed with high-resolution spectrographs (Ledoux et al., 2003, 2006; Noterdaeme et al., 2008; Rafelski et al., 2012; Berg et al., 2015; De Cia et al., 2016).

Significant effort has also been put into follow-up campaigns of GRBs, in which DLAs are typically detected in the optical afterglow spectra (Fynbo et al., 2009; Selsing et al., 2019). More than 100 neutral hydrogen absorbers have now been identified in GRB host absorption systems, with the majority ($\gtrsim 85\%$) being classified as DLAs (Tanvir et al., 2019). The main difference between the host galaxy absorbers observed in GRB afterglows compared to the absorption systems intervening quasar sightlines is that the former population is observed to be substantially more gas-rich on average (Vreeswijk et al., 2004; Jakobsson et al., 2006b; Watson et al., 2006). Comparing the two absorber populations requires a good understanding of the underlying selection bias introduced when building the respective samples. While GRBs are likely to explode

within the central regions of their host galaxies, quasar absorbers are selected depending on their neutral gas cross-section which is related to their size and luminosity (Zwaan et al., 2005). As a consequence, GRB host galaxy absorption systems are expected to show higher gas and metal column densities than quasar absorbers, as is observed (Savaglio et al., 2003; Savaglio, 2006; Prochaska et al., 2007; Fynbo et al., 2008, 2009; Arabsalmani et al., 2015). A schematic of this sightline effect is shown in Fig. 1.2.2. From the figure it is clear that quasar absorbers tend to probe the outer regions of the ISM or the halo gas of the intervening galaxy, whereas GRB sightlines probe the hearts of their star-forming host galaxies.

1.2.1 Gas-phase abundances and kinematics

In addition to the strong Lyα absorption line typically observed in GRB and sporadically in quasar spectra, associated absorption lines from metal transitions are also commonly detected. By deriving the column densities of the observed metal line transitions, it is possible to infer the gas-phase abundances of a specific element, X, in the line of sight. If the column density of neutral hydrogen can additionally be constrained, the measured relative abundances can be compared with the equivalent solar values, providing the metallicity of the absorption system as

$$[\mathrm{X/H}] \equiv \frac{\log N(\mathrm{X})}{\log N(\mathrm{H})} - \frac{\log N(\mathrm{X})_{\odot}}{\log N(\mathrm{H})_{\odot}}$$

where [X/H] = 0 defines solar metallicity of X (with reference values most widely adopted from Asplund et al., 2009). Again, since the gas is predominantly neutral in DLAs, the low-ionization transitions will trace most of the element X abundance. To obtain a reliable estimate of the actual gas-phase metallicity, only volatile or mildly depleted elements such as zinc or sulphur should be used as tracers. Some fraction of the metals in the ISM are also expected to be in the dust-phase, such that they will appear depleted from the observed abundances. By estimating the depletion pattern it is possible to correct for this effect, however, and accurately derive the total metal content of DLAs (see Sect. 1.2.2), in addition to estimate the dust content of the absorbing system.

Since DLAs are believed to be the dominant reservoirs of neutral gas at all redshifts, they are unique tools to map out the cosmic chemical enrichment of the ISM in galaxies through most of cosmic time. For instance, they have been widely used to trace the redshift evolution of the gas-phase metallicity in quasar absorbers (Pettini et al., 1994; Pei et al., 1999; Kulkarni & Fall, 2002; Prochaska et al., 2003; Rafelski et al., 2012, 2014; De Cia et al., 2018) and GRB host absorption systems (Fynbo et al., 2006b; Cucchiara et al., 2015), which both agree on a common evolution of the average gas-phase metallicity as a function of redshift. The latest compilation of quasar DLAs by Berg et al. (2015), observed with high-resolution spectrographs (following De Cia et al. 2018), for which reliable gas-phase metallicies could be derived is shown in the top panel of Fig. 1.2.3. Overplotted are the GRB host absorption systems observed with medium- to high-resolution spectrographs (the largest contribution being from the XS-GRB sample; Selsing et al., 2019) for which an accurate metallicity could be derived. Both absorber populations appear to follow similar trends of increasing metallicities

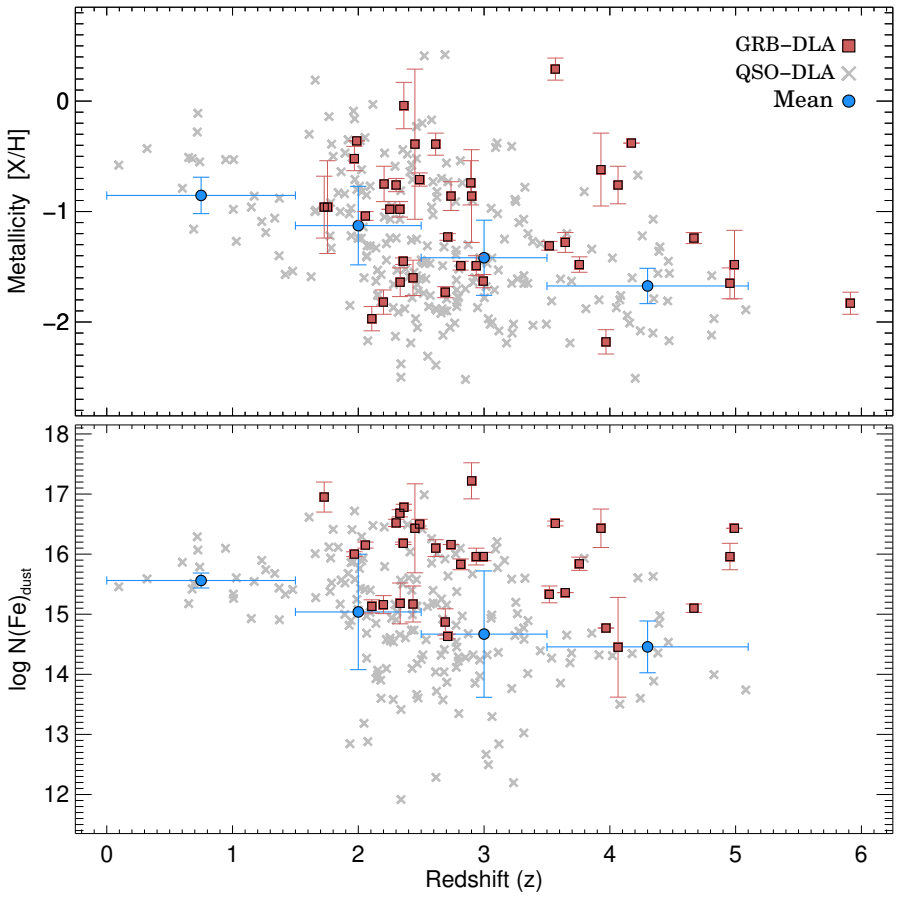

Figure 1.2.3. Redshift evolution of neutral gas-phase metallicity (upper panel) and dust-phase iron column density (lower panel). Grey crosses represent a recent compilation of quasar DLAs (Berg et al., 2015; De Cia et al., 2018) and red squares denote GRB absorbers (e.g. Bolmer et al., 2019). The blue dots represent the average quasar DLA metallicity divided into redshift bins of $0 < z < 1.5$, $1.5 < z < 2.5$, $2.5 < z < 3.5$, and $z > 3.5$ (with the sample variance as the vertical error bars). Both absorber populations are found to show an increase in metal and dust content for decreasing redshifts.

with decreasing redshift.

One important caveat to keep in mind before drawing conclusions for the underlying absorber population is the effect of selection bias, and in particular if a certain type of absorption system is excluded from existing samples. While the high-energy emission from GRBs is virtually unaffected by dust, very dust-obscured sightlines will significantly hamper the spectroscopic follow-up of their optical afterglows and will thus appear as optically 'dark' bursts (Fynbo et al., 2001, 2009; Jakobsson et al., 2004). Typical quasar selection techniques are also subject to a significant dust bias, excluding sightlines with intervening dusty and therefore likely also metal-rich foreground

galaxies (Fall & Pei, 1993; Pontzen & Pettini, 2009; Krogager et al., 2019). We attempt to quantify this selection bias in Chapter 8, for both the quasar and GRB absorber populations.

If the early assumptions that the broad Lyα absorption feature observed toward quasars trace the gaseous, thin disk of proto-type galaxies (Wolfe et al., 1986) is true, then this should also be reflected in the velocity structure seen in the metal line profiles. One approach to quantify the velocity width of the low-ionization lines is by measuring ΔV_{90}, defined as the velocity encompassing 90% of the apparent optical depth, τ (Prochaska & Wolfe, 1997; Ledoux et al., 1998). The velocity width can then be calculated as

$$\Delta V_{90} = c\frac{\lambda_{95} - \lambda_5}{\lambda_0}$$

where λ_0 is the line centroid and λ_5 and λ_{95} are the 5^{th} and 95^{th} percentiles of the distribution of τ for a given line. Based on models including ΔV_{90} and the velocity structure of the absorption line profiles, Prochaska & Wolfe (1997, 1998) concluded that the metal lines observed in quasar DLAs are consistent with probing large rotating disks. In addition, Ledoux et al. (2006) also found a relation between ΔV_{90} and [X/H], which they argued was a consequence of an underlying mass-metallicity relation for the galaxies responsible for the DLA absorption lines. This suggests that the quantity ΔV_{90} holds information about the dynamical mass of the absorbing galaxies.

The dominant metal lines from DLAs observed in quasar and GRB afterglow spectra are from low-ionization line transitions, used to constrain the metallicity and kinematics of the neutral gas as described above. Most absorbers also show lines from higher ionization states such as C IV, Si IV, N V and O VI which is believed to trace the hot circumgalactic halos (e.g. Fox et al., 2007b). The high-ionization lines are typically observed to show larger velocity widths than the low-ionization lines, indicating a larger velocity dispersion in the hot photoionized gas component compared to the neutral gas. Some of these high-ionization lines might also be populated by enhanced ionization if an absorber is close to the background quasar (typically designated as 'proximate' DLAs, Ellison et al., 2010) or from the increased photon flux from the prompt and afterglow emission of the GRB (Prochaska et al., 2008b; Fox et al., 2008). There is at least now conclusive evidence that the GRB can have an effect on the surrounding environment. Based on the detection and line variability of excited fine-structure lines, Vreeswijk et al. (2007) determined that the excited lines are populated by UV-pumping from the GRB afterglow. Based on this model, it is also possible to infer the distance from the GRB to the absorbing cloud (which is typically found to be of the order $d = 0.5 - 2$ kpc) based on the radiation field required to populate the excitated transitions.

In Fig. 1.2.4 is shown a schematic of the different locations of the both the low- and highly-ionized absorbing gas, as observed in the sightline to the GRB from the afterglow spectra. While the majority of the absorbing gas might be located at several kpc from the GRB, a circumburst origin for some of the observed features might not be completely ruled out. For example, Prochaska et al. (2008b) argue that N V could be populated by photoionization from the afterglow to within $d \lesssim 10$ pc from the burst. It is also on the same scale that helium is expected to cause most of the observed soft X-ray absorption (Watson et al., 2013). Connecting these two observables is the focus of Chapter 3, where a systematic study of the circumburst gas and metals surrounding

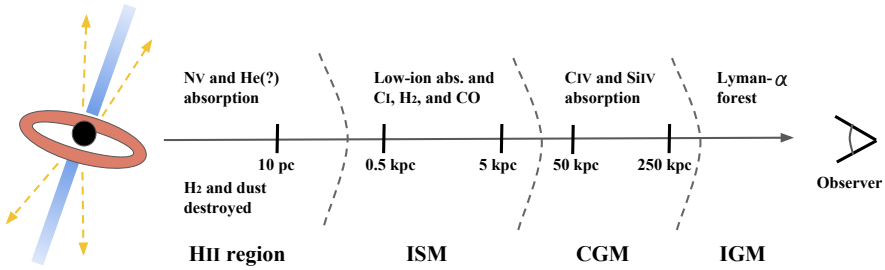

Figure 1.2.4. Schematic showing the location of the different absorption components in the line of sight to a GRB (loosely based on fig. 2.9 from Thöne, 2008). Close to the burst ($d \lesssim 10$ pc), dust and H_2 molecules will be destroyed. N v is expected to be produced here (either from photo-ionization or recombination) and significant He absorption of soft X-ray photons are expected here as well. At $d \approx 0.5 - 2$ kpc the main absorption components from the low-ionization metal lines and fine-structure transitions probe the neutral ISM. Further out at $d \approx 50 - 250$ kpc the high-ionization lines C IV and Si IV are though to probe the hot halo of the cirgumgalactic material. At high-z, absorption components from the intergalactic medium will be present as well.

GRBs is presented as well.

1.2.2 The effect of dust

Depletion of refractory elements

As described above, the gas-phase abundances of the neutral ISM can be derived by measuring the column density of the element, X, and compare it to the neutral hydrogen content. However, refractory elements such as iron typically show very low relative abundances compared to the mildly depleted elements such as zinc and sulphur. For any refractory element, Y, the depletion level can be derived relative to a volatile element, X, as

$$[\mathrm{X/Y}] = \frac{\log N(\mathrm{X})}{\log N(\mathrm{Y})} - \frac{\log N(\mathrm{X})_\odot}{\log N(\mathrm{Y})_\odot}$$

The depleted fraction of a given metal in the dust phase is then $D(\mathrm{Y}) = 1 - 10^{[\mathrm{Y/X}]}$, which also represents the dust-to-metals ratio in the absorbing system. The reason why large fractions of refractory elements are missing from the gas-phase is because they are locked and condensed into dust and therefore appear depleted (e.g. Jenkins, 1987; Savage & Sembach, 1996). These dust grains are primarily made up of O, Si, Mg, and Fe metals (Draine, 2003). The strength of the dust depletion depends primarily on the density and chemical enrichment of the gas. For example, Jenkins (2009) showed that a wide range of abundances in more than 200 Galactic sightlines are tighly connected to each other via a single parameter, the depletion strength F_*. Based on this, De Cia et al. (2016) derived empirical sequences for the relative abundances and demonstrated that they are universally valid for sightlines through the Galactic ISM and high-redshift DLA systems.

From the depletion level, it is possible to derive the amount of refractory elements in the dust-phase of the ISM (Vladilo et al., 2006). For example, the column density of iron in the dust-phase is given as

$$N(\mathrm{Fe})_{\mathrm{dust}} = N(\mathrm{X}) \left(1 - 10^{[\mathrm{Fe/X}]}\right) \left(\frac{\mathrm{Fe}}{\mathrm{X}}\right)_{\odot}$$

where X is again any volatile of mildly depleted element. Studying the redshift evolution of $N(\mathrm{Fe})_{\mathrm{dust}}$ might provide clues for the production and cosmic evolution of dust. In the bottom panel of Fig. 1.2.3, the dust-phase iron column density is shown as a function of redshift for the same samples of quasar and GRB absorbers described in the previous section. It is clear that the GRB absorbers generally show elevated abundances of elements in the dust phase compared to quasar absorbers. $N(\mathrm{Fe})_{\mathrm{dust}}$ also appears to follow a similar evolution trend as the metallicity for the same absorption systems. It is important to caution here though that, particularly at high-z, the large values of $N(\mathrm{Fe})_{\mathrm{dust}}$ especially observed in the GRB absorbers, could also be explained by a deficiency of iron-peak elements which have not had enough time to be produced from type Ia supernovae.

Line-of-sight extinction

Another observable effect of dust is the scattering of light in the line of sight from the emission source to the observer. The amount of scattering is wavelength-dependent, causing the background source to appear 'reddened', and also causes an overall dimming effect. The dust *extinction* properties of the ISM in a galaxy is distinct from the dust *attenuation* properties, which is subject to complex radiative transfer effects reprocessing the stellar light and which also depends on the geometric distribution of the dust, gas, and stars (e.g. Narayanan et al., 2018). The shape of the dust extinction curve is only dependent on the dust composition and grain size distribution of the dust particles located in the line of sight. In Fig. 1.2.5, three different GRB optical afterglow spectra are shown; one showing little to no dust (GRB 161023A), one with a small amount of dust with properties described by a smooth, SMC-like extinction curve (GRB 151021A), and one significantly dust-reddened sightline showing an additional extinction 'bump' (GRB 180325A), known as the 2175 Å dust extinction feature (e.g. Draine, 1989). Carbonaceous dust grains are believed to produce this particular type of extinction (Henning & Salama, 1998), and the overall shape of the extinction curves can be described by a combination of silicates and carbonaceous material (Draine, 2003).

The extinction (or reddenening) curve is typically quantified by the wavelength-dependent extinction A_λ, relative to the V-band extinction, A_V. The extinction can also be expressed in terms of the color excess from the B- to V-band extinction, $A_B - A_V = E(B-V)$, which is linked to the V-band extinction via the total-to-selective reddening paramater, $R_V = A_V/E(B-V)$. This quantity is then simply a measure of the slope of the extinction curve, which is related to the average dust grain size distribution (where larger particles result in higher observed values for R_V). Previously, the most commonly adopted extinction curve models was parametrized by Cardelli et al. (1989) and Pei (1992). A more general formulation was provided by Fitzpatrick & Massa (1990, 2007), which will be used throughout this thesis, that describes the extinction curve through a

set of nine parameters as

$$A_\lambda = \frac{A_V}{R_V}\left(k(\lambda - V) + 1\right) ,$$

where the relative reddening, $k(\lambda - V)$, is given as

$$k(\lambda - V) = \begin{cases} c_1 + c_2 x + c_3 D(x, x_0, \gamma), & \text{for } x \leq 5.9 \\ c_1 + c_2 x + c_3 D(x, x_0, \gamma) + c_4 (x - c_5)^2, & \text{for } x > 5.9 \end{cases} ,$$

and the Lorentzian-like 'Drude' profile representing the 2175 Å dust extinction feature is described as

$$D(x, x_0, \gamma) = \frac{x^2}{(x^2 - x_0^2)^2 + x^2 \gamma^2}$$

with $x = \lambda^{-1}$ in units of μm^{-1}. Basically, this dust model contains two components, one describing the linear UV part of the spectrum via the components c_1 (intercept), c_2 (slope) and the terms c_4 and c_5 describing the far-UV curvature. The second component is the Drude profile representing the 2175 Å extinction bump, controlled by the parameters c_3 (bump strength), x_0 (central wavelength) and γ (width of the bump). The last two parameters are the visual extinction, A_V, and the total-to-selective reddening, R_V. The advantage of such a parametrization of the dust-extinction model, is that it for example allows for the strength and width of the 2175 Å dust bump to be constrained independently, and also provides a way for dust extinction curves with no local analogs to be constructed, which we applied in Chapter 2. The observed dust-reddened spectrum can then be described by a simple model as $F_{\text{obs}} = F_\lambda \times 10^{-0.4 A_\lambda}$. The visual extinction, A_V, can then be estimated assuming a given dust-extinction model when knowing the redshift of the GRB or quasar absorption system and by assumming some underlying intrinsic spectrum. In the case of GRB afterglows, a smooth power-law of the form $F_\lambda = \lambda^{-\beta}$ is typically observed, and is believed to originate from synchrotron radiation emitted from the interaction and deceleration of the ultra-relativistic GRB jet in an external medium (Sari et al., 1998, see also Sect. 1.1.1). To substitute as the intrinsic quasar spectrum, a composite of bright, instrinsically 'blue' quasar spectra are usually applied, which will be demonstrated in Chapter 8.

If the same dust composition and distribution of the overall ISM is probed by either directly measuring the line-of-sight extinction or as inferred from the relative depletion patterns, the dust content is expected to scale. There are, however, an observed discrepancy between the two. One explanation could be that GRB sightlines probe grey dust and the SED-derived A_V will therefore be understimated (Savaglio et al., 2003). Another could be that the two approaches probe dust on different scales and by distinct elements. Reconciling this discrepancy forms the basis of Chapter 5, where the latter scenario is demonstrated to, at least partially, cause some of the tension.

1.2.3 Cold and molecular gas

Since the neutral gas in DLAs provide a natural 'fuel' for star formation, molecular hydrogen is expected to be present in most sightlines. The detections of H_2 in quasar DLA spectra are, however, found to be scarce with an estimated detection rate of

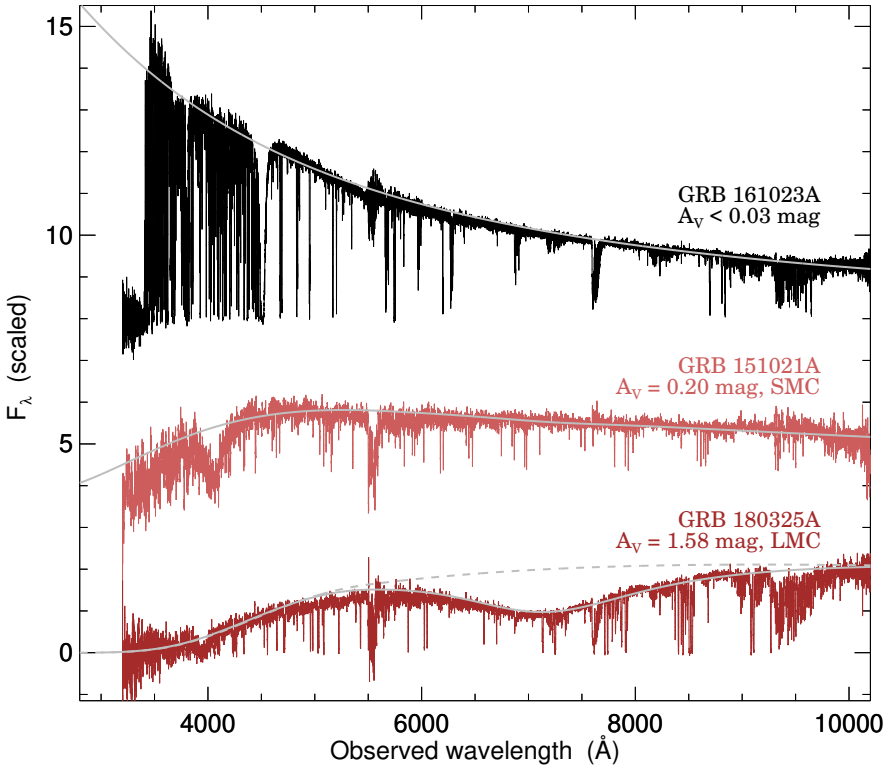

Figure 1.2.5. Three distinct optical afterglow spectra of GRBs at $z \approx 2.5$ illustrating the effect of dust. The spectrum at the top is of GRB 161023A, showing little to no dust extinction (with $A_V <$ 0.03 mag; de Ugarte Postigo et al., 2018). The two bottom spectra show the dust-extinguished optical afterglows of GRB 151021A (with $A_V = 0.20$ mag, see Chapter 4) and GRB 180325A (with $A_V = 1.58$ mag; Zafar et al., 2018a). The latter GRB afterglow also has an additional extinction 'bump' imprinted on the spectrum, known as the 2175 Å dust extinction feature, which is illustrated by the grey dashed line showing the same extinction curve but without the bump.

$\lesssim 10\%$ for the overall population of DLAs (see e.g. Jorgenson et al., 2014; Balashev et al., 2014; Balashev & Noterdaeme, 2018). The detection probability is found to increase for sightlines rich in H I gas though (Noterdaeme et al., 2015a), or showing high metallicities (Petitjean et al., 2006), large dust-to-gas ratios (Ledoux et al., 2003) and significant dust-phase iron column densities (Noterdaeme et al., 2008).

Since GRBs are expected to probe star-forming galaxies, and star-formation rates are driven by the availability of dense, molecular gas, the detection of H_2 absorption features was also expected to be a common occurence in the optical afterglow spectra of GRBs. This was also motivated by their large H I column densities probing the same regimes as observed for H_2-bearing quasar DLAs (Vreeswijk et al., 2004; Watson et al., 2006), which also resembled Galactic molecular clouds (Jakobsson et al., 2006b).

The first unambiguous detection of H_2 imprinted on a GRB afterglow spectrum was, however, first observed in GRB 080607 at $z = 3.0363$ (Prochaska et al., 2009). One initial explanation for the apparent paucity of molecular hydrogen in GRB host galaxies could be that the H_2 molecules are photodissociated by the GRB event itself. The intense prompt γ-ray flash and afterglow emission will, however, only impact gas in the vicinity of the GRB (out to 10 pc; Draine & Hao, 2002). The cold and neutral absorbing gas is typically found to be located at much greater distances from the GRB (see e.g. Fig 1.2.4), which can be inferred either from the time variability of line transitions excited by the GRB afterglow flux or the minimum distance required to sustain a significant fraction of neutral gas (Prochaska et al., 2006). Due to the limited data with high enough quality it was at first difficult to determine if this was a real effect. Based on the XS-GRB afterglow legacy survey, Bolmer et al. (2019) performed the first statistical analysis of the presence of H_2 in GRB afterglow spectra and concluded that there is actually no lack of H_2 in GRB host absorption systems compared to the overall population of quasar DLAs. The overall fraction of H_2 detections are higher in the GRB absorber population (by selection), but above the threshold of $N(\mathrm{H\,I}) > 10^{21.7}\,\mathrm{cm}^{-2}$ where the H I-to-H_2 transition is believed to occur, the detection rates are consistent for both DLA populations.

The absorption signatures of H_2 are the Lyman and Werner (L-W) bands which are located bluewards of the Lyα absorption line, and is therefore only observable from the ground in absorbing galaxies at $z \gtrsim 2$. Due to the location of the L-W bands, high spectral resolution is required to distinguish the line transitions associated with H_2 from the wealth of absorption features from the Lyα forest. High resolution spectra are, however, only obtained for the brightest and therefore also likely less dust-obscured GRBs (Ledoux et al., 2009). The sightlines most likely to exhibit H_2 absorption are therefore also the most difficult to observe due to the faintness of the afterglows. The absorption signatures from neutral atomic-carbon (C I) are another efficient probe of the shielded molecular gas-phase and can be used to study the cold, neutral medium in the ISM. C I is typically observed to be coincident with H_2 in quasar DLAs (e.g. Srianand et al., 2005), so targeting C I systems should reveal absorbers rich in molecular gas (Ledoux et al., 2015). This is the basis of Chapter 4. The coincidence of C I with H_2 is likely related to the ionization potential of C I (11.26 eV) being similar to the energy range of Lyman-Werner photons that can photodissociate H_2 (11.2 – 13.6 eV). The most prominent C I $\lambda\lambda$ 1560,1656 line transitions are also located far from the Lyα forest and can be identified even in low- to medium-resolution spectroscopy.

Determining line abundances

Since the lines associated with H_2 and C I typically originate from cold gas, the intrinsic line broadening is expected to be small. The majority of GRB afterglow spectra studied in this thesis showing C I are observed with the X-shooter spectrograph mounted at the ESO-VLT. In Fig. 1.2.6, it is shown how an observed C I line complex changes drastically depending on the spectral resolution. It is clear from the figure that the instrumental broadening will at some point smooth out the intrinsic profile such that all information of the relative abundances are lost. At low spectral resolution, there might also be so-called 'hidden' saturation (e.g. Prochaska, 2006), where the lines

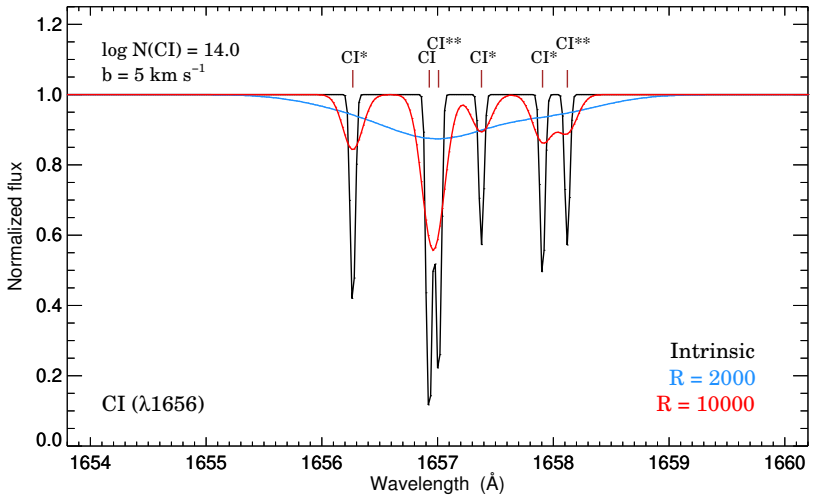

Figure 1.2.6. Synthetic absorption line profiles of the C I λ1656 ground-state and exited transitions. The intrinsic absorption line (in black) with a total column density of $\log N(\mathrm{C\,I}) = 14.0$ and broadening parameter $b = 5\,\mathrm{km\,s^{-1}}$ is shown together with two identical lines but convolved by representative instrumental resolutions of $\mathcal{R} = 2000$ (in blue) and $\mathcal{R} = 10000$ (in red). This illustrates that in low-resolution spectroscopy, the line profiles might be affected by hidden saturation, making intrinsically satured lines appear non-saturated due to instrumental broadening. This effect also removes any informtion on the intrinsic velocity structure.

appear to be well constrained but is in fact intrinsically saturated. The equivalent width (EW) of the lines are, however, not dependent on the resolution so the measured EWs should be the same in all cases: in the example C I line complex shown in Fig. 1.2.6, the convolved versions of the lines are indeed measured to all have total EWs of 0.21 Å. If several components are blended together, however, the measured EWs will tend to underestimate the actual total element abundance. The C I abundances should therefore be carefully derived, which was a large part of the work done for the results presented in Chapter 6.

Typically, the line abundances are derived by modelling the observed lines with Voigt profiles. The Voigt profile is a probability distribution given by a convolution of the Gaussian and Lorentzian distribution functions. For practical purposes, an analytical approximation is typically used (e.g. Tepper-García, 2006), which is also adopted in the line fitting routine used throughout this thesis (`VoigtFit`; Krogager, 2018). Other tools relying on a Bayesian approach to line fitting have also recently been developed (Liang & Kravtsov, 2017; Bolmer et al., 2019). Common to both approaches is that they calculate the optical depth, τ, for the total number of transitions for the observed transmittance of $I(\lambda) = e^{-\tau(\lambda)}$. τ is then determined by the column density of the element X, given a set of atomic parameters describing the line strength, f_i, the damping constant, Λ_i, and the resonance wavelength, λ_i, for any given transition, i. The fit also includes an estimate of the broadening parameter b, which is a combination of turbulent and Doppler broadening and therefore carries information about the velocity and temperature of the

gas. A large part of the work presented in Chapters 3 and 6, is based on deriving column densities for various elements using this approach.

Most of the groundwork for this thesis has now been outlined, laying the foundation for the work presented in the following chapters. The topics covered in this thesis are divided into three parts, each with their own specific focus. The unifying theme, common to all three parts, are the use of GRBs and quasars as probes of dust, gas and metals in the interstellar medium of galaxies through cosmic time.

Part I

The Circumburst Regions of Gamma-Ray Bursts

Chapter 2

Dust in the circumburst medium

This chapter is based on the following article:

Steep extinction towards GRB 140506A reconciled from host galaxy observations: Evidence that steep reddening laws are local

Published in Astronomy & Astrophysics, vol. 601, id. A83, 10 pp. (2017)

Authors:
K. E. Heintz, J. P. U. Fynbo, P. Jakobsson, T. Krühler, L. Christensen, D. Watson, C. Ledoux, P. Noterdaeme, D. A. Perley, H. Rhodin, J. Selsing, S. Schulze, N. R. Tanvir, P. Møller, P. Goldoni, D. Xu & B. Milvang-Jensen

We present the spectroscopic and photometric late-time follow-up of the host galaxy of the long-duration *Swift* γ-ray burst GRB 140506A at $z = 0.889$. The optical and near-infrared afterglow of this GRB had a peculiar spectral energy distribution (SED) with a strong flux-drop at 8000 Å (4000 Å rest-frame) suggesting an unusually steep extinction curve. By analysing the contribution and physical properties of the host galaxy, we here aim at providing additional information on the properties and origin of this steep, non-standard extinction. We find that the strong flux-drop in the GRB afterglow spectrum at < 8000 Å and rise at < 4000 Å (observers frame) is well explained by the combination of a steep extinction curve along the GRB line of sight and contamination by the host galaxy light at short wavelengths so that the scenario with an extreme 2175 Å extinction bump can be excluded. We localise the GRB to be at a projected distance of approximately 4 kpc from the centre of the host galaxy. Based on emission-line diagnostics of the four detected nebular lines, Hα, Hβ, [O II] and [O III], we find the host to be a modestly star forming (SFR $= 1.34 \pm 0.04\ M_\odot\ \mathrm{yr}^{-1}$) and relatively metal poor ($Z = 0.35^{+0.15}_{-0.11}\ Z_\odot$) galaxy with a large dust content, characterised by a measured visual attenuation of $A_V = 1.74 \pm 0.41$ mag. We compare the host to other GRB hosts at similar redshifts

and find that it is unexceptional in all its physical properties. We model the extinction curve of the host-corrected afterglow and show that the standard dust properties causing the reddening seen in the Local Group are inadequate in describing the steep drop. We thus conclude that the steep extinction curve seen in the afterglow towards the GRB is of exotic origin and is sightline-dependent only, further confirming that this type of reddening is present only at very local scales and that it is solely a consequence of the circumburst environment.

2.1 Introduction

Gamma-ray bursts (GRBs) have proven to be valuable tools to probe the interstellar medium (ISM), chemical enrichment and dust content of star-forming galaxies both in the local Universe and out to high redshifts (e.g. Jakobsson et al., 2004; Fynbo et al., 2006b, 2009; Prochaska et al., 2007; Li, 2008; Ledoux et al., 2009; Gehrels et al., 2009; Schady et al., 2012; De Cia et al., 2013; Thöne et al., 2013; Sparre et al., 2014; Hartoog et al., 2015). Specifically, the optical and near-infrared extinction curves seen toward GRB afterglows reveal that they typically can be well-described by similar prescriptions to that of the Milky Way (MW) and the Small and Large Magellanic Clouds (SMC and LMC) (see e.g. Schady et al., 2010; Covino et al., 2013; Japelj et al., 2015). In rare cases, however, the afterglows appear to show flat (also known as grey) extinction curves (Savaglio & Fall, 2004; Perley et al., 2008; Friis et al., 2015) or at the opposite extreme, very steep extinction curves. In the latter case, a prime example is seen towards the afterglow of GRB 140506A (Fynbo et al., 2014) but also reported in the spectral energy distribution (SED) of the afterglow of GRB 070318 (Fynbo et al., 2009; Watson, 2009) and bluewards of the observed 2175 Å bump in GRB 080605A (Zafar et al., 2012; Krühler et al., 2012).

This paper reports on the spectroscopic and photometric late-time follow-up of the host galaxy of GRB 140506A at $z = 0.889$. This GRB was first detected by *Swift* on 2014 May 6, 21:07:36 UT (Gompertz et al., 2014). At 8.8 and 33 hours post-burst, Fynbo et al. (2014) acquired spectra with the X-shooter spectrograph (Vernet et al., 2011) which, together with extensive imaging from the Gamma-Ray burst Optical and Near-infrared Detector (GROND; Greiner et al., 2008), revealed a peculiar optical and near-infrared afterglow and the first detections of He I* and Balmer line absorption in GRBs. In contrast to other GRB afterglow SEDs, which typically can be modelled with a simple power-law with weak SMC-like extinction, a strong, gradual flux drop is seen below 8000 Å (4000 Å rest-frame, see Fig. 2.2.1) that can not be modelled by any of the extinction curves known from the Local Group. By analysing the host we here aim to better constrain the physical origin of this steep extinction curve.

The paper is structured as follows. In Section 2.2 we describe our observations and in Sects. 2.3 and 2.4 we describe how we constrained the properties of the host galaxy with special emphasis on the implications for the interpretation of the extinction derived from the afterglow spectroscopy. In Section 2.5 we summarise and conclude. Throughout the paper we assume a standard flat ΛCDM cosmology with $H_0 = 67.3$ km s^{-1} Mpc^{-1}, $\Omega_m = 0.315$ and $\Omega_\Lambda = 0.685$ (Planck Collaboration et al., 2014). Unless otherwise stated, all magnitudes are given in the AB (Oke, 1974) magnitude system.

2.2 Observations and data reduction

Based on the peculiar (and temporally varying) SED of the optical and near-infrared afterglow of GRB 140506A, acquired at two epochs at $\Delta t = 8.8$ hr and $\Delta t = 33$ hr after the burst, respectively, we decided to observe the host galaxy of the GRB to examine the nature of this in more detail than what can be extracted from the afterglow spectra.

Table 2.2.1. Photometry of the host galaxy from FORS2 and *Spitzer*/IRAC imaging.

Date (Δt)[a]	Filter	Eff. wavelength	Exp. time	Avg. airmass	Seeing[b]	Mag$^{c}_{\rm AB}$
2015-04-29 (357.48 d)	$u_{\rm HIGH}$	3610 Å	3×500 s	1.166	0.″62	25.60 ± 0.30
2015-04-29 (357.50 d)	$g_{\rm HIGH}$	4700 Å	3×300 s	1.171	0.″60	25.47 ± 0.21
2015-06-16 (405.24 d)	$R_{\rm SPECIAL}$	6550 Å	5×200 s	1.323	0.″70	25.16 ± 0.19
2015-06-16 (405.26 d)	$I_{\rm BESS}$	7680 Å	5×200 s	1.280	0.″67	24.46 ± 0.20
2015-07-04 (423.12 d)	IRAC 1	3.6 μ m	2400 s	···	···	23.88 ± 0.30

Notes. [a]The date of observations are listed with the number of days from the trigger in brackets. The time is calculated from the start of observations to the time of trigger. [b]Measured from the full-width-at-half-maximum of non-saturated stellar sources on the stacked images. [c]Magnitudes reported here have been corrected for the Galactic foreground reddening and will be used throughout our analysis.

2.2.1 FORS2 imaging

We acquired late-time photometry with the FOcal Reducer and low dispersion Spectrograph 2 (FORS2; Appenzeller et al., 1998) instrument at the ESO/VLT on 2015 April 29 and June 16. We obtained images of the field of GRB 140506A using the $u_{\rm HIGH}$, $g_{\rm HIGH}$, $R_{\rm SPECIAL}$ and $I_{\rm BESS}$ broadband filters (henceforth, these will be referred to as simply the *u*-, *g*-, *R*- and *I*-band, respectively). In Table 2.2.1 a log of the FORS2 observations is provided together with the measurements of the magnitude of the host galaxy in each filter.

The photometric calibration of the observations in the *u*- and *g*-bands was done using zeropoints measured from reference stars observed at similar airmasses on the nights of the observations of the host galaxy. For the *R*- and *I*-bands we use the zeropoints reported in the ESO archive for the night of observation. All images were taken following a dithering pattern and were bias-subtracted and flat-fielded using standard `IRAF` (Tody, 1993) routines. The images acquired in April were taken under excellent conditions with a median seeing of 0.″61, where for the images obtained in June we report a median seeing of 0.″69. To measure the magnitude of the host we performed aperture photometry of the source in the combined frames of each filter using standard MIDAS routines.

2.2.2 Spitzer/IRAC observations

The position of GRB 140506A was observed by Spitzer/IRAC in the 3.6 μm filter as part of the extended *Swift/Spitzer* GRB Host Galaxy Survey (SHOALS; Perley et al., 2016a, GO program 11116) on 2015 July 4, with a total integration time of 2400 seconds. We

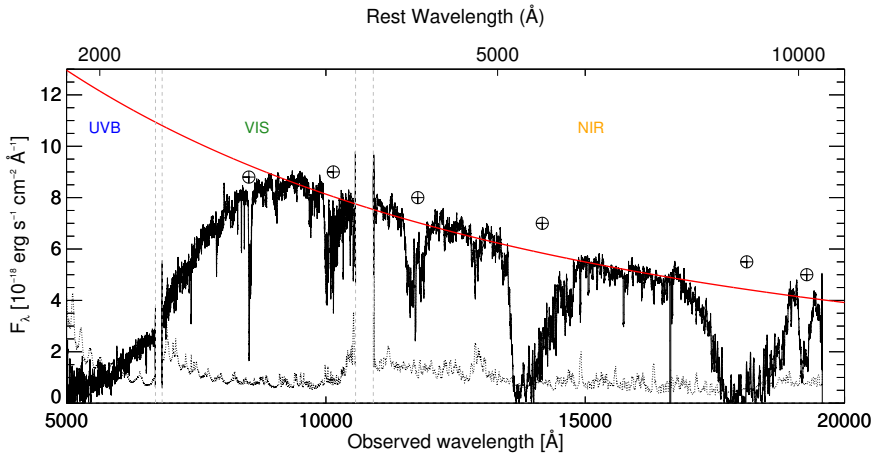

Figure 2.2.1. X-shooter spectrum of the first epoch afterglow (identical to the top panel in Fig. 4 of Fynbo et al., 2014). Regions affected by telluric absorption are marked by the corresponding symbol. The error spectrum is plotted as the dotted line. Overplotted is the best-fit power law following $F_\lambda \propto \lambda^{-\beta}$, fitted to the afterglow continuum at > 8000 Å shown by the red solid line.

downloaded the reduced imaging (PBCD) from the *Spitzer* Heritage Archive. The area close to the GRB host galaxy is affected by a weak pulldown artifact from a nearby star; we fixed this manually by adding a constant term to the affected columns. The host galaxy is faint but clearly detected in this band, and there is no strong blending from any nearby sources. We measure photometry of the galaxy again using standard aperture photometry techniques using the zeropoints in the IRAC handbook for the absolute calibration.

2.2.3 X-shooter spectroscopy

To supplement the FORS2 and *Spitzer* imaging we acquired additional spectra centred on the host galaxy using the X-shooter spectrograph mounted at the ESO/VLT, covering a wavelength range of 3000–24 800 Å (3000–5600, 5500–10 200 and 10 200–24 800 Å for the UVB, VIS and NIR arm, respectively). The follow-up observations of this host were spread out over three nights, on 2015 May 15, June 15 and September 30. The reason for this was that we realised that the heliocentric velocity shift had placed the Hα line on top of a bright sky emission line in May and June. In September the velocity caused by the Earth's orbit was optimal for separating the Hα emission line away from the skyline.

The observations were carried out more than a year after the GRB and we can hence safely assume that there is no significant contribution from the afterglow to the measured fluxes. Extrapolating the temporal flux decay from the GROND afterglow observations suggests that the afterglow contributes less than 5% of the host galaxy flux at this point. The observations were all carried out under good conditions with a seeing between $\sim 0\farcs7 - 1\farcs2$ at airmasses between 1.1 and 1.5. The observations in May

Table 2.2.2. Spectroscopic observations of the host galaxy with X-shooter.

Date (Δt)[a]	Exp. time	Avg. airmass	Seeing[b]
2015-05-15 (373.47 d)	4×600 s	1.198	0.″72
2015-06-15 (404.31 d)	4×600 s	1.184	0.″90
2015-06-15 (404.36 d)	4×600 s	1.173	0.″98
2015-06-15 (404.41 d)	5×600 s	1.268	0.″84
2015-09-30 (511.11 d)	4×600 s	1.233	1.″24
2015-09-30 (511.15 d)	4×600 s	1.332	1.″18
2015-09-30 (511.19 d)	4×600 s	1.492	0.″81

Notes. [a]Same notation as in Table 2.2.1. [b]The seeing is measured from the telescope guide probe.

were carried out in a 4×600 s observing block (OB), while in June and September we acquired three executions of 4×600 s (except for the last OB in June where we acquired 5×600 s), following an ABBA nodding pattern. The slit was aligned with the parallactic angle, and for the multiple executions in June and September we re-aligned the slit between the three executions of the OBs. The slit widths were 1.″0, 0.″9 and 0.″9 in the UVB, VIS and NIR arm, respectively, for all observations. The details for the X-shooter observations are all listed in Table 2.2.2. For this given setup the nominal instrumental resolution in the respective arms are $\mathcal{R}_{\rm UVB} = 5100$, $\mathcal{R}_{\rm VIS} = 8800$ and $\mathcal{R}_{\rm NIR} = 5100$[1] ($\approx$ 59, 34 and 59 km s^{-1}, respectively). From a set of atmospheric emission lines in the VIS and NIR arms we measure resolutions of $\mathcal{R}_{\rm VIS} = 9096$ ($\approx$ 33 km s^{-1}) and $\mathcal{R}_{\rm NIR} = 6977$ ($\approx$ 43 km s^{-1}) at full-width-at-half-maximum (FWHM). These values were determined from sky-lines close to the detected emission lines, and will be used to correct for the intrinsic line widths.

For the X-shooter data reduction we followed the same procedure described in detail in Krühler et al. (2015), so in the following we will only briefly outline our strategy. First we used the ESO X-shooter pipeline (Goldoni et al., 2006; Modigliani et al., 2010) to produce a flat-fielded, rectified and wavelength-calibrated 2D spectrum for every frame in the UVB and VIS arm. For the NIR arm we produced two frames, one for every nod cycle. The resulting 2D frames are then sky-subtracted and rejected for cosmic rays using our own software. The frames are combined by shifting the individual frames and using a weighted average from the signal-to-noise ratio (S/N) to produce one single 2D frame for each arm. We then use a custom-made `Python` code (again see Krühler et al., 2015) to perform optimal extraction on the final 2D frame to obtain the extracted 1D spectrum, using a running Moffat-profile fit to improve the S/N. All wavelengths reported are in vacuum and are corrected for the heliocentric velocity and the Galactic foreground reddening of $E(B-V) = 0.082$ mag (Schlafly & Finkbeiner, 2011).

[1]`https://www.eso.org/sci/facilities/paranal/instruments/xshooter/inst.html`

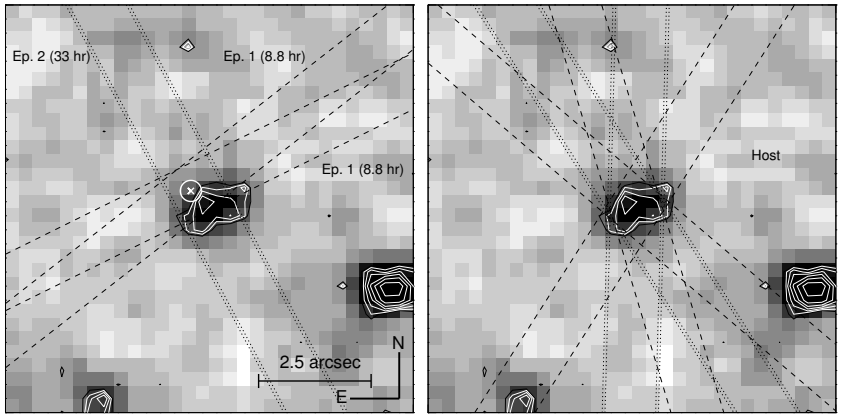

Figure 2.3.1. Close-up of the field of GRB 140506A and its host galaxy from the combined FORS2 I-band image ($7.75'' \times 7.75''$ in both panels). The position of the afterglow is offset $0.''49 \pm 0.03$ (3.92 ± 0.24 kpc at $z = 0.889$) from the host galaxy shown by the white cross with the 3σ uncertainty on the position shown by the surrounding white circle. Schematics of the slit positions used to observe the afterglow and the host are shown during the first and second epoch (left panel) and from the late-time follow-up (right panel). The image has been smoothed to enhance the contrast and the white contours show the relative image flux levels.

2.3 Results

2.3.1 Locating the GRB explosion site

An important piece of information concerning the nature of the steep extinction seen in the optical/near-infrared afterglow of GRB 140506A is the location of the explosion site within its host galaxy. In Figure 2.3.1 we show the projected position of the explosion site relative to the host galaxy in the stacked I-band image obtained with VLT/FORS2. The exact location of the afterglow is determined by coaligning the host image with an image containing the afterglow using a set of reference stars common to both images. The respective centres of the afterglow and the host galaxy was determined by fitting a Gaussian profile to the image profiles. The semi-major axis of the host galaxy, derived from the FWHM of the fitted Gaussian profile, is $0.''96$ (7.68 kpc at $z = 0.889$). The derived position and its 3σ astrometric error is shown by the white cross and white circle, respectively.

We derive an offset of $0.''49 \pm 0.03$ (3.92 ± 0.24 kpc at $z = 0.889$) from the projected position of the afterglow to the centre of the host and show that it originated in a faint region in the outskirts of the galaxy (while GRBs are on average found to explode in the brightest optical regions of their host galaxies, see e.g. Bloom et al., 2002; Fruchter et al., 2006; Lyman et al., 2017). We note that higher resolution is required to securely exclude high-surface brightness at the afterglow position that could be washed out due to ground-based seeing.

The column density of neutral hydrogen ($N_{\rm HI}$) at the GRB explosion sites are typically measured from the broad, damped Lyman-α (Lyα) trough for GRBs at $z \gtrsim 1.8$.

Due to the low redshift of this system, however, we are not able detect this absorption feature. From the *Swift* X-Ray Telescope (XRT) spectra, obtained in photon counting (PC) mode, an intrinsic column density of $N_{\rm H,X} = 6.7^{+1.4}_{-1.3} \times 10^{21}$ cm^{-2} is determined for this burst (see the *Swift*-XRT GRB spectrum repository[2]). This value is among the highest 10% of optically detected bursts (Fynbo et al., 2009), but is typical in *Swift* XRT-observed GRB afterglows (e.g. Campana et al., 2010; Starling et al., 2013; Buchner et al., 2017).

2.3.2 Excluding the 2175 Å extinction bump scenario

The extreme flux-deficit below < 8000 Å (observer frame) seen in the spectrum of the afterglow, is suggested by Fynbo et al. (2014) to be caused by either an extreme 2175 Å bump feature in the extinction curve or due to multiple scattering of light in the nearby environment. The multiple scattering scenario, however, does not seem to be well substantiated in general and was indeed ruled out as the origin of the steep extinction seen towards the supernova SN 2014J (Johansson et al., 2017). The 2175 Å extinction bump feature was motivated by the fact that the binned afterglow spectrum appeared to increase in flux below ~ 4000 Å which would be predicted if the absorption feature was indeed due to a bump in the extinction curve. Even though the 2175 Å extinction bump is seen in some GRB afterglows, they are still rare with only four, robustly detected systems, GRBs 070802 (Krühler et al., 2008; Elíasdóttir et al., 2009), 080607 (Prochaska et al., 2009; Perley et al., 2011; Zafar et al., 2011a), 080605 and 080805 (Zafar et al., 2012). However, none of these are as extreme as what is seen towards GRB 140506A.

To test the hypotheses of the 2175 Å extinction bump, we compare the contribution of the host galaxy to the afterglow (see Fig. 2.3.2). Following the same procedure as was done for the afterglow we bin the spectrum of the host galaxy below 5000 Å in 100 Å bins to match that of the afterglow spectrum. It is evident that the rise seen in the afterglow spectrum is purely due to the afterglow being host-dominated below 4000 Å in the first and second epoch. This then indicates that the scenario with the flux-drop being caused by an extreme 2175 Å extinction bump feature can be safely excluded. This is further supported by the fact that such an extreme bump would be approximately three times as high as seen toward any line-of-sight in the Milky Way (Fitzpatrick & Massa, 2007; Fynbo et al., 2014). See Sect. 8.3.3 for a parametrization of the extinction curve of the host-corrected first epoch afterglow with the bump or "Drude"-profile removed.

Fitting the Fitzpatrick & Massa (2007) extinction curve with the central wavelength of the bump set as a free parameter favours a centre at 2015 Å. It is, however, a poor fit and the associated bump width would be a factor of five larger than that typically probed in the Milky Way. This case then leads the way for a non-standard reddening which will have a crucial impact for our understanding of the properties of dust grains in the non-local Universe. We will discuss this more in Sect. 2.4.

[2] `http://www.swift.ac.uk/xrt_spectra/`

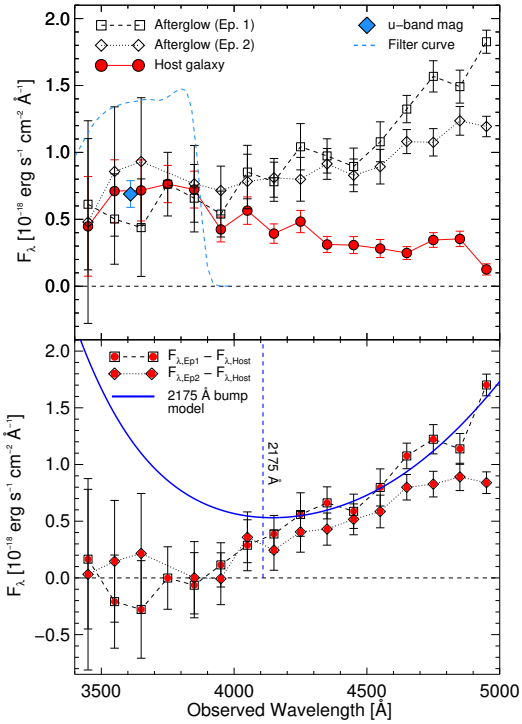

Figure 2.3.2. (*Top panel*): Comparison of the spectra of the first and second epoch afterglow and the spectrum of the host galaxy at $\lambda < 5000$ Å, each binned by 100 Å, together with the measured VLT/FORS2 u-band magnitude of the host. The consistent lower flux in the first epoch afterglow spectrum below 4000 Å is due to the host galaxy being partly outside of the slit (see Fig. 2.3.1). (*Bottom panel*): First and second epoch afterglow spectra with the flux of the host galaxy subtracted. Overplotted is the 2715 Å extinction bump model from Fynbo et al. (2014), which can now be securely excluded as the scenario causing the steep extinction.

2.3.3 Underlying supernova

The magnitudes of the host galaxy measured in the R- and I-bands are approximately one magnitude fainter than what was determined from the GROND late-time photometric follow-up ($R_{\rm FORS2} - r'_{\rm GROND} = 0.94 \pm 0.40$ mag and $I_{\rm FORS2} - i'_{\rm GROND} = 0.94 \pm 0.35$ mag) of the host (Fynbo et al., 2014). This could indicate a contribution from a bright underlying supernova (SN) 70 days (≈ 35 days in rest-frame) after trigger during the GROND observations. If this is true, then the GROND magnitudes implies an observed r'-band SN luminosty of approximately 1.5×10^{39} erg s^{-1}.

2.3.4 Emission line measurements

We were able to detect the prominent Hα and Hβ emission lines as well as emission from the [O II] $\lambda\lambda$ 3726,3729 doublet and the [O III] λ 5007 transition. To extract the line fluxes we fitted a Gaussian function to each line with the continuum set in small regions around the centroid of the fit (±30 Å), free of telluric- and sky-lines. Line widths were first fixed to a common value in the fits. The fit is dominated by the strongest line, Hα. From the fit we then determined the FWHM for each line. This is converted to a velocity dispersion, σ, by subtracting the instrumental broadening, $\mathcal{R}$ (km s^{-1}), quadratically from the fitted FWHM as

Table 2.3.1. Extracted emission-line fluxes.

Transition	Line flux[a]	σ^b	z
[O II] $\lambda\lambda$ 3726 , 3729	19.11 ± 0.60	50.8 ± 4.7	0.88905[c]
Hβ	3.27 ± 0.73	48.6 ± 15.7	0.88905
[O III] λ 5007	7.42 ± 0.72	48.0 ± 13.0	0.88905
Hα	16.47 ± 0.60	49.8 ± 4.7	0.88905

Notes. The values are derived from the best-fit Gaussian functions, measured in a ±30 Å region around the centroid of each line. The listed errors include the propagating errors from the fit. [a]Line fluxes are reported in units of 10^{-18} erg cm^{-2} s^{-1}. [b]Velocity dispersions are in units of km s^{-1} and are corrected for the measured resolution in the respective arms. [c]We only report one redshift and velocity dispersion, since the fit to the [O II] doublet was made with a fixed relation between the two components.

$$\sigma = \sqrt{\mathrm{FWHM}^2 - \mathcal{R}^2}/(2\sqrt{2\ln 2}) \,. \tag{2.1}$$

Based on the strong Hα line we measure an emission-line redshift of $z = 0.88905$ for the host galaxy, consistent with what has been reported in Fynbo et al. (2014) and Krühler et al. (2015). The results of the measured line fluxes and line widths are listed in Table 2.3.1 and shown in Fig. 2.3.3 with the best-fit Gaussian function.

2.3.5 Attenuation of the host

The observed Hα and Hβ emission line fluxes (the ratio of which is known as the Balmer decrement) provides us with the dust attenuation of the whole system toward the H II regions. The intrinsic, dust-corrected ratio of these two lines, r_{int}, assuming a case B recombination and an electron temperature of 10^4 K and a density of $10^2 - 10^4$ cm^{-3}, is Hα/Hβ = 2.87 (Osterbrock, 1989). Using the MW-type extinction curve of Pei (1992) with $R_V = 3.08$, we find that the attenuation at the wavelength of Hα and Hβ is $A_{\mathrm{H}\alpha} = 0.82$ mag and $A_{\mathrm{H}\beta} = 1.17$ mag, for this specific extinction curve normalised to $A_V = 1$ mag, respectively. We thus calculate the visual attenuation toward the H II regions from the Balmer decrement as

$$A_V = \frac{-2.5\log(r_{\mathrm{obs}}/r_{\mathrm{int}})}{A_{\mathrm{H}\alpha} - A_{\mathrm{H}\beta}} = 1.74 \pm 0.41 \text{ mag} \,, \tag{2.2}$$

where in our case, r_{obs} is found to be $(\mathrm{H}\alpha/\mathrm{H}\beta)_{\mathrm{obs}} = 5.04 \pm 0.67$. We note that modelling the spectrum with an SMC-like extinction curve instead (also typically seen in GRB host galaxies; Schady et al., 2010) will not change the results significantly since there is little difference at the wavelength range of the Balmer lines, and that most extinction curves behave similar redwards of the 2175 Å extinction bump. The MW extinction curve of Pei (1992) was also chosen to be consistent with Krühler et al. (2015). See Sect. 2.4 for further discussion on the reddening of the host and the comparison to other GRB host galaxies.

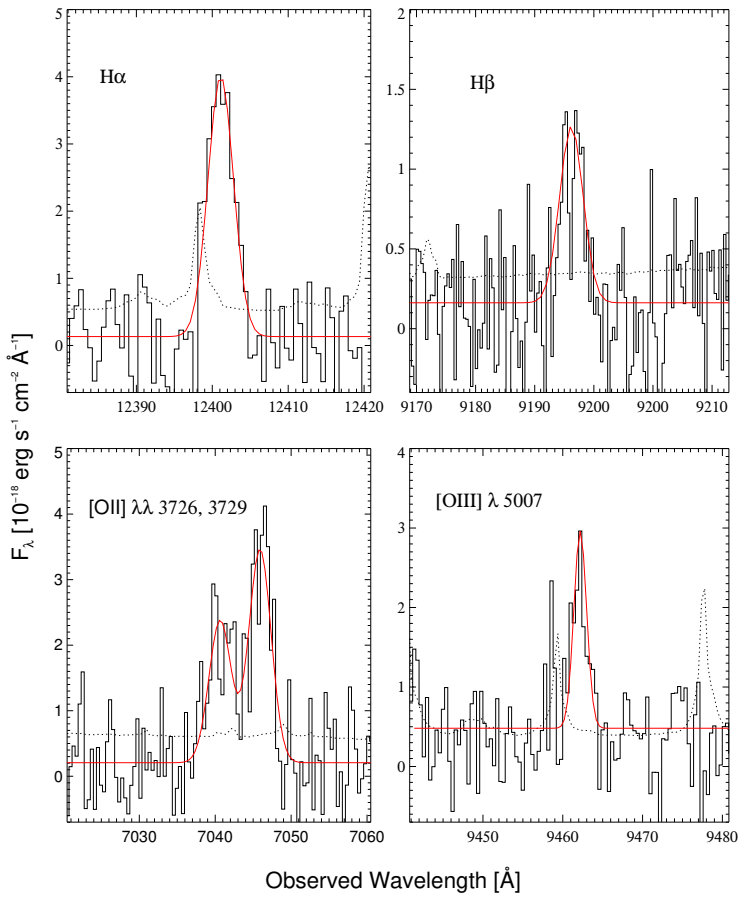

Figure 2.3.3. Emission lines from the optimally-extracted 1D spectrum. In each panel the observed spectrum is shown by the solid line, the error spectrum by the dotted line and the best-fit Gaussian function by the solid, red line. The plotting region shows a zoom-in on the continuum region (±20 Å).

2.3.6 Star formation rate

To measure the star formation rate (SFR) of the host galaxy we calculated the intrinsic, dust-corrected luminosity of the Hα emission line using the luminosity distance computed from the redshift, $z = 0.88905$. This yields a de-reddened line luminosity of $L(\mathrm{H}\alpha) = (2.61 \pm 0.09) \times 10^{41}$ erg s^{-1}, where the applied dust-correction was calculated as

$$L_{\mathrm{dered}} = L_{\mathrm{int}} \times 10^{(0.4 \times A_\lambda)} \quad . \tag{2.3}$$

Using the relation from Kennicutt (1998) and assuming a Salpeter initial mass function (IMF) we calculate a dust-corrected SFR of

$$\mathrm{SFR}(\mathrm{H}\alpha) = 7.9 \times 10^{-42}\, L(\mathrm{H}\alpha)_{\mathrm{dered}} = 2.14 \pm 0.07\ M_{\odot}\ \mathrm{yr}^{-1}\ , \tag{2.4}$$

where, assuming a Chabrier IMF instead, this can be converted to $\mathrm{SFR}(\mathrm{H}\alpha)_{\mathrm{Chab}} = 1.34 \pm 0.04\ M_{\odot}\ \mathrm{yr}^{-1}$ (Treyer et al., 2007). For consistency with Krühler et al. (2015) we refer only to the latter value in Sect. 2.4 in our comparison.

2.3.7 Metallicity

To infer the emission-line metallicity of the host galaxy it is common practice to use the strong-line ratios; [N II]/[O II] (N2O2), ([O II] λ 3727+[O III] λ 4959+[O III] λ 5007)/Hβ (R_{23}), [N II]/Hα (N2) and ([O II]/Hβ)/([N II]/Hα) (O3N2). A detailed discussion on how the strong-line diagnostics can be used as metallicity indicators and a comparison of these is given in Kewley & Ellison (2008). In the following we assume a solar metallicity of $12 + \log(\mathrm{O/H}) = 8.69$ (Asplund et al., 2009).

Due to the non-detection of [N II] in our case (Fig. 2.3.4), we are only able to determine upper limits from the aforementioned strong-line ratios from the 3σ upper limit measured from the continuum at the wavelength of [N II]. From the dust-corrected emission-line fluxes (Eq. 2.3) we compute upper limits on the oxygen abundances of $12 + \log(\mathrm{O/H}) < 8.46$ for N2O2 (Kewley & Dopita, 2002), $12 + \log(\mathrm{O/H}) < 8.37$ for N2 (Pettini & Pagel, 2004) and $12 + \log(\mathrm{O/H}) < 8.67$ for O3N2 (Pettini & Pagel, 2004) corresponding to upper limits of $0.59, 0.49$ & $0.95\ Z/Z_{\odot}$, respectively. The errors and upper limits on all derivations include the scatter in the relations listed in Kewley & Ellison (2008).

To alleviate the limitations from the non-detection of [N II] we make use of the fact that it is also possible to estimate the metallicity based solely on the strong oxygen nebular lines (Pilyugin, 2001; Pilyugin & Thuan, 2005), the so-called P method. The authors advocate that the physical properties of the H II region can be estimated via the excitation parameter, P, here defined as $P = R_3/(R_2 + R_3)$, where R_2 =[O II]/Hβ and R_3 =([O III] λ 4959+[O III] λ 5007)/Hβ. Since we do not detect [O III] λ 4959 we use that $f_{[\mathrm{O\,III}]\,\lambda 4959} = 1/3 \times f_{[\mathrm{O\,III}]\,\lambda 5007}$ (Storey & Zeippen, 2000).

Following the above definitions, we derive an excitation parameter of $P = 0.21 \pm 0.03$. To compute the metallicity we use the relation

$$12 + \log(\mathrm{O/H}) = \frac{R_3 + 106.4P + 106.8P^2 - 3.40P^3}{17.72P + 6.60P^2 + 6.95P^3 - 0.302R_3}\ , \tag{2.5}$$

from Pilyugin & Thuan (2005). Using the value for the excitation parameter found above and the ratio $R_3 = 2.81 \pm 0.45$ this yields an oxygen abundance of $12 + \log(\mathrm{O/H}) = 8.23 \pm 0.16$, corresponding to 35% solar metallicity ($Z = 0.35^{+0.15}_{-0.11}\ Z_{\odot}$). The expected scatter of 0.1 dex in the relation is included in the calculation. This is consistent with the previous upper limits. We will only refer to this value in the remainder of this paper.

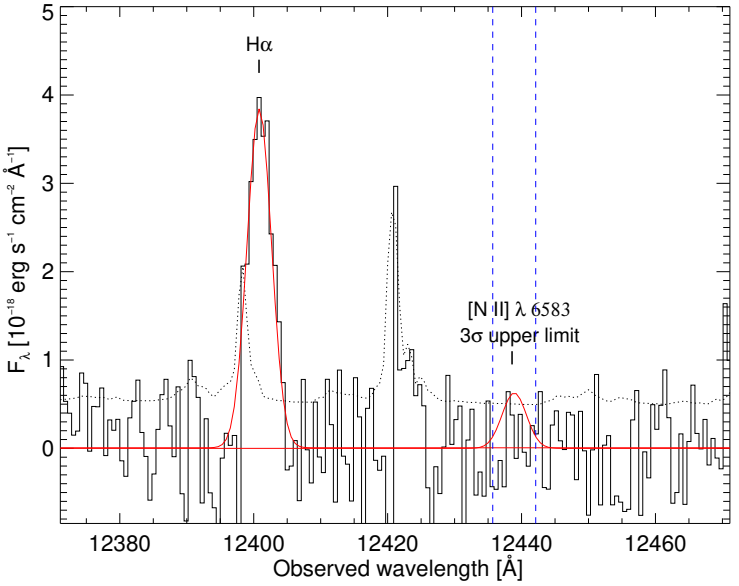

Figure 2.3.4. The 3σ flux limit of [N II] measured from the continuum compared to Hα. We assumed a Gaussian shape of the line profile and measured the limit at the FWHM (dashed blue lines) of that of Hα. The total flux of the continuum at [N II] was then computed from the flux encompassed in this region.

2.4 Discussion

2.4.1 Broad-band SED of the dusty host

To constrain the physical origin of the steep extinction curve seen towards the sightline of GRB 140506A, we first model the SED of the host galaxy. Fitting the observed five broad-band magnitudes reported in Table 2.2.1 in LePhare[3] (Arnouts et al., 1999; Ilbert et al., 2006) yields the host galaxy parameters listed in Table 2.4.1, with a $\chi^2 = 0.98$, and the best-fit stellar population synthesis model shown in Fig. 2.4.1. We obtained the best fit SED by fixing the redshift to $z = 0.88905$ and used a grid of stellar evolution models with varying star formation time scales, age of stellar population and extinction assuming the models from Bruzual & Charlot (2003) based on an IMF from Chabrier (2003) and a Calzetti extinction curve (Calzetti et al., 2000).

The best-fit visual attenuation, A_V^{SED}, and star-formation rate from the broad-band SED agree well with that determined from the emission-line diagnostics. The stellar mass computed by the fit is mainly dominated by the 3.6 μm *Spitzer* photometric data point.

It is evident that the host galaxy does not follow an extinction curve as steep as that seen towards the GRB explosion site. Running the SED fit with the new extinction

[3] `http://www.cfht.hawaii.edu/~arnouts/LEPHARE/lephare.html`

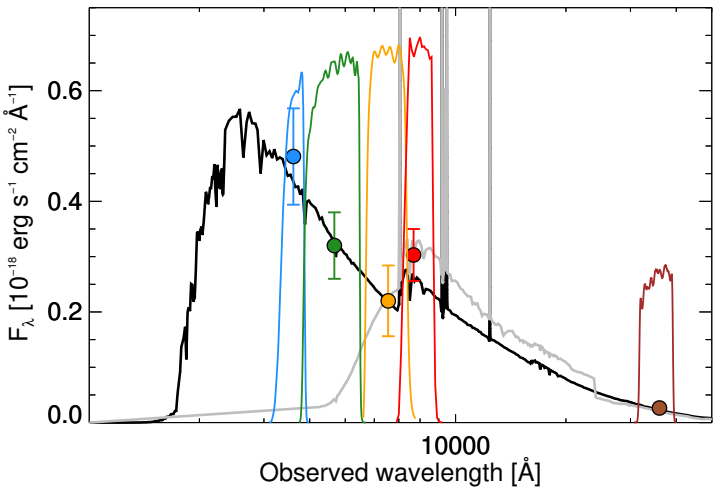

Figure 2.4.1. SED of the host galaxy of GRB 140506A. Overplotted is the best-fit stellar population synthesis model of a galaxy with a 20 Myr old stellar population at a fixed redshift of $z = 0.88905$, reddened by $A_V = 1.62$ mag (black line) following the extinction curve of Calzetti et al. (2000). Overplotted is the same intrinsic SED but reddened by the steep extinction curve seen towards the afterglow instead (grey line) but without the rise in flux at wavelengths below 4000 Å (see text). Also shown are the filter transmission curves for the corresponding five photometric points. The data do not suggest an atypical steep extinction curve for the host, similar to the afterglow sightline.

curve (see next section) in steps of $E(B-V) = [0.0, 0.05, ..., 1.0]$ we find a best-fit with no attenuation, that is all models with the steep extinction curve implemented provides worse fit to the data. As a conclusion, the steep extinction curve toward the afterglow must be sightline dependent and this is evidence for the occurrance of only locally steep extinction curves. The dust properties of the intermediate environment in which the GRB is embedded, strongly imprinted on the afterglow SED, are therefore not representative of the dust properties of the host galaxy as a whole.

2.4.2 Modelling the extinction curve

To further confine the shape of the extinction curve we subtract the flux of the host galaxy from the best-fit SED from the first epoch afterglow. To estimate the reddening we assume that the intrinsic spectrum follows a power-law, $F_\lambda \propto \lambda^{-\beta}$, with $\beta = 1.75$ as derived from the XRT spectrum with a break between the X-rays and optical bands of $\Delta\beta = 0.5$ (following the same procedure as Fynbo et al., 2014). We then run a non-linear least squares curve fitting on the host-subtracted afterglow spectrum using `MPFIT` in `IDL` with the parametrization of Fitzpatrick & Massa (2007), which models the extinction curve through a set of nine parameters. It basically contains two components, one describing the UV linear part of the extinction specified by the parameters c_1 (intercept) and c_2 (slope) and the parameters c_4 and c_5 provide the far-UV curvature and the

Table 2.4.1. Host galaxy parameters from SED fitting.

Extinction law	Calzetti et al. (2000)
Reddening A_V [mag]	1.62 ± 0.21
SFR [$M_\odot$ yr^{-1}]	1.18 ± 0.28
Age [Gyr]	$0.02^{+0.07}_{-0.02}$
$\log(M_*/M_\odot)$	8.35 ± 0.26

other is the Drude component describing the 2175 Å bump by the parameters c_3 (bump strength), x_0 (central wave number) and γ (width of the bump). The last two parameters are the visual extinction, A_V, and the total-to-selective reddening, or the steepness of the reddening law, R_V.

Setting all nine parameters free we find a best-fit almost identical to the extreme 2175 Å extinction bump proposed by Fynbo et al. (2014). However, having excluded any signs of a bump in the extinction curve we instead run the fit assuming $c_3 = 0$, effectively removing the Drude profile representing the bump in the model. We then find the best-fit values of: $c_1 = -0.93$, $c_2 = 3.13$, $c_4 = 3.30$, $c_5 = 2.15$, $R_V = 5.12$ and $A_V = 1.04$ mag, resulting in the extinction curve shown in Fig. 5.4.1 and is defined as

$$\frac{A_\lambda}{A_V} = \begin{cases} \frac{1}{5.12}(-0.93 + 3.13x) + 1 & x < c_5 \\ \frac{1}{5.12}\left(-0.93 + 3.13x + 3.30(x - 2.15)^2\right) + 1 & x > c_5 \end{cases}, \tag{2.6}$$

where $x = \lambda^{-1}$ in units of μm^{-1}. Most notable are the flat or grey total-to-selective extintion parameter, R_V, and the parameter describing the far-UV curvature component, c_4. Comparing these to a simple SMC-type extinction curve as modelled by Gordon et al. (2003) reveals that a typical steeper reddening law, commonly defined by a small value of R_V, is inadequate in reproducing the strong drop. Instead a flat extinction curve is required, mainly to reproduce the relatively blue part of the spectrum at wavelengths above 8000 Å, with the roughly seven times larger value of c_4 compared to that of the SMC (Gordon et al., 2003) modelling the steep drop. The parameters describing the linear component of the UV extinction, c_1 and c_2, also differentiate significantly compared to the relation $c_1 = 2.09 - 2.84c_2$ found by Fitzpatrick & Massa (2007), where we would expext $c_1 = -6.80$ (best-fit $c_1 = -0.93$) based on the c_2 parameter.

From the above derived parametrization of the extinction we attempt to recover the relative reddening curve as well. By again assuming the XRT spectrum with a cooling break as the instrinsic afterglow spectrum, we normalise this power-law to the K-band (at roughly 20 000 Å in regions with no telluric absorption) and then we calculate the relative reddening, $k(\lambda)$, as

$$k(\lambda) = -2.5 \log(D_\lambda / I_\lambda) \ , \tag{2.7}$$

where D_λ denotes the observed data and I_λ refers to the intrinsic spectrum. The resulting reddening curve is shown in Fig. 2.4.3 where we also compare it to the standard extinction curves of the Local Group (that of the MW, the SMC and the LMC). It is evident that the standard reddening laws do not provide a good fit to the data, except in the reddest part of the spectrum.

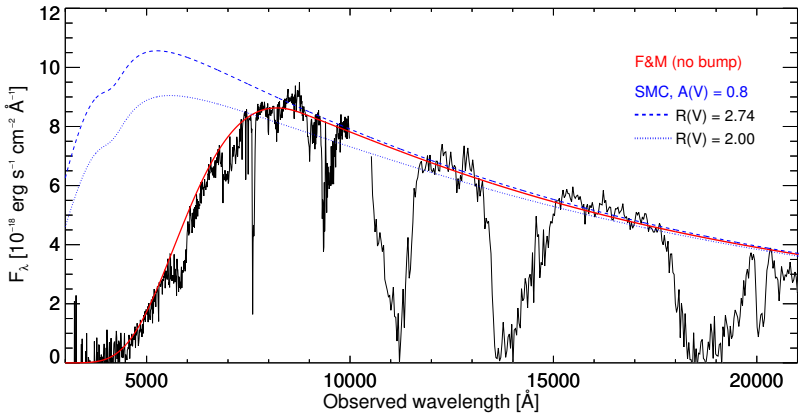

Figure 2.4.2. First epoch afterglow spectra with the flux of the host galaxy from the best-fit SED subtracted. Overplotted is the best-fit Fitzpatrick & Massa (2007) parametrization of the extinction curve with $c_3 = 0$ (no bump) shown by the red solid line. We assume an underlying power-law with slope set by a fit to the X-ray afterglow and assuming a $\Delta\beta = 0.5$ cooling break between the X-rays and the optical. Regions affected by telluric absorption are removed from the fit. Also plotted is the extinction curve of the SMC as described by Gordon et al. (2003) (blue dashed line) and with an decreased total-to-selective reddening, R_V (blue dotted line). These examples proves to show that the extinction can not simply be modelled by a standard or even steeper SMC-type reddening law. The parameters of the best-fit extinction curve diverges significantly from that known from the local analogs, most notable are the c_4 and c_5 values representing the far-UV curvature component, but also the flat value of R_V. These are required to model the extreme drop without assuming a bump in the extinction curve in combination with the otherwise blue spectrum.

2.4.3 Comparison to GRB hosts at $z < 1$

Another potential clue to understand why the afterglow of GRB 140506A is so different from the typical SED of GRB afterglows, is to compare the properties of the host galaxy to other GRB hosts at similar redshifts. We use a subsample of 20 GRB host galaxies at $z < 1$ with metallicity measurements extracted from the full sample of 96 GRB-selected galaxies presented in Krühler et al. (2015). We caution that this is not an unbiased sample but merely a compilation of GRB host galaxies observed with X-shooter. In Fig. 2.4.4 we show the physical properties of this subsample and compare these GRB host galaxies with GRB 140506A. It is evident that this particular host galaxy is a standard GRB host in terms of star formation rate, velocity dispersion and metallicity but with a large, though not abnormal, visual attenuation, A_V.

2.4.4 Comparison to SNe and AGNs

One of the main differences between observed GRB and SN samples is that the explosion sites of GRBs are found much closer to the brighter regions of their respective host galaxies (Fruchter et al., 2006; Lyman et al., 2017).

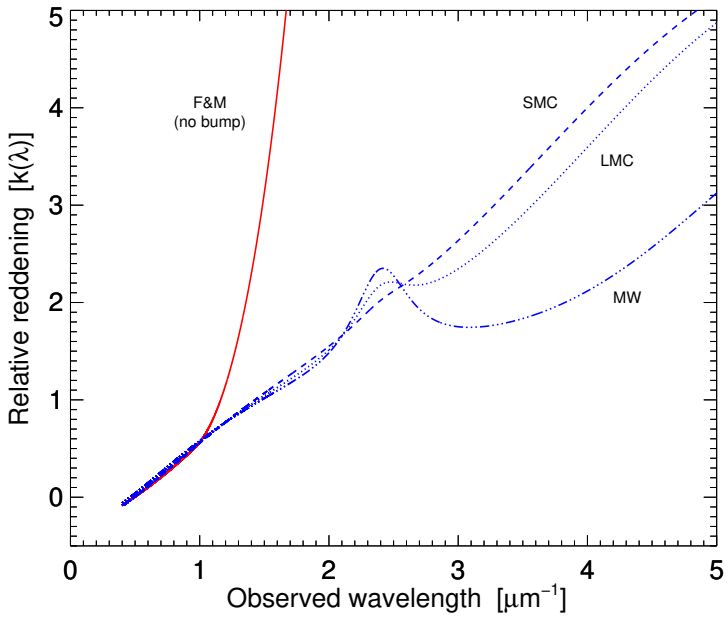

Figure 2.4.3. Reddening curves for the first epoch afterglow spectra with the flux of the host galaxy from the best-fit SED subtracted. Since we do not know the instrinsic brightness of the afterglow the data has been normalised to the flux in the K-band ($\sim$ 20 000 Å). The reddening curves, described by $k(\lambda)$, thus only indicate the relative reddening and not the total extinction. It is clearly shown how the extinction curves of the Local Group, here the MW, SMC and LMC, can only match the best-fit reddening law from the Fitzpatrick & Massa (2007) parametrization at wavelengths longer than 8000 Å (observers frame), at which point the steep extinction curve diverges significantly.

Numerous more cases of SNe with steep extinction curves are observed (e.g. Kriscinunas et al., 2006; Nobili & Goobar, 2008; Folatelli et al., 2010), which are argued could imply a grain size that is small in the specific line of sights compared with the average value for the local ISM (Elias-Rosa et al., 2006, 2008) or a dominating multiple scattering process (Goobar, 2008). See also Amanullah et al. (2014) for a prime example of a steep extinction curve seen towards SN 2014J in M82. Again we wish to highlight that in this specific case the multiple scattering scenario was ruled out (Johansson et al., 2017). Hutton et al. (2014) were able to constrain the global reddening law of M82, showing that standard MW-type extinction is preferred for the galaxy as a whole, which is further evidence that steep extinction is only seen locally. In these studies it is argued that the smaller grain size causing the steep extinction could be fragmentations of larger dust grains disolved due to the large radiation field.

A similar steep extinction curve is observed toward several dust-reddened quasars as well. Fynbo et al. (2013a) found that $\sim$ 30% of the quasars in their sample were reddened following an extinction curve much steeper than what is seen in the local analogs; MW, SMC or LMC (see also Leighly et al., 2014, for a specific example towards the AGN Mrk 231). A similar type of extinction is also seen (but to a lesser extent) in the High

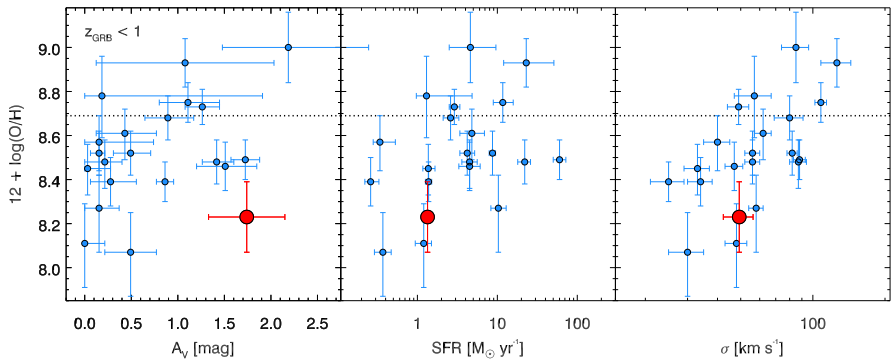

Figure 2.4.4. Comparison of the host galaxy properties of GRB 140506A (large red dot) to 20 other GRB host galaxies at $z < 1$ (small blue dots) with metallicity measurements from Krühler et al. (2015). From left to right the metallicity of each individual host galaxy is shown as a function of: A_V, SFR and σ, measured from emission line diagnostics. The dotted, horizontal line denotes the solar metallicity abundunce (Asplund et al., 2009). The physical properties of the host galaxy of GRB 140506A is inconspicuous, compared to the other GRB host galaxies at $z < 1$.

A_V Quasar (HAQ; Krogager et al., 2015) and the *extended* HAQ (eHAQ; Krogager et al., 2016b) surveys. A subsample of 16 intrinsically reddened quasars from the HAQ survey were examined by Zafar et al. (2015), who found a weighted mean value of $R_V = 2.4$, much steeper than that of the SMC which has a total-to-selective extinction ratio around $R_V \sim 2.9$. We note that even these steep extinction curves do not provide a good fit to the data, due to the still close resemblance to that of the SMC.

2.4.5 Variability of the flux drop

The above cases further suggests that the steep extinction curve observed towards GRB 140506A is not a rare phenomenon, but is more likely attributed to the level of fragmentation of the dust grains surrounding the explosion site. More curios is the temporal variability of the first to the second epoch afterglow spectrum. From a study of the dynamics of large dust grains in molecular clouds, Hopkins & Lee (2016) show that grains with sizes $a > 0.01$ μm can exhibit large fluctuations in the local dust-to-gas ratio. They conclude that small dust grains can be much more clumped than larger dust grains, critical for dust growth and shattering.

If that is the case for the circumburst medium then this might explain the temporally varying afterglow SED. Due to the decrease of the relativistic beaming as the blast wave slows down, the emitting area of the afterglow expands as $(\gamma ct)^2$ (see also the discussion in Fynbo et al., 2014), which yields a factor of six increase in the glowing region producing the afterglow between 8.8 and 33 hr post-burst. If the probed distribution of small and large dust grains is different for such different beam sizes, then this will have an effect on the observed extinction towards the line of sight to the GRB at the two different epochs.

2.5 Conclusions

We have analysed the host galaxy of the mysterious GRB 140506A afterglow, showing an extreme flux-drop below 8000 Å observers frame (4000 Å rest-frame) in the sightline towards the GRB explosion site (Fynbo et al., 2014). This is atypical to the blue power-law SEDs commonly observed for GRB afterglows (e.g. Fynbo et al., 2009). We found that the explosion site of the GRB occurred at a projected distance of ≈ 4 kpc from the galactic centre, in a faint region in the outskirts of the host galaxy, while most GRBs are observed much closer to the centre or in the brightest regions of their respective host galaxies (Fruchter et al., 2006; Lyman et al., 2017).

We found the host galaxy to be moderately forming stars at a rate of $1.34 \pm 0.04\ M_{\odot}$ yr^{-1}. Employing the P method we derived a metallicity of $12 + \log(\mathrm{O/H}) = 8.23 \pm 0.16$ ($Z = 0.35^{+0.15}_{-0.11}\ Z_{\odot}$). This is in good agreement with the $Z - \mathrm{SFR}$ and $Z - \sigma$ relations found for GRB host galaxies at $z < 1$ (Krühler et al., 2015). The host galaxy can be characterised by a large visual attenuation of $A_V = 1.74 \pm 0.41$ mag based on emission line diagnostics.

We excluded the scenario where the rise in flux observed at < 4000 Å in the afterglow spectrum was due to an extreme 2175 Å extinction bump, a feature known from the local LMC and the MW, and showed that it was merely a representation of the dominating host galaxy light at this wavelength. There does not seem to be any similarity between the extinction law of the afterglow and the best-fit for the host galaxy which suggests that the steep extinction seen in the afterglow SED is sightline dependent and only a local effect. The A_V's measured in both cases are high, with a best-fit afterglow extinction of $A_V = 1.04$ mag. This effect could be explained by the intense radiation field from the GRB only fragmenting (in contrast to fully destroying) the surrounding dust particles causing a local only steep extinction.

We modelled the relative reddening and showed that all the standard extinction curves as seen in the Local Group (MW, SMC and LMC) are inadequate in descring the steep drop in combination with the relatively blue underlying power-law spectrum. A similar non-standard, steep extinction curve is observed toward a few other rare cases of GRBs but also in several other types of enigmatic astrophysical objects, such as AGNs and SNe. The phenomenon of steep extinction curves does not seem to be rare globally and also hint that this could contribute (at least partly) to the large fraction of dark GRBs, defined by no optically detected afterglows. A new picture of the dust properties in high energy environment seems to be emerging. The extinction curves with non-local analogs appear to be an important clue to resolve this.

Acknowledgements

We would like to thank the anonymous referee whose comments greatly improved the quality of the paper and arrived in a timely manner. We would also like to thank C. Gall, D. Malesani and B. T. Draine for insightful discussions on the conclusions of the paper. KEH and PJ acknowledge support by a Project Grant (162948–051) from The Icelandic Research Fund. The research leading to these results has received funding from the European Research Council under the European Union's Seventh Framework Program (FP7/2007–2013)/ERC Grant agreement no. EGGS–278202. TK

acknowledges support through the Sofja Kovalevskaja Award to P. Schady from the Alexander von Humboldt Foundation of Germany. LC is supported by YDUN grant DFF – 4090–00079. D.X. acknowledges the support by the One-Hundred-Talent Program of the Chinese Academy of Sciences (CAS), by the Strategic Priority Research Program "Multi-wavelength Gravitational Wave Universe" of the CAS (No. XDB23000000), and by the National Natural Science Foundation of China under grant 11533003.

Chapter 3

Probing gas and metals immediate to GRBs

This chapter is based on the following article:

Highly ionized metals as probes of the circumburst gas in the natal regions of gamma-ray bursts

Published in Monthly Notices of the Royal Astronomical Society, vol. 479, issue 3, 21 pp. (2018)

Authors:
K. E. Heintz, D. Watson, P. Jakobsson, J. P. U. Fynbo, J. Bolmer, M. Arabsalmani, Z. Cano, S. Covino, V. D'Elia, A. Gomboc, J. Japelj, L. Kaper, J.-K. Krogager, G. Pugliese, R. Sánchez-Ramírez, J. Selsing, M. Sparre, N. R. Tanvir, C. C. Thöne, A. de Ugarte Postigo & S. D. Vergani

We present here a survey of high-ionization absorption lines in the afterglow spectra of long-duration gamma-ray bursts (GRBs) obtained with the VLT/X-shooter spectrograph. Our main goal is to investigate the circumburst medium in the natal regions of GRBs. Our primary focus is on the N v $\lambda\lambda$ 1238,1242 line transitions, but we also discuss other high-ionization lines such as O vi, C iv and Si iv. We find no correlation between the column density of N v and the neutral gas properties such as metallicity, H i column density and dust depletion, however the relative velocity of N v, typically a blueshift with respect to the neutral gas, is found to be correlated with the column density of H i. This may be explained if the N v gas is part of an H ii region hosting the GRB, where the region's expansion is confined by dense, neutral gas in the GRB's host galaxy. We find tentative evidence (at 2σ significance) that the X-ray derived

column density, $N_{\mathrm{H,X}}$, may be correlated with the column density of N v, which would indicate that both measurements are sensitive to the column density of the gas located in the vicinity of the GRB. We investigate the scenario where N v (and also O vi) is produced by recombination after the corresponding atoms have been stripped entirely of their electrons by the initial prompt emission, in contrast to previous models where highly-ionized gas is produced by photoionization from the GRB afterglow.

3.1 Introduction

Cosmic lighthouses such as gamma-ray bursts (GRBs) allow the interstellar medium (ISM) of their host galaxies and foreground absorbers to be studied in great detail (e.g. Jakobsson et al., 2004) up to high redshifts. In particular, they enable investigations of the ISM in terms of chemical abundances (Fynbo et al., 2006b; Prochaska et al., 2007; Cucchiara et al., 2015), dust content (Savaglio et al., 2003; Schady et al., 2010; Zafar et al., 2011a; Zafar & Watson, 2013), kinematics (Prochaska et al., 2008a; Arabsalmani et al., 2015, 2018b), and the very local circumburst medium (Møller et al., 2002; Prochaska et al., 2006, 2008b; Fox et al., 2008; Castro-Tirado et al., 2010; Schady et al., 2011). The large majority of GRB afterglow spectra show damped Lyman-α (DLA) absorption, i.e., a neutral hydrogen column density of $N(\mathrm{H\,I}) > 2 \times 10^{20}$ cm^{-2} (Vreeswijk et al., 2004; Jakobsson et al., 2006b; Fynbo et al., 2009; Cucchiara et al., 2015; Tanvir et al., 2019), typically with higher H i column densities than seen in DLAs toward quasars (e.g. Noterdaeme et al., 2009b; Sánchez-Ramírez et al., 2016). This is consistent with the scenario where the GRB explodes in the inner region, or in a dense, star-forming cloud, within its host galaxy (Bloom et al., 2002; Fruchter et al., 2006; Prochaska et al., 2007; Vreeswijk et al., 2007, 2011; Fynbo et al., 2008; Svensson et al., 2010; Lyman et al., 2017).

While the neutral gas-phase ISM in the host galaxy can be studied in great detail with GRBs, it is much more difficult to examine their immediate environments. Due to the hardness of the prompt emission and the extreme luminosity across all wavelengths, GRBs are expected to destroy dust and fully or at least partly ionize the circumburst gas, out to a few tens of pc (Waxman & Draine, 2000; Fruchter et al., 2001; Perna et al., 2003; Watson et al., 2006, 2013). This can potentially erase any traces of the physical conditions of the circumburst material from their optical afterglow spectra. Highly ionized absorption features or X-ray observations of the GRBs might therefore be the only spectroscopically way to probe the circumburst medium. The observed soft X-ray absorption column density is typically larger than that of the neutral gas in GRB host galaxies (Galama & Wijers, 2001; Watson et al., 2007; Campana et al., 2010; Schady et al., 2011), which could indicate that the X-ray absorption probes a significant column of hot, ionized metals that is transparent to UV photons. Another plausible scenario is that the He in the natal H ii region of the GRB is responsible for most of the soft X-ray absorption (Watson et al., 2013; Krongold & Prochaska, 2013). The absorption is likely due to the much larger population of He atoms, and since the abundance of He saturates the He-ionizing UV continuum out to about ten pc from the GRB, it can remain in a neutral or singly-ionized state. This scenario also supports previous models where dust is destroyed and metals are stripped of all their electrons by the GRB out to distances

of tens to hundreds of pc (Waxman & Draine, 2000; Fruchter et al., 2001; Perna et al., 2003; Watson et al., 2006, 2013).

Since the relative location of the absorbing gas cannot be resolved in X-ray spectroscopy, the observed column density probes the total gas column along the line of sight. For this reason the soft X-ray absorption might originate in the intergalactic medium (IGM) or in intervening absorbers. This was argued to be the cause for the observed correlation between the X-ray absorbing column density and redshift (Behar et al., 2011; Arcodia et al., 2016). However, Watson & Jakobsson (2012) and Watson et al. (2013) showed that this trend is largely a consequence of the higher gas column density in GRB hosts at high redshifts (similar to what is observed for main-sequence galaxies, e.g. Magdis et al., 2012) and that at low-z, the dust bias (excluding high X-ray absorbing column density GRBs) is more severe than at high-z. Only at the highest redshifts ($z \gtrsim 4$) is it plausible that a significant component of absorption from intervening matter could be present (Starling et al., 2013).

The long-standing problem of the origin of the soft X-ray absorption could therefore be solved by comparing the high-ionization absorption features seen in optical GRB afterglows to the X-ray derived column density. If a correlation is found between these two quantities, it may be possible to robustly relate the X-ray absorption to the immediate environment of the GRB. In this paper we compile a list of all high-redshift ($z \gtrsim 1.7$), long-duration GRBs with good quality X-shooter spectra to investigate the high-ionization absorption features in GRB afterglows. Such highly ionized absorption lines, in particular N v, has already been studied with high-resolution data though only in small samples (Prochaska et al., 2008b; Fox et al., 2008). Our sample is three times as large as those previously published, and by combining the individual samples we are now able to study the high-ionization absorption features with better statistics.

The paper is structured as follows. In Section 3.2 we present our sample, discuss the imposed selection criteria and evaluate the neutral gas properties (such as $z_{\rm GRB}$, H I column density, metallicity, and dust depletion) of the GRBs in our sample. In Section 3.3 we present our results, with a specific focus on N v which is the best constrained high-ionization absorption line. We provide a discussion of our data in Section 3.4, where we also propose a new scenario for the origin of highly-ionized metals in the vicinity of GRBs. Finally, we conclude on our work in Section 3.5.

Throughout the paper we assume a standard, flat cosmology with $H_0 = 67.8\,{\rm km\,s^{-1}\,Mpc^{-1}}$, $\Omega_m = 0.308$ and $\Omega_\Lambda = 0.692$ (Planck Collaboration et al., 2016). Abundances are expressed relative to solar, i.e. $[{\rm X/H}] = \log N({\rm X})/N({\rm H}) - \log N({\rm X})_\odot/N({\rm H})_\odot$, using solar abundances from Asplund et al. (2009).

3.2 The GRB sample

The sample of GRB afterglows studied here was built by extracting all long-duration GRBs at $z \gtrsim 1.7$ from the VLT/X-shooter GRB (XS-GRB) legacy survey (Selsing et al., 2019). Table 8.2.1 compiles the information of each of the GRBs in our study, including: The time of the observation, the spectroscopic sequence, observing programme, spectral resolution and references for the high-energy detection and X-shooter follow-up. After examining each individual spectrum we imposed additional observational selection

Table 3.1.1. X-Shooter GRB sample and log of observations.

GRB	Trigger (UT) (hh:mm:ss)	Δt^a (hr)	$\mathrm{Mag_{AB}}$ (Acq.)	Exp. time (s)	ESO prog. ID	$\mathcal{R}^b_{\mathrm{UVB/VIS}}$ (km s^{-1})	Notes and refs.
090809	17:31:14	10.2	21.0	4×1800	60.A-9427(A)	53.6 / 31.3	(1,2)
090926A	21:55:48	22.0	17.9	4×600	60.A-9427(A)	49.2 / 28.6	(3,4)
100425A	02:50:45	4.00	20.6	4×600	85.A-0009(B)	52.5 / 30.0	(5,6)
111008A	22:12:58	8.50	21.0	4×2400	88.A-0051(B)	46.2 / 26.5	(7,8)
120119A	04:04:30	1.40	17.0	4×600	88.A-0051(B)	39.5 / 22.7	(9)
120327A	02:55:16	2.10	18.8	4×600	88.A-0051(B)	33.3 / 19.4	(10,11)
120815A	03:55:21	1.69	18.9	4×600	89.A-0067(B)	44.1 / 25.4	(12,13)
120909A	01:42:03	1.70	21.0	2×600	89.A-0067(B)	56.6 / 33.0	RRM, (14,15)
121024A	02:56:12	1.80	20.0	4×600	90.A-0088(B)	41.7 / 24.0	(16,17)
130408A	21:51:38	1.90	20.0	2×600	91.C-0934(C)	39.5 / 22.7	(18,19)
130606A	21:04:39	7.10	19.0	7×600	91.C-0934(C)	37.0 / 21.4	(20,21)
141028A	10:54:46	15.4	20.0	4×600	94.A-0134(A)	53.6 / 30.9	(22,23)
141109A	05:49:55	1.90	19.2	2×1200	94.A-0134(A)	41.7 / 24.2	(24,25)
150403A	21:54:16	10.8	19.1	4×600	95.A-0045(A)	44.8 / 26.1	(26,27)
151021A	01:29:12	0.75	18.2	7×600	96.A-0079(B)	50.0 / 29.1	RRM, (28,29)
151027B	22:40:40	5.00	20.5	4×600	96.A-0079(A)	55.6 / 32.3	(30,31)
160203A	02:13:10	0.30	18.0	11×600	96.A-0079(A)	37.5 / 21.7	RRM, (32,33)
161023A	22:39:24	3.00	17.5	2×600	98.A-0055(A)	46.2 / 26.5	(34,35)

Notes. GCN circulars that reported the gamma-ray burst detection and the subsequent X-shooter afterglow follow-up observations (if available). ^{a}Time of spectroscopic follow-up after GRB trigger; ^{b}Spectral resolution in the UVB and VIS arm.
References. (1) Markwardt et al. (2009); (2) Malesani et al. (2009a); (3) Bissaldi et al. (2009); (4) Malesani et al. (2009b); (7) Saxton et al. (2011); (8) Wiersema et al. (2011); (9) Beardmore et al. (2012); (10) Sbarufatti et al. (2012); (11) Krühler et al. (2012); (12) Pagani et al. (2012a); (13) Malesani et al. (2012); (14) Immler et al. (2012); (15) Hartoog et al. (2012); (16) Pagani et al. (2012b); (17) Tanvir et al. (2012a); (18) Lien et al. (2013); (19) Hjorth et al. (2013); (20) Ukwatta et al. (2013); (21) Xu et al. (2013); (22) Bissaldi et al. (2014); (23) Xu et al. (2014a); (24) D'Avanzo et al. (2014); (25) Xu et al. (2014b); (26) Lien et al. (2015); (27) Pugliese et al. (2015); (28) Melandri et al. (2015); (29) de Ugarte Postigo et al. (2015); (30) Ukwatta et al. (2015); (31) Xu et al. (2015); (32) D'Avanzo et al. (2016); (33) Pugliese et al. (2016); (34) Mereghetti et al. (2016); (35) Tanvir et al. (2016).

criteria to exclude bursts with poor S/N or insufficient coverage of the high-ionization lines (see Sect. 4.2.2). In Sect. 3.2.3 we report the low-ionization properties of the sample such as the systemic redshift, H I column density, gas-phase metallicity, and dust depletion.

3.2.1 Observations and data reduction

The majority of GRBs observed with the VLT/X-shooter spectrograph in our sample were detected by the Burst Alert Telescope (BAT) on-board the *Neil Gehrels Swift Observatory* satellite (Gehrels et al., 2004). The three exceptions are the GRBs 090926A, 141028A, and 161023A, where the first two were detected by *Fermi*-LAT/GBM (Atwood et al., 2009; Meegan et al., 2009) onboard the *Fermi* Gamma-Ray Space Telescope and

the last was detected by the *INTEGRAL* satellite (Winkler et al., 2003).

The localization of each burst was distributed within a few minutes through the GCN which allowed for quick follow-up observations with VLT. Three of the 18 GRB afterglows in our sample (GRBs 120909A, 151021A and 160203A) were observed with the rapid-response mode (RRM; Vreeswijk et al., 2010) available at the ESO/VLT. All bursts were observed within 24 hours after trigger (see also below).

The VLT/X-shooter spectrograph covers the spectral wavelength range from 3000 Å – 24800 Å, divided into three spectroscopic arms (Vernet et al., 2011). The UVB arm covers 3000 Å – 5500 Å, the VIS arm 5500 Å – 10200 Å and the NIR arm 10200 Å – 24800 Å. In the large majority of cases, the spectra were obtained following an ABBA nodding pattern, the slits were aligned with the parallactic angle, selecting slit widths of 1.″0, 0.″9 and 0.″9 for the three arms, respectively. For this setup the nominal instrumental resolutions in the UVB, VIS and NIR arms are 70 $\mathrm{km\,s^{-1}}$, 40 $\mathrm{km\,s^{-1}}$ and 55 $\mathrm{km\,s^{-1}}$. If the seeing on the night of observation is smaller than the slit width projected on the sky, the delivered resolution is enhanced. In the VIS and NIR arms the resolution is determined by fitting a range of telluric absorption lines and extracting the full-width-at-half-maximum (FWHM). Since no tellurics fall in the UVB arm from which we can measure the resolution directly, we extrapolated the ratio of the observed-to-nominal resolution in the VIS arm and assume the same ratio for the observed-to-nominal resolution in the UVB arm. For each burst we list the delivered resolution in the UVB and VIS arm in Table 8.2.1.

All the science spectra were reduced in a consistent manner for the XS-GRB legacy sample. The exact procedure is described in Selsing et al. (2019), so in the following we will only briefly summarize the data reduction strategy. First, the raw spectra were processed through a cosmic-ray removal algorithm (van Dokkum, 2001). Then, each of the exposures were separately reduced using the VLT/X-shooter pipeline, version `2.7.1` or newer (Goldoni et al., 2006; Modigliani et al., 2010), and were subsequently combined in the post-processing. The pipeline produces a flat-fielded, rectified and wavelength-calibrated 2D spectrum for every frame in the UVB, VIS and NIR arm. To extract the final 1D spectra from the combined 2D frames we model the trace using a running Voigt-profile fit. All wavelengths reported throughout the paper are in vacuum and are shifted to the heliocentric velocity. Finally, the spectra were corrected for the Galactic extinction in the line-of-sight using the dust maps of Schlegel et al. (1998) from the most recent update (Schlafly & Finkbeiner, 2011).

3.2.2 Selection criteria

After examining the individual quality of all the spectra we imposed additional observational and brightness constraints to remove bursts with poor signal-to-noise (S/N) ratios (effectively eliminating the majority of sources for which the mean $S/N \lesssim 3$ per wavelength element). The criteria we imposed for the GRB follow-up observations are: *i*) that the GRB was observed with X-shooter within 24 hours after the GRB trigger, *ii*) the brightness measured from the X-shooter acquisition image is brighter than 21.0 mag and *iii*) there is spectral coverage of the Lyα profile and at least the N v doublet of the high-ionization transitions, effectively requiring that the galaxies hosting the bursts are located at $z \gtrsim 1.7$. In total, 18 GRBs observed with the VLT/X-shooter fulfill these

Table 3.2.1. Low ionization properties and N v detection summary.

GRB	$z_{\rm GRB}$	$\log N$(H I) ($\rm cm^{-2}$)	[X/H]	[X/Fe]	Ion	$\log N$(N v) ($\rm cm^{-2}$)	δv ($\rm km\ s^{-1}$)	Refs.
090809	2.73706	21.70 ± 0.20	-0.57 ± 0.10	0.30 ± 0.31	Si	< 14.43	⋯	(1)
090926A	2.10694	21.60 ± 0.07	-1.85 ± 0.10	0.34 ± 0.13	S	14.30 ± 0.19	4 ± 2	(2)
100425A	1.75640	21.05 ± 0.10	-0.96 ± 0.42	⋯	Fe	< 14.63	⋯	(1)
111008A	4.99146	22.30 ± 0.06	-1.70 ± 0.10	0.05 ± 0.13	S	> 14.00	8 ± 10	(3)
120119A	1.72883	22.70 ± 0.20	-0.79 ± 0.42	0.36 ± 0.28	Si	< 15.15	⋯	(4)
120327A	2.81482	22.01 ± 0.09	-1.17 ± 0.11	0.56 ± 0.15	Zn	13.56 ± 0.03	0 ± 1	(5)
120815A	2.35820	21.95 ± 0.10	-1.15 ± 0.12	1.01 ± 0.10	Zn	14.60 ± 0.18	-6 ± 7	(6)
120909A	3.92882	21.70 ± 0.10	-0.66 ± 0.11	0.88 ± 0.16	S	14.75 ± 0.11	-14 ± 4	(1)
121024A	2.30244	21.88 ± 0.10	-0.40 ± 0.12	0.85 ± 0.04	Zn	< 14.35	⋯	(7)
130408A	3.75792	21.80 ± 0.10	-1.24 ± 0.12	0.11 ± 0.26	S	14.44 ± 0.07	-16 ± 2	(1)
130606A	5.91278	19.91 ± 0.02	-1.30 ± 0.08	0.79 ± 0.13	Si	14.50 ± 0.04	-83 ± 1	(8)
141028A	2.33327	20.60 ± 0.15	-0.50 ± 0.38	0.57 ± 0.21	Si	14.28 ± 0.10	-104 ± 20	(4)
141109A	2.99438	22.10 ± 0.20	-1.40 ± 0.22	0.84 ± 0.37	Zn	$\gtrsim 14.85$	13 ± 15	(9,10)
150403A	2.05707	21.80 ± 0.20	-0.80 ± 0.35	1.31 ± 0.43	S	14.73 ± 0.14	-32 ± 3	(9,10)
151021A	2.32975	22.20 ± 0.20	-1.11 ± 0.20	1.15 ± 0.28	Si	14.80 ± 0.46	34 ± 5	(9,10)
151027B	4.06469	20.50 ± 0.20	-1.62 ± 0.24	0.34 ± 0.28	Si	< 13.98	⋯	(9,10)
160203A	3.51871	21.75 ± 0.10	-1.26 ± 0.11	0.59 ± 0.25	S	< 13.58	⋯	(9,11)
161023A	2.71067	20.96 ± 0.05	-1.24 ± 0.09	0.45 ± 0.11	Si	13.66 ± 0.08	-114 ± 6	(12)

References. (1) Cucchiara et al. (2015); (2) D'Elia et al. (2010); (3) Sparre et al. (2014); (4) Wiseman et al. (2017); (5) D'Elia et al. (2014); (6) Krühler et al. (2013); (7) Friis et al. (2015); (8) Hartoog et al. (2015); (9) Tanvir et al. (2019); (10) Thöne et al. (in preparation); (11) Pugliese et al. (in preparation); (12) de Ugarte Postigo et al. (2018).

criteria, see Table 8.2.1 (for the observational details) and Sect. 3.2.3 and Table 3.2.1 (for the low-ionization properties of each).

The N v transition is of particular interest to us since it has been shown that the majority of this highly ionized gas must be located within approximately 1 kpc of the GRB explosion site (Prochaska et al., 2006) or perhaps even within $\lesssim 10$ pc (Prochaska et al., 2008b). Studying these events, together with the low-ionization properties of the host galaxy, allows us to constrain the physical properties of their circumburst medium. Moreover, this line is located in the red wing of the absorption trough of the Lyα line and is easily detected compared to the majority of the high-ionization species that are located in the Lyα forest. The final sample of GRBs observed with VLT/X-shooter presented here is three times the size of previous surveys for N v absorption in GRB afterglows (Prochaska et al., 2008b; Fox et al., 2008) and extends the redshift range out to $z \sim 6$. These former two surveys found a high detection rate of N v in 6/7 GRB afterglows, however, five bursts were common to both samples. From our sample here we can independently assess the detection rate.

For completeness, we also survey the high-ionization species of N v $\lambda\lambda$1238, 1242, O vi $\lambda\lambda$1031, 1037, C iv $\lambda\lambda$1548, 1550, Si iv $\lambda\lambda$1393, 1402, S iv λ1062 and S vi $\lambda\lambda$933, 944. The ionization potential to create these ions are 77.5, 113.9, 47.9, 33.5, 34.8 and 72.6 eV (see also Table 3.3.1). In addition to these, we also look for P v $\lambda\lambda$1117, 1128, which to our knowledge have not been observed in GRB afterglow spectra before.

Furthermore, we include absorption lines that trace the neutral gas, typically Si II or Fe II to 1) determine the systemic redshifts, $z_{\rm GRB}$, and 2) to measure the gas-phase metallicity of the galaxy hosting the GRB (see below). In the Appendix we provide notes on all the individual GRBs in our sample and the detected high-ionization lines.

3.2.3 Low-ionization properties

For each burst, the systemic redshift, $z_{\rm GRB}$, is defined by the position of the peak optical depth in the low-ionization lines (typically Fe II or Si II). We searched for high-ionization absorption features within $z_{\rm GRB} \pm 500$ km s^{-1}, representing the low-velocity components. We did not look for high-velocity components ($500 - 5000$ km s^{-1} relative to $z_{\rm GRB}$), that likely trace outflows that can be driven to high velocities by the burst progenitor (see e.g., Fox et al., 2008; Castro-Tirado et al., 2010), since we are only interested in the immediate environment around the GRB. We list the measured $z_{\rm GRB}$ for each burst in the second column in Table 3.2.1. In the third column, the neutral hydrogen (H I) column density is reported for each GRB where we adopt the values reported in the single papers that examined the individual bursts (see references in the table) or those from the extensive compilation of GRB afterglow H I column densities by Tanvir et al. (2019, and references therein).

Except for GRBs 141109A, 150403A, 151021A, 151027B, 160203A, and 161023A (de Ugarte Postigo et al., 2018), we adopt the gas-phase metallicities reported in the literature (see the references in Table 3.2.1), listed as [X/H], where the ion X is one of the volatile species, Si, S or Zn. In all cases, the dust depletion of the ion X relative to iron, [X/Fe], is also reported. For the remaining six bursts in our sample we use our own fitting tool to derive column densities and gas-phase metallicities of the low-ionization absorption features by performing a series of Voigt-profile fits to the absorption line profiles (the full set of absorption line fits to the XS-GRB sample will be published in Thöne et al., in preparation).

The code is developed in `Python` and is described in detail in Krogager (2018). Simply, the software takes as input the instrumental resolution, the zero-point redshift and the H I column density and returns the redshift of the different velocity components (z), line width (b), and column density ($\log N$) for each species. The derived metallicities and depletion patterns are summarized in Table 3.2.1 and are reported in detail for each burst in the Appendix. We follow the same procedure to derive the column densities of the high-ionization absorption features by fitting the various components and ionization species in each GRB afterglow spectrum independently. Since the N V $\lambda\lambda$ 1238,1242 doublet is located in the red wing of the Lyα absorption trough in bursts with large H I column densities ($\log N({\rm H\,I}) \gtrsim 21$), the continuum flux in this region will be underestimated. To measure the column density of N V we therefore fit the N V and Lyα lines simultanously, using a prior estimate of the H I column density from the already published values. This approach is shown in Fig. 3.2.1 for GRB 090926A (with an H I column density of $\log N({\rm H\,I}) \gtrsim 21.60$), where it is also clearly demonstrated how the Lyα absorption affects the continuum level in the region around the N V doublet. For the non-detections of N V, 3σ upper limits were calculated using $N({\rm N\,V}) = 1.13 \times 10^{20}\, W_{\rm lim}/\lambda_0^2 f$ where $W_{\rm lim}$ is the 3σ upper limit on the rest-frame equivalent width in Å and N(N V) is in cm^{-2}.

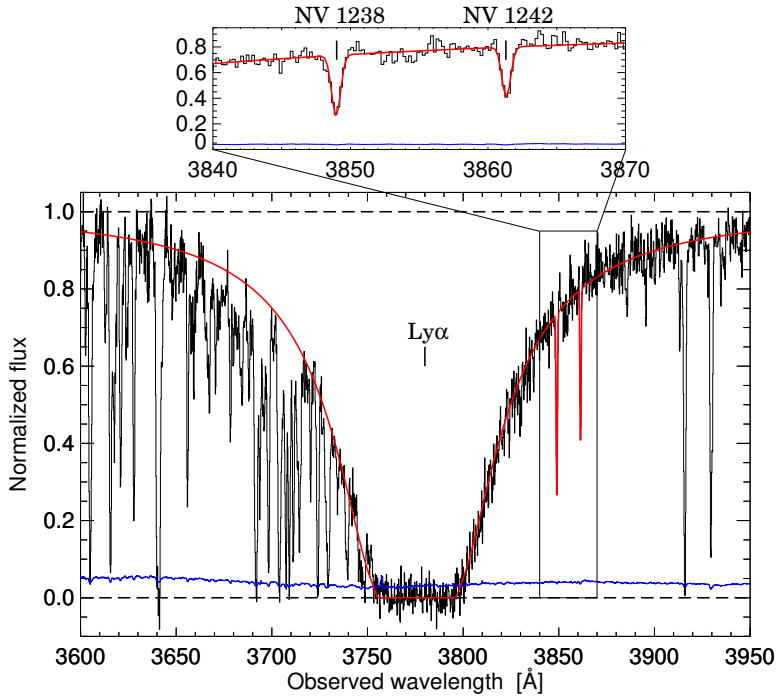

Figure 3.2.1. VLT/X-shooter spectrum of GRB 090926A. In the bottom panel, the black solid line shows the normalized UVB arm spectrum centred on Lyα at $z \approx 2.107$ with the associated error spectrum shown in blue. The best-fit Voigt profiles to the Lyα line and the N v $\lambda\lambda$ 1238,1242 doublet is shown as the solid red line. In the upper panel we show a zoomed-in region of the N v transitions and the same combined Voigt profile fit.

3.3 Results

The results of the Voigt profile fits for each burst are shown in the Appendix (Tables 3.5.1 to 3.5.16 and Figs. 3.5.1 to 3.5.16) together with notes on all the GRB afterglows in our sample. We report the best-fit Voigt profile parameters in individual tables and show the corresponding fit in the figures belonging to each burst. In each of the figures, an example of one of the low-ionization absorption lines is included, where the peak optical depth of this line represents $z_{\rm GRB}$. In Table 3.3.1 we list the results of the Voigt profile fits and show the corresponding best-fit combined line profiles in velocity-space in Fig. 3.3.1 for one of the bursts, GRB 161023A, as an example (but see also de Ugarte Postigo et al., 2018).

In the majority of cases, the high-ionization species O VI, S IV, S VI, and P V are blended with the Lyα forest. Si IV and C IV are detected in all of the GRB afterglow spectra but are both heavily saturated. In this section we therefore focus mainly on the N V doublet that has the advantage of not being saturated (in most cases) compared to some of the other high-ionization lines, and is located in the red wing of the Lyα absorption trough. The medium resolution of the X-shooter spectrograph also ensures

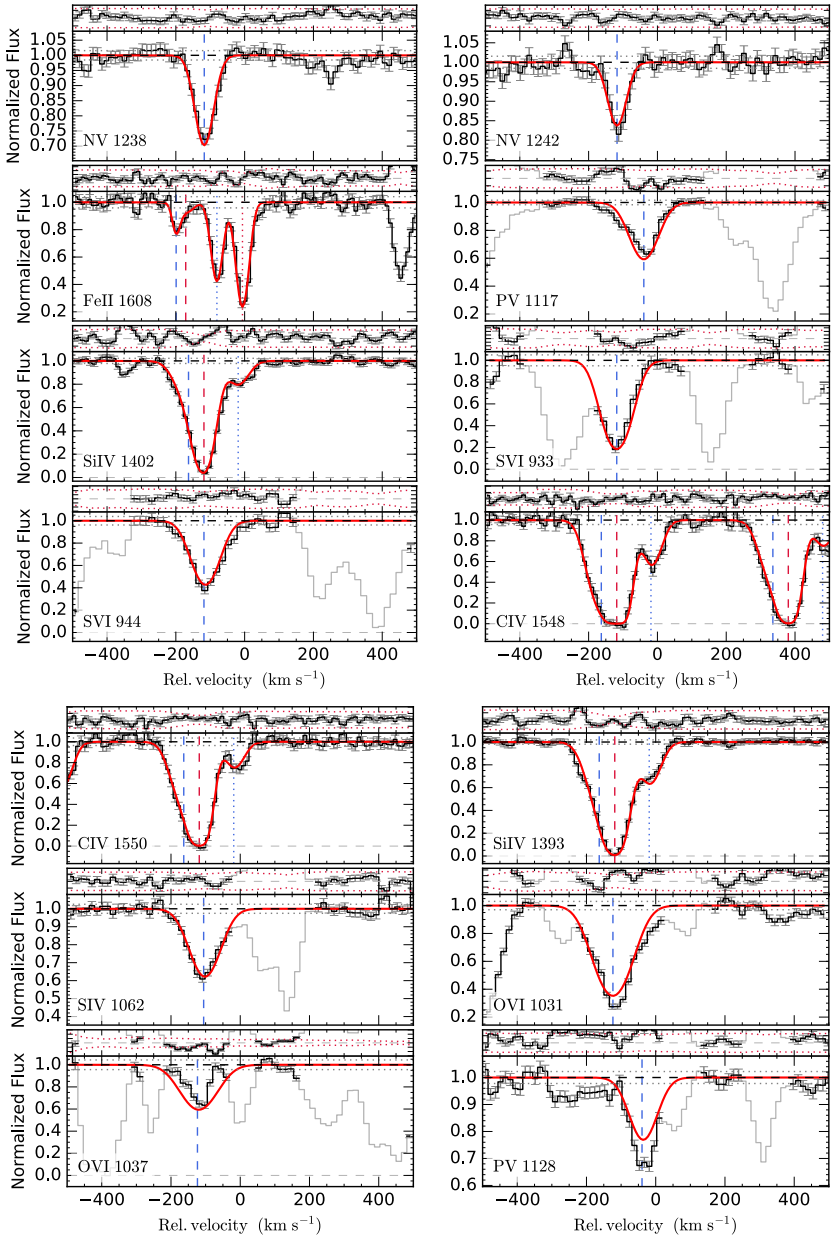

Figure 3.3.1. GRB161023A: Normalized high-ionization absorption-line profiles on a velocity scale relative to $z_{\rm GRB}$. Voigt profile fits are shown in red (solid line) with the center of each velocity component marked with dotted or dashed lines. The part of the spectrum shown in grey is masked out in the fit. The residual spectrum to the best fit is shown at the top of each panel.

Table 3.3.1. Voigt profile fits for GRB 161023A at $z = 2.71067$. The ionization potential (IP) for each transition is also listed.

Ion	IP eV	v_0 (km s^{-1})	b (km s^{-1})	$\log N$ (N in cm^{-2})	$\log N_{\rm total}$ (N in cm^{-2})
N v	77.5	-114 ± 6	30 ± 10	13.66 ± 0.08	13.66 ± 0.08
O vi	113.9	-118 ± 6	78 ± 9	14.59 ± 0.04	14.59 ± 0.04
C iv	47.9	-130 ± 2	44 ± 3	14.91 ± 0.07	14.93 ± 0.07
		-8 ± 4	22 ± 7	13.60 ± 0.04	
Si iv	33.5	-117 ± 4	26 ± 7	14.47 ± 0.18	14.50 ± 0.17
		-27 ± 13	44 ± 17	13.30 ± 0.13	
		-168 ± 65	47 ± 41	13.56 ± 0.75	
S iv	34.8	-104 ± 8	58 ± 12	14.66 ± 0.07	14.66 ± 0.07
S vi	72.6	-121 ± 6	52 ± 8	14.17 ± 0.06	14.17 ± 0.06
P v	65.0	-39 ± 6	49 ± 9	13.54 ± 0.06	13.54 ± 0.06

that the N v doublet is well resolved. Due to the varying quality of the spectra and since the Lyα absorption line and N v doublet lies in the bluemost part of the UVB arm for redshifts $z \approx 1.7$, the detection limit varies from approximately $\log N$(N v) = 13.5 to 15.2. The results of the N v column densities and 3σ upper limits are summarized in Table 3.2.1, where we also list the relative velocity to $z_{\rm GRB}$. For the GRBs with N v detections we find average and median values of $\log N(\mathrm{N\,v})_{\rm avg} = 14.36$ and $\log N(\mathrm{N\,v})_{\rm med} = 14.50$, respectively. We obtain robust fits to all the N v lines, and we find that blending or line saturation is not an issue in the majority of cases (although see the individual tables for the few exceptions). As mentioned above, the column densities for N v are fitted simultaneously with the Lyα line and those values are reported in Table 3.2.1 and in the individual tables in the Appendix. The measured column densities using this approach are, however, mostly consistent (within the 1σ errors) to the values obtained by fitting only the N v lines.

As the large ionization potential of N iv (as well as O v and S v) well exceeds the integrated galactic ionizing radiation from O and B stars that drops strongly above 54 eV due to the He ii ionization edge (Bregman & Harrington, 1986), an additional intense radiation source is required to produce N v. Furthermore, Prochaska et al. (2008b) demonstrated that GRB afterglows can photoionize nitrogen up to N v if the gas is closer than ≈ 10 pc. This, together with the fact that the relative velocities of the N v lines in general are coincident with the UV-pumped fine-structure lines of Si ii and Fe ii (Prochaska et al., 2008b), implies that the observed N v absorption features are related to the material close to the GRB or its progenitor. The following sections are dedicated to investigate the relation between the characteristics of the N v gas and the physical properties of the GRB host galaxy, such as GRB redshift, ISM gas-phase metallicity, dust and metal column density and internal kinematics.

3.3.1 Detection rates

We detect at least two of the surveyed high-ionization absorption features within a few hundred km s^{-1} of $z_{\rm GRB}$ in all 18 GRB spectra. The detection rates are N v (seen in 12/18 cases), O vi (3/18), C iv (18/18), Si iv (18/18), S iv (5/18), S vi (6/18), and P v (4/18). The detection rates of the high-ionization lines that originate in the Lyα forest are to be treated as lower limits since they are, in the majority of cases, heavily blended or located in a spectral region with a poor S/N. Compared to earlier studies of high-ionization lines in GRB afterglows (e.g. Prochaska et al., 2008b; Fox et al., 2008), the detection rate of N v is lower in our sample. Both of the previous samples found that N v was detected in 6/7 GRB afterglow spectra. The single burst, GRB 060607, with a non-detection of N v down to $\log N(\mathrm{N\,v}) < 12.61$, common to both samples, is unique in the sense that it has a very low H i column density. The physical properties of the line of sight to this GRB is therefore most likely significantly different.

While our sample show six non-detections of N v, the limits in the individual GRB afterglow spectra are almost at the same order as the derived N v column densities. To understand why N v is only observed in 12/18 GRB afterglow spectra, our first approach is to examine whether the detection rate is caused by observational constraints. In Fig. 3.3.2 we show the derived column density of N v as a function of hours post-burst at the time of observation and the measured acqusition magnitude (values taken from Selsing et al., in preparation). There appears to be no correlation between any of these parameters. We note, however, that four out of the six bursts with non-detections of N v were faint in the acquisition images at the time of observation, which would suggest that the cause of the non-detections are of observational origin.

Another scenario could be that the luminosity of the afterglow itself is not intense enough to produce highly-ionized metals. To test this scenario we examine the gamma-ray luminosity, $L_{\gamma,\rm int}$ (erg s^{-1}), of each burst and compare it to the N v column density. We extract the gamma-ray fluence, $F_{\gamma,\rm obs}$ (erg cm^{-2}), from the *Swift*/BAT database in the observer frame energy band 15-150 keV. To convert this value to an intrinsic property we calculate $L_{\gamma,\rm int} = F_{\gamma,\rm obs}\, 4\pi\, d_L^2\, (1+z)^{-1}$ (similar to Lien et al., 2016), where d_L is the luminosity distance. We caution that this is a simple approximation, and that a k-correction in principle also should be applied to account for the spectral shape. The results are shown in Fig. 3.3.3. It is clear that the non-detections all belong to intrinsically faint GRBs (as already noted above from the acquisition images) except for GRB 120119A for which we are, however, only able to put a poorly constrained upper limit on N v. For reference, GRB 060607 (with a non-detection reported for N v) has an intrinsic gamma-ray fluence of $\log L_{\gamma,\rm int} = 52.71$. This value is around the median for the GRBs in our sample, suggesting that the non-detection in this case is likely due to the different nature of the galaxy hosting this GRB. For comparison we detect two cases with one and two orders of magnitudes higher N v column densities ($\log N(\mathrm{N\,v}) = 13.5 - 14.5$) with the same intrinsic gamma-ray luminosity, $\log L_{\gamma,\rm int} \approx 52.7$, as GRB 060607.

Since the total isotropic gamma-ray energy is correlated with the X-ray and optical afterglow brightness (Nysewander et al., 2009), it is reasonable to expect that the production of highly ionized metals should be correlated with the radiation field from the GRB itself and the following afterglow radiation. The fact that the strength of N v depends on the intrinsic gamma-ray energy of the GRB then supports a scenario

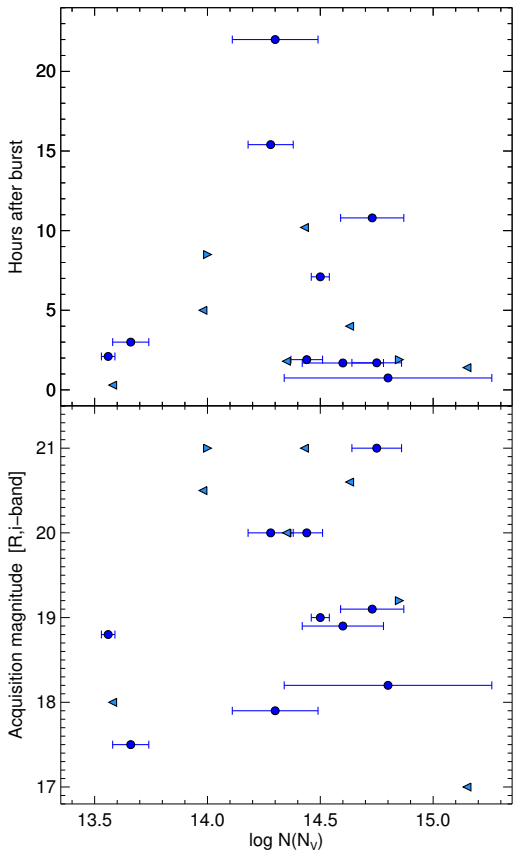

Figure 3.3.2. Detection of N v as a function of time of observation post-burst (upper panel) and acquisition magnitude of the afterglow (bottom panel). Blue dots denote bursts where N v is detected and a column density measured. Light blue triangles are non-detections and the corresponding 3σ upper limit is instead shown.

where N v traces the circumburst medium of the GRB. We will return to this issue in Sect. 3.3.4 where we provide further evidence that N v is a good probe of the metals in the molecular cloud or H II region surrounding the GRB.

3.3.2 Dependence of N v on neutral gas properties

To explore the different factors that might influence the production of N v, we plot the measured N v column densities as a function of redshift in Fig. 3.3.4 and as a function of metallicity, H I column density and dust depletion in Fig. 3.3.5. We include the GRBs from the two previous surveys for N v and high-ionization absorption (Prochaska et al., 2008b; Fox et al., 2008) in both figures. Our sample spans a redshift range of $1.7 < z < 6$ and N v column densities of $13.5 \lesssim \log N(\mathrm{N\,v}) \lesssim 15.0$ (not including non-detections). The probability and strength of N v detection is not dependent on redshift, but we note that the two GRBs at $z > 4$ have higher than average N v column densities.

Comparing the probability and strength of the N v detection to the physical properties related to the neutral gas of the GRB hosts reveals that N v is not dependent on the H I column density and metallicity (see the computed linear Pearson correlation coefficients

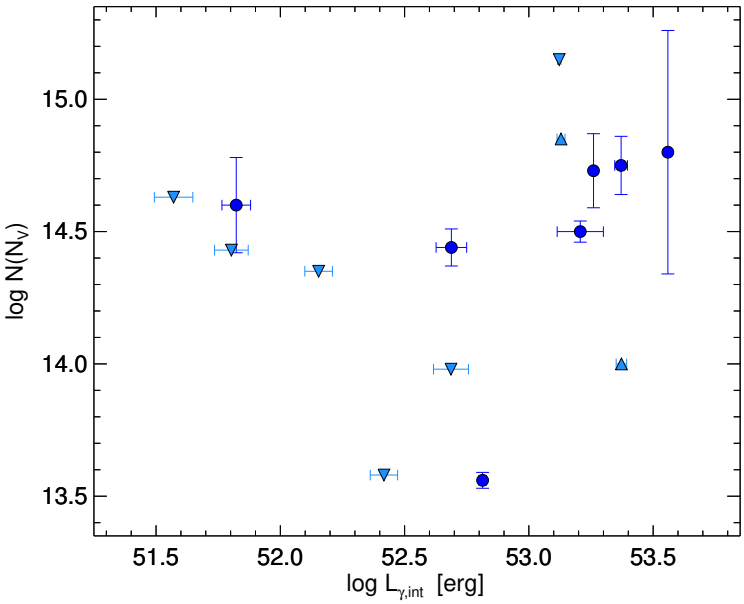

Figure 3.3.3. Detection of N v as a function of the intrinsic gamma-ray luminosity, $L_{\gamma,\mathrm{int}} = F_{\gamma,\mathrm{obs}}\ 4\pi\ d_L^2\ (1+z)^{-1}$, where $F_{\gamma,\mathrm{obs}}$ is the observed BAT fluence in the 15 – 150 keV band. The full sample is shown except for GRBs 090926A, 141028A and 161023A since these were not detected by *Swift*/BAT. The same symbols are used as in Fig. 3.3.2.

in each of the panels in the figure), consistent with previous conclusions. We note, however, that there is a tentative correlation with dust depletion at the 1σ level and that strong N v absorption is predominantly seen at high values of N(H I). Our sample spans metallicites of -1.9 < [X/H] < -0.4, neutral hydrogen column densities of 19.9 < log N(H I) < 22.7 and dust depletion ratios of 0.1 < [X/Fe] < 1.3. We can therefore provide further evidence that the highly-ionized gas in GRBs is not directly related to the properties of the neutral ISM. This is in contrast to what is observed for QSO-DLAs with N v detections, where the detection probability is found to be dependent on metallicity (Fox et al., 2009). Absorbing galaxies toward quasars are not expected to contain intense non-stellar radiation (like GRBs), so the high-ionization absorption in quasar DLAs likely originates in the ISM or in the halo gas (which also explains the lower mean value of log N(N v) = 13.78, and the large percentage (≈ 87%) of non-detections Fox et al., 2009).

3.3.3 Velocity offset of N v

A crucial piece of information about the circumburst medium can be obtained if we can localize the GRB in the host galaxy and derive its immediate physical conditions. However, deep, resolved imaging of GRB host galaxies is required to accurately locate the GRB explosition sites and to investigate the physical properties of their surrounding

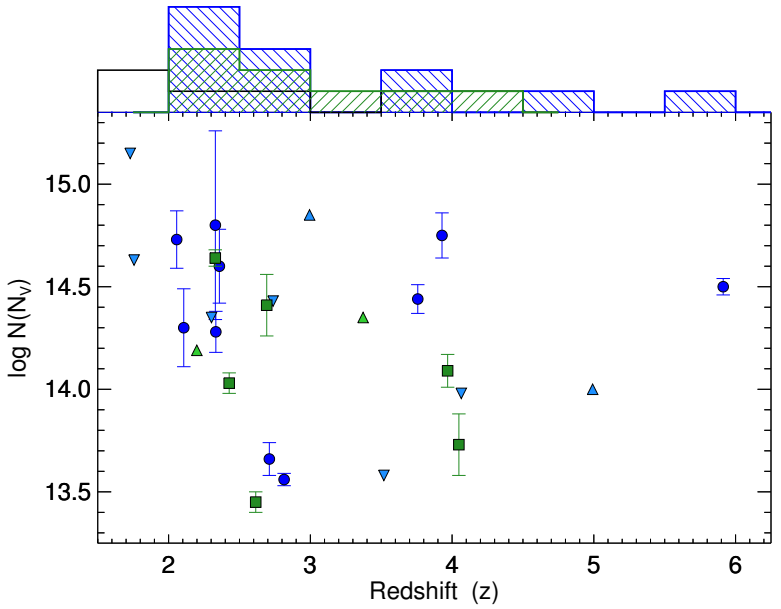

Figure 3.3.4. The column density of N v as a function of redshift. In the bottom panel, the same symbols are again used as in Fig. 3.3.2 and 3.3.3 for GRBs in our sample. We have included N v detections from two previous GRB surveys (Prochaska et al., 2008b; Fox et al., 2008), shown here as the green squares and upward facing triangles (lower limits). In the upper panel we show the redshift distribution of the GRBs in our sample with (blue filled) and without (solid line) N v detections as histograms. The full sample spans a large redshift range of $1.7 < z < 6$. In addition, the distribution of the included GRBs with N v detections from previous surveys is shown as the green filled histogram.

medium. Such maps are very challenging to obtain for GRB hosts at high redshifts (Tanvir et al., 2012b, although see e.g. McGuire et al. (2016) where *HST* imaging was sufficient to resolve the location of the GRB 130606A close to the centre of its host). Instead, we can examine the relative velocity of the main component of high-ionization absorption, assuming that it represents discrete clouds in the host galaxy, to see how it coincides with the low-ionization components tracing the neutral ISM gas. Detailed studies of the velocity components of high-ionization lines can also potentially reveal the scales of which the intervening gas absorbs the photons from the GRB afterglow, shown e.g. for GRB 021004 (Møller et al., 2002; Castro-Tirado et al., 2010).

We compare the relative velocity of the strongest N v component to $z_{\rm GRB}$ as a function of metallicity and H I column density in Fig. 3.3.6. If the strongest, high-ionization components are aligned with the peak optical depth of the low-ionization profiles, they likely originate in the same cloud. If GRBs preferably occur in metal-poor environments it is reasonable to expect that the metal-rich GRB host galaxies would show high-ionization components separated from the strongest low-ionization metal components. We do not find any statistically significant correlation between the relative velocity of the high-ionization components to $z_{\rm GRB}$ as a function of metallicity.

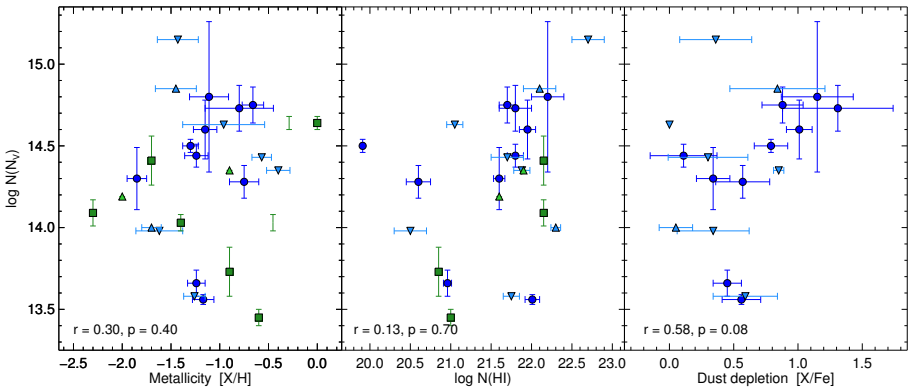

Figure 3.3.5. The column density of N v compared to low-ionization properties. We show the detection of N v in our sample, and the detections from the previous two GRB surveys for N v, as a function of metallicity (left panel), H I column density (middle panel), and dust depletion (right panel). In each panel the computed r and p values are shown. The same symbols are used as in Fig. 3.3.4.

We do note, however, that at higher metallicities the scatter around $z_{\rm GRB}$ increases. This is likely due to a mass-metallicity scaling relation, where the more metal-rich GRBs are consistently more massive (and thus physically larger; Ledoux et al., 2006; Arabsalmani et al., 2018b). This allows for a greater range of internal velocities of possible star-forming clouds.

We find that the relative velocity of N v to $z_{\rm GRB}$ depends on the H I column density of the GRB. While an approximate linear function could describe the relation between the two quantities quite well (see the r and p values in the bottom panel of Fig. 3.3.6), an alternative is that the data instead show two populations: One with large H I column densities ($\log N({\rm H\,I}) > 21.5$) for which N v is aligned with $z_{\rm GRB}$ and one with low H I column densities ($\log N({\rm H\,I}) < 21.0$) for which the N v component is separated by $\approx 80-120\,{\rm km\,s^{-1}}$ relative to the peak optical depth of the low-ionization profiles. While we do not find any correlation between N v and H I column densities, such that the immediate environment of the GRB is directly related to the H I column density, we argue that the data instead shows a confinement effect. We propose a scenario where the pressure of dense ($\log N({\rm H\,I}) > 21.5$) clouds confine the H II region or molecular cloud, in which the GRB exploded, to the part of the galaxy with the largest amount of neutral gas. In more diffuse clouds ($\log N({\rm H\,I}) < 21.0$) the star-forming region is not as confined by the gas pressure. From the lower panel of Fig. 3.3.6 it can also be seen that only blueshifts of high-ionization components are measured with a relative velocity of $\approx -100\,{\rm km\,s^{-1}}$. This would also be explained by the confinement scenario where the diffuse H I gas is not dense enough to counterbalance the effect of stellar winds originating from massive stars in the H II region. Stellar winds causing the expansion of the H II region is also of the order $\approx 100\,{\rm km\,s^{-1}}$ (Dyson, 1977), which would explain why we only observe the blueshifted component: the absorbing material is expanding and thus move towards us in the line of sight to the GRB explosion site. If this scenario

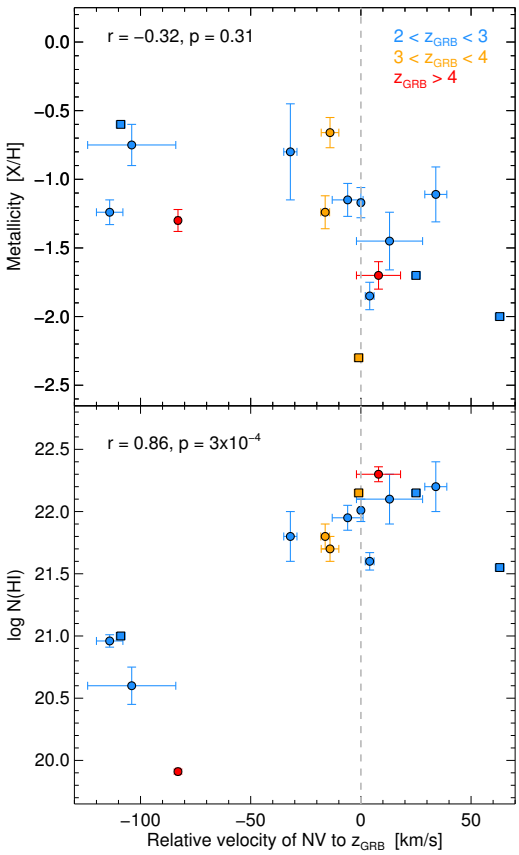

Figure 3.3.6. The relative velocity of the strongest component of N v compared to $z_{\rm GRB}$ as a function metallicity (upper panel) and H I column density (lower panel). The dots (our sample) and squares (bursts from the previous samples) representing the GRBs are color-coded as a function of redshift. In both panels the computed r and p values are shown. The dashed line intercept the GRBs for which the position of the strongest high-ionization absorption component is consistent with the strongest low-ionization absorption component in relative velocity space.

is true, then we would also expect that the relative velocity of the fine-structure lines are slightly less blueshifted compared to N v, since the are typically measured to be at distances around a few hundred pc from the GRB. Only one of the GRBs in all three high-ionization line samples have a simultaneous measurement of N v (at $\delta v \approx -80$ km s^{-1}) and a fine-structure line (GRB 130606A; Hartoog et al., 2015), which shows a slightly smaller blueshift of Si II* at $\delta v \approx -50$ km s^{-1}. For more of such cases, the relative velocity of the fine-structure and high-ionization would be valuable to examine.

3.3.4 The circumburst gas

The majority of GRB afterglows observed with *Swift*/XRT show soft X-ray absorption in excess of Galactic (e.g. Galama & Wijers, 2001; Watson et al., 2002). While the X-ray absorption is believed to be dominated by metals, its origin has yet to be fully understood. Some authors claim that it traces the IGM along the line of sight (e.g. Behar et al., 2011; Campana et al., 2015) due to the increasing soft X-ray column density with redshift, however, no such trend has been observed e.g. toward quasars (Eitan & Behar, 2013). Since the Galactic X-ray absorption is also well accounted for (Willingale

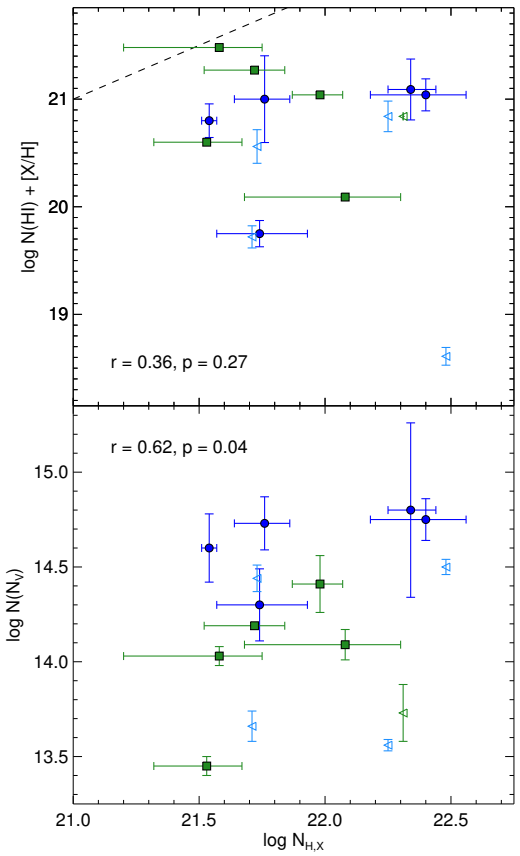

Figure 3.3.7. The *Swift*/XRT soft X-ray derived metal column density, $N_{\rm H,X}$, as a function of the UV/optical metal column density, $\log N(\mathrm{H\,I})$ + [X/H], (upper panel) and the N v column density (bottom panel). In both panels the computed r and p values are shown. In the upper panel the 1:1 ratio between the two distinct metal column densities is represented as the dashed line. Only the GRBs from our sample and the two previous samples with N v detections are plotted in both panels. Open triangles denote GRBs with upper limits on $N_{\rm H,X}$.

et al., 2013), this indicates that the observed excess X-ray derived absorption column density is likely located at the GRB redshift. Furthermore, the derived X-ray absorption is typically found to be larger than the column density of neutral hydrogen (Watson et al., 2007, 2013; Campana et al., 2010) and the metal column density of the neutral gas (Galama & Wijers, 2001; Schady et al., 2010; Zafar et al., 2011a; Greiner et al., 2011) related to the dust extinction, A_V, of the ISM (Zafar & Watson, 2013). This is also demonstrated in the upper panel of Fig. 3.3.7 where we compare the the X-ray derived column density and the optically derived metal column density of the neutral ISM ($\log N(\mathrm{H\,I})$ + [X/H]) for the bursts with N v detections from our sample and the two previous samples of Prochaska et al. (2008b) and Fox et al. (2008). The X-ray column densities are either adapted from the literature (e.g., Campana et al., 2010, but see the notes in the Appendix) or from the *Swift*/XRT repository[1]. We confirm the trend of significantly larger X-ray derived metal column densities and observe no correlation with the optically derived metal column density. This indicates that the soft X-ray absorption is not dominated by the neutral gas of the ISM in GRB host galaxies.

[1] `http://www.swift.ac.uk/xrt_spectra/`

This suggests that the large X-ray absorption originates in a much smaller region, possibly close to the GRB. The main difficulty in studying the circumburst medium of GRBs is that they are so energetic that they are expected to destroy dust and ionize gas to very large distances from the burst, thereby largely removing this circumburst gas from tracers in the optical afterglow spectra. Previously, it has been postulated that the majority of the X-ray absorption might originate from highly ionized gas (Schady et al., 2011) or from helium (Watson et al., 2013) in the immediate, circumburst environment of the GRB, constituting the H II region. Therefore, the most viable tool to study the circumburst material is likely from hot gas signatures or to observe the gas at X-ray wavelengths. No strong correlations are yet observed, however, thereby constraining the use of the soft X-ray absorption as a diagnostic tool to study the circumburst medium of GRBs.

Prochaska et al. (2008b) suggest that both the N V column density and the X-ray absorption should be sensitive to the metals in the vicinity of the GRB. If N V is produced by photoionization from the GRB afterglow, and the X-ray photons are absorbed at the same approximate distance, we would expect a correlation between the two measurements. In the lower panel of Fig. 3.3.7 we demonstrate for the first time that there is indeed evidence for such a correlation. Combining our sample with the two previous samples we find that by computing the linear Pearson correlation coefficients for the N V column density as a function of the X-ray derived absorption column density yield $r = 0.62$ and $p = 0.04$ (excluding upper limits), i.e., the null hypothesis is rejected at more than 2σ. GRB 141028A is located outside the plotting region with an upper limit on $\log N_{\rm H,X}$ of <23 cm^{-2} to better illustrate the linear correlation. Subtracting the optically derived metal column density from the X-ray absorption column yields a similar result, indicating that the metals in the neutral gas-phase in the ISM provide a negligible contribution to the X-ray absorption. The fact that there is marginal evidence for a correlation between N V and the X-ray absorption also suggests that the majority of the X-ray derived column density originates in the host galaxies of GRBs and not e.g., in the intergalactic medium (IGM) or intervening systems. The scenario where the X-ray absorption traces the H II region or (former) molecular cloud in which the GRB exploded is also supported by the observed correlation between the X-ray column density and the surface luminosity (Lyman et al., 2017) since both are expected to be related to a region of intense star formation.

3.4 Discussion

3.4.1 Highly-ionized gas from recombination

While it has previously been shown by Prochaska et al. (2008b) that N V can be produced by photoionization from the GRB afterglow, their model relies on no prior ionization of the circumburst gas, e.g. by the initial prompt emission from the GRB. Based on the correlation between N V and the X-ray derived metal column density, $N_{\rm H,X}$, we infer that the relative abundance of nitrogen is related to the total metal column density inferred from X-ray absorption. In the following we examine whether N V absorption could be dominated by the recombination of nitrogen stripped of electrons by the prompt emission (as suggested by e.g. Watson et al., 2013) out to a few pc. We demonstrate that

the observed column density of N v (and also O vi for a few cases) can be reproduced by the recombination of nitrogen (and oxygen) atoms using simple approximations. However, the temporal evolution of the column densities of these ions should be quite pronounced.

The recombination rate for a given transition is $R = \alpha\, n_e\, n_i$, where α is the recombination rate for the specific atom. The recombination time is therefore of the order $t_{\rm rec} \propto 1/(\alpha\, n_e)$. For the gas temperature ($T \approx 10^4$ K) and density ($n_e = 4 \times 10^3$ cm^{-3}) in a typical H ii region, and assuming that the total recombination coefficient $\alpha = 3 \times 10^{-9}$ for N v (Goshu, 2017, though this value is two orders of magnitude higher than the sum of the radiative and dielectronic recombination rate coefficients), this yields a recombination time of $t_{\rm rec} \approx 10^5$ s (i.e. about a day). Then, assuming the relative solar abundance of N to H is 6.7×10^{-5} (Asplund et al., 2009), we find that an absorber with 10^{22} cm^{-2} (typically observed in X-rays) yields 6.7×10^{17} nitrogen atoms cm^{-2}. Assuming all the nitrogen of interest is completely stripped of electrons immediately following the burst, and every other source of N iv ionizing photons is negligible, the fraction of nitrogen in the N v state can be determined following the recombination series and assuming the electron density remains approximately constant over this time. Under the order of magnitude assumption that the recombination coefficients of N v–N viii are the same, the general equation for the expected column density of N v can be written as $N(\mathrm{N\,v}) = \frac{1}{6} N(\mathrm{N}) \times (\alpha\, n_e\, \Delta t_{\rm rest})^3\, e^{-\alpha\, n_e\, \Delta t_{\rm rest}}$, where $N(\mathrm{N}) = N_{\rm H,X} \times (\mathrm{N/H})_\odot$, e.g. $N(\mathrm{N}) = 6.7 \times 10^{17}$ cm^{-2} for an X-ray absorber with 10^{22} cm^{-2}. At the typical time of observation, a somewhat high density of $\sim 2 \times 10^4$ cm^{-3} is required so that $\sim 10^{-3}$ of the nitrogen atoms will have recombined from N viii to N v to give a value of $\log N(\mathrm{N\,v})/\mathrm{cm}^{-2} \sim 14.6$, consistent with the linear correlation between $N_{\rm H,X}$ and N v found in Sect. 3.3.4. In the above we have assumed the recombination rate from Goshu (2017) for N v and that this is the same for N v to N viii. If the recombination rate is an order of magnitude lower or higher this would then yield electron densities of 2×10^5 cm^{-3} and 2×10^3 cm^{-3} instead, respectively.

Since O vi is expected to be produced by recombination in this scenario as well, we would expect the relative abundance of N v to O vi to be consistent with the solar ratio. This must be the case since the recombination rate is roughly the same for both ions and since N v and O vi are both lithium-like atoms with three electrons. In the recombination scenario, both atoms are therefore populated on the same time scales from fully ionized to N v and O vi, respectively. From the five bursts with robust measurements of both N v and O vi in our sample, and from Fox et al. (2008), we find that the ratios are in the range $N(\mathrm{N\,v})$ / $N(\mathrm{O\,vi}) = 0.08 - 0.38$ (with a mean and median ratio of ≈ 0.19), which is of the same order as the solar abundance ratio ($(\mathrm{N/O})_\odot \approx 0.13$; Asplund et al., 2009). The observed relative abundance ratio is more difficult to explain in the photoionization scenario, since O vi has a much higher ionization potential (≈ 115 eV) than N v (≈ 77 eV). We note that the [N/O] abundance ratios in low-metallicity systems are typically sub-solar (Pettini et al., 2008), exacerbating this inconsistency further.

However, in the pure recombination scenario sketched roughly above, the column density of N v should be very sensitive to the electron density and should be very time-dependent, with a value that initially rises very quickly in the first several hours after the burst and then drops exponentially at about a day, depending on the density and recombination rate coefficients. We cannot entirely exclude this simple scenario

based on the current data. GRB 120327A is the only GRB in our sample with two time-separated measurements of N v and shows no significant variability from 2 hours to 30 hours ($1\,\sigma$ difference is 26% of the first measurement). In most scenarios, we would expect a change of two orders of magnitude over this time. However, since that GRB has only upper limits to the X-ray column density it cannot be excluded that the points straddle a rise and fall centred around 1 day. In addition, our current data do not show a strong correlation with time taking the bursts as an ensemble. Time-series observations of N v in the future would be very valuable to completely rule out the simple recombination-dominated hypothesis, since for most reasonable H II region electron densities, we would expect the column density of N v to rise strongly with time, such that a substantial fraction of nitrogen atoms are recombined at 10^5 s ($\approx$ 1 day) compared to 10^4 s, easily ruling out (or confirming) a recombination-dominant scenario. The recombination outlined above excludes a contribution to the high-ionization column densities from photoionization by the GRB afterglow as suggested by Prochaska et al. (2008b). This effect almost certainly needs to be considered to properly model the time-variation of the column density in the high-ionization lines. As it is, neither the recombination or the photoionization scenarios are in agreement with the observed non-varying N v abundance and more time-resolved data is required to resolve this issue in both models.

3.4.2 Hot gas in GRB host galaxy halos

There is now positive evidence that the N v (and likely also O VI) absorption features seen in GRB afterglows originate in the circumburst medium of GRBs. We note, however, that these ions are also observed in the Galactic halo[2] (Savage et al., 1997; Sembach et al., 2003; Wakker et al., 2012) but rarely with column densities as large as that observed for the GRB sample. Prochaska et al. (2008b) use this argument, together with theoretical predictions, to exclude the galactic halo gas as the origin of N v and O VI absorption in GRB afterglows. The presence of N v and O VI absorption (though rare) in DLAs and sub-DLAs in the line-of-sight toward quasars (Fox et al., 2007b, 2009), however, likely originate from their galactic halos. Similar low column densities, as in the local Galactic halo, are observed for these samples. Moreover, the column density of N v in these quasar absorbers is found to be correlated with the column density and velocity width of C IV (Fox et al., 2009) which supports a circumgalactic origin.

The fact that the velocity width of C IV is generally more extended than the neutral gas profiles (e.g. Ledoux et al., 1998; Wolfe & Prochaska, 2000; Fox et al., 2007a) is in good agreement with a model where C IV originates in the hot gas constituting the galactic halos (Maller et al., 2003). That the same is true for C IV and Si IV absorption observed in GRB afterglows was motivated by e.g. Fox et al. (2008) who found that the velocity widths of these ions are similar to those observed for DLAs toward quasars (Fox et al., 2007a), with multiple components in a velocity range of several hundred km s^{-1} around $z_{\rm GRB}$ (although still with a larger average C IV column density).

With the advent of space borne UV spectroscopy, interstellar absorption lines of highly-ionized species (C IV, Si IV, N v, and O VI) have also been detected in several

[2]Here we use the term Galactic halo to distinguish the hot gas surrounding the host from the neutral ISM of the galaxy.

Galactic sight lines towards OB-type stars (e.g., Black et al., 1980). These detections demonstrate the presence of highly ionized "coronal" gas in the disk (and halo) of the Milky Way as well as in other nearby galaxies (Lehner et al., 2011). The absorption by C IV and Si IV exhibits broad and narrow components, while only broad components are seen in N V and O VI. The narrow components are associated with the vicinities of O-type stars and their surrounding supershells. The broad components trace collisionally ionized gas ($T > 10^5$ K) in the hot ISM.

It is not possible to robustly measure the column densities of C IV and Si IV for the GRBs in our sample due to heavy saturation. We confirm, however, that the velocity widths of these ions are generally much larger than the line profiles of the low-ionization lines and N V. Moreover, the peak optical depth of C IV and Si IV is not aligned with N V, except in a few cases where all three ions are aligned with $z_{\rm GRB}$. In conclusion, while C IV and Si IV absorption likely originate in the galactic halos of DLAs and sub-DLAs toward quasars and surrounding GRB hosts, N V and O VI absorption is caused by gas at two distinct regions in the two cases; one from the hot halo gas around DLA and sub-DLAs toward quasars and the other from the gas in the vicinity of the GRB explosion site (though also with a possible small contribution from the hot halo gas).

3.5 Concluding remarks

We have performed a survey for high-ionization absorption in 18 afterglow spectra of long-duration GRBs at $z \approx 1.7-6$ observed with VLT/X-shooter. We surveyed the high-ionization species of N V, O VI, C IV, Si IV, S IV, S VI and P V, but focus on N V since it is the least saturated and blended of these ions. Out of the 18 bursts, we detect N V in 12 of the cases, all having large column densities for which we found average and median values of $\log N({\rm N\,V})_{\rm avg} = 14.36$ and $\log N({\rm N\,V})_{\rm med} = 14.50$, respectively. We place 3σ upper limits on N V for the remaining six bursts and show that the non-detections are likely either related to the intrinsic or observed faintness of the GRBs, resulting in poor signal-to-noise ratios at the spectral region covering the N V doublet.

By comparing the strength of N V to the neutral gas properties in individual bursts such as metallicity, H I column density and dust depletion, both from our sample and previous samples from the literature, we found no correlation between any of these measurements. This suggests that the gas responsible for the N V absorption is unrelated to the properties of the neutral gas in the GRB host galaxy ISM. We found, however, that for GRBs with H I column densities below $\approx 10^{21}$ cm^{-2}, the line profile of N V is offset by $\delta v \approx -100$ km s^{-1} relative to $z_{\rm GRB}$, whereas for higher H I column densities the N V gas is kinematically "cold", where $|\delta v| \lesssim 30$ km s^{-1}. This suggests a scenario where the natal H II region of the GRB containing the N V gas is confined by the pressure from the surrounding neutral gas in the ISM.

It has been argued that since we observe soft X-ray absorption in excess of Galactic in the majority of GRB afterglows, there must be a significant column density of highly ionized gas within GRB host galaxies. Based on our sample and two previous samples from the literature we found that the X-ray derived metal column density, $N_{\rm H,X}$, is positively correlated (at 2σ significance) with the column density of N V. Since the line profiles of N V are also found to be coincident in velocity with the UV-pumped

fine-structure absorption lines, we affirm that both measurements likely trace the column density of metals in the circumburst medium of the GRB. We then demonstrate that a simple model, where the initial prompt emission from the GRB has stripped the electrons from the surrounding gas entirely, can reproduce the observed column densities of N v and O vi via recombination. We here assumed that the gas is fully ionized out to ≈ 10 pc within the first few seconds after the GRB, and that the gas has $T = 10^4$ K and an electron density of $n_e = 2 \times 10^4$ cm^{-3} typical for H ii regions.

We would like to encourage future and more detailed modelling of the proposed recombination scenario. Such a model would also have to include the later contribution from photoionization by the afterglow to the observed column densities. A complementary approach would be to measure variations in the column density of N v as a function of time in GRB afterglow spectra. We searched for such a temporal variation in the first and second epoch VLT/X-shooter spectra of GRB 120327A (obtained at $\Delta t_{\rm obs} \approx 2.1$ and 30.6 h), but the equivalent width of N v is not observed to vary with statistical significance. A similar result was found by Prochaska et al. (2008b) for GRBs 050730 and 050820. Finally, if the recombination scenario proposed here is true we would expect to observe strong emission features from the transitions of e.g N vii to N vi and N vi to N v. These line emissions might be possible to observe for low-z GRBs but will require a telescope that is sensititive in the near- and far-ultraviolet.

Acknowledgements

We would like to thank the referee for a clear and thorough report, which greatly improved the presentation of the results in the paper. We also wish to thank K. Wiersema and P. Møller for enlightening discussions. KEH and PJ acknowledge support by a Project Grant (162948–051) from The Icelandic Research Fund. JK acknowledges financial support from the Danish Council for Independent Research (EU-FP7 under the Marie-Curie grant agreement no. 600207) with reference DFF–MOBILEX–5051–00115. JJ acknowledges support from NOVA and NWO-FAPESP grant for advanced instrumentation in astronomy. AG acknowledges the financial support from the Slovenian Research Agency (research core funding No. P1-0031 and project grant No. J1-8136). AdUP, CCT and ZC acknowledge support from the Spanish Ministry of Economy and Competitivity under grant number AYA 2014-58381-P. AdUP and CCT acknowledge support from Ramon y Cajal fellowships (RyC-2012-09975 and RyC-2012-09984). AdUP acknowledges support from a grant from the BBVA foundation for researchers and cultural creators. ZC acknowledges support from the Juan de la Cierva Incorporación fellowship IJCI-2014-21669 and from the Spanish research project AYA 2014-58381-P. RS-R acknowledges support from ASI (Italian Space Agency) through the Contract n. 2015-046-R.0 and from European Union Horizon 2020 Programme under the AHEAD project (grant agreement n. 654215).

Appendix

Notes on individual GRBs

GRB 090809 at $z = 2.73706$

The spectrum of GRB 090809A was secured 10.2 hours after trigger with an acquisition magnitude of 21.0 mag. The H I column density is adopted from Tanvir et al. (2019) and was used for the determination of the metallicity. From the fit to Si II λ 1808, Thöne et al. (in preparation) find [Si/H] = -0.76 ± 0.20. We detect high-ionization absorption features from C IV and Si IV and measure an upper limit for N V of $\log N(\mathrm{N\,V}) < 14.43$ (see Fig. 3.5.1). The spectral data has low S/N at the location of the other surveyed high-ionization species. The detected high-ionization features are consistent with a single velocity component at $\approx z_{\mathrm{GRB}}$. The X-ray derived metal column density used in Sect. 3.3.4 for this burst is from the *Swift*/XRT database[3].

GRB 090926A at $z = 2.10694$

The spectrum of GRB 090926A was secured 22.0 hours after trigger with an acquisition magnitude of 17.9 mag. The H I column density and metallicity are adopted from D'Elia et al. (2010). We detect high-ionization absorption features from N V, C IV, Si IV, S IV and O VI (see Fig. 3.5.2). The absorption lines from S VI $\lambda\lambda$ 933,944 are located outside the spectral coverage of the UVB arm at this redshift. There is a strong absorption feature at $-200\,\mathrm{km\,s^{-1}}$ relative to z_{GRB} at the position of P V λ 1117, but since we do not detect P V λ 1128 at the same redshift this is likely an unrelated line. The strongest component of the high-ionization features is located at z_{GRB}, where C IV and Si IV show an additional component at $\approx -75\,\mathrm{km\,s^{-1}}$ relative to z_{GRB}. The velocity components of N V are best fit following the low-ionization lines, represented by Si II λ 1526 in the figure. The line profiles of O VI show two strong components, one at z_{GRB}, the other at $\approx -200\,\mathrm{km\,s^{-1}}$ relative to z_{GRB}. The X-ray derived metal column density used in Sect. 3.3.4 for this burst is from Zafar et al. (2018b).

GRB 100425A at $z = 1.75640$

The spectrum of GRB 100425A was secured 4.0 hours after trigger with an acquisition magnitude of 20.6 mag. The H I column density and metallicity are adopted from Cucchiara et al. (2015). We detect high-ionization absorption features from C IV and Si IV (see Fig. 3.5.3) and measure an upper limit for N V of $\log N(\mathrm{N\,V}) < 14.63$. We caution, however, that all features are located in regions with poor spectral S/N and O VI, S IV, and S VI are outside the spectral coverage of the UVB arm. Because of this we do not report column densities for these transitions. No information on the velocity components are available from C IV and Si IV, except that the absorption line profiles cover $\approx -100 < z_{\mathrm{GRB}} < +100\,\mathrm{km\,s^{-1}}$. The X-ray derived metal column density used in Sect. 3.3.4 for this burst is from the *Swift*/XRT database[4].

[3] http://www.swift.ac.uk/xrt_spectra/00359530/
[4] http://www.swift.ac.uk/xrt_spectra/00420398/

GRB 111008A at $z = 4.99146$

The spectrum of GRB 111008A was secured 8.5 hours after trigger with an acquisition magnitude of 21.0 mag. The H I column density and metallicity are adopted from Sparre et al. (2014). We detect high-ionization absorption features from N V, C IV, and Si IV (see Fig. 3.5.4). The absorption lines from C IV and Si IV are saturated and partly blended so we do not report column densities for these transitions. We report a non-detection of the remaining surveyed high-ionization species, but caution that they are all located in spectral regions with poor S/N. No information on the velocity components are available from C IV and Si IV, except that the absorption line profiles cover $\approx -200 < z_{\rm GRB} < +100\,{\rm km\,s^{-1}}$. N V is consistent with a single velocity component at $\approx z_{\rm GRB}$, but we are only able to infer a lower limit N V due to line saturation. The X-ray derived metal column density used in Sect. 3.3.4 for this burst is from Zafar et al. (2018b).

GRB 120119A at $z = 1.72883$

The spectrum of GRB 120119A was secured 1.4 hours after trigger with an acquisition magnitude of 17.0 mag. The H I column density is adopted from Tanvir et al. (2019) and was used for the determination of the metallicity. Thöne et al. (in preparation) measure $[{\rm Si/H}] = -1.43 \pm 0.21$ from a fit to S II $\lambda\lambda$ 1808. We detect high-ionization absorption features from C IV and Si IV (see Fig. 3.5.5) and measure an upper limit for N V of $\log N({\rm N\,V}) < 15.15$. We caution, however, that N V is located in a region with poor spectral S/N and O VI, S IV, and S VI are outside the spectral coverage of the UVB arm. The absorption lines from C IV and Si IV are heavily saturated and partly blended so we do not report column densities for these transitions. We report a non-detection of the remaining surveyed high-ionization species, but caution that they are all located in spectral regions with poor S/N. No information on the velocity components are available from C IV and Si IV, except that the absorption line profiles cover $\approx -700 < z_{\rm GRB} < 0\,{\rm km\,s^{-1}}$. The X-ray derived metal column density used in Sect. 3.3.4 for this burst is from Zafar et al. (2018b).

GRB 120327A at $z = 2.81482$

The spectrum of GRB 120317A was secured 2.1 hours after trigger with an acquisition magnitude of 18.8 mag. The H I column density, metallicity and high-ionization absorption lines are adopted from D'Elia et al. (2014). They detect all the surveyed high-ionization absorption features except for S IV and are consistent with being located at the central velocity component (out of three extending from $\approx \pm 100\,{\rm km\,s^{-1}}$ relative to $z_{\rm GRB}$) of the low-ionization species. They measure $\log N({\rm N\,V/cm^{-2}}) = 13.56 \pm 0.03$ which was used in our analysis. The X-ray derived metal column density used in Sect. 3.3.4 for this burst is from the *Swift*/XRT database[5].

[5] `http://www.swift.ac.uk/xrt_spectra/00518731/`

GRB 120815A at $z = 2.35820$

The spectrum of GRB 120815A was secured 1.69 hours after trigger with an acquisition magnitude of 18.9 mag. The H I column density, metallicity and X-ray derived metal column density used in Sect. 3.3.4 for this burst are adopted from Krühler et al. (2013). We detect high-ionization absorption features from N V, C IV, and Si IV (see Fig. 3.5.6). The absorption lines from C IV and Si IV are saturated and the derived column densities should only be considered as lower limits. We report a non-detection of the remaining surveyed high-ionization species, but caution that they are all located in spectral regions with poor S/N. The high-ionization line profiles are best fit with two velocity components at $z_{\rm GRB}$ and $\approx -23\,{\rm km\,s^{-1}}$ relative to $z_{\rm GRB}$, similar to the low-ionization absorption lines, represented by Si II λ 1808 in the figure.

GRB 120909A at $z = 3.92882$

The spectrum of GRB 120909A was secured 1.7 hours after trigger using the rapid-response mode with an acquisition magnitude of 21.0 mag. The H I column density is adopted from Tanvir et al. (2019) and was used for the determination of the metallicity. Thöne et al. (in preparation) measure [S/H] $= -0.66 \pm 0.11$ from a combined fit to S II $\lambda\lambda$ 1250,1253. We detect high-ionization absorption features from N V, C IV, Si IV, S IV, and S VI (see Fig. 3.5.7). We only fit Voigt profiles to N V and Si IV since the other lines are either blended or saturated. P V is located in spectral region with poor S/N and O VI is heavily blended with the Lyα forest. The main velocity component of the high-ionization absorption lines is located at $z_{\rm GRB}$, represented by S II λ 1250 in the figure. In addition, there is also a small component at $\approx -125\,{\rm km\,s^{-1}}$ relative to $z_{\rm GRB}$. The X-ray derived metal column density used in Sect. 3.3.4 for this burst is from the *Swift*/XRT database[6].

GRB 121024A at $z = 2.30244$

The spectrum of GRB 121024A was secured 1.8 hours after trigger with an acquisition magnitude of 20.0 mag. The H I column density and metallicity are adopted from Friis et al. (2015). We detect high-ionization absorption from C IV and Si IV (see Fig. 3.5.8) and measure an upper limit for N V of $\log N({\rm N\,V}) < 14.35$. Both of these two absorption lines are saturated and the derived column densities should only be considered as lower limits. We report a non-detection of the remaining surveyed high-ionization species, but caution that they are all located in spectral regions with poor S/N. The velocity components of C IV and Si IV show a weak, ionized cloud at $z_{\rm GRB}$, and a highly complex distribution at -600 to $-100\,{\rm km\,s^{-1}}$ relative to $z_{\rm GRB}$. For comparison, the low-ionization absorption line profiles, represented by Fe II λ 1608 in the figure, show two strong components, one at $z_{\rm GRB}$ and one at $-400\,{\rm km\,s^{-1}}$ relative to $z_{\rm GRB}$. The X-ray derived metal column density used in Sect. 3.3.4 for this burst is from the *Swift*/XRT database[7].

[6] http://www.swift.ac.uk/xrt_spectra/00533060/
[7] http://www.swift.ac.uk/xrt_spectra/00536580/

GRB 130408A at $z = 3.75792$

The spectrum of GRB 160408A was secured 1.9 hours after trigger with an acquisition magnitude of 20.0 mag. The H I column density is adopted from Tanvir et al. (2019) and was used for the determination of the metallicity. Thöne et al. (in preparation) measure [Si/H] = -1.38 ± 0.12 from a combined fit to Si II $\lambda\lambda$ 1526,1808. We detect high-ionization absorption features from N V, C IV, Si IV, and S VI. The three features O VI, P V, and S IV are all blended (see Fig. 3.5.9) and therefore we do not attempt to measure their column densities. The absorption line profile of N V is consistent with a single velocity component. The velocity components of C IV, Si IV, and S VI follow the same distribution as for the low-ionization line profiles, represented in the figure by Si II λ 1808. The X-ray derived metal column density used in Sect. 3.3.4 for this burst is from the *Swift*/XRT database[8], but corrected for the measured redshift.

GRB 130606 at $z = 5.91278$

The spectrum of GRB 130606A was secured 7.1 hours after trigger with an acquisition magnitude of 19.0 mag. The H I column density, metallicity and X-ray derived metal column density used in Sect. 3.3.4 for this burst are adopted from Hartoog et al. (2015). Since the intervening intergalactic medium have a high neutral fraction, the continuum on the blue side of the Lyα absorption feature is completely suppressed. Therefore, we only searched for high-ionization absorption lines redwards of Lyα. We detect N V, C IV, and Si IV, all with multiple velocity components (see Fig. 3.5.10). C IV and Si IV are both saturated so the column densities derived for these two species should only be considered as lower limits. While the velocity components of C IV and Si IV are consistent with the low-ionization absorption line profiles, represented by Si II λ 1260 in the figure, N V has two main components at $\approx \pm 100\,\mathrm{km\,s^{-1}}$ compared to z_{GRB}.

GRB 141028A at $z = 2.33327$

The spectrum of GRB 141028A was secured 15.4 hours after trigger with an acquisition magnitude of 20.0 mag. The H I column density is adopted from Tanvir et al. (2019) and was used for the determination of the metallicity. Thöne et al. (in preparation) measure [Si/H] = -0.75 ± 0.15 from a combined fit to Si II $\lambda\lambda$ 1260,1526. We detect high-ionization absorption features from N V, C IV, Si IV, and P V (see Fig. 3.5.11). S VI,$\lambda\lambda$ 933,944 are located bluewards of the spectral coverage of the UVB arm and the region around O VI and S IV has poor S/N. The main velocity components of the high-ionization absorption line profiles are located at $\approx -100\,\mathrm{km\,s^{-1}}$ from z_{GRB}. N V and P V are both well fit with a single velocity component whereas Si IV and C IV show three and four velocity components, respectively. The X-ray derived metal column density used in Sect. 3.3.4 for this burst is from the *Swift*/XRT database, but corrected for the measured redshift[9].

[8] http://www.swift.ac.uk/xrt_spectra/00553132/
[9] http://www.swift.ac.uk/xrt_spectra/00020420/

GRB 141109A at $z = 2.99438$

The spectrum of GRB 141109A was secured 1.9 hours after trigger with an acquisition magnitude of 19.2 mag. The H I column density is adopted from Tanvir et al. (2019) and was used for the determination of the metallicity. Thöne et al. (in preparation) measure [Zn/H] $= -1.45 \pm 0.21$ from a combined fit to Zn II $\lambda\lambda$ 2026,2062. We detect high-ionization absorption features from N V, C IV, Si IV, S VI, P V, and S IV (see Fig. 3.5.12). Strong absorption from Si IV, C IV, and P V are observed and all features are mildly saturated. The velocity components and column densities of Si IV and C IV are hard to disentangle since they are both blended and are located in regions with poor S/N. The main component of N V is located at $\approx 13\,\mathrm{km\,s^{-1}}$ from z_{GRB} and while being best fit by two components we only trust the one central fit. We are also only able to derive a lower limit to the column density for N V due to line saturation. The detections of S VI,$\lambda\lambda$ 933,944, P V,$\lambda\lambda$ 1117,1128, and S IV λ 1062 are tentative since they all appear blended with the Lyα forest. If the detections of P V,$\lambda\lambda$ 1117,1128 are real, those are the only features with blueshifted velocity components compared to z_{GRB}, the other are at -400 to $0\,\mathrm{km\,s^{-1}}$. The X-ray derived metal column density used in Sect. 3.3.4 for this burst is from the *Swift*/XRT database[10].

GRB 150403A at $z = 2.05707$

The spectrum of GRB 150403A was secured 10.8 hours after trigger with an acquisition magnitude of 19.1 mag. The H I column density is adopted from Tanvir et al. (2019) and was used for the determination of the metallicity. Thöne et al. (in preparation) measure [S/H] $= -0.80 \pm 0.35$ from a combined fit to S II $\lambda\lambda$ 1250,1253. We detect high-ionization absorption features from N V, C IV, and Si IV (see Fig. 3.5.13). Strong absorption from Si IV and C IV are observed and both features are mildly saturated. The four velocity components of both of these line profiles are similar to the low-ionization absorption features, represented in the figure by Si II λ 1526, and the total line profiles extend from $-200\,\mathrm{km\,s^{-1}}$ to $+200\,\mathrm{km\,s^{-1}}$. We find N V $\lambda\lambda$ 1238,1242 to have a single velocity component centered at $\approx -32\,\mathrm{km\,s^{-1}}$ relative to z_{GRB}. The spectral region around the lines S VI $\lambda\lambda$ 933,944 are not covered by the UVB arm. O VI $\lambda\lambda$ 1031,1037 are also located in a region with a poor to no spectral signal. The X-ray derived metal column density used in Sect. 3.3.4 for this burst is from the *Swift*/XRT database[11].

GRB 151021A at $z = 2.32975$

The spectrum of GRB 151021A was secured 0.75 hours after trigger using the rapid-response mode with an acquisition magnitude of 18.2 mag. The H I column density is adopted from Tanvir et al. (2019) and was used for the determination of the metallicity. Thöne et al. (in preparation) measure [Si/H] $= -1.11 \pm 0.20$ from a combined fit to Si II $\lambda\lambda$ 1526,1808. We detect high-ionization absorption features from N V, C IV, and Si IV (see Fig. 3.5.14). Strong absorption from Si IV and C IV are observed and both features are mildly saturated. The five velocity components of both of these line profiles are similar to the low-ionization absorption features, represented in the figure

[10] http://www.swift.ac.uk/xrt_spectra/00618024/
[11] http://www.swift.ac.uk/xrt_spectra/00637044/

by Si II λ 1526, and the total line profiles extend from $-200\,\mathrm{km\,s^{-1}}$ to $+100\,\mathrm{km\,s^{-1}}$. We report a weak detection of N V $\lambda\lambda$ 1238,1242 with a single velocity component centered at $\approx 34\,\mathrm{km\,s^{-1}}$ relative to z_{GRB}. For the remaining high-ionization absorption lines we surveyed we report a non-detection but caution that the spectral region around those lines have poor S/N. The X-ray derived metal column density used in Sect. 3.3.4 for this burst is from the *Swift*/XRT database[12].

GRB 151027B at $z = 4.06463$

The spectrum of GRB 151027B was secured 5 hours after trigger with an acquisition magnitude of 20.5 mag. The H I column density is adopted from Tanvir et al. (2019) and was used for the determination of the metallicity. Thöne et al. (in preparation) measure [Si/H] $= -1.62 \pm 0.24$ from a fit to Si II λ 1526. We detect high-ionization absorption features from C IV and Si IV (see Fig. 3.5.15) and measure an upper limit for N V of $\log N(\mathrm{N\,V}) < 13.98$. We report a non-detections of N V and P V but caution that the spectral regions covering these two lines have poor S/N. S VI, O VI, and S IV, if present, are all blended. The velocity components of C IV and Si IV follow the same distribution as the low-ionization absorption line profiles, represented in the figure by Si II λ 1526. They show two components separated by only $\approx 10\,\mathrm{km\,s^{-1}}$, but the total line profile covers $\pm 100\,\mathrm{km\,s^{-1}}$ around z_{GRB}. The X-ray derived metal column density used in Sect. 3.3.4 for this burst is from the *Swift*/XRT database[13].

GRB 160203A at $z = 3.51871$

The spectrum of GRB 161023A was secured 0.3 hours after trigger using the rapid-response mode with an acquisition magnitude of 18.0 mag. The H I column density is adopted from Tanvir et al. (2019) and was used for the determination of the metallicity. Thöne et al. (in preparation) measure [S/H] $= -1.26 \pm 0.11$ from a combined fit to S II $\lambda\lambda\lambda$ 1250,1253,1259. We detect high-ionization absorption features from C IV, Si IV, S IV, and S VI (see Fig. 3.5.16) and measure an upper limit for N V of $\log N(\mathrm{N\,V}) < 13.58$. Strong absorption from Si IV and C IV are observed and both features are mildly saturated with a single (Si IV) or two (C IV) velocity components. We report a non-detection of N V in this burst, but caution that the spectral region around the absorption feature has poor S/N. The most prominent high-ionization absorption features are centered at $\approx -70\,\mathrm{km\,s^{-1}}$. There are tentative detections of O VI and P V but these features are heavily blended with unrelated lines from the Lyα forest. We were thus not able to securily fit an absorption profile to these lines. The X-ray derived metal column density used in Sect. 3.3.4 for this burst is from the *Swift*/XRT database[14].

GRB 161023A at $z = 2.71067$

The spectrum of GRB 161023A was secured 3 hours after trigger with an acquisition magnitude of 17.5 mag. The H I column density is adopted from Tanvir et al. (2019) and was used for the determination of the metallicity. Thöne et al. (in preparation)

[12] http://www.swift.ac.uk/xrt_spectra/00660671/
[13] http://www.swift.ac.uk/xrt_spectra/00661869/
[14] http://www.swift.ac.uk/xrt_spectra/00672525/

measure [Si/H] = -1.24 ± 0.09 from a combined fit to Si II $\lambda\lambda\lambda$ 1260,1526,1808. We detect high-ionization absorption features from N V, O VI, C IV, Si IV, S IV, S VI, and P V (see Fig. 3.3.1). Strong absorption from Si IV and C IV are observed and both features are mildly saturated with 2 – 3 velocity components. A single component at $\approx -120\,\mathrm{km\,s^{-1}}$ is seen in N V, P V, S VI, O VI, S IV. This is in contrast with the multiple velocity components seen in the low-ionization absorption features represented by Fe II λ 1608 in Fig. 3.3.1. We caution that the lines S VI λ 933, O VI $\lambda\lambda$ 1031,1037, S IV λ 1062, and P V λ 1128 are blended with unrelated absorption features from the Lyα forest. The X-ray derived metal column density used in Sect. 3.3.4 for this burst is from the *Swift*/XRT database[15].

[15] http://www.swift.ac.uk/xrt_spectra/00020709/

Voigt profile fits – tables & figures

Table 3.5.1. Voigt profile fits for GRB 090809 at $z = 2.73706$.

Ion	v_0 (km s^{-1})	b (km s^{-1})	$\log N$ (N in cm^{-2})	$\log N$(total) (N in cm^{-2})
N v	···	···	···	< 14.43

Table 3.5.2. Voigt profile fits for GRB 090926A at $z = 2.10694$.

Ion	v_0 (km s^{-1})	b (km s^{-1})	$\log N$ (N in cm^{-2})	$\log N$(total) (N in cm^{-2})
N v	4 ± 2	15 ± 3	14.30 ± 0.19	14.30 ± 0.19
C iv	-6 ± 5	16 ± 3	15.94 ± 0.78	15.94 ± 0.78
	-76 ± 14	63 ± 13	13.62 ± 0.11	
Si iv	-6 ± 5	16 ± 3	15.19 ± 0.62	15.19 ± 0.62
	-76 ± 14	63 ± 13	13.32 ± 0.11	
S iv	0 ± 2	15 ± 3	14.79 ± 0.15	14.79 ± 0.15

Table 3.5.3. Voigt profile fits for GRB 100425A at $z = 1.75640$.

Ion	v_0 (km s^{-1})	b (km s^{-1})	$\log N$ (N in cm^{-2})	$\log N$(total) (N in cm^{-2})
N v	···	···	···	< 14.63

Table 3.5.4. Voigt profile fits for GRB 111008A at $z = 4.99146$.

Ion	v_0 (km s^{-1})	b (km s^{-1})	$\log N$ (N in cm^{-2})	$\log N$(total) (N in cm^{-2})
N v[a]	8 ± 10	50 ± 15	> 14.00	> 14.00

Table 3.5.5. Voigt profile fits for GRB 120119A at $z = 1.72883$.

Ion	v_0 (km s^{-1})	b (km s^{-1})	$\log N$ (N in cm^{-2})	$\log N$(total) (N in cm^{-2})
N v	⋯	⋯	⋯	< 15.15

Table 3.5.6. Voigt profile fits for GRB 120815A at $z = 2.35820$.

Ion	v_0 (km s^{-1})	b (km s^{-1})	$\log N$ (N in cm^{-2})	$\log N$(total) (N in cm^{-2})
N v	-6 ± 7	16 ± 8	14.60 ± 0.18	14.60 ± 0.18
C iv	0 ± 2	18 ± 3	17.54 ± 0.18	17.55 ± 0.18
	-23 ± 2	38 ± 5	15.46 ± 0.12	
Si iv	0 ± 2	18 ± 3	17.40 ± 0.43	17.40 ± 0.43
	-23 ± 2	38 ± 5	14.87 ± 0.37	

Table 3.5.7. Voigt profile fits for GRB 120909A at $z = 3.92882$.

Ion	v_0 (km s^{-1})	b (km s^{-1})	$\log N$ (N in cm^{-2})	$\log N$(total) (N in cm^{-2})
N v	-14 ± 4	41 ± 6	14.75 ± 0.11	14.75 ± 0.11

Table 3.5.8. Voigt profile fits for GRB 121024A at $z = 2.30244$.

Ion	v_0 (km s^{-1})	b (km s^{-1})	$\log N$ (N in cm^{-2})	$\log N$(total) (N in cm^{-2})
N v	⋯	⋯	⋯	< 14.35

Table 3.5.9. Voigt profile fits for GRB 130408A at $z = 3.75792$.

Ion	v_0 (km s^{-1})	b (km s^{-1})	$\log N$ (N in cm^{-2})	$\log N$(total) (N in cm^{-2})
N V	-16 ± 2	31 ± 4	14.44 ± 0.07	14.44 ± 0.07
C IV	65 ± 3	16 ± 2	13.71 ± 0.04	15.12 ± 0.05
	0 ± 2	13 ± 3	10.83 ± 0.01	
	-17 ± 2	28 ± 14	15.11 ± 0.05	
Si IV	65 ± 3	16 ± 2	13.12 ± 0.02	14.42 ± 0.05
	0 ± 2	13 ± 3	13.60 ± 0.02	
	-17 ± 2	28 ± 14	14.32 ± 0.04	
S VI	65 ± 3	16 ± 2	13.50 ± 0.02	14.37 ± 0.05
	0 ± 2	13 ± 3	13.75 ± 0.02	
	-17 ± 2	28 ± 14	14.17 ± 0.04	

Table 3.5.10. Voigt profile fits for GRB 130606A at $z = 5.91278$.

Ion	v_0 (km s^{-1})	b (km s^{-1})	$\log N$ (N in cm^{-2})	$\log N$(total) (N in cm^{-2})
N V	64 ± 1	13 ± 2	13.78 ± 0.03	14.50 ± 0.04
	-11 ± 4	57 ± 11	13.92 ± 0.06	
	-83 ± 1	19 ± 1	14.16 ± 0.03	
	-174 ± 4	28 ± 6	13.27 ± 0.07	

Table 3.5.11. Voigt profile fits for GRB 141028A at $z = 2.33327$.

Ion	v_0 (km s^{-1})	b (km s^{-1})	$\log N$ (N in cm^{-2})	$\log N$(total) (N in cm^{-2})
N V	-104 ± 20	10 ± 4	14.28 ± 0.10	14.28 ± 0.10
C IV	96 ± 7	35 ± 2	14.11 ± 0.02	14.96 ± 0.05
	-24 ± 3	66 ± 3	14.17 ± 0.02	
	-88 ± 11	25 ± 14	14.71 ± 0.03	
Si IV	107 ± 23	49 ± 3	13.47 ± 0.04	14.94 ± 0.07
	-39 ± 10	67 ± 7	13.69 ± 0.04	
	-89 ± 11	12 ± 4	14.87 ± 0.06	
P V	-67 ± 21	28 ± 12	14.86 ± 0.04	14.86 ± 0.04

Table 3.5.12. Voigt profile fits for GRB 141109A at $z = 2.99438$.

Ion	v_0 (km s^{-1})	b (km s^{-1})	$\log N$ (N in cm^{-2})	$\log N$(total) (N in cm^{-2})
N v[a]	13 ± 15	9 ± 3	$\gtrsim 14.85$	$\gtrsim 14.85$

Table 3.5.13. Voigt profile fits for GRB 150403A at $z = 2.05707$.

Ion	v_0 (km s^{-1})	b (km s^{-1})	$\log N$ (N in cm^{-2})	$\log N$(total) (N in cm^{-2})
N v	-32 ± 3	48 ± 11	14.73 ± 0.14	14.73 ± 0.14
C iv	44 ± 2	99 ± 3	14.84 ± 0.07	15.75 ± 0.10
	22 ± 2	69 ± 3	15.16 ± 0.07	
	-50 ± 4	5 ± 3	14.24 ± 0.02	
	-196 ± 5	22 ± 5	15.52 ± 0.04	
Si iv	120 ± 4	58 ± 7	13.93 ± 0.03	14.58 ± 0.08
	23 ± 2	55 ± 7	13.89 ± 0.05	
	-10 ± 4	4 ± 2	12.64 ± 0.03	
	-195 ± 5	42 ± 5	14.33 ± 0.04	

Table 3.5.14. Voigt profile fits for GRB 151021A at $z = 2.32975$.

Ion	v_0 (km s^{-1})	b (km s^{-1})	$\log N$ (N in cm^{-2})	$\log N$(total) (N in cm^{-2})
N v	34 ± 5	31 ± 19	14.80 ± 0.46	14.80 ± 0.46
C iv	47 ± 2	15 ± 3	12.21 ± 0.07	18.26 ± 0.17
	0 ± 2	19 ± 3	18.26 ± 0.10	
	-52 ± 4	18 ± 3	11.25 ± 0.02	
	-121 ± 5	35 ± 5	13.90 ± 0.04	
	-160 ± 7	2 ± 3	14.70 ± 0.06	
Si iv	47 ± 4	15 ± 7	13.88 ± 0.03	15.32 ± 0.07
	0 ± 2	19 ± 3	15.28 ± 0.05	
	-52 ± 4	18 ± 3	13.55 ± 0.03	
	-121 ± 5	35 ± 5	13.57 ± 0.04	
	-160 ± 7	2 ± 3	12.27 ± 0.02	

Table 3.5.15. Voigt profile fits for GRB 151027B at $z = 4.06463$.

Ion	v_0 (km s^{-1})	b (km s^{-1})	$\log N$ (N in cm^{-2})	$\log N$(total) (N in cm^{-2})
N V	⋯	⋯	⋯	< 13.98
C IV	0 ± 2	55 ± 3	13.53 ± 0.04	14.82 ± 0.09
	-9 ± 2	28 ± 3	14.80 ± 0.08	
Si IV	0 ± 2	55 ± 7	13.64 ± 0.04	14.38 ± 0.10
	-9 ± 2	28 ± 3	14.29 ± 0.08	

Table 3.5.16. Voigt profile fits for GRB 160203A at $z = 3.51871$.

Ion	v_0 (km s^{-1})	b (km s^{-1})	$\log N$ (N in cm^{-2})	$\log N$(total) (N in cm^{-2})
N V	⋯	⋯	⋯	< 13.58
C IV	-64 ± 2	17 ± 3	14.54 ± 0.07	14.56 ± 0.07
	-4 ± 2	15 ± 3	13.22 ± 0.04	
Si IV	-117 ± 4	26 ± 7	14.47 ± 0.18	14.50 ± 0.17
S IV	-68 ± 4	39 ± 2	14.46 ± 0.07	15.79 ± 0.14
	-173 ± 34	28 ± 20	14.77 ± 0.08	
	-230 ± 34	42 ± 20	15.72 ± 0.13	
S VI	-89 ± 6	49 ± 8	14.22 ± 0.06	14.22 ± 0.06

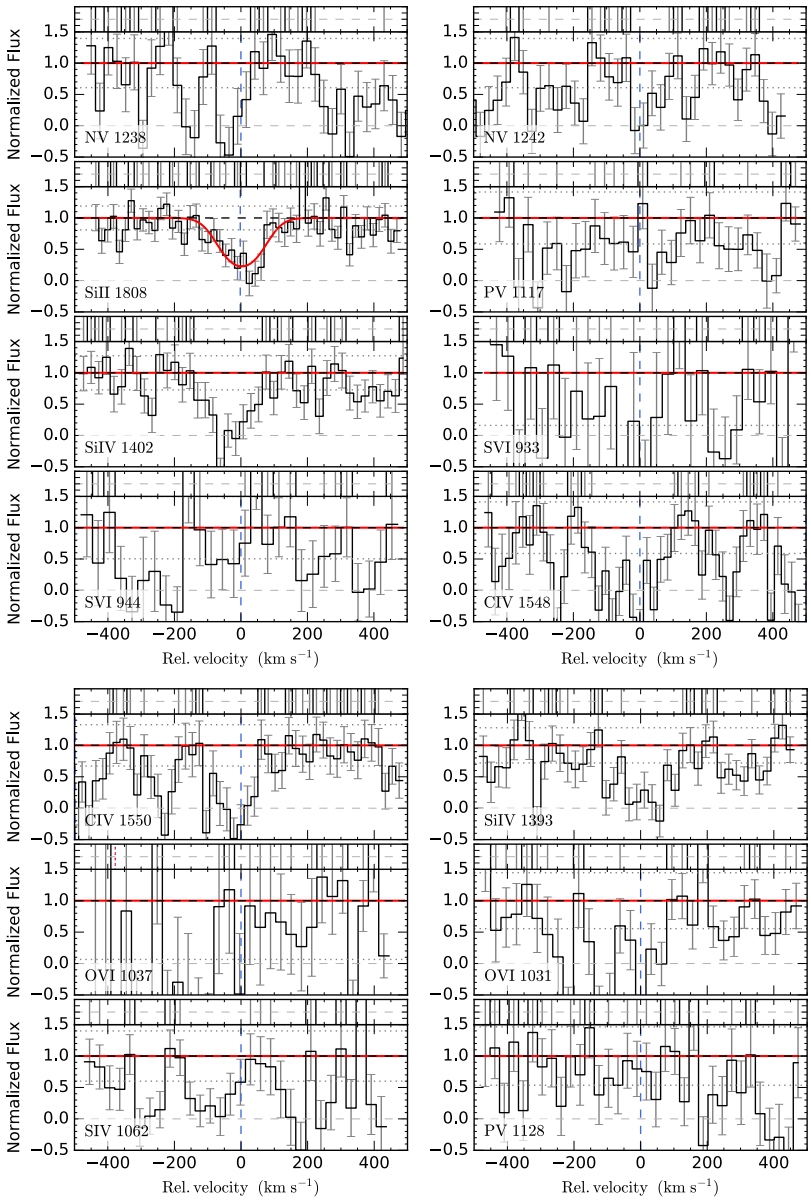

Figure 3.5.1. GRB090809.

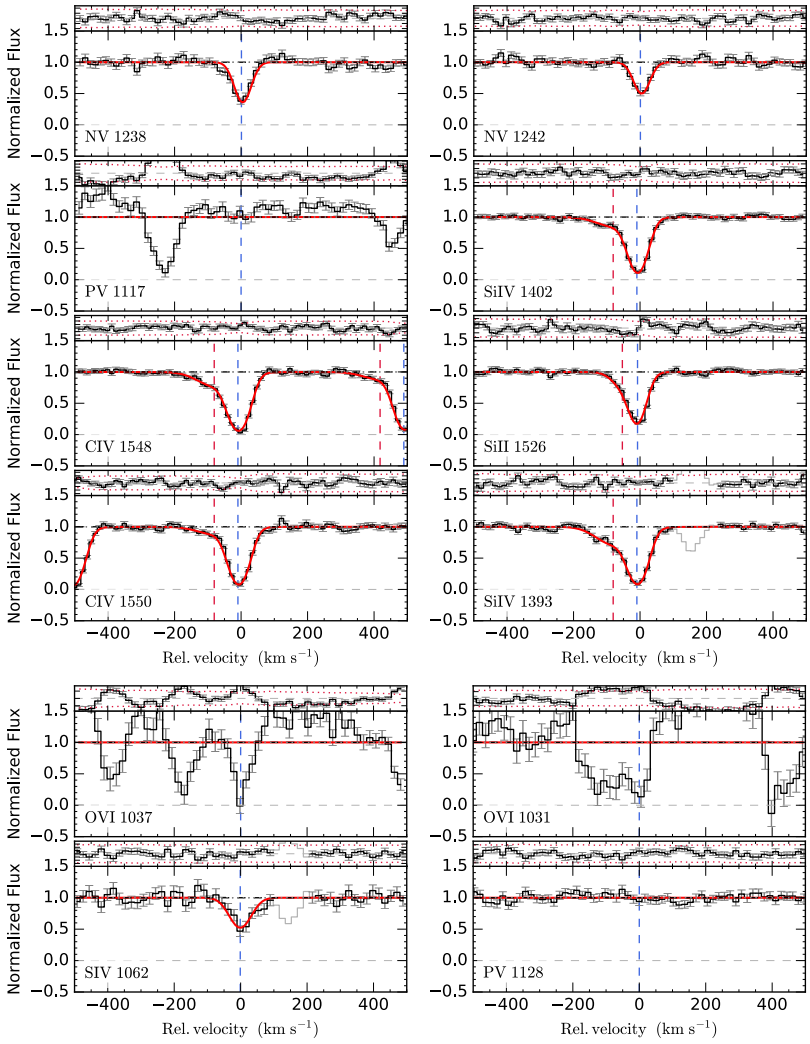

Figure 3.5.2. GRB090926A.

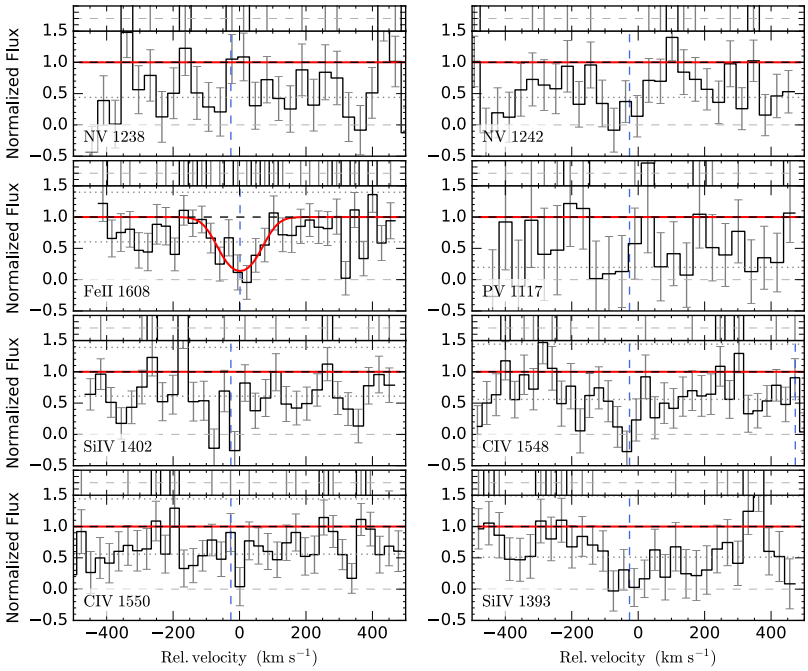

Figure 3.5.3. GRB100425A. The spectrum has been binned by a factor of 2.

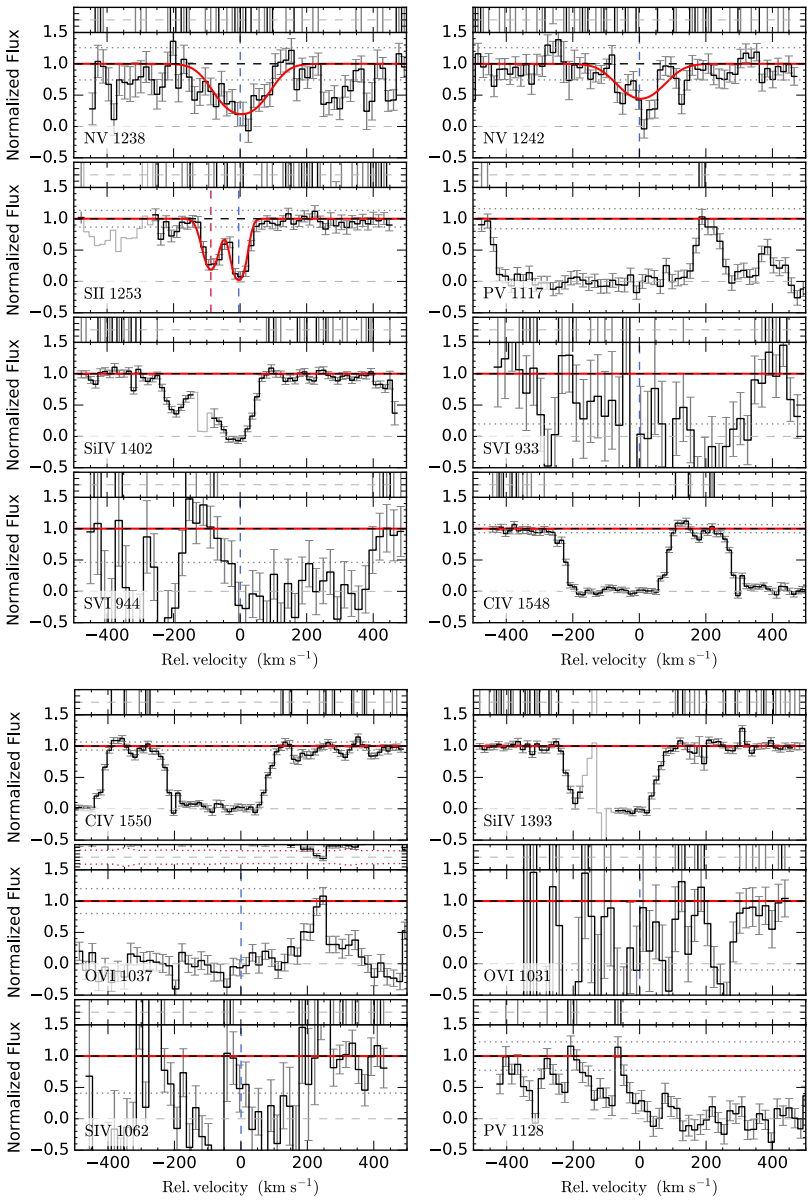

Figure 3.5.4. GRB111008A. The spectrum has been binned by a factor of 2.

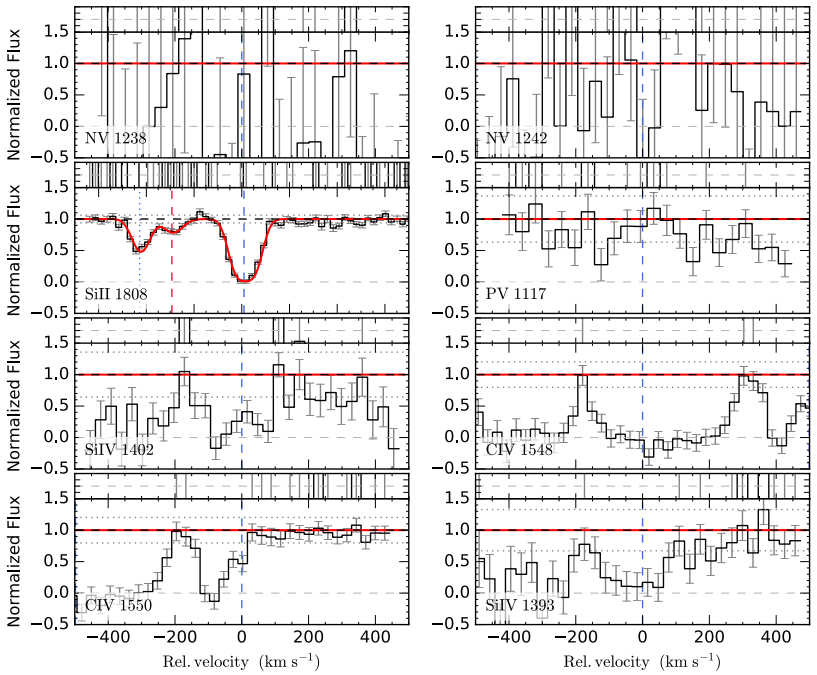

Figure 3.5.5. GRB120119A. The spectrum has been binned by a factor of 2.

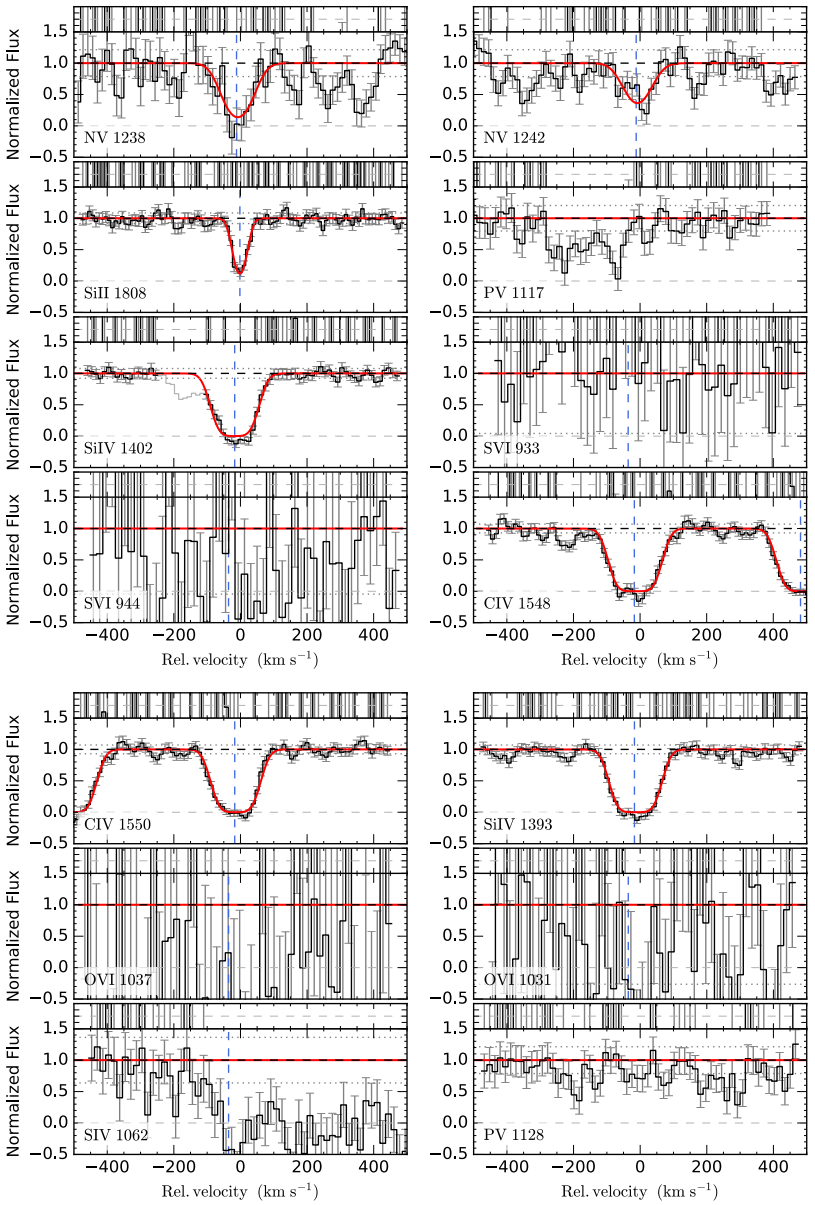

Figure 3.5.6. GRB120815A.

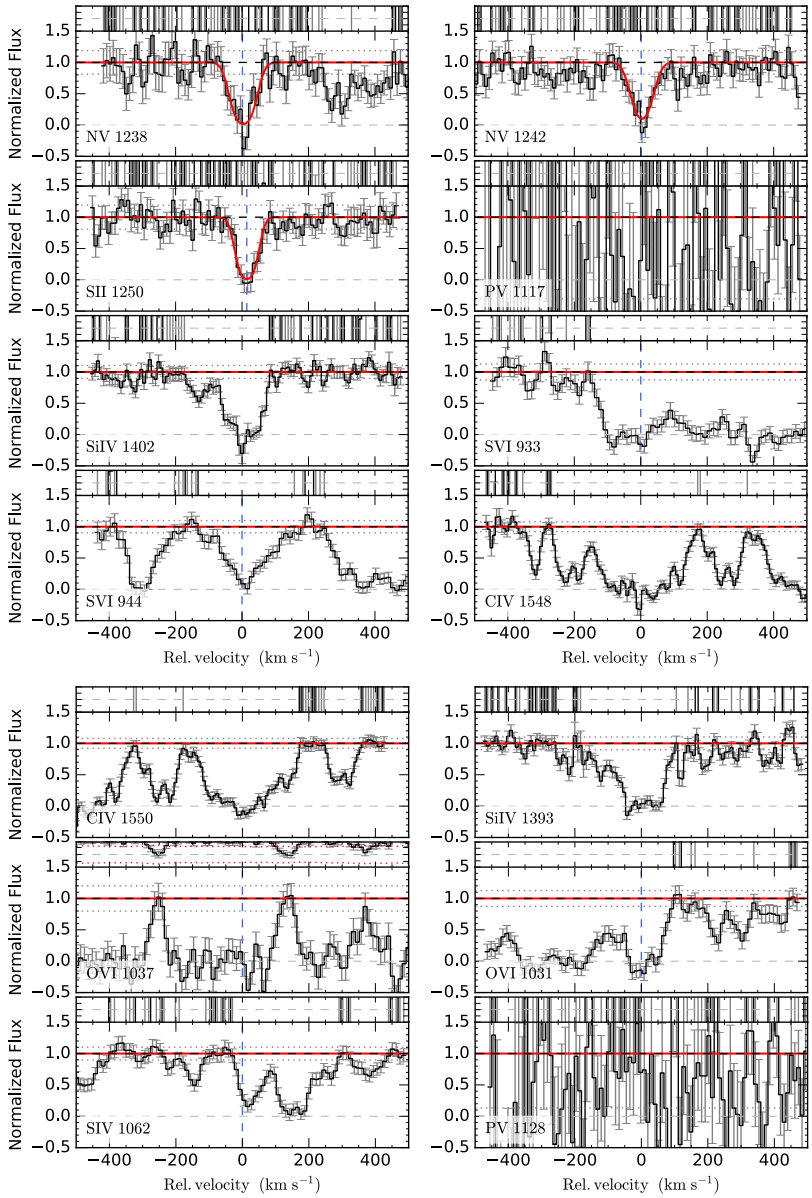

Figure 3.5.7. GRB120909A.

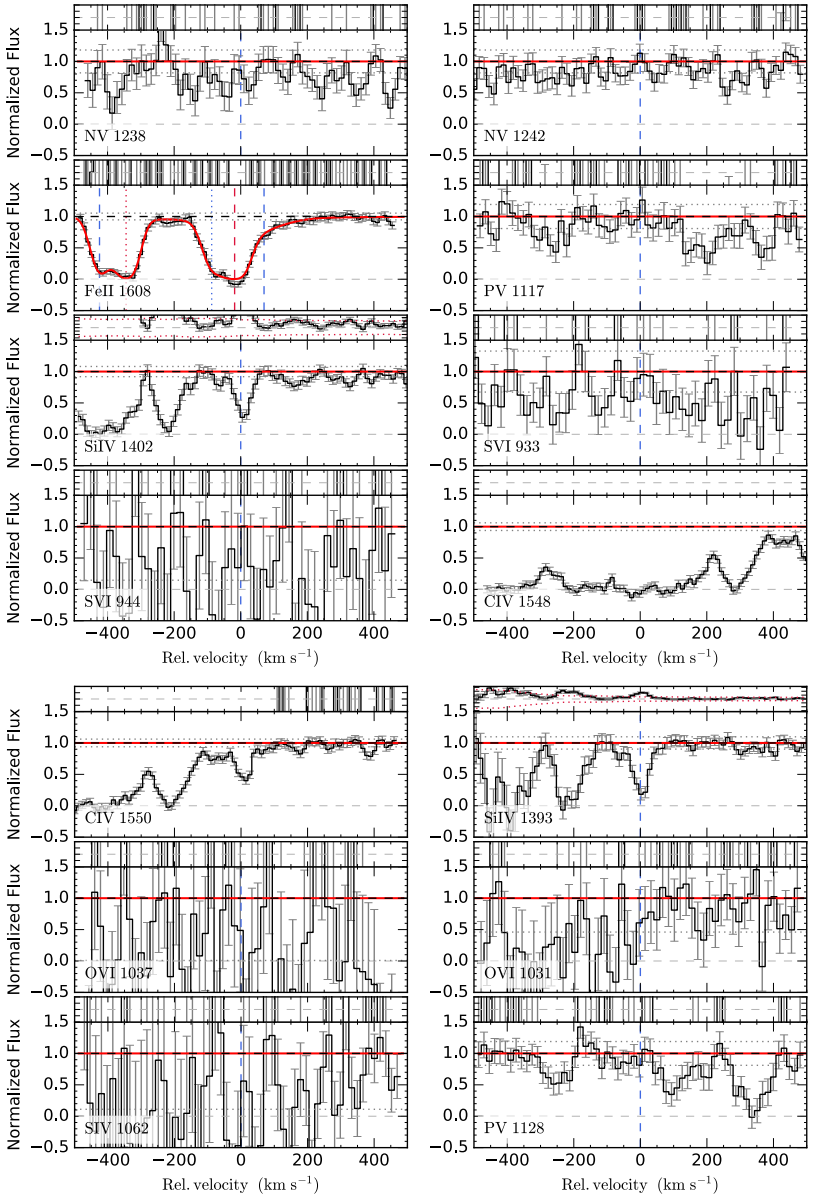

Figure 3.5.8. GRB121024A.

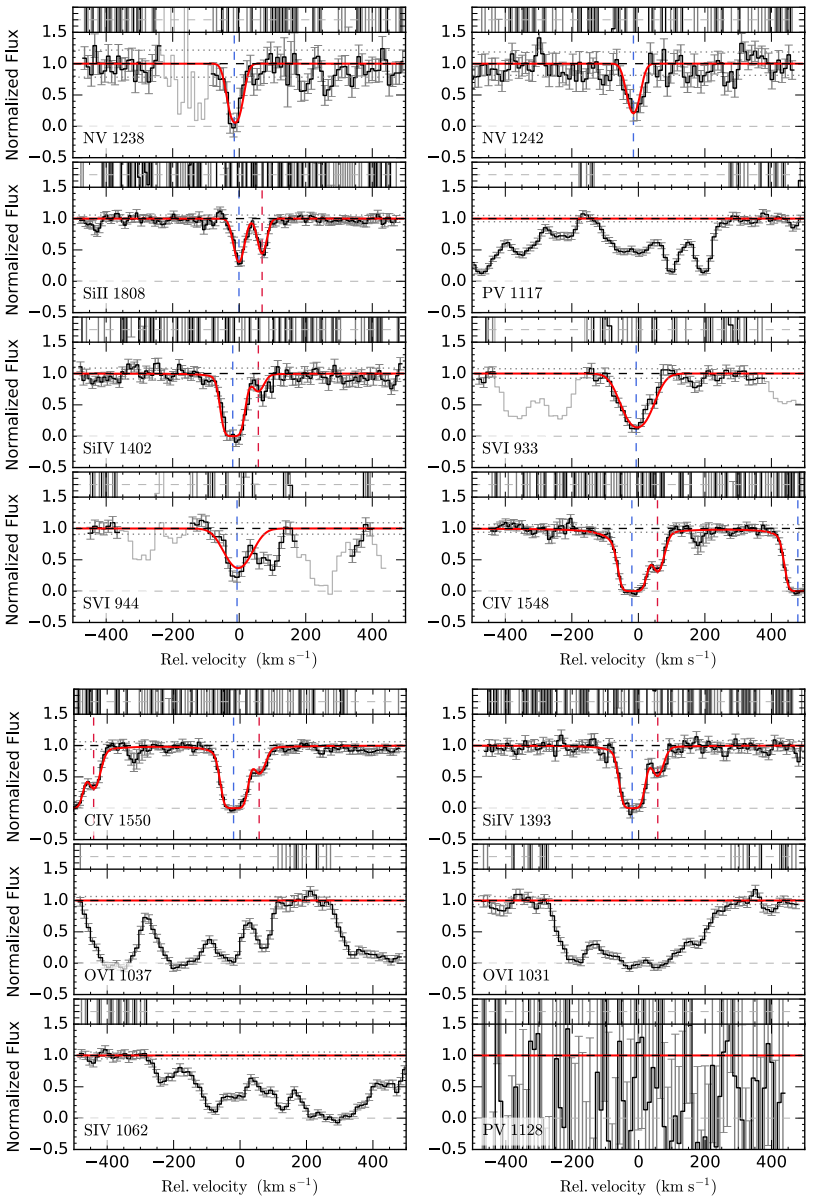

Figure 3.5.9. GRB130408A.

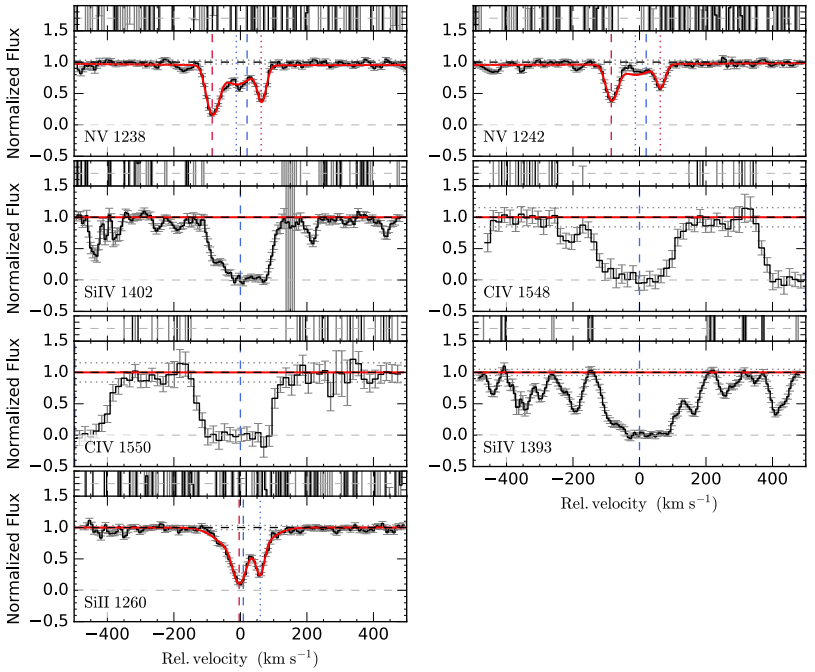

Figure 3.5.10. GRB130606A.

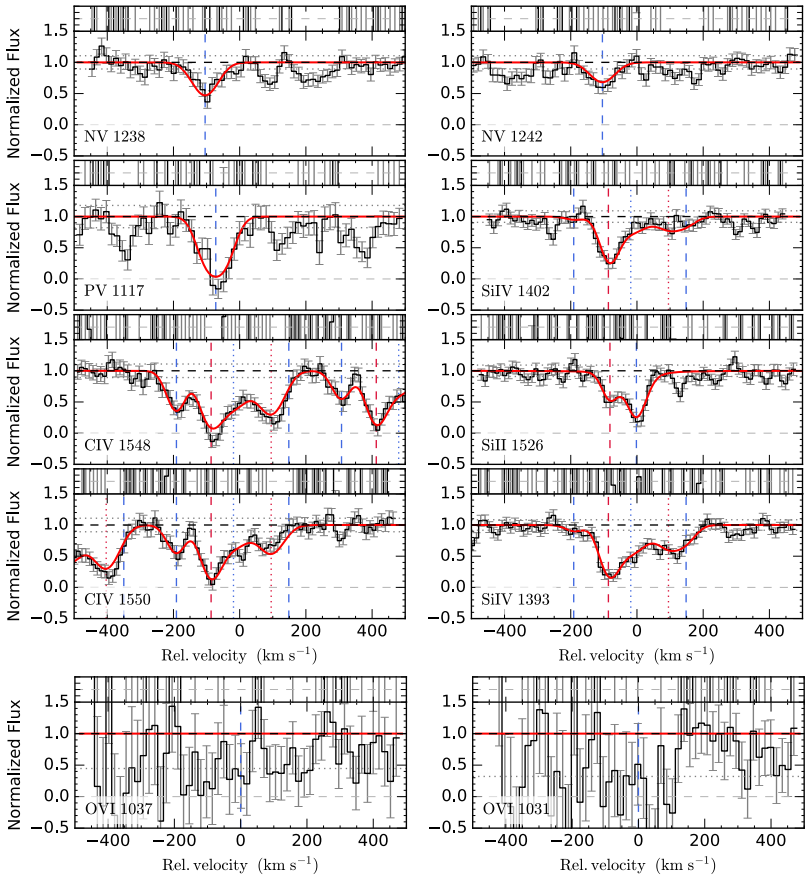

Figure 3.5.11. GRB141028A.

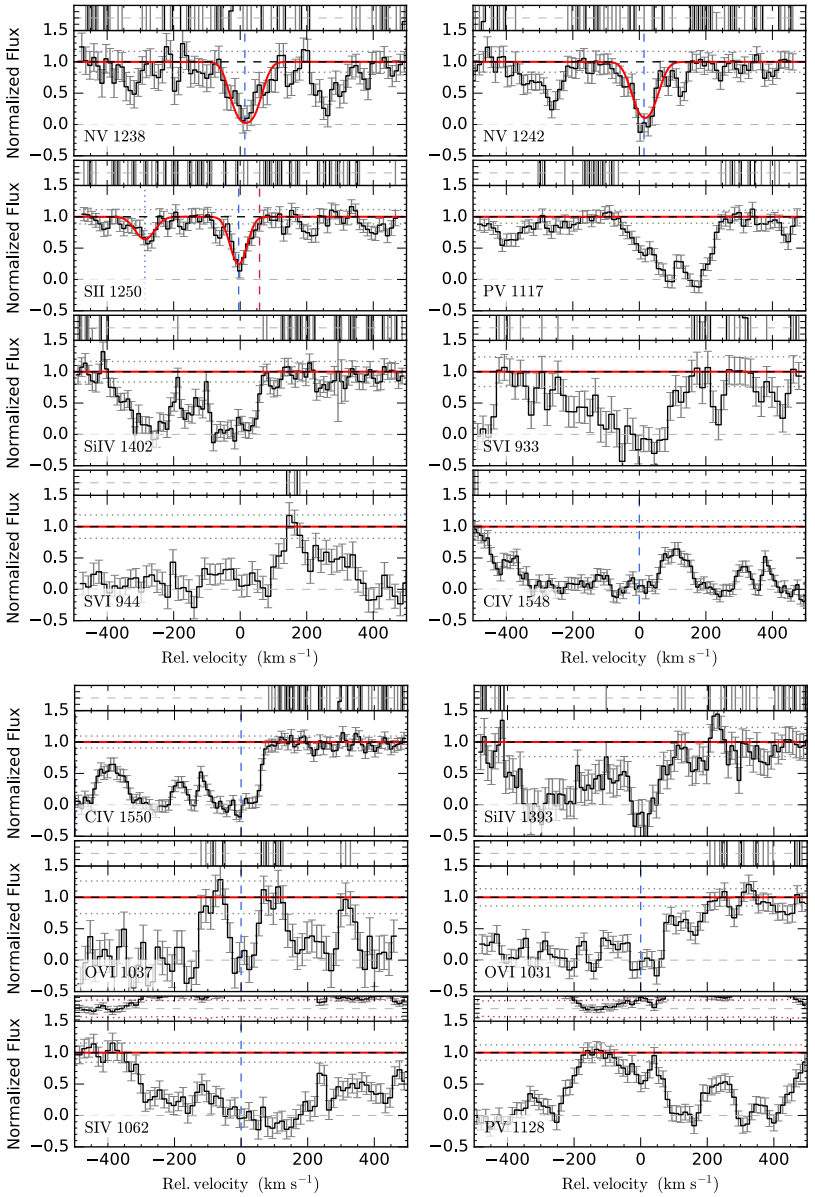

Figure 3.5.12. GRB141109A.

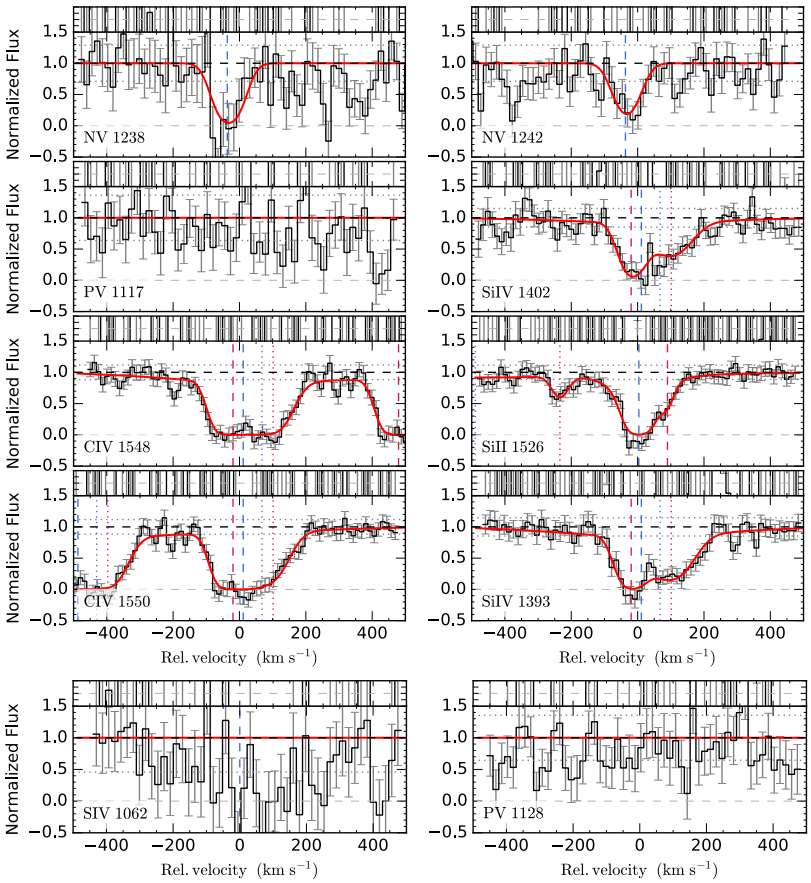

Figure 3.5.13. GRB150403A.

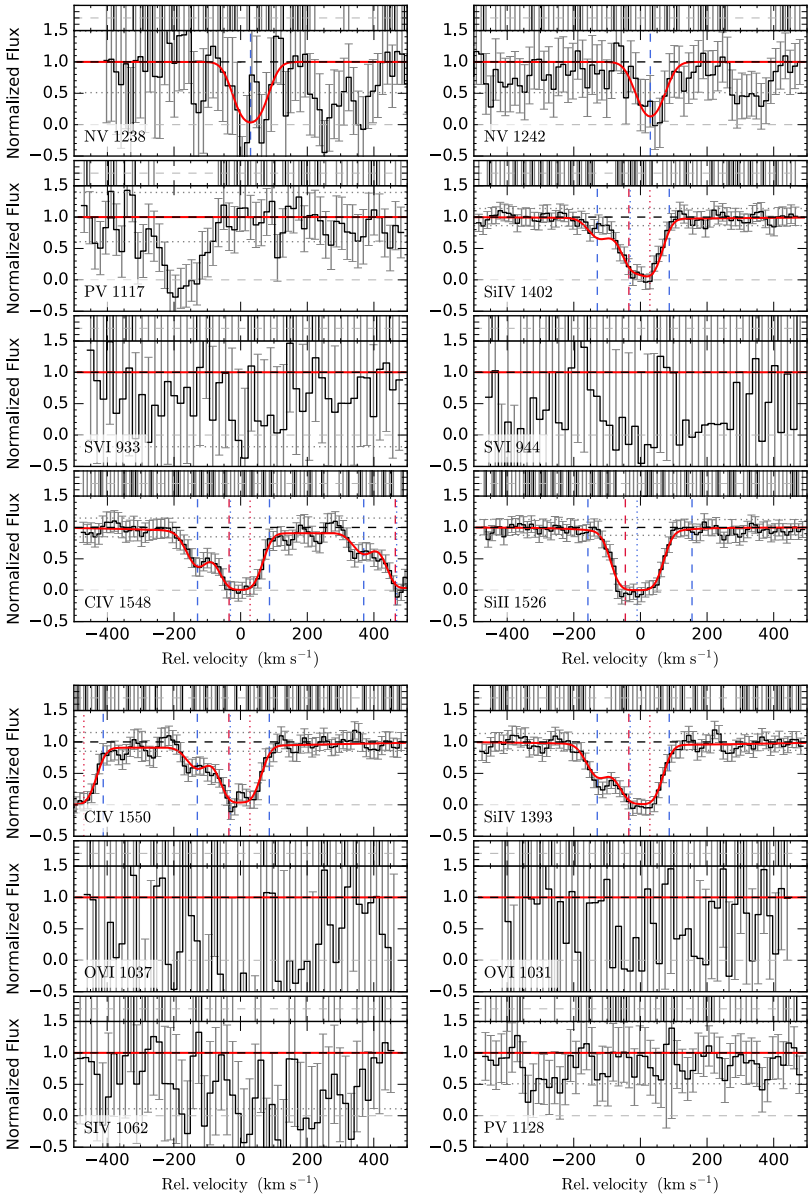

Figure 3.5.14. GRB151021A.

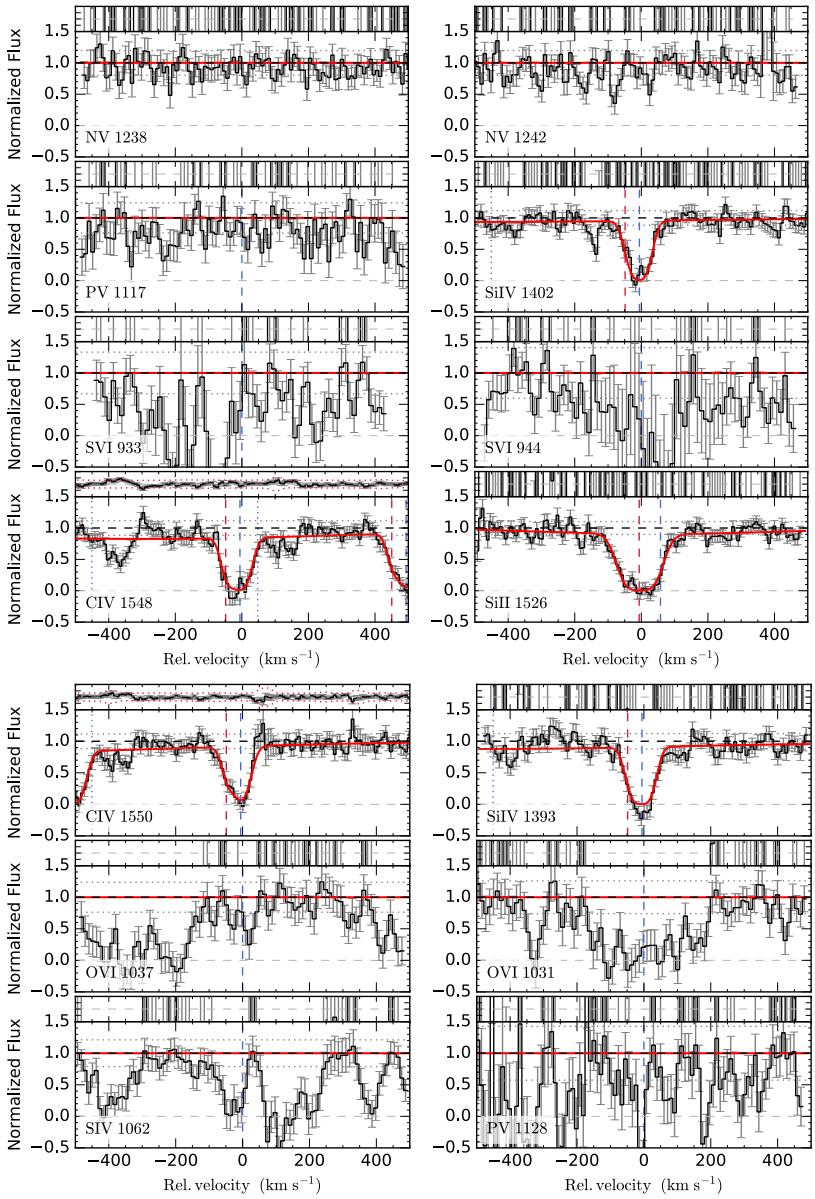

Figure 3.5.15. GRB151027B.

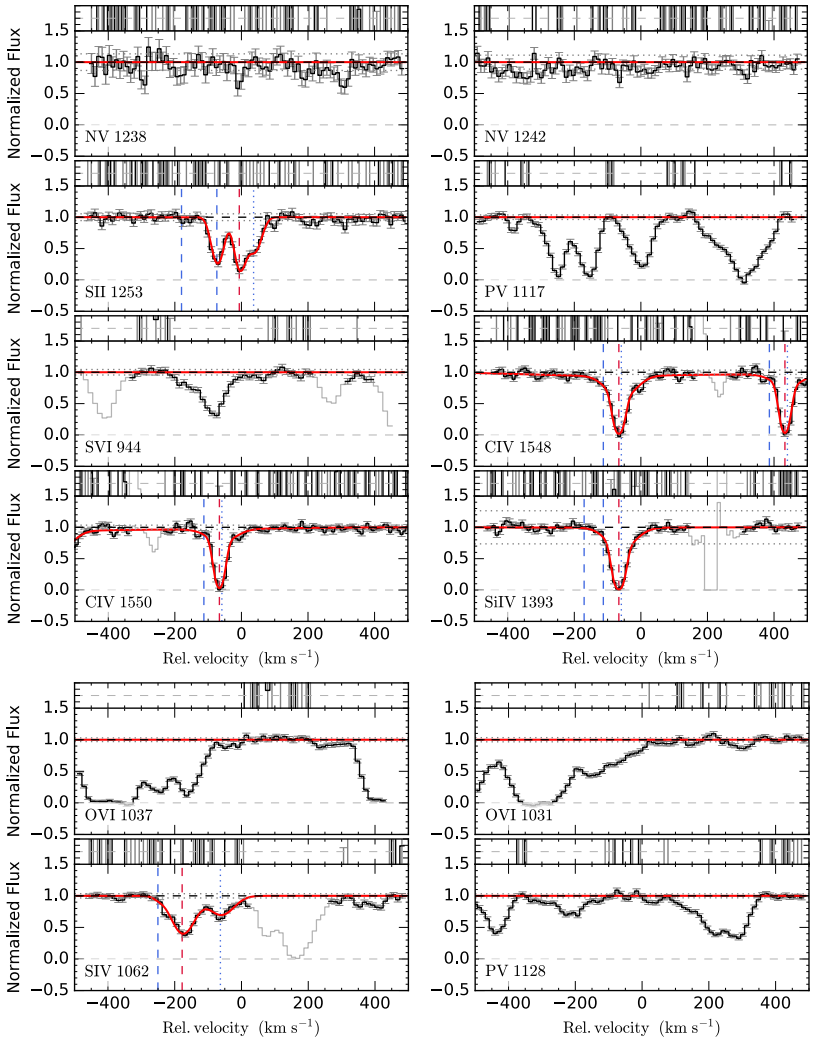

Figure 3.5.16. GRB160203A.

Part II

Cold and Molecular Gas in High-Redshift GRB Hosts

Chapter 4

Identifying high-redshift molecular clouds

This chapter is based on the following article:

Cold gas in the early Universe. Survey for neutral atomic-carbon in GRB host galaxies at $1 < z < 6$ from optical afterglow spectroscopy

Published in Astronomy & Astrophysics, vol. 621, id. A20, 13 pp. (2019)

Authors:
K. E. Heintz, C. Ledoux, J. P. U. Fynbo, P. Jakobsson, P. Noterdaeme, J.-K. Krogager, J. Bolmer, P. Møller, S. D. Vergani, D. Watson, T. Zafar, A. De Cia, N. R. Tanvir, D. B. Malesani, J. Japelj, S. Covino & L. Kaper

We present a survey for neutral atomic-carbon (C I) along gamma-ray burst (GRB) sightlines, which probes the shielded neutral gas-phase in the interstellar medium (ISM) of GRB host galaxies at high redshift. We compile a sample of 29 medium- to high-resolution GRB optical afterglow spectra spanning a redshift range through most of cosmic time from $1 < z < 6$. We find that seven ($\approx 25\%$) of the GRBs entering our statistical sample have C I detected in absorption. It is evident that there is a strong excess of cold gas in GRB hosts compared to absorbers in quasar sightlines. We investigate the dust properties of the GRB C I absorbers and find that the amount of neutral carbon is positively correlated with the visual extinction, A_V, and the strength of the 2175 Å dust extinction feature, $A_{\rm bump}$. GRBs with C I detected in absorption are all observed above a certain threshold of $\log N({\rm H\,I})/{\rm cm}^{-2} + [{\rm X/H}] > 20.7$ and a dust-phase iron column density of $\log N({\rm Fe})_{\rm dust}/{\rm cm}^{-2} > 16.2$. In contrast to the SED-derived dust properties,

the strength of the C I absorption does not correlate with the depletion-derived dust properties. This indicates that the GRB C I absorbers trace dusty systems where the dust composition is dominated by carbon-rich dust grains. The observed higher metal and dust column densities of the GRB C I absorbers compared to H_2- and C I-bearing quasar absorbers is mainly a consequence of how the two absorber populations are selected, but is also required in the presence of intense UV radiation fields in actively star-forming galaxies.

4.1 Introduction

Long-duration gamma-ray bursts (GRBs) are the most energetic class of cosmic explosions and are believed to originate from the deaths of massive stars (e.g. Woosley & Bloom, 2006). Their immense brightness makes them detectable even out to the epoch of reionization at $z \gtrsim 8$ (Salvaterra et al., 2009; Tanvir et al., 2009, 2018; Cucchiara et al., 2011). Since GRBs are expected to probe star formation (Wijers et al., 1998; Christensen et al., 2004; Jakobsson et al., 2005; Kistler et al., 2009; Robertson & Ellis, 2012; Greiner et al., 2015) and star-formation rates are driven by the availability of dense gas, GRBs offer a potentially ideal probe of the physical conditions in the cold, neutral gas-phase of the interstellar medium (ISM) in star-forming galaxies through most of cosmic time.

It is even possible to detect absorption by molecular hydrogen in the host directly by the presence of Lyman-Werner bands. However, to date, only four GRB afterglow spectra have a robust detection of H_2 in absorption (Prochaska et al., 2009; Krühler et al., 2013; D'Elia et al., 2014; Friis et al., 2015). One explanation for the dearth of molecular hydrogen in GRB host galaxies could be that the H_2 molecules are photodissociated by the GRB event itself. The intense prompt γ-ray flash and afterglow emission will, however, only impact gas in the vicinity of the GRB (out to $\lesssim 10$ pc; Draine & Hao, 2002). The gas producing absorption lines in GRB optical spectra is typically found to be located several hundred parsecs from the GRB explosition site (D'Elia et al., 2007; Prochaska et al., 2006; Vreeswijk et al., 2007, 2011). If there is a lack of detection of cold and molecular gas, it should be intrinsic to the GRB host galaxy properties.

While quasar selection is subject to a significant bias excluding sightlines with intervening dusty and therefore also metal-rich foreground galaxies (Fall & Pei, 1993; Boisse et al., 1998; Vladilo & Péroux, 2005; Pontzen & Pettini, 2009; Fynbo et al., 2013a, 2017; Krogager et al., 2015, 2016b,a, 2019; Heintz et al., 2018a), the high-energy emission from GRBs on the other hand is unaffected by dust. The spectroscopic follow-up observations of GRB afterglows are, however, still much less likely to be successful for the most dust-obscured sightlines, the so-called "dark" bursts (Fynbo et al., 2001, 2009; Jakobsson et al., 2004; van der Horst et al., 2009; Perley et al., 2009, 2013; Greiner et al., 2011; Krühler et al., 2011; Watson & Jakobsson, 2012) since observations with high-resolution spectrographs and good signal-to-noise ratios (due to the transient nature of GRBs) are only obtained for the brightest afterglows (Ledoux et al., 2009).

It is still unclear whether the apparent lack of molecular gas in GRB host galaxies is an intrinsic property or simply due to observational limitations (though an effort has

recently been made by Bolmer et al. 2019 to quantify this). The absorption signatures of H_2 are the Lyman and Werner bands which are located bluewards of the Lyman-α (Lyα) absorption line and in the Lyα forest. High-resolution spectra are therefore helpful to disentangle the H_2 transitions from the Lyα forest and to derive reliable H_2 column densities. As stated above, such samples will suffer from a bias against the most metal-rich and dust-obscured bursts (Ledoux et al., 2009). These host galaxy properties are, however, found to be essential for the detection probability of H_2 (Ledoux et al., 2003; Petitjean et al., 2006; Noterdaeme et al., 2008, 2015a; Krühler et al., 2013). In addition, due to the UV-steep extinction curves typically observed in GRB sightlines (Zafar et al., 2018b), the observed flux in the Lyman-Werner bands will be attenuated much more strongly than the visual extinction, A_V. The sightlines most likely to exhibit H_2 absorption are therefore also the most difficult to observe due to the faintness of the afterglows.

The absorption signatures from neutral atomic-carbon (C I) are another probe of the shielded gas-phase and can be used to study the cold, neutral medium in the ISM. Ledoux et al. (2015) searched for the absorption features of C I in a large sample of quasar spectra from the Sloan Digital Sky Survey (SDSS). Neutral carbon is typically observed to be coincident with H_2 in quasar DLAs (Srianand et al., 2005) and is found to be the optimal tracer of molecular gas in low-metallicity, star-forming galaxies (Glover & Clark, 2016) based on numerical simulations. This is likely related to the ionization potential of C I (11.26 eV) being similar to the energy range of Lyman-Werner photons that can photodissociate H_2 (11.2 – 13.6 eV). The C I $\lambda\lambda$ 1560,1656 transitions are also located far from the Lyα forest and can be identified even in low- to medium-resolution spectroscopy. The feasibility of this approach was verified by the spectroscopic follow-up campaign of the C I-selected quasar absorbers, where H_2 was detected in absorption in all cases (Noterdaeme et al., 2018). This sample also shows a constant C I to CO ratio, suggesting that neutral carbon actually probes a deeper, more shielded regime of the ISM than the diffuse atomic and molecular gas-phases (see also e.g. Snow & McCall, 2006).

In this paper, we follow a similar approach to Ledoux et al. (2015) but survey C I absorption in GRB optical afterglow spectra. We compile a list of $z > 1$ GRB afterglows, spanning over a decade of optical and near-infrared (NIR) spectroscopic observations, by combining the sample presented by Fynbo et al. (2009) and the GRB afterglow legacy survey by Selsing et al. (2019). Our goal is to investigate the environments of GRB hosts with neutral carbon detected in absorption (henceforth simply referred to as GRB C I absorbers or C I systems) in terms of their dust properties and chemical abundances. Since it is only possible to observe the Lyα transition from the ground and thus derive gas-phase abundances at $z \gtrsim 1.7$, we rely on the GRBs in this redshift range to examine the chemical abundances of the GRB C I absorbers, whereas the dust properties can be studied at all redshifts. This survey also opens a potential route to test whether the proposed lack of molecular gas in GRB host galaxies is an intrinsic property or simply a consequence of observational limitations. In this paper, we present the results of this survey and the basic properties of GRB C I absorbers. These are compared to GRB host absorption systems without the presence of C I and to other types of "cold gas" absorbers (i.e. with H_2 and/or C I detected in absorption) in quasar sightlines.

The paper is structured as follows. In Sect. 4.2 we present our sample and describe the observations and selection criteria, where Sect. 4.3 is dedicated to discuss the sample properties and completeness. In Sect. 4.4 we show our results, with specific focus on the properties of GRB host galaxies with C I absorption compared to those without. For our discussion, we compare the sample of GRBs with prominent amounts of cold, neutral gas to similar samples of cold gas absorbers in quasar sightlines in Sect. 4.5. Finally, in Sect. 4.6 we conclude on our work.

Throughout the paper, errors denote the 1σ confidence level and magnitudes are reported in the AB system. We assume a standard flat cosmology with $H_0 = 67.8\,\mathrm{km\,s^{-1}\,Mpc^{-1}}$, $\Omega_m = 0.308$ and $\Omega_\Lambda = 0.692$ (Planck Collaboration et al., 2016). Gas-phase abundances are expressed relative to the Solar abundance values from Asplund et al. (2009), where $[\mathrm{X/Y}] = \log N(\mathrm{X})/N(\mathrm{Y}) - \log N(\mathrm{X})_\odot/N(\mathrm{Y})_\odot$.

4.2 The GRB sample

The sample of GRBs studied here was built by extracting all bursts from the VLT/X-shooter GRB (XS-GRB) afterglow legacy survey (Selsing et al., 2019), combined with the GRB afterglow sample of Fynbo et al. (2009, hereafter F09). We also include the recent discovery of a strong C I absorber towards GRB 180325A, which also shows a prominent 2175 Å dust extinction feature (Zafar et al., 2018a). We subsequently imposed additional observational selection criteria to exclude late-time host galaxy observations and afterglow spectra with poor spectral quality or low spectral resolution. In this section we detail the GRB afterglow observations (Sect. 4.2.1) and selection criteria (Sect. 4.2.2). In Sect. 4.3 we present the properties of our final sample in terms of C I rest-frame equivalent width (Sect. 4.3.1) and dust extinction, A_V (Sect. 4.3.2). An overview of the full sample is provided in Table 8.2.1.

4.2.1 Observations and sample compilation

The majority of the GRB afterglows in our sample were detected by the Burst Alert Telescope (BAT) mounted on the Neil Gehrels *Swift* Observatory (*Swift*; Gehrels et al., 2004). The few exceptions were detected by the *Fermi* Gamma-Ray Space Telescope (Atwood et al., 2009; Meegan et al., 2009) or by the *INTEGRAL* satellite (Winkler et al., 2003).

The GRB afterglows from the F09 sample were observed using a range of low- to high-resolution spectrographs ($\mathcal{R} \approx 300 - 45\,000$), but we only include GRBs observed with $\mathcal{R} > 2000$ (see below). The more recent GRB afterglow sample by Selsing et al. (2019) was obtained homogenously with the VLT/X-shooter spectrograph (Vernet et al., 2011), covering a broad spectral range (300 – 2480 nm) in a single exposure by splitting the light into three spectroscopic arms (called the UVB, VIS and NIR ams). We refer the reader to the sample papers for a description of the observational details and the specifics of the data reduction. All the spectra used in our analysis have been corrected for the foreground Galactic extinction using the dust maps of Schlegel et al. (1998) and Schlafly & Finkbeiner (2011). All wavelengths throughout the paper are reported in vacuum and are shifted to the heliocentric reference frame.

Table 4.2.1. GRB afterglow sample properties.

GRB	$z_{\rm GRB}$	$\log N$(H I) (cm^{-2})	$W_{\rm r}(\lambda 1560)$ (Å)	$W_{\rm r}(\lambda 1656)$ (Å)	[X/H]	Ion	A_V (mag)	Refs.
F09 sample								
050730	3.9693	22.10 ± 0.10	< 0.03	< 0.03	-2.18 ± 0.11	S	0.12 ± 0.02	(1, 2)
050820A	2.6147	21.05 ± 0.10	< 0.12	< 0.13	-0.39 ± 0.10	Zn	0.27 ± 0.04	(3, 4)
050922C	2.1995	21.55 ± 0.10	< 0.03	< 0.03	-1.82 ± 0.11	S	0.09 ± 0.03	(3, 5)
060210	3.9133	21.55 ± 0.15	0.78 ± 0.03	⋯	> -0.83	Si	0.57 ± 0.08	(6, 5)
060607A	3.0749	16.95 ± 0.03	< 0.05	< 0.07	⋯	⋯	0.08 ± 0.08	(7, 8)
061121	1.3145	⋯	0.49 ± 0.04	0.25 ± 0.04	⋯	⋯	0.55 ± 0.10	(5)
070802†	2.4511	21.50 ± 0.20	0.70 ± 0.35	1.36 ± 0.32	-0.46 ± 0.63	Zn	1.19 ± 0.15	(9, 2)
071031	2.6918	22.15 ± 0.05	< 0.03	< 0.03	-1.73 ± 0.05	Zn	< 0.07	(3, 2)
080310	2.4274	18.70 ± 0.10	< 0.11	< 0.14	-1.20 ± 0.20	Si	0.19 ± 0.05	(10, 8)
080413A	2.4330	21.85 ± 0.15	< 0.03	< 0.03	-1.60 ± 0.16	Zn	< 0.59	(3, 11)
080605†	1.6403	⋯	0.64 ± 0.23	0.38 ± 0.15	⋯	⋯	0.50 ± 0.13	(12)
080607*,†	3.0368	22.70 ± 0.15	2.17 ± 0.08	2.03 ± 0.04	> -0.20	O	2.33 ± 0.46	(13, 2)
XS sample								
090926A	2.1069	21.60 ± 0.07	< 0.05	< 0.06	-1.85 ± 0.10	S	< 0.04	(14, 15)
100814A	1.4390	⋯	< 0.06	< 0.06	⋯	⋯	< 0.07	(15)
120119A	1.7288	22.44 ± 0.12	0.51 ± 0.05	0.77 ± 0.06	-0.96 ± 0.28	Zn	1.02 ± 0.11	(16, 15)
120327A*	2.8148	22.01 ± 0.09	< 0.03	< 0.03	-1.17 ± 0.11	Zn	< 0.03	(17)
120815A*	2.3581	21.95 ± 0.10	$(0.12 \pm 0.08)^{*}$	$(0.21 \pm 0.05)^{*}$	-1.15 ± 0.12	Zn	0.19 ± 0.04	(18, 15)
121024A*	2.3024	21.88 ± 0.10	$(0.08 \pm 0.05)^{*}$	$(0.11 \pm 0.07)^{*}$	-0.70 ± 0.10	Zn	0.26 ± 0.07	(19, 15)
130408A	3.7579	21.70 ± 0.10	< 0.05	< 0.06	-1.24 ± 0.12	S	0.21 ± 0.05	(6, 20)
130606A	5.9129	19.91 ± 0.02	< 0.10	< 0.10	-1.30 ± 0.08	Si	< 0.07	(21, 15)
141028A	2.3334	20.55 ± 0.07	< 0.14	< 0.21	-0.73 ± 0.34	Zn	0.13 ± 0.09	(16)
141109A	2.9944	22.10 ± 0.20	< 0.11	< 0.11	-1.40 ± 0.22	Zn	$0.11 \pm 0.03^{\ddagger}$	(22, 23)
150403A	2.0571	21.80 ± 0.20	0.34 ± 0.03	0.50 ± 0.04	-0.80 ± 0.35	S	$0.12 \pm 0.02^{\ddagger}$	(22, 23)
151021A	2.3299	22.20 ± 0.20	< 0.17	< 0.28	-1.11 ± 0.20	Si	$0.20 \pm 0.03^{\ddagger}$	(22, 23)
151027B	4.0647	20.50 ± 0.20	< 0.09	< 0.09	-1.62 ± 0.24	Si	0.10 ± 0.05	(22, 23, 20)
160203A	3.5185	21.75 ± 0.10	< 0.03	< 0.03	-1.26 ± 0.11	S	$< 0.10^{\ddagger}$	(24)
161023A	2.7106	20.97 ± 0.01	< 0.03	< 0.03	-1.11 ± 0.07	Zn	0.09 ± 0.03	(25)
170202A	3.6450	21.55 ± 0.10	< 0.10	< 0.08	-1.15 ± 0.13	S	< 0.12	(22, 23, 20)
180325A†	2.2486	22.30 ± 0.14	0.58 ± 0.05	0.85 ± 0.05	> -0.98	Zn	1.58 ± 0.12	(26)

Notes. All GRB afterglows with spectral coverage of the C I $\lambda\lambda$ 1560,1656 line transitions listed here are selected within a completeness limit of $W_{\rm r}(\lambda 1560) > 0.2$ Å. GRB 180325A is listed separately since it is not part of the F09 or XS-GRB sample papers. *GRB afterglows where a detection of H_2 in absorption has been reported in the literature. †Bursts with a prominent detection of the 2175 Å dust extinction feature. *Tentative detection of C I below the imposed detection threshold. $^{\ddagger}A_V$ measurements from this work.
References. The H I column densities, metallicities and visual extinctions are from: (1) D'Elia et al. (2007); (2) Zafar et al. (2011a); (3) Ledoux et al. (2009); (4) Schady et al. (2012); (5) Covino et al. (2013); (6) Cucchiara et al. (2015); (7) Fynbo et al. (2009); (8) Kann et al. (2010); (9) Elíasdóttir et al. (2009); (10) De Cia et al. (2012); (11) Zafar & Watson (2013); (12) Zafar et al. (2012); (13) Prochaska et al. (2009); (14) D'Elia et al. (2010); (15) Zafar et al. (2018a); (16) Wiseman et al. (2017); (17) D'Elia et al. (2014); (18) Krühler et al. (2013); (19) Friis et al. (2015); (20) Zafar et al. (2018c); (21) Hartoog et al. (2015); (22) Selsing et al. (2019); (23) Thöne et al. (in preparation); (24) Pugliese et al. (in preparation); (25) de Ugarte Postigo et al. (2018); (26) Zafar et al. (2018a).

4.2.2 Selection criteria and C I line identification

We only include GRBs from the F09 and the XS-GRB sample for which there is spectral coverage of the C I $\lambda\lambda$ 1560,1656 line transitions. To exclude afterglow spectra that are host dominated and have poor signal-to-noise ratios (S/N) we imposed the following observational and brightness contraints for the GRB follow-up observations

1. The GRB was observed within 24 hours after the trigger.
2. The brightness measured from the acquisition image is brighter than ≤ 21.0 mag.
3. The rest-frame detection limit of C I λ 1560 is 0.2 Å (at 3σ).
4. The spectral resolution $\mathcal{R}$ is higher than 2000.

The third criterion is defined such that we exlude bursts for which the upper limit on $W_{\rm r}(\lambda 1560)$ cannot be constrained within 0.2 Å. We thus define this as our completeness limit and only consider GRB C I absorbers with $W_{\rm r}(\lambda 1560) > 0.2$ Å in our statistical sample. The fourth criterion is only relevant for the F09 afterglow sample and is imposed to exclude the large fraction of bursts with $\mathcal{R} \approx 300$ for which C I is practically impossible to detect even at large S/N. We adopt the C I line detections and equivalent width measurements from the F09 paper, but measure the upper limits on C I for the rest of the GRBs entering our sample. Most bursts from F09 included in our sample already have derived upper limits on the column density of C I down to deep limits by Ledoux et al. (2009), but we report them in terms of equivalent widths here for consistency.

Since we require the spectral regions of the C I $\lambda\lambda$ 1560,1656 transitions to be covered, this effectively results in a redshift lower limit of $z_{\rm min} = \lambda_{\rm min}/1560 - 1 \approx 1.0 - 1.2$ for a spectral cut-off, $\lambda_{\rm min}$, of 300 to 350 nm. For typical optical spectrographs, where observations up to around 900 nm is possible, the redshift upper limit is $z_{\rm max} \approx 5.8$, whereas for the VLT/X-shooter spectrograph, both C I line transitions can in principle be observed up to $z_{\rm max} \approx 15$ (though with gaps due to the atmospheric transparency in the NIR). We are therefore able to probe a much larger redshift range than is possible for e.g. C I absorbers toward quasars observed as part of the SDSS survey (Ledoux et al., 2015). To measure the chemical abundances of the GRB host galaxies (such as the neutral hydrogen column density, metallicity and dust depletion), however, requires that the GRBs are located at $z \gtrsim 1.7$ for the spectra to encompass the wavelength region where the Lyα absorption line can be observed from the ground.

4.3 Data analysis and sample properties

In the final GRB afterglow sample, a total of 29 bursts (12/17 from the F09 and the XS-GRB samples, respectively) fulfill our imposed selection criteria and thus constitute our parent sample. Below we detail our measurements of the C I $\lambda\lambda$ 1560,1656 equivalent widths for the detections and tentative detections in the XS-GRB sample (see Fynbo et al., 2009, for the C I line detections and measurements from their sample). We also include GRB 060210 from the F09 sample as a C I absorber in our sample even though C I λ 1656 is not detected, due to its wavelength region being outside the spectral coverage, since the other transitions C I $\lambda\lambda\lambda$ 1260,1277,1328 are detected. We report the

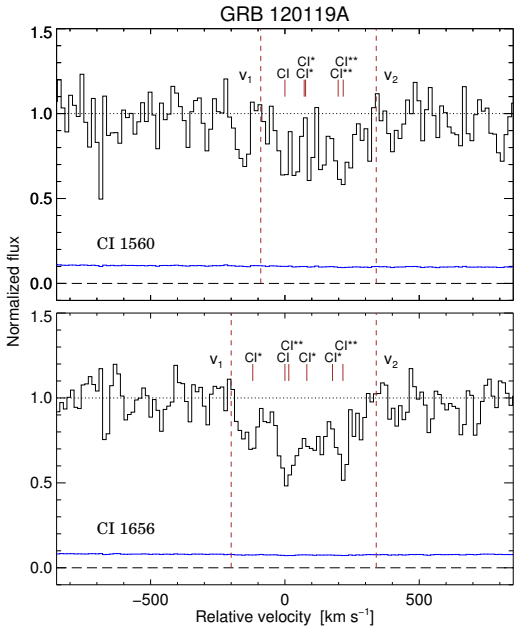

Figure 4.3.1. VLT/X-shooter spectrum of the GRB 120119A in velocity space, centred on the ground-state of the C I $\lambda\lambda$ 1560,1656 absorption lines at $z = 1.7291$. The black solid line shows the spectrum and the associated error is shown in blue. The spectrum has been binned by a factor of two. The ground-state and fine-structure lines of the C I $\lambda\lambda$ 1560,1656 transitions are marked above each of the absorption profiles. The profiles have been integrated over the velocity range indicated by the dashed red lines from v_1 to v_2 to measure the equivalent widths. C I is detected above the completeness limit in this system.

full set of C I $\lambda\lambda$ 1560,1656 equivalent width measurements and the derived 3σ upper limits for the GRBs with non-detections of C I in Table 8.2.1.

4.3.1 Equivalent width of C I

For all GRBs we provide the total rest-frame equivalent widths of the C I $\lambda\lambda$ 1560,1656 absorption lines and list them in Table 8.2.1. We attribute all the absorption to the ground-state of C I, even though the fine-structure transitions C I* and C I** also contribute (Srianand et al., 2005; Noterdaeme et al., 2017). This is, however, to be consistent with the measurements from the F09 sample and to directly compare our results to the sample of quasar C I absorbers from Ledoux et al. (2015). We determine the rest-frame equivalent widths of the C I $\lambda\lambda$ 1560,1656 absorption features by fitting the continuum around each of the lines and then integrate the absorption profile contained below the normalized flux level which encompasses all the C I $\lambda\lambda$ 1560,1656 ground-state and fine-structure transitions.

GRB 120119A

The spectrum of GRB 120119A at $z = 1.7288$ is presented in the work by Wiseman et al. (2017). We adopt the H I column density of $\log N(\mathrm{H\,I/cm^{-2}}) = 22.44 \pm 0.12$ and the derived metallicity [Zn/H] $= -0.96 \pm 0.28$ from their work. Zafar et al. (2018b) measured a visual extinction of $A_V = 1.02 \pm 0.11$ mag and found no evidence for the presence of the 2175 Å dust extinction feature. In Fig. 4.3.1, we show a part of the spectrum centred on the C I $\lambda\lambda$ 1560,1656 line transitions. The absorption profiles have been integrated over the velocity range indicated by the dashed red lines from v_1 to v_2

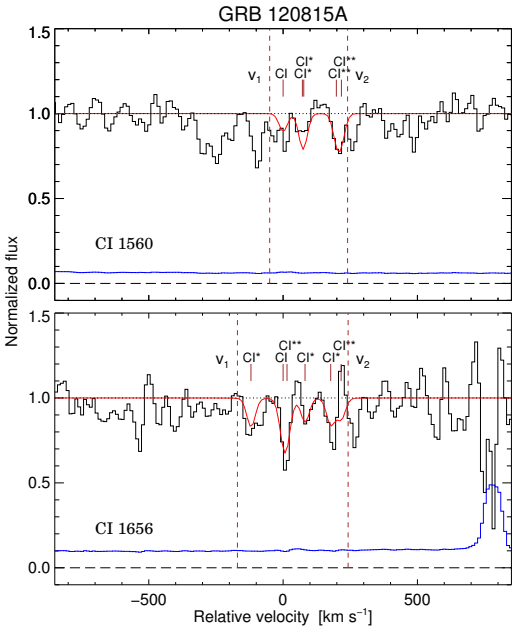

Figure 4.3.2. Same as Fig. 4.3.1 but for GRB 120815A, centred on z = 2.3581. Consistent absorption profiles are also detected in C I λ 1277 and C I λ 1328. Overplotted in red are the best-fit Voigt profiles. C I is detected below the completeness limit in this system.

to measure the equivalent widths and include the ground-state and fine-structure lines. We measure total C I rest-frame equivalent widths of $W_r(\lambda 1560) = 0.51 \pm 0.05$ Å and $W_r(\lambda 1656) = 0.77 \pm 0.06$ Å.

GRB 120815A

The spectrum of GRB 120815A at $z = 2.3581$ is presented in the work by Krühler et al. (2013). We adopt the H I column density of $\log N(\mathrm{H\,I}/\mathrm{cm}^2) = 21.95 \pm 0.10$ and the derived metallicity [Zn/H] = -1.15 ± 0.12 from their work. They also detect absorption lines from H_2 with a column density of $\log N(H_2/\mathrm{cm}^2) = 20.54 \pm 0.13$, which yields a molecular gas fraction of $\log f(H_2) = -1.14 \pm 0.15$, and C I with a column density of $\log N(\mathrm{C\,I}/\mathrm{cm}^2) = 13.41 \pm 0.11$. Zafar et al. (2018b) measured a visual extinction of $A_V = 0.19 \pm 0.04$ mag and found no evidence for the presence of the 2175 Å dust extinction feature. We measure equivalent widths of $W_r(\lambda 1560) = 0.12 \pm 0.08$ Å and $W_r(\lambda 1656) = 0.21 \pm 0.05$ Å (shown in Fig. 4.3.2). The equivalent width of C I λ 1560 is below the detection threshold of $W_r^{\mathrm{lim}} = 0.2$ Å, however, and we therefore only report the C I in this system as a tentative detection. To verify the detection we compared the velocity components seen for the C I $\lambda\lambda$ 1560,1656 lines to the normalized flux at the region of the C I $\lambda\lambda$ 1277,1328 line transitions and found consistent results. Based on these four sets of C I ground-state and fine-structure lines we fit Voigt profiles to all components and line transitions to further demonstrate the robustness of the detection. The best fit is shown in Fig. 4.3.2 as the red solid line. We then also measured the equivalent widths directly from the Voigt-profile model and found consistent results.

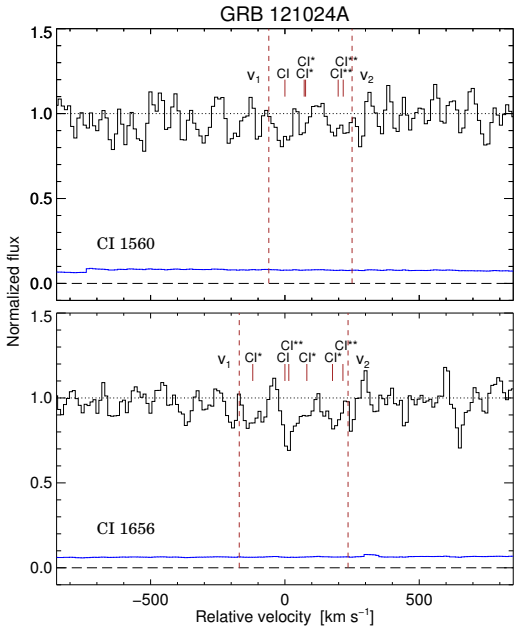

Figure 4.3.3. Same as Fig. 4.3.1 but for GRB 121024A, centred on z = 2.3021. C I is detected below the completeness limit in this system.

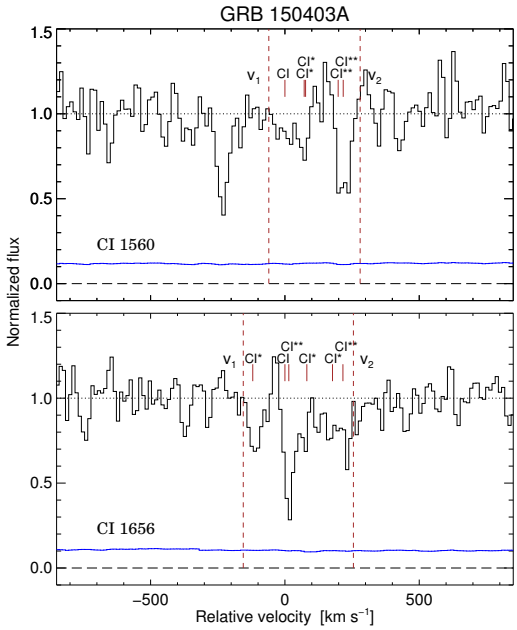

Figure 4.3.4. Same as Fig. 4.3.1 but for GRB 150403A, where the ground-state transitions are centred on z = 2.0569. C I is detected above the completeness limit in this system.

GRB 121024A

The spectrum of GRB 121024A at $z = 2.3024$ is presented in the work by Friis et al. (2015). We adopt the H I column density of $\log N(\mathrm{H\,I/cm^2}) = 21.88 \pm 0.10$ and the

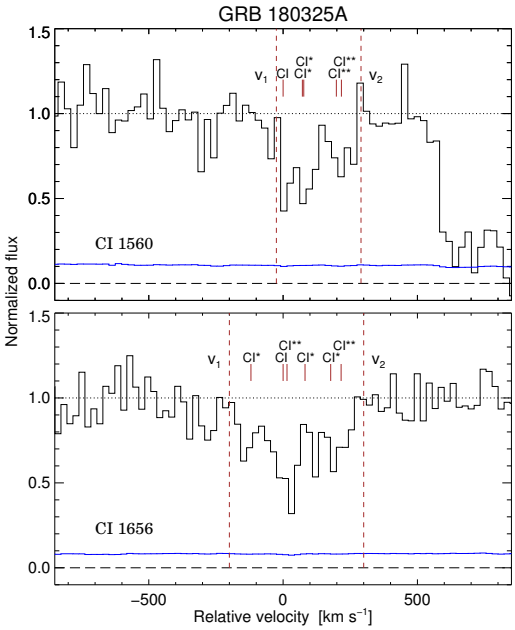

Figure 4.3.5. Same as Fig. 4.3.1 but for GRB 180325A, where the ground-state transitions are centred on $z = 2.2494$. C I is detected above the completeness limit in this system. The spectrum has been binned by a factor of two.

derived metallicity [Zn/H] $= -0.70 \pm 0.10$ from their work. They also detect absorption lines from H_2 with a column density of $\log N(H_2/\mathrm{cm}^2) \approx 19.8$, which yields a molecular gas fraction of $\log f(H_2) \approx -1.4$. They do not report a detection of C I, but after re-examing the spectrum we identify the ground-state and fine-structure lines belonging to the C I $\lambda\lambda$ 1560,1656 transitions (see Fig. 4.3.3). Zafar et al. (2018b) measured a visual extinction of $A_V = 0.19 \pm 0.04$ mag for this GRB and found no evidence for the presence of the 2175 Å dust extinction feature. We measure equivalent widths of $W_\mathrm{r}(\lambda 1560) = 0.08 \pm 0.05$ Å and $W_\mathrm{r}(\lambda 1656) = 0.11 \pm 0.07$ Å. The equivalent width of C I λ 1560 is below the detection threshold of $W_\mathrm{r}^\mathrm{lim} = 0.2$ Å, however, and we therefore only report the C I in this system as a tentative detection.

GRB 150403A

The spectrum of GRB 150403A at $z = 2.0571$ is presented in the work by Selsing et al. (2019) from which we adopt the H I column density of $\log N(\mathrm{H\,I}/\mathrm{cm}^2) = 21.80 \pm 0.20$. Detailed measurements of the gas-phase abundances for this burst will be presented in the work by Thöne et al. (in preparation), but see also Heintz et al. (2018b) where they report [S/H] $= -0.80 \pm 0.35$. In this work we measure a visual extinction of $A_V = 0.20 \pm 0.03$ mag (see below), and find no evidence for the presence of the 2175 Å dust extinction feature. The C I $\lambda\lambda$ 1560,1656 line transitions are readily detected in the spectrum (see Fig. 4.3.4) and we measure equivalent widths of $W_\mathrm{r}(\lambda 1560) = 0.34 \pm 0.03$ Å and $W_\mathrm{r}(\lambda 1656) = 0.50 \pm 0.04$ Å.

GRB 180325A

The spectrum of GRB 180325A at $z = 2.2486$ is presented in the work by Zafar et al. (2018a). We adopt the H I column density of $\log N(\mathrm{H\,I/cm^2}) = 22.30 \pm 0.14$, the derived metallicity [Zn/H] = > -0.98, the measured visual extinction, $A_V = 1.58 \pm 0.12$ mag, and the measured C I equivalent widths $W_\mathrm{r}(\lambda 1560) = 0.58 \pm 0.05$ Å and $W_\mathrm{r}(\lambda 1656) = 0.85 \pm 0.05$ Å from their work (see also Fig. 4.3.5). They also detect a strong 2175 Å dust extinction feature, the strength of which follow the correlation expected from the C I equivalent widths (Ma et al., 2018).

4.3.2 Dust extinction

Due to their immense luminosity and well-known intrinsic power-law spectra, GRBs are an ideal probe of dust in star forming galaxies and in the line of sight out to high redshifts (Zafar et al., 2011a,b; Greiner et al., 2011; Covino et al., 2013; Bolmer et al., 2018). GRB extinction curves can typically be described by similar prescriptions as that of the Small Magellanic Cloud (SMC), but can in rare cases also show a prominent 2175 Å extinction bump known locally from sightlines in the Milky Way (MW) and towards the Large Magellanic Cloud (LMC) (e.g. Krühler et al., 2008; Elíasdóttir et al., 2009; Prochaska et al., 2009; Perley et al., 2011; Zafar et al., 2012, 2018a). GRB afterglows have recently been found to show slightly steeper extinction curves on average than that of e.g. the SMC (Zafar et al., 2018b). Even more unusual extinction features have also been observed, such as flat or "grey" (Savaglio & Fall, 2004; Perley et al., 2008; Friis et al., 2015) or very steep (Fynbo et al., 2014; Heintz et al., 2017) reddening curves. By utilizing the simple and smooth intrinsic power-law spectra of GRBs, the specific extinction curves can be well-constrained and provide a measure of the visual extinction, A_V, in the line of sight to the GRB, in addition to the overall dust composition and grain size distribution.

The majority of the GRB afterglows in our parent sample already have published measurements of the extinction. Here we provide values of A_V for four additional bursts (GRBs 141109A, 150403A, 151021A, and 160203A) observed with VLT/X-shooter (see Table 8.2.1) using the approach detailed in the sections below. Our procedure is similar to previous determinations of A_V's in GRBs from the literature, although we do not rely on multi-epoch photometry to normalize the X-ray to the optical spectra. We find consistent results using our approach, compared to already published values of A_V in GRB sightlines.

Intrinsic afterglow SED

The continuum emission from a GRB afterglow is believed to be dominated by synchrotron radiation described by a single or broken power-law (Sari et al., 1998). It has also been verified observationally that the intrinsic X-ray spectrum derived from the *Swift*/XRT can be used as proxy for the intrinsic optical spectrum, typically with a cooling break of $\Delta\beta = 0.5$ (Zafar et al., 2011a). The X-ray spectral slope in photon units, Γ, is given by a fit to the *Swift*/XRT spectrum in the dedicated repository[1]. From

[1] http://www.swift.ac.uk/xrt_spectra/

the photon index, the prescription for the intrinsic optical spectral slope as a function of wavelength is given as

$$F_\lambda = F_0\,\lambda^{(\Gamma-\Delta\beta-3)}\,, \tag{4.1}$$

or as a function of frequency, $F_\nu = F_0\,\nu^{(\Gamma-\Delta\beta-2)}$. In the following analysis we will use the photon index from the *Swift*/XRT database to derive the intrinsic spectral slope and allow for the slope change due to the cooling break to take a value to take a value of $\Delta\beta = 0.0$ or 0.5.

Ideally, the optical/NIR and X-ray spectral energy distributions (SEDs) should be fit together to get an estimate of the intrinsic slope (see e.g. Watson et al., 2006; Greiner et al., 2011; Schady et al., 2012; Japelj et al., 2015; Bolmer et al., 2018). To do so, however, requires that multiple photometric data points are available to normalize the optical and X-ray spectra to the same epoch using their respective lightcurves. A subset of the GRBs observed with VLT/X-shooter that have coinciding multi-epoch photometry have already been published by Japelj et al. (2015) and Zafar et al. (2018b). Using Eq. 4.1 we can estimate the A_V in an alternative way, not relying on near-simultaneous photometric observations. To improve the absolute flux calibration of the VLT/X-shooter spectra, although not particularly important for our approach, we rescale the VIS arm to the measured acquisition magnitude (typically *R*-band). The flux of the GRB in the UVB and NIR arms are then scaled to match the VIS arm spectrum.

Dust-extinction model

The observed optical/NIR flux from the GRB afterglow is extinguished due to absorption or scattering by dust particles located in the line of sight to the burst. In the majority of cases the dominant contribution is from dust in the GRB host galaxy (after correcting for the Galactic extinction). The observed afterglow spectrum can therefore be described as

$$F_\lambda^{\rm obs} = F_\lambda \times 10^{-0.4 A_\lambda}\,, \tag{4.2}$$

where A_λ is the extinction as a function of wavelength, λ, in the GRB host galaxy. The visual extinction, A_V, can then be estimated assuming a given dust-extinction model when knowing the redshift of the GRB and using the intrinsic spectral shape as measured from the X-ray spectrum.

We fit the combined X-shooter spectrum with the dust-extinction model of Fitzpatrick & Massa (1990) which parametrizes the extinction curve through a set of eight parameters. The extinction curve is defined as

$$A_\lambda = \frac{A_V}{R_V}\left(k(\lambda - V) + 1\right)\,, \tag{4.3}$$

where the relative reddening, $k(\lambda - V)$, is given as

$$k(\lambda - V) = c_1 + c_2 x + c_3 D(x, x_0, \gamma) + c_4 F(x)\,, \tag{4.4}$$

with

$$F(x) = \begin{cases} 0.539(x-5.9)^2 + 0.056(x-5.9)^3 & \text{for } x \geq 5.9 \\ 0 & \text{for } x < 5.9 \end{cases}\,, \tag{4.5}$$

and the Lorentzian-like Drude profile representing the 2175 Å extinction bump, observed locally in some sightlines in the MW and the LMC, is described as

$$D(x, x_0, \gamma) = \frac{x^2}{(x^2 - x_0^2)^2 + x^2\gamma^2} \ , \tag{4.6}$$

where $x = (1\ \mu\mathrm{m})/\lambda$. Basically, this dust-extinction model contains two components, one describing the linear UV part of the spectrum via the components c_1 (intercept), c_2 (slope) and the term $c_4 F(x)$ describing the far-UV curvature. The second component is the Drude profile, controlled by the parameters c_3 (bump strength), x_0 (central wavelength) and γ (width of the bump). The last two parameters are the visual extinction, A_V, and the total-to-selective reddening, R_V. The advantage of such a parametrization of the dust-extinction model is that it allows for, e.g., the strength and width of the 2175 Å bump to be fitted independently (Jiang et al., 2010; Ledoux et al., 2015; Ma et al., 2017; Noterdaeme et al., 2017) and to model extinction curves with no local analogs (Fynbo et al., 2014; Amanullah et al., 2014; Heintz et al., 2017). We do not observe any evidence for the 2175 Å extinction bump or an unusual steep (or flat) reddening curve in the four GRBs examined in this work.

We derive the rest-frame visual extinction, A_V, by normalizing the intrinsic power-law spectrum to the flux in the NIR arm in the wavelength region of a typical K-band. We then fit the observed spectrum using three different reddening laws: SMC and LMC as parametrized by Gordon et al. (2003) and the slightly steeper reddening law inferred for the average GRB afterglow derived by Zafar et al. (2018a), all using the Fitzpatrick & Massa (1990) prescription. We fix the redshift of the dust component to z_{GRB} and then only vary A_V. In Fig. 4.3.6 we show an example of one of the fits for GRB 151021A. In this case we measure $A_V = 0.20 \pm 0.03$ mag and find that the extinction is best fit with the SMC reddening law. To verify our approach we also fit the XS-GRBs for which the visual extinction has already been measured and find consistent results. Our derived A_V values are provided in Table 8.2.1.

4.3.3 Sample properties

The C I detections are reported in Table 8.2.1. It is detected robustly (i.e. with $W_{\mathrm{r}}(\lambda 1560) > 0.2$ Å) in eight GRBs, five from the F09 sample (GRBs 060210, 060607A, 061121, 080605, and 080607) and three from the XS-GRB sample (GRBs 120119A, 150403A, and 180325A). We do not include GRB 180325A in the following statistical analysis since it is not part of the two sample papers and was added specifically because of its detection of C I. In the statistical sample, seven of the GRB afterglows ($\approx 25\%$) thus have C I detected in absorption, with an approximately 40% detection rate in the F09 sample and $\approx 15\%$ in the XS-GRB sample. The reason for the larger detection in the F09 sample is likely due to most of the afterglows have been obtained with more sensitive, low-resolution spectrographs compared to the bursts observed with the VLT/X-shooter instrument. Due to the usage of more sensitive, low-resolution spectrographs pre-X-shooter, a larger fraction of faint bursts that are potentially more obscured due to larger dust columns entered the F09 sample. As a consequence, this sample will contain more dust obscured afterglows, and therefore a higher detection probability of C I is expected. This is also evident from Table 8.2.1, showing that the bursts from

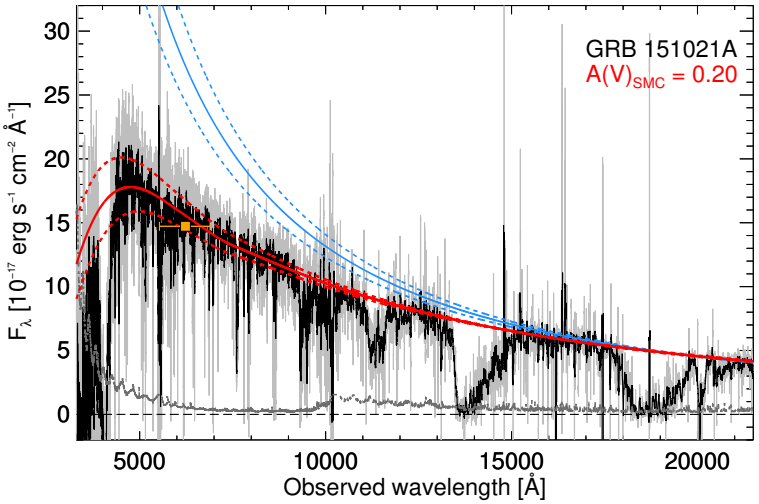

Figure 4.3.6. Fit of the dust extinction, A_V, to the spectrum of GRB 151021A. The grey and black lines show the full raw and binned X-shooter spectrum, respectively. The corresponding raw error spectrum is shown as the bottom dark grey line. The spectrum was normalized to the acquisition magnitude overplotted as the orange square. The intrinsic afterglow spectrum derived from the *Swift*/XRT spectrum with a slope change of $\Delta\beta = 0.5$ is shown as the blue solid line with the errors on the power-law slope shown as the blue, dashed lines. An extinction curve with the best fit value of $A_V = 0.20 \pm 0.03$ mag is shown as the red, solid line and the error on the fit is shown by the red, dashed lines.

the F09 sample have on average higher values of A_V (with a mean of $A_V = 0.54$ mag) than those from the XS-GRB sample (mean of $A_V = 0.18$ mag). Furthermore, the two fractions are even consistent within $\approx 1\sigma$ when taking into account the low number statistics (Cameron, 2011). We also identify absorption from C I in GRBs 120815A and 121024A but below the sample completeness limit and we therefore do not include them in the statistical sample.

Our full sample spans a redshift range of $z = 1 - 6$ with C I absorption detected up to $z \approx 4$ in GRB 060210. C I is also detected in all GRBs where H_2 has previously been reported in absorption via the Lyman-Werner bands, except for GRB 120327A (which has a low molecular fraction) for which we place upper limits of $W_r(\lambda 1560) < 0.03$ Å and $W_r(\lambda 1656) < 0.03$ Å. This GRB is observed to have an insignificant amount of dust ($A_V < 0.03$ mag, D'Elia et al., 2014), however, which would be consistent with the non-detection of C I (see Sect. 4.4).

In general, there is a strong excess of cold gas in GRB hosts compared to absorbers in quasar sightlines (Ledoux et al., 2015), where about one percent of intervening C I absorbers were found with a completeness of around 40% at $W_r^{\rm lim} = 0.2$ Å. The strong excess of cold gas is not unexpected since GRBs probe more central regions of their host galaxies whereas quasars probe random sightlines through intervening absorbers. Due to higher ISM pressure, the covering fraction of the cold, neutral gas is also expected to be higher closer to the galactic centre.

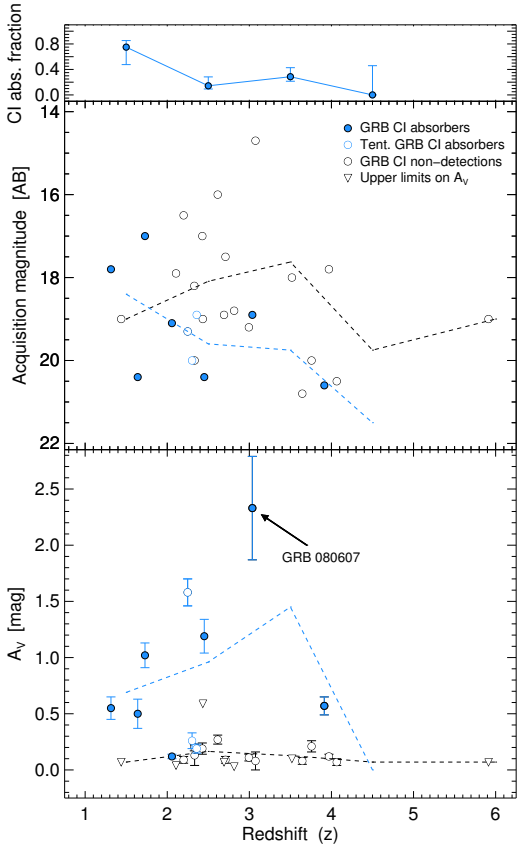

Figure 4.3.7. Redshift distribution as a function of GRB brightness at the time of observation (middle panel) and dust extinction, A_V (bottom panel). Blue filled circles denote the GRBs in our statistical sample with C I detected in absorption. Black empty circles mark the GRBs in our sample without C I, where triangles represent upper limits on A_V. In the middle and bottom panels, the dashed lines show the mean acquisition magnitudes and A_V values for the GRBs without (black) and with (blue) C I detected in absorption in different bins: $1 < z < 2$, $2 < z < 3$, $3 < z < 4$, and $z > 4$. In the top panel the fraction of GRB C I absorbers is shown in the same redshift interval. The GRBs with C I detected below the completeness limit are shown by the blue empty circles, and are not included in the analysis.

In the top panel of Fig. 4.3.7 we show the fraction of GRB C I absorbers as a function of redshift, binned by $\Delta z = 1$ from $z = 1 - 4$ (where the errors are calculated assuming small number statistics, see Cameron, 2011). The GRB C I absorber fraction is high at $1 < z < 2$ with $\approx 75\%$, where for $z > 2$ the fraction ranges from $\approx 20\% - 30\%$. Here we only consider the C I detections from the statistical sample, thereby excluding GRBs 120815A, 121024A, and 180325A (but include them in the figure as empty blue circles). In the middle panel of Fig. 4.3.7, the redshift distribution is shown as a function of the observed acquisition magnitude (typically in the R-band). We observe that the GRB afterglows with C I detected in absorption on average have fainter magnitudes. In the bottom panel of Fig. 4.3.7 the redshift distribution is shown as a function of the visual extinction, A_V, for each burst. In general, the GRB C I absorbers are found to be the most dust-reddened systems at all redshifts, shown by the curves representing the mean of the two populations.

In our full sample of GRB C I absorbers, only four afterglows (GRBs 070802, 080605, 080607, and 180325A) have a robust detection of the 2175 Å dust extinction feature. All four have considerable visual extinctions ($A_V > 0.5$ mag, Zafar et al., 2012, 2018a) and strong C I equivalent widths of $W_r(\lambda 1560) \gtrsim 0.6$ Å. Only three other GRBs with C I absorption in our full sample, namely GRBs 060210, 061121 and 120119A,

have $A_V > 0.5$ mag as well, but do not show any indication of the 2175 Å dust extinction feature. For the GRBs 060210 and 061121, Covino et al. (2013) found a best fit with an SMC-like extinction curve, though only based on its broad-band photometry. Initially, Japelj et al. (2015) found a best fit with an LMC-like extinction curve for GRB 120119A but Zafar et al. (2018b) argue that it was a false detection based on the unbinned X-shooter spectrum and found a best fit with an SMC-like extinction curve instead. In the statistical sample of GRB C I absorbers, about 40% thus show the presence of the 2175 Å dust extinction feature (consistent with the quasar C I absorber sample; Ledoux et al., 2015).

4.4 Results

The left panel of Fig. 4.4.1 shows the C I equivalent width as a function of the visual extinction, A_V, for the GRB C I absorbers. We also overplot the quasar C I absorbers from Ledoux et al. (2015) and the 2175 Å dust extinction feature absorbers, all with C I detected in absorption as well, from Ma et al. (2017, 2018). We find a strong linear correlation (with Pearson correlation coefficients of $r = 0.80$ and $p = 0.02$) between A_V and $W_r(\lambda 1560)$ for the GRB C I absorbers. We also note that C I is only detected in systems with $A_V \gtrsim 0.1$ mag, classifying the GRB C I systems as translucent interstellar clouds (see e.g. Snow & McCall, 2006).

In the right panel of Fig. 4.4.1 we again show the C I equivalent widths but as a function of the strength of the 2175 Å dust extinction feature, $A_{\rm bump}$, defined as $A_{\rm bump} = \pi c_3/(2\gamma R_V) \times A_V$. Only in five GRB absorbers to date has the 2175 Å dust extinction feature been unambiguously observed (Krühler et al., 2008; Elíasdóttir et al., 2009; Prochaska et al., 2009; Perley et al., 2011; Zafar et al., 2012, 2018a), where C I is detected in four of them (the non-detection in the last afterglow, GRB 080805, is poorly constrained due to low S/N, however, see Zafar et al., 2012). Here, we plot the four GRB C I absorbers with a clear presence of the 2175 Å dust extinction feature (see Table 8.2.1), where we have extracted the bump parameters for the four cases from the literature (Zafar et al., 2011a, 2018a) and thus extend the analysis of Zafar et al. (2012). We also include the upper limits on the bump strength as measured for the other GRB C I absorber assuming the smooth SMC bar prescription by Gordon et al. (2003). We find evidence for a positive correlation between the amount of neutral carbon and the bump strength for the GRB C I absorbers. With only four detections of the 2175 Å dust extinction feature in GRB C I absorbers, however, we are still limited by low number statistics. This relation has already been established by Ledoux et al. (2015) and Ma et al. (2018) for a larger number of quasar C I absorbers, but the addition of the small sample of GRB C I systems support this correlation and verify it at $A_{\rm bump} > 1$ mag as well.

The fact that C I absorbers are associated with significant dust columns is now firmly established (Ledoux et al., 2015; Ma et al., 2018). This could be related to larger dust columns more effectively shielding the neutral carbon or simply that C I scales with the overall amount of carbon which is dominant in the dust-phase. Nevertheless, it is established that in the cold neutral gas-phase, the amount of shielded gas and dust are connected. We note that among the quasar C I absorbers, some systems have large

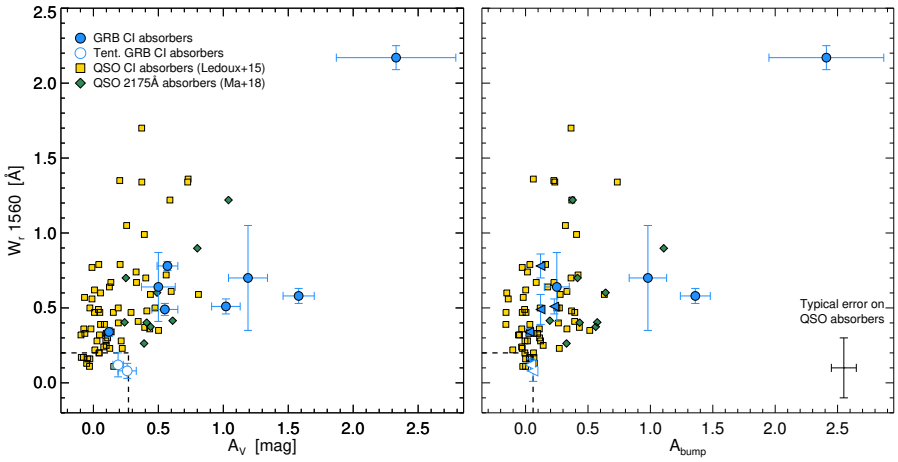

Figure 4.4.1. C I λ 1560 rest-frame equivalent width as a function of dust extinction, A_V (left panel) and 2175 Å bump strength, $A_{\rm bump}$ (right panel). The blue filled circles denote the GRBs with C I detected in absorption (empty blue circles show the GRBs with C I detected below the completeness limit), where the filled blue left-pointing triangles in the right panel represent the upper limit on $A_{\rm bump}$ derived for the other GRB C I absorbers (assuming an SMC bar extinction curve). The yellow squares show the quasar C I absorbers from Ledoux et al. (2015) and the green diamond symbols represent the quasar 2175 Å dust extinction feature absorbers from Ma et al. (2018). The dashed lines mark the $W_{\rm r}(\lambda\,1560)$ detection limit and maximum A_V and $A_{\rm bump}$ for the GRBs with non-detections of C I.

$W_{\rm r}(\lambda\,1560)$ but low extinction values which might indicate that these absorbers are metal-rich but with low gas content. The fact that no quasar C I absorbers with $A_V > 1$ mag have been detected might be due to a more severe dust bias in quasar DLA samples than for GRB afterglows (e.g. Heintz et al., 2018a). However, it could also simply be related to the fact that quasar DLAs are rarely observed with large N(H I) whereas GRB absorbers typically probe dense, central-galactic environments. We also find that the 2175 Å dust extinction feature is only detected in GRBs with significant extinctions of $A_V > 0.5$ mag and strong C I absorption of $W_{\rm r}(\lambda\,1560) > 0.6$ Å.

In Fig. 4.4.2 we show the relation between A_V and the column density of neutral hydrogen (H I) for the GRBs at $z \gtrsim 1.7$ in our sample and again compare them to the quasar C I absorbers from Ledoux et al. (2015) and the 2175 Å dust extinction feature absorbers from Ma et al. (2017, 2018). For reference, the average dust-to-gas ratios from specific Galactic sightlines and toward the SMC bar, the mean LMC and the LMC2 supershell from Gordon et al. (2003) are shown as well. In general, the GRB C I systems (and also the general sample of GRB absorbers) seem to have lower dust-to-gas ratios than the average Milky Way sightline, with a median value of $A_V/N(\text{H I}) = 7.92 \times 10^{-23}$ mag cm^{-2}. In the different regimes of H I covered by GRBs and the quasar absorbers, it is evident that the dust-to-gas ratio is significantly lower for the GRB C I systems than what is observed for the quasar C I absorbers. This is likely a consequence of the on average lower metallicities of the GRB host absorption systems (Zafar et al., 2011a)

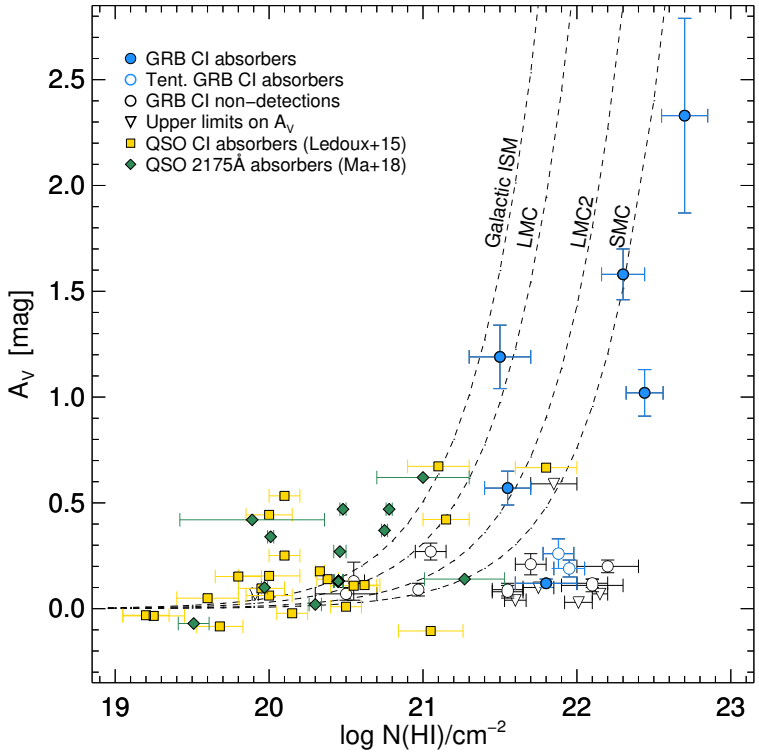

Figure 4.4.2. Column density of neutral hydrogen (H I) as a function of dust extinction, A_V, i.e. the dust-to-gas ratio. Blue filled circles again denote the GRBs with C I detected in absorption (empty blue circles show the GRBs with C I detected below the completeness limit). Black empty circles mark the GRBs in our samples without C I, where triangles represent bursts with upper limits on A_V. The yellow squares show the quasar C I absorbers from Ledoux et al. (2015) and the green diamond symbols represent the quasar 2175 Å dust extinction feature absorbers from Ma et al. (2018). Overplotted are the average dust-to-gas ratios from specific sightlines in the Local Group (MW, LMC, LMC2 and SMC) from Gordon et al. (2003).

and the fact that the dust-to-metals ratio decrease with decreasing metallicity (e.g. De Cia et al., 2013; Wiseman et al., 2017).

For the majority of the GRBs at $z \gtrsim 1.7$, we also obtained values for the metallicity, [X/H], from the literature (see Table 8.2.1). This, together with the H I column density, yields the metal column density of the GRB absorbers, related to the dust column density (Vladilo et al., 2006; Zafar & Watson, 2013). In the left panel of Fig. 4.4.3 we show the metallicity as a function of H I column density for the GRBs in our parent sample. While the full sample spans a large range of $18.7 < \log N(\mathrm{H\,I})/\mathrm{cm}^{-2} < 22.7$ and -2.2 < [X/H] < -0.2, it is clear that the GRB C I absorbers are all located above the threshold $\log N(\mathrm{H\,I})/\mathrm{cm}^{-2}$ + [X/H] > 20.7 (marked as the dashed line). Bolmer et al. (2019) also found consistent results for H_2-bearing GRB absorbers, though extended to lower metallicities. We note that in the study of Ledoux et al. (2009), none of the

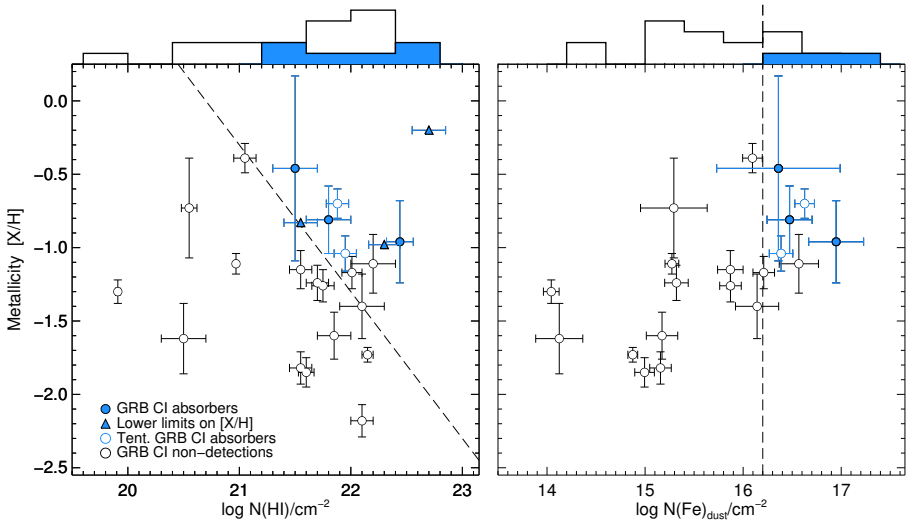

Figure 4.4.3. Metallicity distribution as a function of H I column density (left panel) and dust-phase iron column density, $N(\mathrm{Fe})_{\mathrm{dust}}$ (right panel). Only the subsets of the full GRB sample with both a metallicity and $N(\mathrm{H\,I})$ measurements (left) and depletion values (right) are shown. Blue filled circles again denote the GRBs with C I detected in absorption (empty blue circles show the GRBs with C I detected below the completeness limit). Black empty circles mark the GRBs in our samples without C I, where triangles represent bursts with lower limits on [X/H]. In the left panel, the dashed line corresponds to $\log N(\mathrm{H\,I})/\mathrm{cm}^{-2}$ + [X/H] = 20.7, above which all the observed systems with detected C I are located and in the right panel the dashed line mark $\log N(\mathrm{Fe})_{\mathrm{dust}}/\mathrm{cm}^{-2} = 16.2$. At the top of both panels there are histograms of H I column density (left) and dust-phase iron column density (right) of the GRB absorbers with (filled blue) and without (black line) C I detected in absorption.

GRBs in their sample have $\log N(\mathrm{H\,I})/\mathrm{cm}^{-2}$ + [X/H] > 20.7. This threshold discovered here would then explain the non-detections of H_2 and C I absorption features in their high-resolution sample (as speculated; Ledoux et al., 2009; Krühler et al., 2013).

To investigate more directly the influence of dust on the detection of C I, we derive the column density of iron locked into the dust-phase, defined as $N(\mathrm{Fe})_{\mathrm{dust}} = (1 - 10^{-[\mathrm{X/Fe}]})\,N(\mathrm{X})\,(\mathrm{Fe/X})_{\odot}$ (e.g. Vladilo et al., 2006). This quantity has been identified as the primary driver of the detection of H_2 molecules in quasar absorbers (Noterdaeme et al., 2008). Only for a subset of the GRB afterglows in our sample at $z \gtrsim 1.7$, has the dust depletion, [X/Fe], been measured. Here it is assumed that X is a non-refractory element (typically Zn or S, but see e.g. Jenkins, 2009; De Cia et al., 2016) and that the intrinsic ratio is Solar. In the right panel of Fig. 4.4.3 we again show the metallicity but as a function of $N(\mathrm{Fe})_{\mathrm{dust}}$ for a subset of the GRB afterglow sample. We again observe a clear detection threshold of $\log N(\mathrm{Fe})_{\mathrm{dust}}/\mathrm{cm}^{-2} > 16.2$, above which all the GRB C I absorbers are located.

We find no correlation between the metal or dust column density and the amount of neutral carbon. That is, a certain amount of metals is necessary to form dust and characterize absorbers with detected C I. However, the strength of $W_{\mathrm{r}}(\lambda 1560)$ is found to

be positively correlated only with the dust-reddening, A_V. Moreover, since the GRB C I absorbers are linked to the 2175 Å dust extinction feature and also exclusively found at high $N(\mathrm{Fe})_{\mathrm{dust}}$, they must trace both carbon- and iron-rich dust, but the dust composition is likely predominantly carbon-rich since the amount of visual extinction, A_V, and the detection probability of the 2175 Å dust extinction feature are found to be correlated with the amount of neutral carbon.

Above the detection thresholds of $\log N(\mathrm{H\,I})/\mathrm{cm}^{-2} + [\mathrm{X/H}] > 20.7$ and $\log N(\mathrm{Fe})_{\mathrm{dust}}/\mathrm{cm}^{-2} > 16.2$, two more GRBs (120815A and 121024A) are also observed with C I detected below the completeness limits. Two other bursts (GRBs 120327A and 151021A) are observed in this region as well but without C I detected in absorption down to limits of $W_{\mathrm{r}}(\lambda 1560) < 0.03$ Å and $W_{\mathrm{r}}(\lambda 1560) < 0.17$ Å, respectively. GRB 120327A has a reported detection of H_2, although with a low molecular fraction and dust extinction (D'Elia et al., 2014).

4.5 The diversity of cold gas absorbers

The presence of cold and molecular gas is regulated by the amount of dust in the ISM, that both serves to enhance the formation of molecular hydrogen onto dust grains but also lower the photo-dissociation rate by dust- and self-shielding. The detection probability of H_2 in quasar absorption systems is specifically found to be a function of metallicity and/or dust depletion (Ledoux et al., 2003; Srianand et al., 2005; Petitjean et al., 2006; Noterdaeme et al., 2008). In Fig. 4.5.1 we again plot the metallicity as a function of H I column density (similar to Fig. 4.4.3) but now we focus on various types of absorption systems in which C I or H_2 (or both) have been detected. This is to investigate the diversity of the different types of these cold gas absorbers. We include the GRB C I absorbers from this study, the quasar C I absorbers from Ledoux et al. (2015) with existing metallicities from Zou et al. (2018), and the quasar absorbers selected on the basis of the 2175 Å dust extinction feature, all showing the presence of C I, from Ma et al. (2017, 2018). For the comparison, we only include the systems with $W_{\mathrm{r}}(\lambda 1560) > 0.2$ Å from the quasar absorber samples to match our completeness limit. We also include the quasar absorbers with H_2 detections from the high-resolution VLT/UVES sample by Noterdaeme et al. (2008).

We observe a notable difference between the GRB and quasar absorber populations: quasar absorbers with C I or H_2 detected in absorption are observed at significantly lower metal column densities than that of the GRB C I absorbers. In Fig. 4.5.1 we mark the lower limit in the H I-metallicity plane for which C I and H_2 has been detected in quasar absorbers as the bottom dashed line (at $\log N(\mathrm{H\,I})/\mathrm{cm}^{-2} + [\mathrm{X/H}] \approx 19.5$). As can be seen from the figure, the cold neutral gas-phase is only observed in GRB hosts with metal column density ~ 10 times larger than typically observed for quasar absorbers selected on the basis of C I within the same completeness limit of $W_{\mathrm{r}}(\lambda 1560) > 0.2$ Å. We caution that Fig. 4.5.1 mainly demonstrates the various selections from which these cold gas absorbers have been identified. GRB sightlines are expected to probe systematically higher metal column densities than quasar absorbers and the reason for the GRB C I absorbers to not be detected at lower metal column densities could simply be related to the small sample size not properly sampling the lower end of the parameter

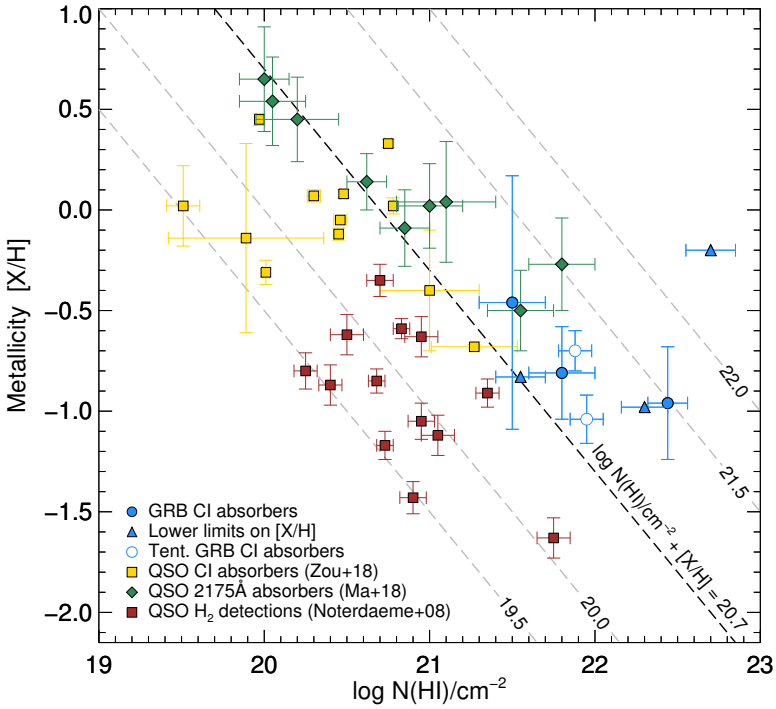

Figure 4.5.1. Comparison of the metallicity distribution as a function of H I column density for quasar and GRB absorbers with C I or H_2 detections. Blue filled circles again denote the GRBs with C I detected in absorption (empty blue circles show the GRBs with C I detected below the completeness limit). Overplotted are the quasar absorbers with H_2 detections from the VLT/UVES sample (dark red squares), quasar absorbers selected for the presence of the 2175 Å dust extinction feature (green diamonds) and quasar absorbers selected for the presence of C I absorption (yellow squares). Only systems with $W_r(\lambda 1560) > 0.2$ Å from each of the C I samples are shown. The dashed lines mark constant values of $\log N(\mathrm{H\,I})/\mathrm{cm}^{-2}$ + [X/H] as indicated at each line.

space. We emphasize, however, that the GRB afterglows observed with UVES as part of the F09 sample have $\log N(\mathrm{H\,I})/\mathrm{cm}^{-2}$ + [X/H] in the same range ($\log N(\mathrm{H\,I})/\mathrm{cm}^{-2}$ + [X/H] = 19.7 – 20.7), but show non-detections of C I (and H_2) down to similar deep limits as derived for the quasar H_2 absorbers. The non-detections in the GRB UVES sample could also be a consequence of the low sample size. However, while the general fraction of absorbers with cold gas in quasar sightlines is small (5 – 10% estimated for H_2-bearing quasar absorbers; Noterdaeme et al., 2008; Balashev et al., 2014; Balashev & Noterdaeme, 2018), the fraction increases significantly at $\log N(\mathrm{H\,I})/\mathrm{cm}^{-2}$ + [X/H] > 20 (to $\gtrsim$ 60%; Noterdaeme et al., 2015a) and it would therefore be surprising that we do not detect C I in the GRB UVES sample solely due to the small sample size. A more plausible cause for the non-detection of C I in the GRB UVES sample is that it only consists of the brightest afterglows and therefore as a consequence is biased against dusty and metal-rich GRBs (Ledoux et al., 2009).

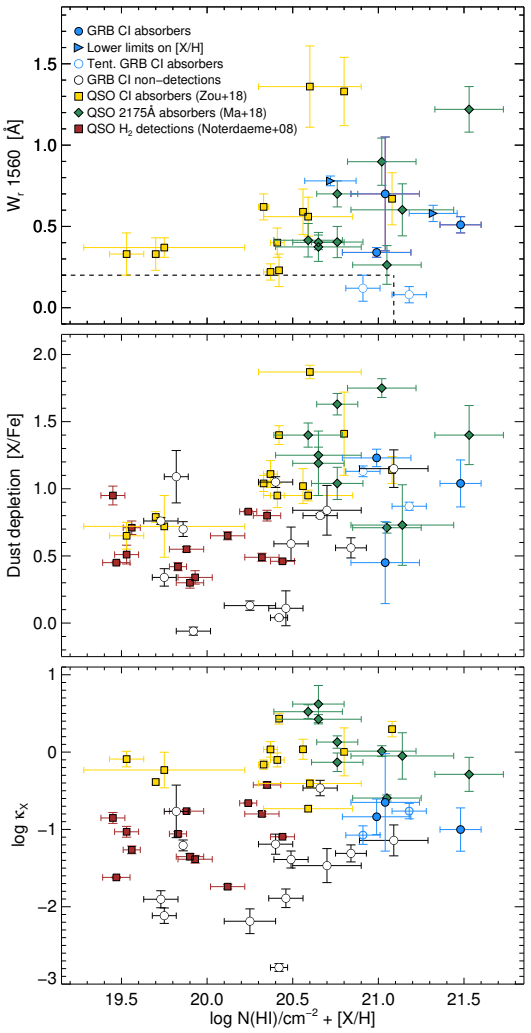

Figure 4.5.2. $\log N(\mathrm{H\,I})/\mathrm{cm}^{-2}$ + [X/H], as a function of $W_\mathrm{r}(\lambda\,1560)$ (top), dust depletion, [X/Fe], (middle) and depletion-derived dust-to-gas ratio, κ_X, (bottom) for quasar and GRB absorbers with C I or H_2 detections. The same symbols are used as in Fig. 4.5.1, but here we also include the GRB afterglows with non-detections of C I (marked by the dashed lines in the top panel and as black empty circles in the bottom panels).

The quasar absorbers selected on the basis of the 2175 Å dust extinction feature appear mostly above the same threshold of $\log N(\mathrm{H\,I})/\mathrm{cm}^{-2}$ + [X/H] > 20.7 as the GRB C I absorbers, though at higher metallicities and lower H I column densities. Among the quasar absorbers, the C I-selected systems appear to follow the same trend as the H_2-bearing absorbers, but are predominantly more metal-rich (as expected). On average, the GRB C I absorbers are the most gas-rich sightlines, with metal column densities comparable only to the quasar absorbers selected on the presence of the 2175 Å dust extinction feature.

In Fig. 4.5.2 we compare the same samples examined above but study different dust indicators as a function of the metal column density. Here, we again include the GRBs in which C I is not detected. First, we show that the metal column density is not correlated with the amount of neutral carbon represented by $W_\mathrm{r}(\lambda\,1560)$ in any of the

samples. Then, we investigate the detection probability of C I in GRB afterglows as a function of dust depletion, [X/Fe], in the middle panel of Fig. 4.5.2. This is motivated by the study of Ledoux et al. (2003), who found that the detection probability of H_2 in quasar absorbers is connected to the level of [X/Fe]. One burst, GRB 070802, with C I detected in absorption, has a modest depletion value ([X/Fe] = 0.46) and the remaining GRB C I systems have [X/Fe] > 0.7. However, there are several other GRBs without the presence of C I absorption features observed with similar high depletion values. This suggests that the presence of C I in GRB hosts is not particularly related to the amount of dust derived from the gas-phase depletion level. Following Ledoux et al. (2003), we instead examine the dependence on the dust-to-gas ratio determined from the depletion level, described as $\kappa_X = 10^{[X/H]}(1 - 10^{-[X/Fe]})$. They found that quasar H_2 absorbers were only detected at $\log\kappa_X \gtrsim -1.5$, so this quantity could be more directly related to the presence of cold and molecular gas. Contrary to the dust depletion, we find a more distinct threshold for GRB C I absorbers to appear only above a certain depletion-derived dust-to-gas ratio of $\log\kappa_X \gtrsim -1$ (see the bottom panel of Fig. 4.5.2). Only two of the GRB absorbers with non-detections of C I (GRBs 050820A and 141028A) show the same depletion-derived dust-to-gas ratios. We note from Fig. 4.5.2, that κ_X is higher on average for the quasar H_2 absorbers compared to the GRBs with non-detections of C I. This could possibly explain why cold gas is detected in these particular quasar absorbers and not in the GRB absorbers with comparable metal column densities.

We therefore argue that the detection threshold of C I is primarily a function of the metal and dust column density. The fact that the cold neutral gas-phase in GRB hosts is only observed at metal and dust column densities more than an order of magnitude larger than for typical quasar absorbers is likely due to how these two absorber populations are selected. However, it could also be evidence of denser environments or more intense UV fields in the ISM of the star-forming GRB host galaxies (as speculated; Tumlinson et al., 2007; Whalen et al., 2008). Finally, we note from Fig. 4.5.1 that C I or H_2-bearing quasar absorbers with high metal column densities are scarse. This deficit is likely not physical, however, but instead related to selection bias in quasar samples, systematically evading foreground absorbers rich in metals, dust and molecules (Krogager et al., 2016a; Fynbo et al., 2017; Heintz et al., 2018a). Such a bias might also exist to a lesser extent in GRB afterglow samples. This bias will not affect the results of this paper, however, only underestimate the underlying population of GRB C I absorbers.

4.6 Conclusions

In this work we presented a survey for neutral atomic-carbon (C I) in a sample of 29 medium- to high-resolution GRB afterglow spectra. We detected the absorption features of the C I $\lambda\lambda$ 1560,1656 line transitions in seven bursts ($\approx 25\%$) in our statistical sample at redshifts ranging from $1 < z < 4$. These GRB C I absorbers probe the shielded cold, neutral gas-phase of the ISM in their host galaxies and previous studies found the detection of C I to be directly linked to the presence of molecular hydrogen (Srianand et al., 2005; Noterdaeme et al., 2018).

Our goals were to characterize the dust properties (such as the amount of extinction and the strength of the 2175 Å dust extinction feature) and the chemical abundances

of these GRB C I absorbers. We found that the amount of neutral carbon is positively correlated with the visual extinction, A_V, and the strength of the 2175 Å dust extinction feature (as also observed for quasar C I absorbers; Ledoux et al., 2015; Ma et al., 2018). These relations support a scenario where it is predominantly carbonaceous dust grains that produce the characteristic bump (Henning & Salama, 1998; Draine, 2003). The average dust-to-gas ratio of the GRB C I absorbers was found to be significantly smaller than observed for quasar C I absorbers and in typical Milky Way sightlines, with a median value of $A_V/N(\mathrm{H\,I}) = 7.92 \times 10^{-23}$ mag cm^{-2}. We showed that C I is only observed in GRB host absorption systems above a certain threshold of $\log N(\mathrm{H\,I})/\mathrm{cm}^{-2}$ + [X/H] and dust-phase iron column densities of $\log N(\mathrm{Fe})_{\mathrm{dust}}/\mathrm{cm}^{-2} > 16.2$. The connection of the GRB C I systems to the 2175 Å dust extinction feature and the large values of $N(\mathrm{Fe})_{\mathrm{dust}}$ indicate that the C I absorbers trace dusty systems with a dust composition that both consist of carbon- and iron-rich dust grains, but is dominated by the carbon-rich dust.

The fact that the metal and dust column densities of the GRB C I absorbers are higher than observed for C I- and H_2-bearing quasar absorbers is primarily a consequence of how these two absorber populations are selected, but is also consistent with a scenario where GRB hosts have more intense galactic UV fields than the galaxy counterparts of the quasar absorbers. We also investigated the detection probability of C I as a function of other dust tracers such as the gas-phase depletion, [X/Fe], and the depletion-derived dust-to-gas ratio, κ_{X}. We found that the metal and dust column densities are the primary driver for the presence of C I in GRB hosts, although the amount of neutral carbon is not correlated with either. Instead, the amount of neutral carbon is positively correlated with the visual extinction, A_V, but is detected down to relatively small visual extinctions of $A_V \approx 0.1$ mag.

We argue that C I has a number of advantages as a tracer of the cold neutral medium in GRB hosts due to the observational limitations of identifying H_2 absorption features in the majority of GRB afterglow spectra. A more detailed analysis of the relations between H_2, C I and CO column densities in GRB absorbers is needed to better constrain the physical properties of the cold gas. Follow-up observations of the host galaxies of the GRB C I absorbers identified here at millimetre wavelengths with e.g. ALMA would also be interesting to pursue in the future.

Acknowledgements

We would like to thank the referee for a clear, constructive and concise report that greatly improved the presentation of the results from this work. We also wish to thank the large European GRB collaboration and the dedicated ToO advocates staying on alert at all times, day and night. Without the swift reaction of this team, such a large number of good quality GRB afterglow spectra would never have been gathered. KEH and PJ acknowledge support by a Project Grant (162948–051) from The Icelandic Research Fund. The Cosmic Dawn Center is funded by the DNRF. JK and PN acknowledge funding from the French *Agence Nationale de la Recherche* under grant no ANR-17-CE31-0011-01. SDV acknowledges the support of the French National Research Agency (ANR) under contract ANR-16-CE31-0003. JJ acknowledges support from NOVA and NWO-FAPESP grant for advanced instrumentation in astronomy.

Chapter 5

Dust in the molecular gas-phase of the ISM

This chapter is based on the following article:

On the dust properties of high-redshift molecular clouds and the connection to the 2175 Å extinction bump

Published in Monthly Notices of the Royal Astronomical Society, vol. 486, issue 2, 12 pp. (2019)

Authors:
K. E. Heintz, T. Zafar, A. De Cia, S. D. Vergani, P. Jakobsson, J. P. U. Fynbo, D. Watson, J. Japelj, P. Møller, S. Covino, L. Kaper & A. C. Andersen

We present a study of the extinction and depletion-derived dust properties of gamma-ray burst (GRB) absorbers at $1 < z < 3$ showing the presence of neutral carbon (C I). By modelling their parametric extinction laws, we discover a broad range of dust models characterizing the GRB C I absorption systems. In addition to the already well-established correlation between the amount of C I and visual extinction, A_V, we also observe a correlation with the total-to-selective reddening, R_V. All three quantities are also found to be connected to the presence and strength of the 2175 Å dust extinction feature. While the amount of C I is found to be correlated with the SED-derived dust properties, we do not find any evidence for a connection with the depletion-derived dust content as measured from [Zn/Fe] and $N(\mathrm{Fe})_{\mathrm{dust}}$. To reconcile this, we discuss a scenario where the observed extinction is dominated by the composition of dust particles confined in the molecular gas-phase of the ISM. We argue that since the depletion level trace non-carbonaceous dust in the ISM, the observed extinction in GRB C I absorbers

is primarily produced by carbon-rich dust in the molecular cloud and is therefore only observable in the extinction curves and not in the depletion patterns. This also indicates that the 2175 Å dust extinction feature is caused by dust and molecules in the cold and molecular gas-phase. This scenario provides a possible resolution to the discrepancy between the depletion- and SED-derived amounts of dust in high-z absorbers.

5.1 Introduction

One of the key constituents of galaxy formation and chemical evolution is the interplay and connection between dust, gas and metals in the interstellar medium (ISM). Since stars form in molecular clouds, identifying the cold neutral gas-phase in the ISM of galaxies in the early Universe will provide imperative clues to the onset of star formation. A powerful probe of the ISM in high-redshift galaxies are damped Lyman-α absorbers (DLAs), which can be observed toward background quasars (Wolfe et al., 2005) or in gamma-ray burst (GRB) host galaxies (Jakobsson et al., 2006b; Fynbo et al., 2009).

Detailed information of the gas, metal and dust content of DLAs can be derived from absorption-line analyses or from the extinguished spectral energy distribution (SED). The optical afterglows of GRBs provide a unique tool to study the absolute extinction curves of their host galaxies because of their simple power-law spectra (e.g. Schady et al., 2010; Greiner et al., 2011; Zafar et al., 2011a; Covino et al., 2013), which is more difficult to constrain in quasar sightlines due to the more unknown variation in the underlying spectrum (but see e.g. Vladilo et al., 2006; Jiang et al., 2011; Ledoux et al., 2015; Krogager et al., 2016a; Noterdaeme et al., 2017; Fynbo et al., 2017; Heintz et al., 2018a). In addition, the extinction curves provide information about the dust content, composition and grain size distribution compared to the attenuation of the GRB host (which can be studied in emission after the afterglow has faded, e.g. Corre et al., 2018), since the latter effect is a combination of reprocessed photons, dust-star geometry and radiative transfer effects (Narayanan et al., 2018).

An alternative tracer of dust is the depletion of refractory elements such as silicon and iron from the gas-phase of the ISM (Savaglio et al., 2003; Jenkins, 2009; De Cia et al., 2016). It is expected that the amount of dust derived from the SED, typically represented as the visual extinction, A_V, should then scale with the elements in the dust-phase (Vladilo et al., 2006; De Cia et al., 2013). However, there appears to be a discrepancy between the SED- and depletion-derived dust properties of GRB host absorption systems (Savaglio & Fall, 2004; D'Elia et al., 2014; Wiseman et al., 2017). This inconsistency might be due to the fact that iron (typically used to represent the dust-phase and argued to be the most reliable depletion measure; De Cia et al., 2018) does not trace most of the dust mass that will otherwise impact the inferred extinction (Zafar & Watson, 2013; Dwek, 2016). Another possibility is that the SED-derived visual extinction is underestimated if the typical grain size distribution is large, resulting in grey extinction (Savaglio et al., 2003). We note though that Bolmer et al. (2018) found that this tension is relieved at $z \gtrsim 4$, at least in H_2-bearing GRB absorbers, and that Zafar & Møller (2019) showed that A_V is related to the total column density of refractory elements.

The cause of this putative discrepancy between the dust content inferred from the

Table 5.1.1. GRB C I absorber sample. C I $\lambda\lambda$ 1560,1656 rest-frame equivalent widths are from Paper I.

GRB	$z_{\rm GRB}$	$W_{\rm r}(\lambda 1560)$ (Å)	$W_{\rm r}(\lambda 1656)$ (Å)
061121	1.3145	0.49 ± 0.04	0.25 ± 0.04
070802	2.4511	0.70 ± 0.35	1.36 ± 0.32
080605	1.6403	0.64 ± 0.23	0.38 ± 0.15
080607	3.0368	2.17 ± 0.08	2.03 ± 0.04
120119A	1.7288	0.51 ± 0.05	0.77 ± 0.06
120815A	2.3581	0.12 ± 0.08	0.21 ± 0.05
121024A	2.3024	0.08 ± 0.05	0.11 ± 0.07
150403A	2.0571	0.34 ± 0.03	0.50 ± 0.04
180325A	2.2486	0.58 ± 0.05	0.85 ± 0.05

extinguished afterglow SED and the gas-phase depletion levels, might also be related to a too simplistic view of the location of the dust. Recent studies of GRB and quasar absorbers have for instance found that the visual extinction, A_V, and the strength of the 2175 Å extinction bump feature is correlated with the amount of neutral atomic-carbon (C I; Zafar et al., 2012; Ledoux et al., 2015; Ma et al., 2018; Heintz et al., 2019a). Absorption features from C I are often found to be coincident with H_2 (Srianand et al., 2005; Jorgenson et al., 2010; Noterdaeme et al., 2018) and is therefore believed to be a good tracer of the cold and molecular gas-phase of the ISM. These relations indicate that C I traces dust-rich systems and that the amount of cold, shielded gas and dust are connected.

Carbonaceous material could produce the rare 2175 Å bump (Stecher & Donn, 1965; Weingartner & Draine, 2001), since carbonaceous grain growth requires neutral atomic-carbon and molecules in the ISM (Henning & Salama, 1998). The 2175 Å dust extinction feature is ubiquitously observed locally in the MW (Fitzpatrick & Massa, 2007) and in the LMC (Gordon et al., 2003), but is mostly elusive in the SMC and in extragalactic sightlines (Gordon et al., 2003; Noll et al., 2009; Zafar et al., 2012; Zeimann et al., 2015; Ledoux et al., 2015; Ma et al., 2018). The strength and width of the characteristic feature vary with the surrounding environment but its central wavelength have been found to remain invariant (Fitzpatrick & Massa, 1986, 2007). Early studies have suggested that graphite or polycyclic aromatic hydrocarbons (PAHs) are responsible for the 2175 Å dust extinction feature (Stecher & Donn, 1965; Draine & Lee, 1984; Léger et al., 1989; Blanco et al., 1996; Li & Greenberg, 1997; Henning & Salama, 1998; Weingartner & Draine, 2001; Draine, 2003). More recently, Mishra & Li (2017) reported that the strength of the 2175 Å dust extinction feature is related to the amount of carbon in the dust-phase for a sample of 46 Galactic sightlines, further supporting carbonaceous dust grains as the carriers producing the 2175 Å dust bump.

In this paper, we study a sample of C I absorbers identified by Heintz et al. (2019a, hereafter Paper I) in GRB sightlines, with the aim of investigating the mineralogy, dust composition and grain size distribution of the cold and molecular gas-phase in these high-

z absorbers. Here, for the first time, we attempt to distinguish the different contributions of various elements that could be the carrier of the 2175 Å dust bump and affect the shape of the extinction curve at high redshifts. This sample of GRB C I absorbers has the advantage that for example the total-to-selective reddening parameter, R_V, can be well constrained compared to similar systems in quasar sightlines. Spectroscopy of the optical afterglows of the GRBs in this sample (at a redshift range of $1 < z < 3$) thus provides a unique way to study the dust content of molecular clouds in star-forming galaxies at the peak of cosmic star formation. We have acquired elementel abundances and derived extinction curves for each of the GRB C I absorbers entering our sample, and combined with previous literature measurements we examine the distinct dust-phase of this unique sample of GRB C I absorbers.

We have structured the paper as follows. In Sect. 5.2, we present the GRB C I absorber sample, including their basic individual properties such as redshift, gas-phase abundances and C I content. In Sect. 5.3, we describe our approach of computing the dust extinction laws and we provide our results in Sect. 5.4. We discuss a specific scenario on the location of the dust in the sightline to the GRB C I absorbers in Sect. 5.5, and conclude on our work in Sect. 5.6. Throughout the paper, errors denote the 1σ confidence level. We assume a standard flat cosmology with $H_0 = 67.8\,\mathrm{km\,s^{-1}\,Mpc^{-1}}$, $\Omega_m = 0.308$ and $\Omega_\Lambda = 0.692$ (Planck Collaboration et al., 2016). Gas-phase abundances are expressed relative to the Solar abundance values from Asplund et al. (2009), where $[\mathrm{X/Y}] = \log N(\mathrm{X})/N(\mathrm{Y}) - \log N(\mathrm{X})_\odot/N(\mathrm{Y})_\odot$, following the recommendations of Lodders et al. (2009) on whether to use the photospheric or meteoritic values (or their average).

5.2 Sample

The identification of GRB C I absorbers in Paper I was based on bursts observed as part of the GRB afterglow sample by Fynbo et al. (2009) and the VLT/X-shooter GRB (XS-GRB) afterglow legacy survey (Selsing et al., 2019). Neutral atomic-carbon was detected in ten GRB optical afterglow spectra obtained with low- to medium-resolution spectrograhps ($\mathcal{R} = 1000 - 10\,000$). The detection rate was found to be $\approx 25\%$ in the full statistical sample of GRBs compiled in Paper I at a completeness limit of $W_\mathrm{r}(\lambda 1560) = 0.2$ Å. An overview of the GRBs with C I identified in absorption is provided in Table 5.1.1, also including those bursts not entering the statistical sample from Paper I. The only C I-bearing GRB absorber from Paper I not included in this work is GRB 060210. This burst was excluded from our analysis because the X-ray spectrum from the *Swift*/XRT appears to be affected by X-ray flaring at the time when the optical spectrum was obtained. It is therefore not possible to constrain the intrinsic slope of the SED of this GRB, required to quantify the dust-extinction model. We note that Curran et al. (2007) also find an offset between the X-ray and optical slopes based on their R- and I-band photometric data.

For all the nine GRB C I systems studied here, we provide the gas-phase abundances of H I, Zn II, Si II, and Fe II in Table 5.2.1, where available from the literature. In the Appendix, an individual note on each GRB is given with references to where the literature values were obtained from. Based on the gas-phase abundances, we also list the derived metallicity, [Zn/H], the dust depletion, [Zn/Fe], and the dust-phase

Table 5.2.1. Gas-phase abundances of the GRB C I absorbers. References for the individual bursts and gas-phase abundances are given in the Appendix under the dedicated notes on each GRB.

GRB	$\log N$(H I) (cm^{-2})	$\log N$(Zn II) (cm^{-2})	$\log N$(Si II) (cm^{-2})	$\log N$(Fe II) (cm^{-2})	[Zn/H]	[Zn/Fe]	$\log N(\mathrm{Fe})_{\mathrm{dust}}$ (cm^{-2})	$\log N(\mathrm{Si})_{\mathrm{dust}}$ (cm^{-2})
061121	⋯	13.76 ± 0.06	⋯	16.20 ± 0.03	⋯	0.51 ± 0.07	16.55 ± 0.06	⋯
070802	21.50 ± 0.20	13.60 ± 0.60	⋯	16.10 ± 0.10	-0.46 ± 0.63	0.45 ± 0.61	16.36 ± 0.41	⋯
080605	⋯	13.53 ± 0.08	15.88 ± 0.10	14.66 ± 0.11	⋯	1.82 ± 0.14	16.47 ± 0.08	16.34 ± 0.09
080607	22.70 ± 0.15	> 13.56	> 16.21	> 16.48	> -0.20*	⋯	⋯	⋯
120119A	22.44 ± 0.12	14.04 ± 0.25	16.67 ± 0.35	15.95 ± 0.25	-0.96 ± 0.28	1.04 ± 0.35	16.95 ± 0.30	16.69 ± 0.32
120815A	21.95 ± 0.10	13.47 ± 0.06	16.34 ± 0.16	15.29 ± 0.05	-1.04 ± 0.12	1.13 ± 0.08	16.39 ± 0.06	15.58 ± 0.51
121024A	21.88 ± 0.10	13.74 ± 0.03	> 16.35	15.82 ± 0.05	-0.70 ± 0.10	0.87 ± 0.06	16.63 ± 0.03	> 16.44
150403A	21.73 ± 0.02	13.32 ± 0.04	> 15.80	15.54 ± 0.07	-1.04 ± 0.04	0.63 ± 0.08	16.15 ± 0.05	> 16.09
180325A	22.30 ± 0.14	> 14.09	> 16.12	> 16.68	> -0.77	⋯	⋯	⋯

Notes. *This value represents the lower limit on [O/H] measured from the equivalent width of O I λ 1355, following Prochaska et al. (2009).

iron and silicon column density, $N(\mathrm{Fe})_{\mathrm{dust}}$ and $N(\mathrm{Si})_{\mathrm{dust}}$, for each GRB where possible. The actual metallicity of the C I systems are likely higher than reported here since Zn also depletes (although mildly) on dust grains. The dust-corrected metallicity can be computed as [M/H] = [Zn/H] + δ_{Zn}, where δ_{Zn} is given by the level of depletion, assuming some empirically derived depletion sequence coefficients for Zn (e.g. De Cia et al., 2016). We will in the further analysis, however, only study [Zn/H] since it is a directly measured quantity, but note that the actual metallicity could be higher. Dust depletion patterns are gaining more prevalence as a universal measure of the dust content in the ISM of different environments (from the Milky Way to high-redshift DLAs) and specifically the relative abundance ratio of zinc to iron, [Zn/Fe], is found to be an ideal tracer of dust in the ISM (De Cia et al., 2018). The dust-phase iron column density, $N(\mathrm{Fe})_{\mathrm{dust}}$, is in most cases also found to be correlated with the visual extinction, A_V, derived from the SED of the optical to X-ray afterglow spectra (Vladilo et al., 2006; De Cia et al., 2013), further supporting the use of depletion patterns as a tracer of dust in the ISM.

In Paper I, we found that C I was exclusively identified in GRB host absorption systems with large metal column densities ($\log N(\mathrm{X}) = \log N(\mathrm{H\,I}) + [\mathrm{X/H}] > 20.7$), dust-phase iron column densities of $\log N(\mathrm{Fe})_{\mathrm{dust}} \gtrsim 16.2$ and constitutes the most dust-reddened population of GRBs at all redshifts. This is not unexpected, since a large metal and dust content is required to shield the neutral gas from the ambient galactic UV field. From Table 5.2.1 we find that the neutral hydrogen column density ranges from $\log N(\mathrm{H\,I}) = 21.5 - 22.7$ and that the GRB C I absorbers have abundances between one-tenth of solar to solar values. We refer the reader to Paper I for a detailed discussion of the metal content of the GRB C I systems, where we also compared them to C I-bearing quasar absorbers. Here we focus on the SED-derived dust properties of the systems, which we derive for each individual burst (combined with literature measurements), and investigate how this relates to the depletion-derived dust properties in this type of cold gas absorbers. While this can in principle also be studied in quasar absorbers, it is typically much easier to constrain the specific dust-extinction models in sightlines to GRBs since their intrinsic spectra are simple, smooth power-laws.

5.3 SED analysis

To model the parametric extinction laws of each of the individual GRBs in our sample, we follow the same procedure as Zafar et al. (2018b). We refer to their work for the explicit details of the fitting procedure, and only briefly summarize the methodology below. Zafar et al. (2018b,a) already determined the extinction curve parameters for the GRBs 120119A, 120815A, 121024A, and 180325A entering our sample, so here we provide only the best fits for GRBs 061121, 070802, 080605, 080607, and 150403A, using the same dust model for consistency.

The intrinsic GRB afterglow spectrum is believed to be emitted as synchrotron radiation from the interaction of the ultra-relativistic jet and the ISM. As a consequence, the intrinsic SED of the afterglow is expected to follow a power-law with $F_\nu = \nu^{-\beta}$. In some cases, a change in the spectral slope of $\Delta\beta = 0.5$ between the optical and X-ray spectra is observed (Zafar et al., 2011a; Greiner et al., 2011), known as the cooling break (Sari et al., 1998). The observed, dust extinguished spectrum can therefore be modeled as $F_\nu^{\rm obs} = F_\nu\, 10^{-0.4 A_\lambda}$, where A_λ is the extinction due to dust absorption and scattering as a function of wavelength.

We used the spectral fitting package `XSPEC v. 12.9` to fit the rest-frame optical to near-infrared SEDs of the GRB afterglows, assuming a single or broken power-law together with the parametric dust model from Fitzpatrick & Massa (1990, hereafter F&M 90). In systems where a broken power-law is preferred, a cooling break ($\nu_{\rm break}$) is required between the intrinsic spectral optical ($\beta_{\rm opt}$) and X-ray ($\beta_{\rm X}$) slopes and were fitted such that the change in slope is fixed to $\Delta\beta = 0.5$. The X-ray data are taken from the *Swift* archive facility (Evans et al., 2009) and for each case the spectrum in the 0.3 – 10 keV range is reduced around the SED mid-time with in `XSELECT`. We then fix the total Galactic equivalent hydrogen column density, $N_{\rm H,Gal}$, for the X-ray spectra to the values from Willingale et al. (2013) but leave the rest-frame GRB host galaxy equivalent hydrogen column density, $N_{\rm H,X}$, as a free parameter. The F&M 90 dust model allows the individual extinction curves to be fit through a set of eight parameters and is defined as

$$A_\lambda = \frac{A_V}{R_V}\left(c_1 + c_2 x + c_3 D(x, x_0, \gamma) + c_4 F(x) + 1\right), \tag{5.1}$$

where

$$D(x, x_0, \gamma) = \frac{x^2}{(x^2 - x_0^2)^2 + x^2\gamma^2} \tag{5.2}$$

and

$$F(x) = \begin{cases} 0.539(x-5.9)^2 + 0.056(x-5.9)^3 & \text{for } x \geq 5.9 \\ 0 & \text{for } x < 5.9 \end{cases}, \tag{5.3}$$

with $x = \lambda^{-1}$ in units of $\mu{\rm m}^{-1}$. Basically, this dust model contains two components, one describing the linear UV part of the spectrum via the components c_1 (intercept), c_2 (slope) and the term $c_4 F(x)$ describing the far-UV curvature. The second component is the Drude profile representing the 2175 Å extinction bump, controlled by the parameters c_3 (bump strength), x_0 (central wavelength) and γ (width of the bump). The last two parameters are the visual extinction, A_V, and the total-to-selective reddening, R_V. For the systems where the 2175 Å extinction bump is not detected, we fix the Drude components

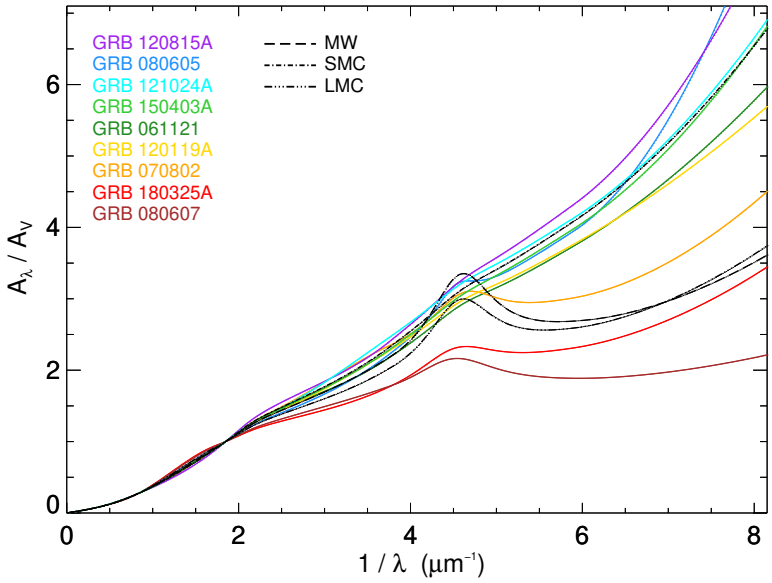

Figure 5.4.1. Individual extinction curves of the GRB C I absorbers. Each curve has been color-coded as a function of the total-to-selective extinction, R_V, violet representing a dust grain size distribution composed of small grains and red a dust composition with predominantly larger dust grain sizes. The 2175 Å dust extinction feature appears to be more prominent for larger values of R_V. For comparison, the average extinction curves observed in the MW, SMC, and LMC are also shown.

to $\gamma = 1\,\mu\mathrm{m}^{-1}$ and $x_0 = 4.6\,\mu\mathrm{m}^{-1}$ but leave c_3 as a free parameter (even though Zafar et al., 2015, 2018b, found that fixing $c_3 = 0$ reduces the χ^2). We compute the 3σ upper limits on the bump strength instead, given by c_3, to compare to the GRBs where the 2175 Å extinction bump is clearly detected.

5.4 Results

Overall, we find a broad range of distinct dust models characterizing the GRB C I absorbers. The individual best fit extinction curves are shown in Fig. 5.4.1. In Table 5.4.1 we list the set of best fit parameters for the F&M 90 dust model for the GRBs 061121, 070802, 080605, 080607, and 150403A determined in this work, including previously published values for GRBs 120119A, 120815A, 121024A, and 180325A from Zafar et al. (2018b,a). The equivalent hydrogen column density, $N_{\mathrm{H,X}}$, together with the reduced χ^2, the number of degrees of freedom (dof), the null hypothesis probability (NHP) for the best fit, and the F-test probability (to determine preference over single or broken power-laws) is given in the Appendix for each of the GRBs examined in this work. The broken power-law model is considered a better fit for the cases where the F-test probability is smaller than 5% (see also Zafar et al., 2018b,c).

In our sample, four out of nine cases ($\approx 45\%$) show a prominent 2175 Å dust

Table 5.4.1. The best fit F&M 90 extinction curve parameters for the X-ray to the optical/near-infrared afterglow SEDs of the GRB C I absorbers. The best fit curve coefficients are from [a]Zafar et al. (2018b), [b]Zafar et al. (2018a) or derived in this work.

GRB	c_1	c_2	c_3	c_4	γ	x_0 (λ^{-1})	R_V	A_V (mag)	$A_{\rm bump}$ (mag)
061121	-4.63 ± 0.13	2.11 ± 0.11	< 0.46	0.34 ± 0.12	1.00	4.60	$2.88^{+0.23}_{-0.27}$	$0.46^{+0.11}_{-0.15}$	< 0.16
070802	0.03 ± 0.23	0.88 ± 0.17	1.56 ± 0.27	0.45 ± 0.09	0.99 ± 0.01	4.63 ± 0.01	$2.72^{+0.61}_{-0.54}$	$1.20^{+0.15}_{-0.15}$	1.09 ± 0.34
080605	-6.12 ± 0.84	2.66 ± 0.39	0.46 ± 0.11	1.84 ± 0.50	0.60 ± 0.08	4.53 ± 0.01	$3.27^{+0.88}_{-0.92}$	$0.48^{+0.13}_{-0.11}$	0.18 ± 0.08
080607	1.14 ± 0.34	0.36 ± 0.11	3.05 ± 0.72	0.17 ± 0.05	1.22 ± 0.05	4.51 ± 0.02	$4.14^{+1.05}_{-1.09}$	$2.58^{+0.42}_{-0.45}$	2.45 ± 0.97
120119A[a]	-4.13 ± 0.08	2.09 ± 0.07	< 0.43	0.22 ± 0.10	1.00	4.60	$2.99^{+0.24}_{-0.18}$	$1.02^{+0.11}_{-0.11}$	< 0.26
120815A[a]	-4.77 ± 0.08	2.14 ± 0.07	< 0.32	0.82 ± 0.08	1.00	4.60	$2.38^{+0.09}_{-0.09}$	$0.19^{+0.04}_{-0.04}$	< 0.05
121024A[a]	-4.23 ± 0.06	2.20 ± 0.08	< 0.35	0.57 ± 0.05	1.00	4.60	$2.81^{+0.20}_{-0.16}$	$0.26^{+0.07}_{-0.07}$	< 0.06
150403A	-4.83 ± 0.08	2.23 ± 0.05	< 0.35	0.59 ± 0.02	1.00	4.60	< 2.81	< 0.13	< 0.03
180325A[b]	-1.95 ± 0.39	1.28 ± 0.17	2.92 ± 0.19	0.52 ± 0.19	1.16 ± 0.06	4.54 ± 0.03	$4.58^{+0.37}_{-0.39}$	$1.58^{+0.10}_{-0.12}$	1.36 ± 0.19

Notes. The strength of the 2175 Å extinction bump is calculated as $A_{\rm bump} = \pi c_3/(2\gamma R_V) \times A_V$. The reduced χ^2, the number of degrees of freedom (dof), the null hypothesis probability (NHP) for the best fit, and the F-test probability is given in the Appendix for each individual GRB.

extinction feature (GRBs 070802, 080605, 080607, and 180325A). Six systems ($\approx 65\%$) show relatively steep extinction curves with $R_V = 2.4 - 3.0$ (GRBs 061121, 070802, 120119A, 120815A, 121024A, and 150403A), where the other three systems ($\approx 35\%$) show more "flat" extinction curves with $R_V = 3.3 - 4.5$ (i.e. GRBs 080605, 080607, and 180325A). We also measure a large variation in bump strength between the individual systems, in the range $A_{\rm bump} = 0.2 - 2.5$ mag.

In general, we find that the amount of C I is connected to the dust properties inferred from the extinguished SED, such as A_V, R_V and $A_{\rm bump}$. To quantify this we show pairwise scatter plots and histograms of different dust tracers color-coded as a function of $W_{\rm r}(\lambda 1560)$ in Fig. 5.4.2. Due to the small sample size and relatively large error bars, the observed trends are only found to be correlated at $1 - 2\sigma$ significance. The connection of A_V and $A_{\rm bump}$ with C I is already well-established for quasar (Ledoux et al., 2015; Ma et al., 2018) and GRB (Zafar et al., 2012; Heintz et al., 2019a) absorption systems, but here we include the additional information derived from the slope of the extinction, as inferred from R_V. The observed trend between A_V and $W_{\rm r}(\lambda 1560)$ indicates that larger amounts of cold gas is found in more dusty sightlines, where the additional trend with R_V also suggests that the dust grain size distribution are on average larger in these sightlines as well. Contrary to this, we observe no relation between A_V, R_V or the amount of C I to the typically used depletion-derived dust tracers such as the zinc-to-iron depletion level, [Zn/Fe], and the dust-phase iron column density, $N({\rm Fe})_{\rm dust}$ (see also Paper I).

We caution that since it is not possible to infer the depletion of the two strongest C I absorbers (GRBs 080607 and 180325A), the apparent non-correlation between the amount of C I to [Zn/Fe] and $N({\rm Fe})_{\rm dust}$ might be biased. However, even without those systems we are still probing a large range of depletion values (i.e. [Zn/Fe] = 0.5 – 2), without seeing any trends with either A_V, R_V, $A_{\rm bump}$, or $W_{\rm r}(\lambda 1560)$. Also, for the bursts

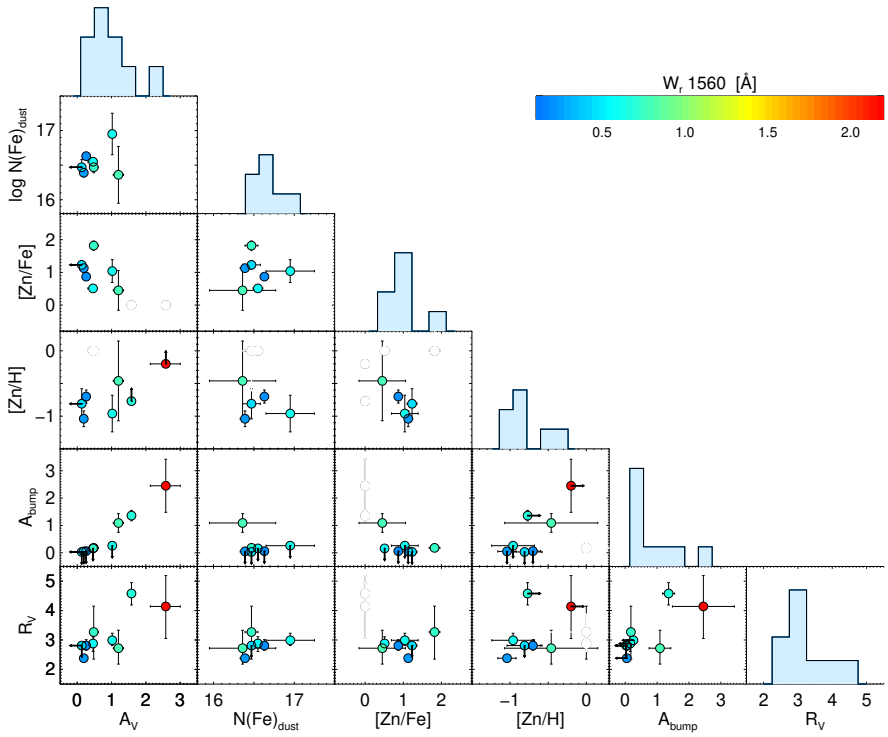

Figure 5.4.2. Pairwise scatter plots showing a comparison of different dust tracers, color-coded as a function of the rest-frame equivalent width of C I λ 1560. The SED-derived dust properties, i.e. A_V, R_V and $A_{\rm bump}$ are compared to the commonly used depletion-derived dust tracers, the zinc-to-iron depletion, [Zn/Fe], and the dust-phase iron column density, $N(\mathrm{Fe})_{\rm dust}$. Positive trends with C I are mainly observed for the SED-derived dust properties but also tentatively for the metallicity, [Zn/H] (see main text). For GRB 080607 we show the estimated lower limit on the [O/H]-derived metallicity instead of [Zn/H], as also listed in Table 5.2.1.

where the depletion could be derived, the GRB showing the strongest extinction bump (GRB 070802) shows the lowest value of [Zn/Fe] and $N(\mathrm{Fe})_{\rm dust}$. Finally, if we assume that e.g. GRB 080607 has solar metallicity (Prochaska et al., 2009), then the depletion of the system would be around [Zn/Fe] $\sim$ 1.1 following the relation from Ledoux et al. (2003), which would still not produce any trend with A_V, R_V, $A_{\rm bump}$, or $W_{\rm r}(\lambda 1560)$. We therefore argue that, even based on the small sample size, the amount of C I and SED-derived dust properties is unlikely to be connected to the depletion-derived dust content for these particular absorbers. In the following section we will attempt to provide a resolution to this apparent discrepancy.

5.5 Discussion

5.5.1 The presence of carbon-rich dust in molecular clouds

The previously observed trend between A_V and the amount of C I indicates that whenever the GRB sightline intersects a molecular cloud, the amount of cold gas (C I in this case) is connected to the amount of dust derived from the extinction. Including the additional trend with R_V observed in this work, it is clear that the average grain size distribution of the dust particles in the molecular cloud are also related to these properties. This would suggest that the C I systems are dust-rich with a composition dominated by carbonaceous material (as already speculated in Paper I), that the dust grain size distribution mainly consists of large dust grains, and that this carbon-rich dust dominates the shape of the extinguished SED. Here we argue for a simple scenario to explain these relations: The amount of C I simply reflects how deep into the intervening molecular cloud the GRB sightline probes, where we expect larger dust columns, dust grains and higher C I column densities to be present closer to the centre of the cloud (Bolatto et al., 2013). Below we will outline some of the key points that support this scenario.

First, we argue that when cold and molecular gas is detected in GRB sightlines (i.e. from absorption features of C I and/or H_2) it is not related to the molecular gas associated with the GRB progenitor star. It has been found that the intense γ-ray flash, the afterglow emission or UV photons from the natal H II region of the GRB will destroy dust and photo-dissociate H_2 (and therefore also ionize C I) out to $\approx 10-100$ pc (Waxman & Draine, 2000; Fruchter et al., 2001; Draine & Hao, 2002; Perna et al., 2003; Whalen et al., 2008). In addition, Ledoux et al. (2009) showed that photo-dissociation is effective out to distances of ≈ 500 pc from the GRB explosion site in the case of GRB 050730. Since the physical sizes of dense, molecular gas clouds are often found to be small ($l = 0.1-1$ pc, e.g. Balashev et al., 2011; Krogager et al., 2016a), any neutral and molecular gas in the vicinity of the GRB is likely completely ionized or photo-dissociated by the burst itself. Some molecular gas could be detected from the far end of giant molecular clouds though, if these are intersecting typical GRB sightlines. Moreover, the bulk of the absorbing material in GRB hosts is typically found to be located at distances $0.5-2$ kpc (Vreeswijk et al., 2007; Ledoux et al., 2009; D'Elia et al., 2009b,a) from the explosion site. For instance, Prochaska et al. (2009) inferred at minimum distance of $d \gtrsim 100$ pc of the molecular cloud observed towards GRB 080607 based on the presence of Mg I and C I. Any intervening molecular cloud does therefore likely not belong to the molecular gas associated with the GRB progenitor star but is located further away ($0.5-2$ kpc) in the line-of-sight to the burst. Bolmer et al. (2019) reached a similar conclusion and argued that this scenario could also explain why the strongest H_2-bearing GRB and quasar absorbers are more dust-depleted due to increased dust production and shielding in these systems, compared to the general observed trend between dust depletion and metal column density.

In this scenario, A_V will as a consequence primarily trace dust located in the molecular gas-phase of the intervening absorber. Alternatively, more massive galaxies with on average larger dust columns along the sightline through the ISM (Krühler et al., 2011; Perley et al., 2013; Zafar et al., 2018c; Corre et al., 2018), could contain larger amounts of C I due to more efficient shielding throughout the ISM. However, a

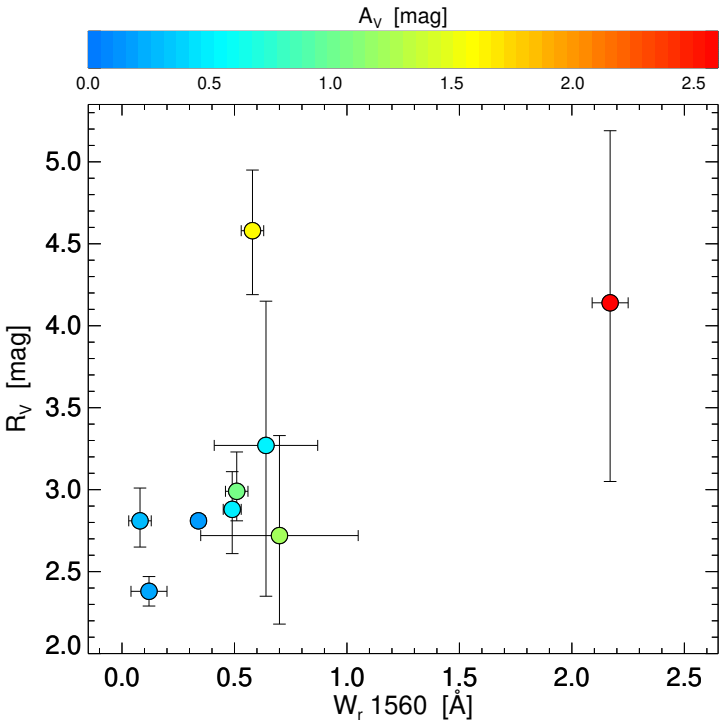

Figure 5.5.1. The total-to-selective extinction, R_V, as a function of the rest-frame equivalent width of C I λ 1560. The filled circles represent the GRB C I absorbers from Paper I studied in this work, color-coded as a function of the visual extinction, A_V. Increasingly dense environments expected for large amounts of C I appears to be sensitive to the variation in the grain-size distribution and the total amount of dust.

massive galaxy with an associated dust-rich ISM would not necessarily contain larger dust grains (i.e. larger R_V). Indeed, no such correlation is observed in the Small and Large Magellanic Clouds (SMC and LMC), the Milky Way (MW; Gordon et al., 2003; Fitzpatrick & Massa, 2007) or in average high-redshift GRB absorbers (excluding bursts with C I and/or H_2 detections; Zafar et al., 2018b,c). Since A_V and R_V appears to be correlated in our sample of GRB C I absorbers, it is a reasonable assumption that they are regulated by the same physical processes and thus originates from the same molecular cloud. This further supports that the SED-derived dust properties in GRB C I absorbers characterize the dust composition and grain size distribution of the dust in the molecular gas-phase and not in ISM of the GRB host galaxies.

The amount of C I is then expected to correlate with the SED-derived dust extinction, but not necessarily with other dust tracers such as the dust depletion, [Zn/Fe], and the dust-phase iron column density, $N(\mathrm{Fe})_{\mathrm{dust}}$ (as observed, see Fig. 5.4.2). Since dust can form if there are sufficient dense and cold gas available, non-carbonaceous dust grains will specifically form via grain-growth in the ISM if there is a large reservior of metals available as well (mostly O, Fe, Si, and Mg; Draine, 2003; De Cia et al., 2016), whereas

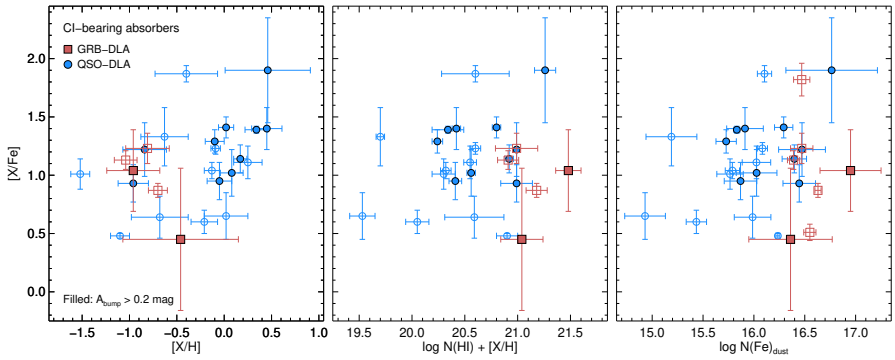

Figure 5.5.2. Dust depletion as a function of metallicity (left), metal column density (middle) and dust-phase iron column density (right) of quasar (blue) and GRB (red) C I absorption systems. Filled symbols denote C I absorbers where the 2175 Å dust extinction feature has been securily detected with $A_{\rm bump} > 0.2$ mag. There appears to be no correlation with the detection of the 2175 Å dust bump to the gas and depletion-derived dust content of the absorbers.

carbon-rich dust will form if there is instead sufficient carbon available. Based on this, we therefore argue that in the ISM, the amount of dust is well-represented by either the derived depletion level, e.g. [Zn/Fe] (De Cia et al., 2018) and/or the dust-phase iron abundance, since these quantities trace non-carbonaceous dust. If this scenario is true, we predict that A_V is only correlated to the non-carbonaceous dust tracers (such as $N(\mathrm{Fe})_{\rm dust}$; Vladilo et al., 2006; De Cia et al., 2013) if the GRB and quasar sightline does not intersect a molecular cloud. If instead, a molecular cloud consisting of significant amounts of carbon (in the form of C I or CO) intervenes the GRB and quasar sightline, the carbon-rich dust will significantly change the shape of the extinction curve, such that $N(\mathrm{Fe})_{\rm dust}$ or the depletion-derived A_V is no longer a good representation of the integrated dust composition but only contributes mildly to the overall shape of the extinguished SED. This could also explain why Bolmer et al. (2019) found that there is more carbon-rich dust in GRB hosts at $z > 4$, simply due to the smaller amounts of dust grains formed from grain growth in the ISM at this epoch.

Finally, we note that Ramírez-Tannus et al. (2018) found a correlation between the strength of diffuse interstellar bands (DIBs; e.g. Cami & Cox, 2014) with the amount of dust towards the star-forming region M17, but an anti-correlation with R_V. The strongest DIBs are, however, believed to originate in the diffuse ISM, such that the anti-correlation with R_V is likely only connected to the 'warm' gas-phase of the ISM and not to the molecular gas. We will discuss this further in Sect. 5.5.3.

5.5.2 Dust composition of molecular clouds at high-z

Following the arguments laid out above, it is now possible to constrain the dust composition and grain size distribution of these intervening, high-z molecular clouds. First, we note from Fig. 5.5.1 that the variation in the grain-size distribution observed in this work support a model where small dust grains condense into large grains in increas-

ingly dense environments (Draine, 1990; Weingartner & Draine, 2001). The relatively steep extinction curves observed toward GRBs 061121, 070802, 120119A, 120815A, 121024A, and 150403A indicate a grain size distribution composed mainly of small ($\lesssim 0.25\,\mu$m) silicate grains in the ISM (Mishra & Li, 2017). The extinction curves observed toward GRBs 080605, 080607, and 180325A, however, require large average grain sizes ($\approx 0.4-0.5\,\mu$m) and a significant contribution from small carbonaceoues dust grains to reproduce the observed 2175 Å dust extinction feature (see the section below).

We expect R_V to be larger in these dust-rich GRB environments, simply because the intervening dust could have a large distribution of grain sizes and better conditions for growth in the more shielded inner regions of the molecular clouds. On the other hand, for sightlines probing the outer regions of the molecular clouds such a grain size distribution is also expected, since small grains are more easily destroyed by the ambient UV flux and therefore only the largest grains remain. This will in turn help to reduce the amount of ionizing photons that will photo-ionize C I to C II.

5.5.3 The origin of the 2175 Å dust extinction feature

Based on a sample of quasar absorbers selected solely on the basis of the 2175 Å dust extinction feature, Ma et al. (2018) found that all such systems are associated with strong absorption features from C I. However, only ≈ 30% of C I-selected absorbers show the characteristic dust bump at a detectable level (Ledoux et al., 2015). To further explore the conditions required for high-redshift, C I-bearing absorbers to simultanously show the presence of the 2175 Å dust extinction feature and whether this dust bump is produced in the ISM, we have compiled a sample of quasar C I systems for which constraints of the extinction bump have been derived and compare them to the GRB C I absorbers studied here, in terms of [Zn/Fe], [Zn/H], $\log N(\mathrm{H\,I})$ + [Zn/H], and $N(\mathrm{Fe})_{\mathrm{dust}}$, in Fig. 5.5.2. The sample of C I-bearing quasar absorbers is comprised of the C I-selected systems from Ledoux et al. (2015) with gas-phase abundances derived by Zou et al. (2018), and additional individual systems from the literature (Guimarães et al., 2012; Krogager et al., 2016a; Krogager, 2018; Noterdaeme et al., 2017; Balashev et al., 2017; Ranjan et al., 2018; Geier et al., 2019). While the C I absorbers showing a significant 2175 Å dust bump (at more than 2σ, i.e. $A_{\mathrm{bump}} > 0.2$ mag; Ledoux et al., 2015) generally have large metal and depletion-derived dust contents, there appears to be no clear correlation for the detection probability of this feature with any of these absorption-line measured abundances. We note that Ma et al. (2017) found a tentative anti-correlation between the bump strength and depletion (though mainly scatter-dominated), which is however not supported by the GRB and quasar C I absorbers studied here. This suggests that the carriers producing the 2175 Å dust extinction feature is also not located in the 'warm' neutral gas-phase of the ISM.

If the 2175 Å dust extinction feature is instead connected to the molecular gas-phase of the ISM, we would expect from the scenario outlined in the previous sections that the detection probability and strength of this feature is better correlated with the SED-derived dust properties. In GRB and quasar sightlines, the detection and strength of the 2175 Å dust extinction feature has previously been found to be connected to dusty sightlines (Ledoux et al., 2015; Ma et al., 2018; Corre et al., 2018) and the amount of

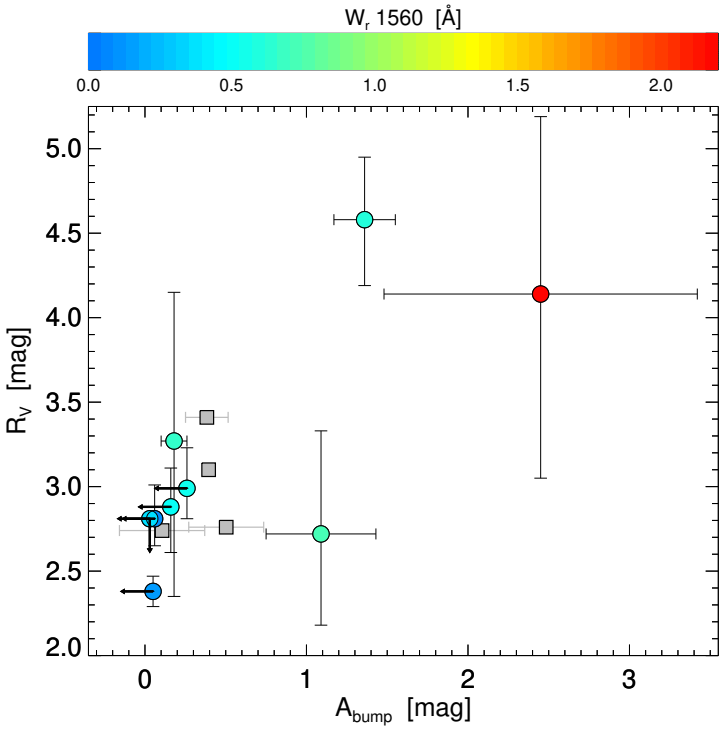

Figure 5.5.3. The total-to-selective extinction, R_V, as a function of the 2175 Å bump strength, $A_{\rm bump}$. The colored filled circles represent the GRB C I absorbers from Paper I studied in this work, color-coded as a function rest-frame equivalent width of C I λ 1560. Grey squares show the mean bump strength of the quasar C I absorbers from Ledoux et al. (2015), divided into the four different extinction curves used in the fit (represented by R_V) where the error bars denote the scatter in absorbers. The carriers producing the 2175 Å dust extinction feature appears to be more prominent in systems with larger amounts C I and with a grain size distribution composed of larger dust grains.

C I in the absorbing systems (Zafar et al., 2012; Ledoux et al., 2015; Ma et al., 2018; Heintz et al., 2019a). In Fig. 5.5.3, we explore the connection between the characteristic bump and the grain size distribution, represented by R_V (Draine, 2003). We find that the carriers producing the 2175 Å dust extinction feature in GRB hosts appears to be more prominent in systems with large amounts of C I and a grain size distribution composed mainly of large dust grains. The quasar C I absorber population appears to also be consistent with this, though only limited information is available on the slope of the extinction, R_V (Ledoux et al., 2015). If R_V and C I is indeed connected to large dust grains and cold neutral gas observed deep into molecular clouds, the 2175 Å dust extinction feature must by association be produced in the same molecular cloud.

Finally, Cortzen et al. (2019) recently found that PAHs are connected to the molecular gas-phase in star-forming galaxies. If PAHs then contribute to or are the sole carrier of the 2175 Å dust extinction feature (as argued by Li & Draine, 2001; Draine & Li,

2007), this would further support the scenario where the bump is produced by carriers located in molecular clouds. In addition, since the bump strength is not connected to the presence of DIBs (Xiang et al., 2011), this excludes the scenario where the carriers of the 2175 Å dust extinction feature is located in the 'warm' neutral ISM. This would also explain why GRB 070802, showing a strong 2175 Å extinction bump, stands out as a clear outlier in the relation between A_V and $N(\mathrm{Fe})_{\mathrm{dust}}$ (De Cia et al., 2013), simply because a significant dust component from the carbon-rich dust in the molecular cloud affects the shape of the SED but not the gas-phase depletions.

5.6 Conclusions

In this work, we studied the dust properties of a sample of nine C I-selected GRB absorption systems at $1 < z < 3$ with the goal of characterizing the mineralogy, dust composition and grain size distribution of the cold and molecular gas-phase in the ISM of these absorbers. This is the first time that a distinction between the various elements contributing to the observed extinction curve, in particular the 2175 Å dust bump, has been attempted at high redshift. We derived parametric extinction curves for a subset of the sample, and combined with literature measurements we identified a broad range of dust models representing the full set of GRB C I absorbers. In addition to the already established relations between the amount of C I and the visual extinction, A_V, and the strength of the 2175 Å extinction bump, A_{bump} (Zafar et al., 2012; Ledoux et al., 2015; Ma et al., 2018; Heintz et al., 2019a) we found evidence for an additional trend between the strength of the C I absorption feature and the total-to-selective reddening parameter, R_V. Contrary to this, we found no connection between the amount of C I to the dust depletion, [Zn/Fe], or the dust-phase iron abundance, $N(\mathrm{Fe})_{\mathrm{dust}}$, but note a tentative correlation with the gas-phase metallicity, [Zn/H]. We, therefore, further advocate against using the depletion-derived dust content as a tracer of the total line-of-sight extinction (as also previously cautioned; Savaglio & Fall, 2004; Wiseman et al., 2017), at least when the individual dust components cannot be securily identifed.

We discussed a scenario where the main dust component causing the observed line-of-sight extinction in the GRB C I absorbers is located in the intervening, C I-bearing molecular cloud. We argued that such a scenario could explain the connection of C I with only the SED-derived dust properties, and reconcile the apparent discrepancy between the extinction and depletion-derived dust properties. Here, the main component causing the observed extinction is carbon-rich dust in the molecular cloud which is not sensitive to the amount of depleted, non-carbonaceous metals in the dust-phase of the ISM. Consistently, we found that the detection and strength of the 2175 Å dust extinction feature is also not linked to any of the non-carbonaceous dust indicators, but better correlated with A_V, R_V and the amount of C I. Moreover, the characteristic dust bump appears to be possibly linked to carbonaceous dust grains and the molecular gas-phase of the ISM, supporting PAHs as potential carriers of the 2175 Å dust extinction feature. We also note that Mishra & Li (2017) did not find any correlation between the extinction parameters and silicon in the dust-phase, but did find that the 2175 Å dust bump scales with the amount of carbon in the dust-phase in Galactic sightlines. This is consistent with the above interpretation of the GRB absorbers showing significant C I abundances.

The evidence for the validity of such a scenario in high-redshift C I-bearing absorbers as presented here, is still only based on tentative correlations and should be verified if more GRB C I systems, especially with the 2175 Å dust extinction feature, are observed. Modelling the individual contributions from a large dust component located in the molecular gas-phase of the ISM and a secondary component in the 'warm' neutral medium would also be beneficial to further understand the observed dust content of high-redshift star-forming galaxies.

Acknowledgements

We would like to thank the referee for providing a clear, constructive and concise report that greatly improved the interpretations presented here. We would also like to thank Karl Gordon for an enlightening discussion in the early stages of this work. KEH and PJ acknowledge support by a Project Grant (162948–051) from The Icelandic Research Fund. The Cosmic Dawn Center is funded by the DNRF.

Appendix

Notes on individual GRBs

GRB 061121

This GRB was first detected by *Swift* and reported by Page et al. (2006). For this case we derived the extinction curve parameters listed in Table 5.4.1 and the best fit model and A_V are shown in Fig. 5.6.1. The spectra examined in this work are obtained with the Keck/LRIS spectrograph and published by Fynbo et al. (2009). The gas-phase abundances listed in Table 5.2.1 are from Zafar & Møller (2019). In addition to the parametric dust model we also obtain the best fit for the equivalent neutral hydrogen column density of $N_{\rm H,X} < 0.94 \times 10^{22}\,{\rm cm}^{-2}$, the optical slope, $\beta_{\rm opt} = 0.41 \pm 0.10$, the X-ray slope, $\beta_{\rm X} = 0.91 \pm 0.11$, and the break frequency, $\log \nu_{\rm break} = 16.70 \pm 0.15\,{\rm Hz}$. The SED fits well with a broken power-law (with an F-test probability of <0.01) and the resulting reduced χ^2 together with the number of degrees of freedom is $\chi^2/({\rm dof}) = 1657/6161$, with a null hypothesis probability of 100% for the best fit model. These results are consistent with the best fit models derived by Schady et al. (2010) and Covino et al. (2013), which are based solely on photometry.

GRB 070802

This GRB was first detected by *Swift* and reported by Barthelmy et al. (2007). For this case we derived the extinction curve parameters listed in Table 5.4.1 and the best fit model and A_V are shown in Fig. 5.6.2. The spectrum examined in this work is from the VLT/FORS2 spectrograph and published by Elíasdóttir et al. (2009); Fynbo et al. (2009). In addition to the parametric dust model we also obtain the best fit for the equivalent neutral hydrogen column density of $N_{\rm H,X} < 2.91 \times 10^{22}\,{\rm cm}^{-2}$. The SED fits well with a single power-law (with an F-test probability of 1.00) with a slope of $\beta_{\rm opt,X} = 0.88 \pm 0.06$ and the resulting reduced χ^2 together with the number of degrees

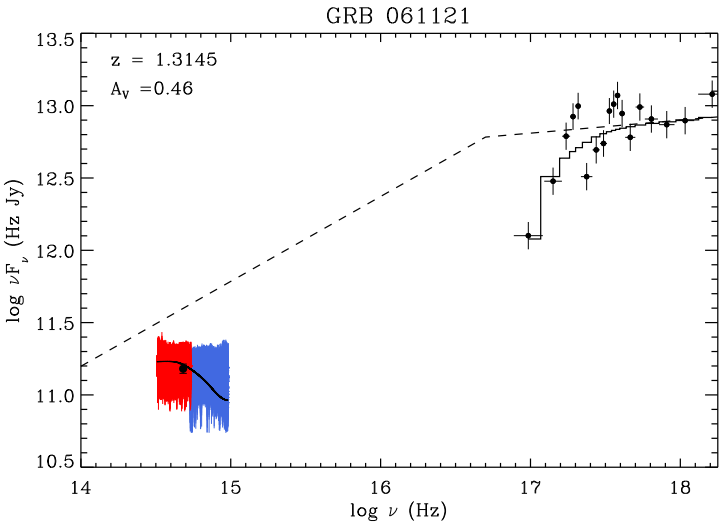

Figure 5.6.1. The observed afterglow SED of GRB 061121. The *Swift*/XRT data is indicated by the black points on the right. The blue and red colours correspond to the blue and red arm spectra obtained with the Keck/LRIS, respectively. The black overlaid point on the optical afterglow spectrum is the photometric point obtained from the acquisition camera. The errors on the spectroscopic and photometric data are also plotted. The best fit extinguished (solid lines) and intrinsic spectral slope (dashed line) are shown in black.

of freedom is $\chi^2/(\mathrm{dof}) = 750/1382$, with a null hypothesis probability of 100% for the best fit model. This GRB shows a clear presence of the 2175 Å extinction bump (as first reported by Krühler et al., 2008; Elíasdóttir et al., 2009) and Zafar et al. (2011a) have fitted the parametric dust model prescribed by Fitzpatrick & Massa (2007) to the same optical afterglow examined here. Our results are consistent with their best fit model, but we will use the results from fitting the SED with the F&M 90 parametrization in this work for consistency.

GRB 080605

This GRB was first detected by *Swift* and reported by Sbarufatti et al. (2008). For this case we derived the extinction curve parameters listed in Table 5.4.1 and the best fit model and A_V are shown in Fig. 5.6.3. The spectrum examined in this work is obtained with the VLT/FORS2 spectrograph and published by Fynbo et al. (2009). The gas-phase abundances listed in Table 5.2.1 are from Zafar & Møller (2019). In addition to the parametric dust model we also obtain the best fit for the equivalent neutral hydrogen column density of $N_{\mathrm{H,X}} = (0.60 \pm 0.05) \times 10^{22}\,\mathrm{cm}^{-2}$. The SED fits well with a single power-law (with an F-test probability of 1.00) with a slope of $\beta_{\mathrm{opt,X}} = 0.62 \pm 0.02$ and the resulting reduced χ^2 together with the number of degrees of freedom is $\chi^2/(\mathrm{dof}) = 724/841$, with a null hypothesis probability of 100% for the best fit model. Zafar et al. (2011a) have fitted the parametric dust model prescribed by Fitzpatrick & Massa (2007) to the same optical afterglow examined here. Our results

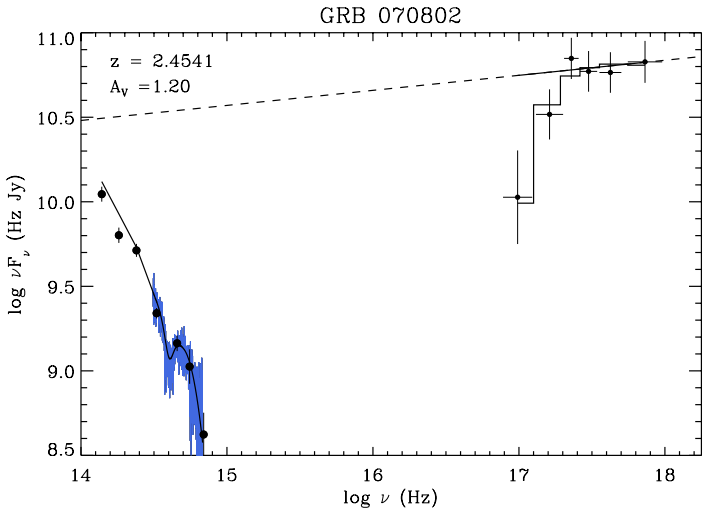

Figure 5.6.2. Same plot connotation as in Fig. 5.6.1 but for GRB 070802 observed with the VLT/FORS2.

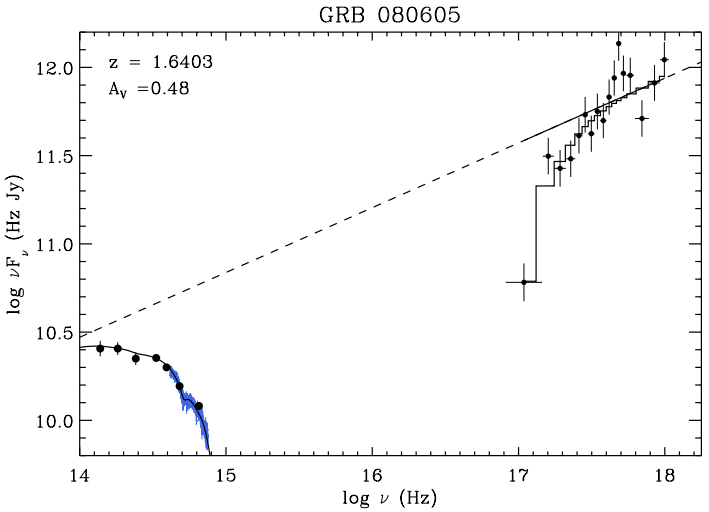

Figure 5.6.3. Same plot connotation as in Fig. 5.6.1 but for GRB 080605 observed with the VLT/FORS2.

are mostly consistent with their best fit model, except that we find a smaller visual extinction of ≈ 0.5 mag compared to their estimate of $A_V \approx 1.2$ mag. This discrepancy is likely due to larger best fit value for R_V of ≈ 3.3 compared to the results by Zafar et al. (2011a) who found a slightly steeper slope for the extinction curve of $R_V \approx 2.9$.

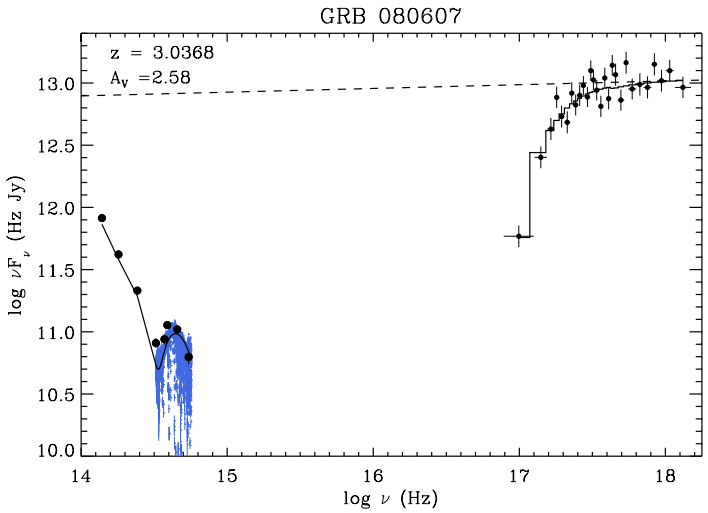

Figure 5.6.4. Same plot connotation as in Fig. 5.6.1 but for GRB 080607 observed with the Keck/LRIS.

GRB 080607

This GRB was first detected by *Swift* and reported by Mangano et al. (2008). For this case we derived the extinction curve parameters listed in Table 5.4.1 and the best fit model and A_V are shown in Fig. 5.6.4. The spectrum examined in this work is obtained with the Keck/LRIS spectrograph and published by Prochaska et al. (2009); Fynbo et al. (2009). In addition to the parametric dust model we also obtain the best fit for the equivalent neutral hydrogen column density of $N_{\rm H,X} = (3.79^{+0.24}_{-0.22}) \times 10^{22}$ cm^{-2}. The SED fits well with a single power-law (with an F-test probability of 1.00) with a slope of $\beta_{\rm opt,X} = 0.99 \pm 0.05$ and the resulting reduced χ^2 together with the number of degrees of freedom is $\chi^2/({\rm dof}) = 326/481$, with a null hypothesis probability of 100% for the best fit model. This GRB presents the first detection of H_2 in the optical afterglow spectrum, shows a clear sign of the 2175 Å extinction bump (Prochaska et al., 2009) and is one of the most luminous bursts ever detected (Perley et al., 2011). Zafar et al. (2011a) have fitted the parametric dust model prescribed by Fitzpatrick & Massa (2007) to the same optical afterglow examined here. Our results are consistent with their best fit model, but we will use the results from fitting the SED with the F&M 90 parametrization here for consistency.

GRB 120119A

This GRB was first detected by *Swift* and reported by Beardmore et al. (2012). The data presented here were obtained with the VLT/X-shooter spectrograph, published by Selsing et al. (2019) and have been examined by Japelj et al. (2015) and Zafar et al. (2018b). We adopt the extinction curve parameters from Zafar et al. (2018b, see Table 5.4.1) since they fit for the full F&M 90 parametrization (whereas Japelj et al.,

2015, only fit for A_V assuming either an MW, SMC or LMC-like extinction curve). While both found a significant visual extinction, Japelj et al. (2015) claimed a detection of the 2175 Å extinction bump, although the best-fit LMC extinction curve overpredicts the strength of the bump. Modelling the full F&M 90 parametric extinction law does not show a significant 2175 Å bump, however (see Zafar et al., 2018b), and were are thus only able to provide upper limits on $A_{\rm bump}$. We adopt the column densities of H I and the low-ionization lines listed in Table 5.2.1 from Wiseman et al. (2017).

GRB 120815A

This GRB was first detected by *Swift* and reported by Pagani et al. (2012a). The data presented here were obtained with the VLT/X-shooter spectrograph and published and examined by Krühler et al. (2013) but we adopt the extinction curve parameters from Zafar et al. (2018b, see Table 5.4.1). The GRB is found to exhibit a moderate amount of extinction with $A_V = 0.1 - 0.3$ mag and does not show any indication of the 2175 Å extinction bump (Krühler et al., 2013; Japelj et al., 2015; Zafar et al., 2018b). We adopt the column densities of H I and the low-ionization lines listed in Table 5.2.1 from Krühler et al. (2013).

GRB 121024A

This GRB was first detected by *Swift* and reported by Pagani et al. (2012b). The data presented here were obtained with the VLT/X-shooter spectrograph and published and examined by Friis et al. (2015). We adopt the extinction curve parameters from Zafar et al. (2018b, see Table 5.4.1) for this burst. Friis et al. (2015) found a very steep extinction curve ($R_V > 15$) is required to explain the SED, but that is by assuming that the SED-inferred amount of dust, A_V, can be derived from the dust depletion and metallicity (which is typically not the case; De Cia et al., 2013; Wiseman et al., 2017). Instead, Zafar et al. (2018b) found that the GRB is well-fitted with a single power-law and a featureless extinction curve with $R_V \approx 2.8$. We adopt the column densities of H I and the low-ionization lines listed in Table 5.2.1 from Friis et al. (2015).

GRB 150403A

This GRB was first detected by *Swift* and reported by Lien et al. (2015). The data presented here were obtained with the VLT/X-shooter spectrograph and published by Selsing et al. (2019). The gas-phase abundances listed in Table 5.2.1 are from Bolmer et al. (2019). For this case we derived the extinction curve parameters listed in Table 5.4.1 and the best fit model and A_V are shown in Fig. 5.6.5. In addition to the parametric dust model we also obtain the best fit for the equivalent neutral hydrogen column density of $N_{\rm H,X} = (0.22^{+0.12}_{-0.11}) \times 10^{22}$ cm^{-2}. The SED fits well with a single power-law (with an F-test probability of 1.00) with a slope $\beta_{\rm opt,X} = 0.57^{+0.14}_{-0.12}$ and the resulting reduced χ^2 together with the number of degrees of freedom is χ^2/(dof) = 31652/41269, with a null hypothesis probability of 100% for the best fit model.

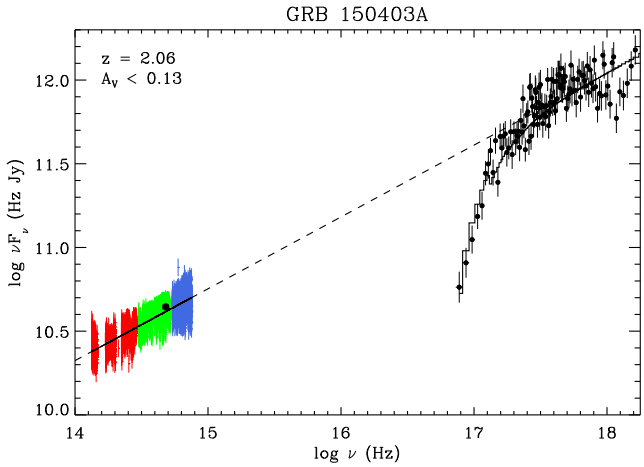

Figure 5.6.5. Same plot connotation as in Fig. 5.6.1 but for GRB 150403A observed with the VLT/X-shooter. The blue, green and red colours correspond to the UVB, VIS and NIR arm spectra, respectively.

GRB 180325A

This GRB was first detected by *Swift* and reported by Troja et al. (2018). The data presented here were obtained with the VLT/X-shooter spectrograph and published and examined by Zafar et al. (2018a). We adopt the extinction curve parameters listed in Table 5.4.1 and the column densities of H I and the low-ionization lines listed in Table 5.2.1 from their work. This GRB exhibit a clear presence of the 2175 Å extinction bump, first noted in the low-resolution NOT/ALFOSC spectra by Heintz et al. (2018b) obtained only 11 minutes post-burst. Subsequently, D'Avanzo et al. (2018) followed up this GRB with the VLT/X-shooter, confirming the detection of the 2175 Å extinction bump and detected several absorption lines and the nebular emission lines [O II], [O III], and Hα. Zafar et al. (2018a) found that the four different epochs of the GRB afterglow show consistent dust properties. We will use the best fit extinction curve parameters from the first epoch VLT/X-shooter spectrum in this work.

Chapter 6

Physical properties of molecular clouds in GRB hosts

This chapter is based on the following article:

New constraints on the physical conditions in H_2-bearing GRB-host damped Lyman-α absorbers

Submitted to Astronomy and Astrophysics.

Authors:
K. E. Heintz, J. Bolmer, C. Ledoux, P. Noterdaeme, J.-K. Krogager, J. P. U. Fynbo, P. Jakobsson, S. Covino, V. D'Elia, M. De Pasquale, D. H. Hartmann, L. Izzo, J. Japelj, D. A. Kann, L. Kaper, P. Petitjean, A. Rossi, R. Salvaterra, P. Schady, J. Selsing, R. Starling, N. R. Tanvir, C. C. Thöne, A. de Ugarte Postigo, S. D. Vergani, D. Watson, K. Wiersema & T. Zafar

We report the detections of molecular hydrogen (H_2), vibrationally-excited H_2 (H_2^*), and neutral atomic carbon (C I), which is believed to be an efficient tracer of molecular gas, in two new afterglow spectra of GRBs 181020A ($z = 2.938$) and 190114A ($z = 3.376$), observed with X-shooter at the VLT. Both host-galaxy absorption systems are characterized by strong DLAs and substantial amounts of molecular hydrogen with $\log N(\mathrm{H\,I}, H_2) = 22.20 \pm 0.05,\ 20.40 \pm 0.04$ (GRB 181020A) and $\log N(\mathrm{H\,I}, H_2) = 22.15 \pm 0.05,\ 19.44 \pm 0.04$ (GRB 190114A). The DLA metallicites, depletion levels and dust extinctions are within the typical regimes probed by GRBs with [Zn/H] $= -1.57 \pm 0.06$, [Zn/Fe] $= 0.67 \pm 0.03$, and $A_V = 0.27 \pm 0.02$ mag (GRB 181020A) and [Zn/H] $= -1.23 \pm 0.07$, [Zn/Fe] $= 1.06 \pm 0.08$, and $A_V = 0.36 \pm 0.02$ mag (GRB 190114A). In addition, we examine the molecular gas content of all known H_2-bearing GRB-DLAs

and explore the physical conditions and characteristics required to simultaneously probe C I and H_2^*. We confirm that H_2 is detected in all C I- and H_2^*-bearing GRB absorption systems, but that these rarer features are not necessarily detected in all GRB H_2 absorbers. We find that a large molecular fraction of $f_{H_2} \gtrsim 10^{-3}$ is required for C I to be detected. The defining characteristic for H_2^* to be present is less clear, though a large H_2 column density is an essential factor. We find that observed line profiles of the molecular gas tracers are kinematically 'cold', with narrow and small velocity offsets $\delta v < 20\,\mathrm{km\,s^{-1}}$ from the bulk of the neutral absorbing gas. We then derive the H_2 excitation temperatures of the molecular gas and find that they are relatively cold with $T_{ex} \approx 100 - 300\,\mathrm{K}$. Finally, we demonstrate that even though the X-shooter GRB afterglow campaign has been successful in recovering several H_2-bearing GRB-host absorbers, this sample is still hampered by a significant dust bias excluding the most dust-obscured H_2 absorbers from identification. C I and H_2^* could open a potential route to identify molecular gas even in low metallicity or highly dust-obscured bursts, though they are only efficient tracers for the most H_2-rich GRB-host absorption systems.

6.1 Introduction

Long-duration gamma-ray bursts (GRBs) are linked to the deaths of massive stars (see e.g. Woosley & Bloom, 2006). These cosmological beacons originate at redshifts as high as $z \gtrsim 8$ (Salvaterra et al., 2009; Tanvir et al., 2009), and appear to be promising tracers of star formation, especially at high ($z \gtrsim 3$) redshifts (e.g. Greiner et al., 2015; Perley et al., 2016b; Palmerio et al., 2019). GRBs are typically followed by a short-lived, multiwavelength afterglow emission (e.g. Mészáros, 2006), which, when bright enough, can serve as a powerful probe of the conditions in the star-forming regions and the interstellar medium (ISM) in their host galaxies (Jakobsson et al., 2004; Fynbo et al., 2006b; Prochaska et al., 2007). The absorption in GRB host galaxy lines-of-sight is typically found to be highly neutral-hydrogen-rich (Vreeswijk et al., 2004; Watson et al., 2006; Fynbo et al., 2009) and most of them are classified as damped Lyman-α absorbers (DLAs; Wolfe et al., 1986). These systems are similar to those previously observed in the spectra of bright quasars, which are produced by intervening galaxies in the line of sight. The DLAs provide the most effective and detailed probe of neutral gas at high redshifts (see e.g. Wolfe et al., 2005, for a review). GRB host-galaxy absorbers are among the strongest DLAs, probing the central-most regions of their hosts, compared to typical quasar DLAs that are more likely to probe the outskirts of the intervening galaxies (Fynbo et al., 2009). This makes GRB-DLAs the ideal probes of the ISM in high-redshift star-forming galaxies (reaching $z \sim 8$, e.g. Salvaterra, 2015; Bolmer et al., 2018; Tanvir et al., 2018).

Given their direct link to star-formation and the very high column densities of neutral gas typically detected in GRB afterglow spectra (e.g. Jakobsson et al., 2006b), it was anticipated that most GRB absorbers would show the presence of molecular hydrogen H_2 (Galama & Wijers, 2001). The observed low detection rate of H_2 was therefore initially a puzzle, indicating an apparent lack of molecular gas in GRB-host absorption systems (e.g. Tumlinson et al., 2007). The observed H_2 deficiency was attributed to the typical low metallicities of the GRB-host absorbers observed with

high-resolution spectrographs (Ledoux et al., 2009), or due to stronger UV radiation fields (Whalen et al., 2008; Chen et al., 2009). Since the absorption signatures of H_2 are the Lyman-Werner bands located bluewards of the Lyman-α line, the search for H_2 from the ground was also limited to $z \gtrsim 2$. The first hint of molecular gas in GRB-host absorption systems came from the tentative detection of H_2 in GRB 060206 (Fynbo et al., 2006b). However, it was not until the remarkable afterglow spectrum of GRB 080607 that the first unequivocal detection of H_2 in a GRB-host absorber was securely reported (Prochaska et al., 2009). The immense luminosity of this GRB (Perley et al., 2011) and the high H_2 column density made it possible to detect the absorption features from the UV Lyman-Werner bands, even in the low-resolution optical spectroscopy obtained of this GRB afterglow. Since then, six more H_2-bearing GRB absorbers have been securely detected (Krühler et al., 2013; D'Elia et al., 2014; Friis et al., 2015; Bolmer et al., 2019). Except for GRB 080607, all of these were observed with the more-sensitive, medium-resolution X-shooter spectrograph on the Very Large Telescope (VLT) as part of the extensive VLT/X-shooter GRB (XS-GRB) afterglow legacy survey (Selsing et al., 2019).

Star-formation is driven and regulated by the availability of dense gas, which is expected to be in molecular form in the ISM (McKee & Ostriker, 2007; Kennicutt & Evans, 2012). Identifying and characterizing the molecular gas-phase is therefore vital to understand how stars are formed. At high redshifts, the presence of H_2 is most commonly inferred indirectly from other molecular gas tracers such as CO in emission-selected galaxy surveys (Solomon & Vanden Bout, 2005; Carilli & Walter, 2013), but its relation to H_2 at high-z and in the low-metallicity regime is still uncertain (Bolatto et al., 2013). Detecting the features from H_2, and other molecular gas species in absorption, therefore provides a unique window into the typical molecular gas content of high-z, star-forming galaxies. Recently, Heintz et al. (2019a) also showed that neutral atomic carbon (C I) could be used as a tracer of H_2 in GRB absorbers, suggesting that a relatively large fraction ($\sim 25\%$) of GRB sightlines intersects molecular clouds, also in the low-resolution spectroscopic GRB afterglow sample of Fynbo et al. (2009). Rarer molecules have also been detected in GRB afterglows, such as CH^+ in GRB 140506A (Fynbo et al., 2014) and vibrationally-excited H_2 (H_2^*) in GRBs 080607 and 120815A (Sheffer et al., 2009; Krühler et al., 2013). Identifying H_2-bearing clouds from these alternative molecular gas tracers might prove to be even more effective, since they can be detected even in low-resolution spectroscopy, and in very dust-obscured GRB afterglows at lower redshifts.

Here we present the observations and detection of H_2 in the two host-galaxy absorption systems of GRB 181020A at $z = 2.938$ and GRB 190114A at $z = 3.376$. These two systems bring the total number of observed H_2-bearing GRB absorbers up to nine. Both afterglow spectra also show absorption features from C I and exhibit the third and fourth known detections of H_2^* in GRB-host absorption systems, respectively. The aim of this work is to explore the defining characteristics required for the H_2-bearing GRB absorbers to simultaneously probe C I and H_2^* and consequently quantify the use of the latter as alternative tracers of molecular-rich gas.

The paper is structured as follows. In Sect. 6.2, we present the observations of the two new GRB optical afterglows and the compiled sample of GRB-host absorbers with detected molecules. The absorption-line abundance analysis is described in Sect. 6.3,

with specific focus on the identified molecular gas tracers. The results related to the defining characteristics of GRB-host absorption systems to show the presence of H_2, C I, and H_2^* is provided in Sect. 6.4. In Sect. 6.5, we explore the physical conditions of the molecular gas and discuss the potential implications of a significant dust bias affecting the H_2-detection probability in GRB-host absorbers. Finally, in Sect. 6.6 we present the conclusions of our work. Throughout the paper, errors denote the 1σ confidence level (unless stated otherwise) and column densities are expressed in units of cm^{-2}. We assume a standard flat cosmology with $H_0 = 67.8\,km\,s^{-1}\,Mpc^{-1}$, $\Omega_m = 0.308$ and $\Omega_\Lambda = 0.692$ (Planck Collaboration et al., 2016). Gas-phase abundances are expressed relative to the solar abundance values from Asplund et al. (2009), where $[X/Y] = \log(N(X)/N(Y)) - \log(N(X)_\odot/N(Y)_\odot)$, following the recommendations by Lodders et al. (2009). Wavelengths are reported in vacuum.

6.2 Observations and sample description

The GRBs 181020A and 190114A were both detected by the Burst Alert Telescope (BAT; Barthelmy et al., 2005) onboard the *Neil Gehrels Swift Observatory* (*Swift* hereafter; Gehrels et al., 2004), as reported by Moss et al. (2018) and Laporte et al. (2019). We obtained optical to near-infrared afterglow spectra of both GRBs with the VLT/X-shooter instrument (Vernet et al., 2011). The spectrum of GRB 181020A was acquired (at the start of exposure) 5.7 hrs after the GRB with an acquisition magnitude of $R \sim 17.3$ mag (Fynbo et al., 2018). GRB 190114A was observed only 15 min after trigger with an acquisition magnitude of $R \sim 18.7$ mag, using the rapid-response mode (RRM) (de Ugarte Postigo et al., 2019). The optical to near-infrared spectra of both GRBs were taken simultaneously in the UVB, VIS and NIR arms of VLT/X-shooter with slit-widths of 1.″0, 0.″9, 0.″9, respectively. The observations were performed under excellent conditions with average seeing and airmasses of 1.″02, 1.25 (GRB 181020A) and 0.″47, 1.29 (GRB 190114A). Both spectra show very high signal-to-noise ratios (S/N), with S/N $\gtrsim 30$ at $\lambda_{obs} = 6700$ Å in the VIS arm spectra.

We reduced the afterglow spectra in a similar manner as described in Selsing et al. (2019). The only update is that the reductions are based on the most recent version `v. 3.2.0` of the ESO X-shooter pipeline (Modigliani et al., 2010). The final extracted 1D spectra are moved to the barycentric frame of the Solar system in the post-processing and corrected for Galactic extinction along the line-of-sight to the bursts using the dust maps of Schlegel et al. (1998), but with the updated values from Schlafly & Finkbeiner (2011). We infer the delivered spectral resolution from the observed width of a set telluric absorption features in the VIS and NIR arms and rescale the nominal UVB arm resolution accordingly. To verify this, we also estimated the delivered resolution by fitting the spectral trace in the UVB arm with a Gaussian and derived the resolution from the full-width-at-half-maximum (FWHM) as $FWHM = 2\sqrt{2\ln 2}\sigma$, which yielded consistent results.

To complement the analysis of the molecular content and the physical conditions in GRBs 181020A and 190114A, we compile a sample of bursts selected from the VLT/X-shooter GRB (XS-GRB) afterglow legacy survey (Selsing et al., 2019) and the Stargate (PI: N. R. Tanvir) public data. This sample constitutes all GRBs observed with

Table 6.2.1. Sample properties of the H_2- and/or C I-bearing XS-GRB absorbers.

GRB	z_{GRB}	$\log N(\mathrm{H\,I})$ ($\mathrm{cm^{-2}}$)	$\log N(H_2)$ ($\mathrm{cm^{-2}}$)	$\log f_{H_2}$	$\log N(\mathrm{C\,I})^a$ ($\mathrm{cm^{-2}}$)	$\log N(\mathrm{CO})^a$ ($\mathrm{cm^{-2}}$)	[X/H]	A_V (mag)
120119A	1.7288	22.44 ± 0.12	⋯	⋯	$\gtrsim 14.9$	< 15.7	-0.96 ± 0.28	1.02 ± 0.11
120327A	2.8143	22.07 ± 0.01	17.39 ± 0.13	-4.38 ± 0.14	< 14.3	< 15.3	-1.49 ± 0.03	< 0.03
120815A	2.3582	22.09 ± 0.01	20.42 ± 0.08	-1.39 ± 0.09	14.24 ± 0.14	< 15.0	-1.45 ± 0.03	0.19 ± 0.04
120909A	3.9290	21.82 ± 0.02	17.25 ± 0.23	-4.27 ± 0.25	< 14.0	< 14.2	-1.06 ± 0.12	0.16 ± 0.04
121024A	2.3005	21.78 ± 0.02	19.90 ± 0.17	-1.59 ± 0.18	13.91 ± 0.08	< 14.4	-0.76 ± 0.06	0.26 ± 0.07
141109A	2.9940	22.18 ± 0.02	18.02 ± 0.12	-3.86 ± 0.14	< 14.7	< 15.9	-1.63 ± 0.06	0.11 ± 0.03
150403A	2.0571	21.73 ± 0.02	19.90 ± 0.14	-1.54 ± 0.15	$\gtrsim 14.3$	< 14.9	-1.04 ± 0.04	< 0.13
180325A	2.2496	22.30 ± 0.14	⋯	⋯	$\gtrsim 14.5$	< 15.9	> -0.96	1.58 ± 0.12
181020A	2.9379	22.20 ± 0.05	20.40 ± 0.04	-1.51 ± 0.06	13.98 ± 0.05	< 13.3	-1.57 ± 0.06	0.27 ± 0.02
190114A	3.3764	22.15 ± 0.05	19.44 ± 0.04	-2.40 ± 0.07	13.54 ± 0.08	< 13.3	-1.23 ± 0.07	0.36 ± 0.02
080607	3.0363	22.70 ± 0.15	21.20 ± 0.20	-1.23 ± 0.24	$> 15.1^b$	16.5 ± 0.3	$> -0.2^c$	2.58 ± 0.45

Notes. References for the measurements of the neutral and molecular gas-phase abundances and A_V can be found in the Appendix. [a]The measured 2σ upper or lower limits are provided for each GRB. [b]The lower limit on the total C I column density for GRB 080607 is inferred from the rest-frame equivalent width of C I (see Sect. 6.3.4). [c]The lower limit on the metallicity for GRB 080607 is derived from the [O/H] abundance following Prochaska et al. (2009).

VLT/X-shooter to date that directly or indirectly show the presence of molecular gas. We have extracted all afterglows with known detections of molecular hydrogen (Krühler et al., 2013; D'Elia et al., 2014; Friis et al., 2015; Bolmer et al., 2019) and/or neutral atomic carbon (Zafar et al., 2018a; Heintz et al., 2019a), which has been found to be a good tracer of molecular gas (see e.g. Srianand et al., 2005; Noterdaeme et al., 2018). This collection is therefore not an unbiased representation of the GRB population as a whole, but rather a compilation of GRB afterglows where a determination of the relative gas content and the physical conditions in the molecular gas-phase is possible (see instead Bolmer et al. 2019 and Heintz et al. 2019a for statistical analyses of the presence of H_2 and C I in GRB afterglows). In total, we compiled ten XS-GRBs with H_2 and/or C I detected in absorption, listed in Table 6.2.1. Throughout the paper we will also compare our results to the only other GRB with a known detection of H_2 in absorption, GRB 080607 (Prochaska et al., 2009).

6.3 Data analysis

6.3.1 Atomic and molecular hydrogen

In the high S/N afterglow spectra of GRBs 181020A and 190114A, we clearly detect the absorption features from H_2 bluewards of the broad Lyα absorption trough (see Figs. 6.3.1 and 6.3.2). We measure the column densities of atomic and molecular hydrogen by simultaneously fitting the absorption lines from H I and the H_2 Lyman-Werner bands following the same routine as described in Bolmer et al. (2019). Here, the absorption lines are modelled with Voigt profiles and fitted simultaneously with the continuum flux of the GRB afterglow. The absorption lines are then convolved with the delivered spectral resolution in the UVB arm spectra of $\mathcal{R} = 6750$ (or $44.4\,\mathrm{km\,s^{-1}}$, GRB 181020A) and $\mathcal{R} = 7020$ (or $42.7\,\mathrm{km\,s^{-1}}$, GRB 190114A). The fitting routine is

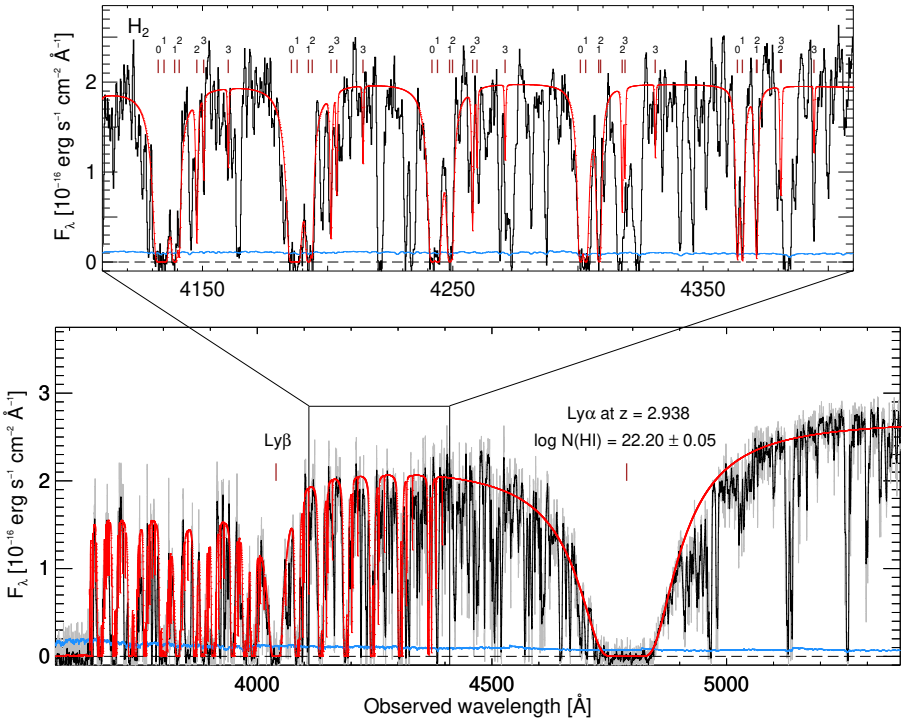

Figure 6.3.1. VLT/X-shooter UVB arm spectrum of GRB 181020A showing absorption features from the H I Lyα, Lyβ and H_2 Lyman-Werner band line transitions. The raw spectrum is shown in grey with the associated error spectrum in blue. A binned version of the spectrum is overplotted in black. A synthetic spectrum of the best fit model to H I and H_2 is shown as the red solid line and the Lyα and Lyβ absorption features are marked at the observed redshift of $z = 2.938$. The top panel shows a zoom-in of a subset of the most constraining Lyman-Werner band line transitions from molecular hydrogen. The redshifted wavelengths of the strongest rotational levels $J = 0, 1, 2, 3$ are marked above each line.

a custom-made `Python` module, based on the Markov Chain Monte Carlo (MCMC) Bayesian inference library `PyMC 2.3.7` (see Bolmer et al., 2019, for further details). For GRB 181020A we derive a total H I column density of $\log N(\mathrm{H\,I}) = 22.20 \pm 0.05$, consistent with Tanvir et al. (2019), at a redshift of $z = 2.938$, and for GRB 190114A we derive $\log N(\mathrm{H\,I}) = 22.15 \pm 0.05$ at $z = 3.376$. In both afterglow spectra, we detect all the rotational levels up to $J = 3$ (see Sect. 6.5.1 for further discussion on the $J \geq 4$ levels).

To determine the H_2 abundances we tied the redshifts and b-parameters in the fit for all the detected rotational levels, and find a best fit assuming a single absorption component. For GRB 181020A we measure column densities of $\log N(H_2, J = 0, 1, 2, 3) = 20.14 \pm 0.05$, 20.06 ± 0.03, 18.38 ± 0.21, and 18.05 ± 0.25, and thus a total H_2 column density of $\log N(H_2) = 20.40 \pm 0.04$ with a broadening parameter of $b = 3 \pm 2\,\mathrm{km\,s^{-1}}$. For GRB 190114A we derive $\log N(H_2,\ J = 0, 1, 2, 3) = 19.28 \pm 0.05$, 18.90 ± 0.03, 17.92 ± 0.02, and 17.62 ± 0.25 resulting in a total H_2 column density of $\log N(H_2) =$

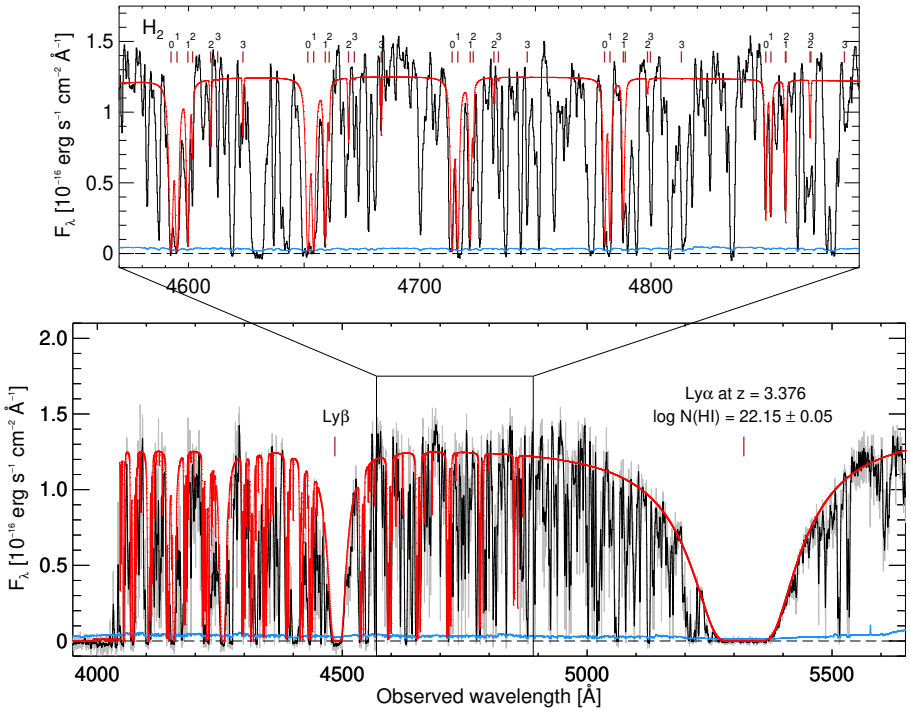

Figure 6.3.2. VLT/X-shooter UVB arm spectrum of GRB 190114A showing absorption features from the H I Lyα, Lyβ and H_2 Lyman-Werner band line transitions. The raw spectrum is shown in grey with the associated error spectrum in blue. A binned version of the spectrum is overplotted in black. A synthetic spectrum of the best-fit model to H I and H_2 is shown as the red solid line and the Lyα and Lyβ absorption features are marked at the observed redshift of $z = 3.376$. The top panel shows a zoom-in of a subset of the most constraining Lyman-Werner band line transitions from molecular hydrogen. The redshifted wavelengths of the strongest rotational levels $J = 0, 1, 2, 3$ are marked above each line.

19.44 ± 0.04 with a broadening parameter of $b = 2 \pm 1$ km s^{-1}. Since the lowest rotational levels ($J = 0, 1$) of H_2 are damped in both cases, the determination of the column density in these levels is not sensitive to b. Because these transitions dominate the H_2 content, the estimates of the total N(H_2) in both cases should be robust. While both fits are consistent with a single absorption component, we caution that at this resolution the observed line profiles might be comprised of a number of narrower features such that inferred H_2 abundances represent the integrated H_2 column density. Synthetic spectra of the best-fit models of H I and H_2 in GRBs 181020A and 190114A are shown in Figs. 6.3.1 and 6.3.2, overplotted on the UVB arm spectra.

For the remaining GRBs in our sample, column densities of atomic and molecular hydrogen have been derived previously in the literature. Throughout the paper, we report the column densities measured by Bolmer et al. (2019) to be consistent within the sample, except for GRBs 120119A and 180325A, where we adopt the derived H I

column densities from Wiseman et al. (2017) and Zafar et al. (2018a), respectively (since they were not part of the statistical sample of Bolmer et al. 2019). For a more detailed analysis of some of the individual systems, see the dedicated single-burst papers (e.g. for GRB 120327A: D'Elia et al. 2014; GRB 120815A: Krühler et al. 2013; and GRB 121024A: Friis et al. 2015).

6.3.2 Gas-phase abundances and dust extinction

In addition to the H I and H_2 transition lines we detect a wealth of low-ionization metal absorption features in the afterglow spectra of GRBs 181020A and 190114A. To determine the gas-phase abundances, we again fit a range of Voigt profiles to a set of carefully-selected absorption lines, free of tellurics or unrelated blends. The host absorber towards GRB 181020A shows a complex velocity structure with five identified strong absorption components (see Fig. 6.6.1 for a few examples showing this structure). The absorption line profiles in the host absorber of GRB 190114A show a simpler velocity structure, with one dominant component and an additional weaker component at $\delta v = -40\,\mathrm{km\,s^{-1}}$ (see Fig. 6.6.2). We constrain the column densities from the weakest transition lines of each element by fixing the velocity structure to that observed in the strongest line complexes.

For GRB 181020A we derive column densities of $\log N(\mathrm{Fe}) = 15.47 \pm 0.01$, $\log N(\mathrm{Zn}) = 13.19 \pm 0.03$, and $\log N(\mathrm{Cr}) = 14.16 \pm 0.02$, resulting in a gas-phase metallicity of $[\mathrm{Zn/H}] = -1.57 \pm 0.06$ and dust-depletion $[\mathrm{Zn/Fe}] = 0.67 \pm 0.03$. Following De Cia et al. (2016) we compute a dust-corrected metallicity, [M/H] = [X/H] - δ_X (where δ_X is inferred from the iron-to-zinc depletion), of $[\mathrm{M/H}] = -1.39 \pm 0.05$. For GRB 190114A we measure gas-phase abundances of $\log N(\mathrm{Fe}) = 15.37 \pm 0.04$, $\log N(\mathrm{Zn}) = 13.48 \pm 0.04$, and $\log N(\mathrm{Cr}) = 13.95 \pm 0.05$, resulting in a metallicity of $[\mathrm{Zn/H}] = -1.23 \pm 0.07$ and dust-depletion $[\mathrm{Zn/Fe}] = 1.06 \pm 0.08$. This yields a dust-corrected metallicity of $[\mathrm{M/H}] = -0.94 \pm 0.06$. The gas-phase abundances of GRBs 181020A and 190114A, together with literature values for the other GRBs in our sample, are summarized in Table 6.2.1. Again, we adopt the values derived by Bolmer et al. (2019) for the majority of the sample, except for GRBs 120119A and 180325A (see the Appendix for details).

The visual extinction A_V along the line-of-sight to both GRBs were measured following the same approach as in Heintz et al. (2019a). Briefly, this assumes a simple underlying power-law shape of the afterglow spectrum, with a wavelength-dependent extinction coefficient A_λ imposed as $F_{\mathrm{obs}} = F_\lambda \times 10^{-0.4A_\lambda}$ where $F_\lambda = \lambda^{-\beta}$. We then fit the underlying power-law slope and extinction coefficient simultaneously. Using the extinction-curve parametrization from Gordon et al. (2003), we find a best fit with an SMC-like extinction curve in both GRB sightlines and measure $A_V = 0.27 \pm 0.02$ mag (for GRB 181020A, see Fig. 6.6.3) and $A_V = 0.36 \pm 0.02$ mag (for GRB 190114A, see Fig. 6.6.4). We do not find any indication of the 2175 Å dust extinction bump in either of the bursts, so we derive upper limits on the bump strength, $A_{\mathrm{bump}} = \pi c_3/(2\gamma R_V) \times A_V$, of $A_{\mathrm{bump}} < 0.07$ mag (GRB 181020A) and $A_{\mathrm{bump}} < 0.09$ mag (GRB 190114A) at 3σ. The measured visual extinction along the line-of-sight toward GRBs 181020A and 190114A, together with literature values for the other GRBs in our sample, are again summarized in Table 6.2.1.

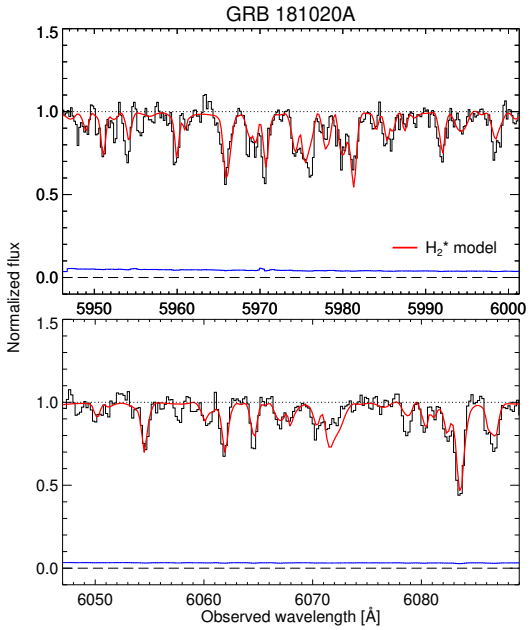

Figure 6.3.3. Normalized VLT/X-shooter VIS arm spectrum of GRB 181020A showing regions encompassing a subset of the strongest H_2^* lines. The black solid lines show the data, the blue lines the associated error and the red lines the best-fit model.

6.3.3 Vibrationally-excited molecular hydrogen

After clearly establishing the presence of H_2 in both the afterglow spectra of GRBs 181020A and 190114A, we searched for the so-far rarely detected absorption features from vibrationally-excited H_2 (H_2^*) (see Bolmer, 2019). The vibrationally-excited levels of H_2 are expected to be populated by UV pumping from the GRB afterglow (Draine, 2000), but to date it has only been securely detected in two afterglow spectra, those of GRB 080607 (Sheffer et al., 2009) and GRB 120815A (Krühler et al., 2013). We performed the search by using the synthetic spectrum from Draine & Hao (2002), downgraded to the resolution of the given arm (in both cases the VIS arm, with $\mathcal{R} \sim 11\,000$). In the fit, we include any intervening metal lines and match the model to the whole spectrum redwards of Lyα up until 1650 Å (rest frame). We use PyMC (as described in Sect. 6.3.1) to sample the posteriors of the optical depth τ and the redshift of the H_2^* absorption lines, as well as the continuum flux.

We clearly detect H_2^* in both afterglow spectra of GRBs 181020A and 190114A. Even including the uncertainty on the continuum flux due to the wealth of absorption features from H_2^*, we consider the detections highly significant due to the overall excellent match with the data and fit to several strong individual lines. For GRB 181020A we derive a column density of $\log N(H_2^*) = 16.28 \pm 0.05$, with the best-fit model shown in Fig. 6.3.3. For GRB 190114A, we measure $\log N(H_2^*) = 16.13 \pm 0.13$, with the best-fit model shown in Fig. 6.3.4. We caution that small deviations of the spectrum from the model are expected due to the different initial conditions, such as the luminosity of the GRB afterglow, dust content and shielding, and distance to the absorbing cloud (Krühler et al., 2013). A detailed modelling of the lines will be provided in a follow-up paper to constrain the origin of H_2^* (Bolmer et al. in preparation). The H_2^* column

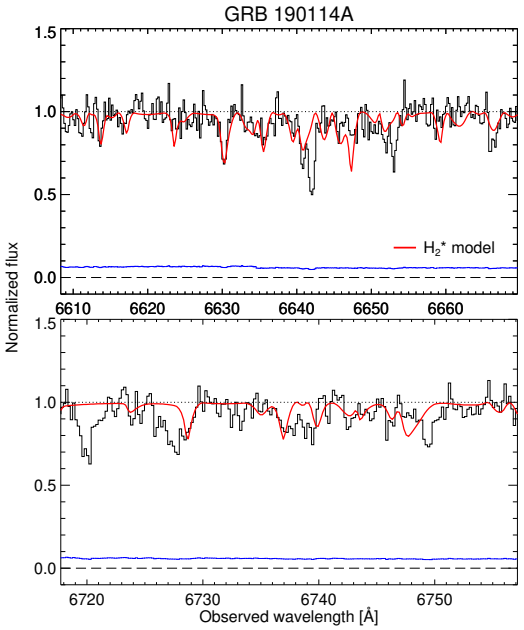

Figure 6.3.4. Same as Fig. 6.3.3 but for GRB 190114A.

densities of GRBs 181020A and 190114A are of the same order as the one observed in GRB 120815A, all being roughly an order of magnitude lower than what was observed in GRB 080607 (Sheffer et al., 2009). For the other GRBs in our sample, we are able to place upper limits on the H_2^* column density typically 5 – 10 times lower than those observed in GRBs 120815A, 181020A and 190114A using the same routine (see also Bolmer et al., 2019).

6.3.4 Neutral atomic carbon

In addition to H_2 and H_2^*, we also detect absorption features from C I in both afterglow spectra of GRBs 181020A and 190114A, which has been found to be an efficient tracer of molecule-rich gas. Recently, Heintz et al. (2019a) surveyed C I in a large sample of GRB afterglows observed both with low- and medium-resolution spectrographs (including some of the XS-GRBs in the sample presented here). To be consistent with the part of the sample observed with low-resolution spectrographs (where meaningful column densities cannot be derived) and with the survey for C I in high-z quasar absorbers (Ledoux et al., 2015), only the total C I equivalent widths were measured in that study. In this work, we attempt to derive the C I column densities for all the XS-GRBs, including the sample studied in Heintz et al. (2019a), by fitting a set of Voigt profiles to the relevant transitions. For this, we use the `Python` module `VoigtFit`[1] (Krogager, 2018), where the absorption line profiles again have been convolved with the delivered instrumental resolution, either in the UVB arm (when $z_{\rm GRB} < 2.5$, typically at $\mathcal{R} = 50\,{\rm km\,s^{-1}}$) or in the VIS arm (when $z_{\rm GRB} > 2.5$, typically at $\mathcal{R} = 30\,{\rm km\,s^{-1}}$).

[1] `https://github.com/jkrogager/VoigtFit`

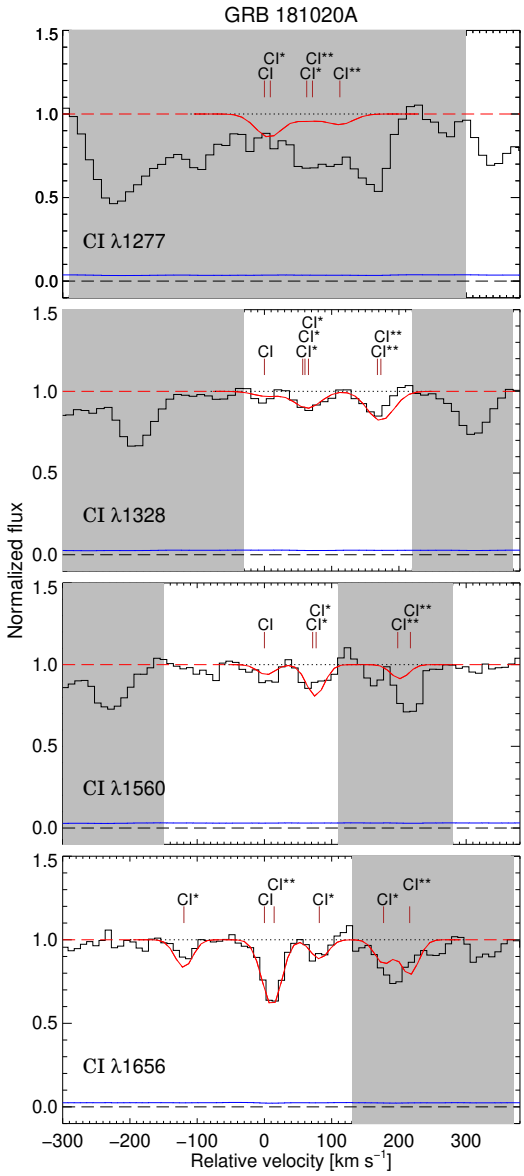

Figure 6.3.5. Normalized VLT/X-shooter VIS arm spectrum of GRB 181020A in velocity space, centred on the ground-state transition of C I at $z = 2.93786$. Again, the black solid lines show the data, the blue lines the associated error and the red lines the best-fit model. The C I ground-state and excited line transitions are marked above each of the absorption profiles. Gray shaded regions were ignored in the fit.

The three fine-structure levels ($J = 0, 1, 2$) of neutral carbon's ground-state triplet, here denoted C I, C I*, C I**, respectively, are all resolved in the VLT/X-shooter spectra (see also e.g. Krogager et al., 2016a; Ranjan et al., 2018). We simultaneously fitted the three fine-structure levels, assuming a single component and by tying the Doppler parameters and redshifts. This is based on the assumption that the excited fine-structure levels (C I* and C I**) share the same physical origin as the ground level (C I) and therefore follow the same kinematic structure.

For GRB 181020A we derive column densities of $\log N(\mathrm{C\,I}, \mathrm{C\,I}^*, \mathrm{C\,I}^{**}) = 12.82 \pm 0.13$, 13.45 ± 0.05, and 13.78 ± 0.07, and thus a total C I column density of $\log N(\mathrm{C\,I}) = 13.98 \pm 0.05$ with a best-fit broadening parameter of $b = 3.9 \pm 0.8\,\mathrm{km\,s^{-1}}$. The best-fit Voigt profiles are shown in Fig. 6.3.5. We only detect a single absorption component across the four line complexes so we fixed this in the fit and masked out any unrelated or blended features. The fit was only constrained by the C I $\lambda\lambda\lambda$ 1328,1560,1656 transition lines, since the C I λ 1277 line is significantly blended with tellurics and unrelated absorption features. For GRB 190114A we compute relative C I abundances of $\log N(\mathrm{C\,I}, \mathrm{C\,I}^*, \mathrm{C\,I}^{**}) = 12.79 \pm 0.15$, 13.12 ± 0.15, and 13.19 ± 0.11, and thus a total C I column density of $\log N(\mathrm{C\,I}) = 13.54 \pm 0.08$. In this case, we fixed the broadening parameter to $b = 5\,\mathrm{km\,s^{-1}}$, since the fit could not converge on a realistic b-value due to significant blending of several of the lines. The best-fit model with fixed $b = 5\,\mathrm{km\,s^{-1}}$ is shown in Fig. 6.3.6. It was only possible to perform the fit on the C I $\lambda\lambda\lambda$ 1328,1560,1656 line transitions, since the C I λ 1277 line is located in the overlap region between the UVB and VIS arm. We only detect a single absorption component across the three line complexes in this case as well, so we fixed this in the fit and masked out any unrelated or blended features. The line profiles seem to exclude values of $b \gtrsim 5\,\mathrm{km\,s^{-1}}$ and $b \lesssim 3\,\mathrm{km\,s^{-1}}$, both when considering the line widths and the relative optical depths.

For the other GRBs in our sample where C I is detected, the derived column densities are listed in Table 6.2.1. Here, we also provide upper limits for the H_2-bearing GRB absorbers which show non-detections of C I assuming $b = 2\,\mathrm{km\,s^{-1}}$ to be consistent with the limits derived for the abundance of CO (Bolmer et al., 2019). In the Appendix, a more detailed description of the fit performed for each individual GRB is given, together with plots showing the best-fit Voigt profiles and tables listing the derived column densities for each of the excited states and Doppler parameters. For the bursts where C I is most prominent (GRBs 120119A, 150403A, and 180325A) we only provide the 2σ lower limit on the total column density in Table 6.2.1 since the lines are intrinsically saturated. For GRBs 120815A, 121024A, 181020A, and 190114A we provide the derived total C I column densities in Table 6.2.1. We caution, however, that since we are not able to distinguish additional narrow absorption components at the observed spectral resolution, these values should in principle only represent the lower limits on $N(\mathrm{C\,I})$ due to the possible effect of 'hidden' saturation (e.g., Prochaska, 2006). Nevertheless, note that the inferred b-parameters and column densities are consistent with similar C I absorption systems observed toward quasars (e.g. Srianand et al., 2005).

For GRB 080607 (Prochaska et al., 2009) we derive a lower limit on the total C I column density based on the equivalent width measurements from Fynbo et al. (2009) of $\log N(\mathrm{C\,I}) > 15.1$. To estimate this abundance more precisely, we compare the C I equivalent widths derived by Ledoux et al. (2015) for the quasar C I absorbers with the total column densities measured in the high-resolution spectra of the same absorption systems (Noterdaeme et al., 2018). From a linear fit to the data (excluding the systems with $\log N(\mathrm{C\,I}) > 14.5$, at which point the line profiles become saturated) we find a correlation of

$$\log W_\mathrm{r}(\lambda 1560) = 0.8 \log N(\mathrm{C\,I}) - 11.98 \tag{6.1}$$

with a scatter of $\sigma = 0.3$ dex (see Fig. 6.3.7). For GRB 080607 we then estimate $\log N(\mathrm{C\,I}) = 15.4 \pm 0.3$ based on this relation, consistent with the lower limit inferred from the equivalent width. To be conservative, we will only consider the lower limit for

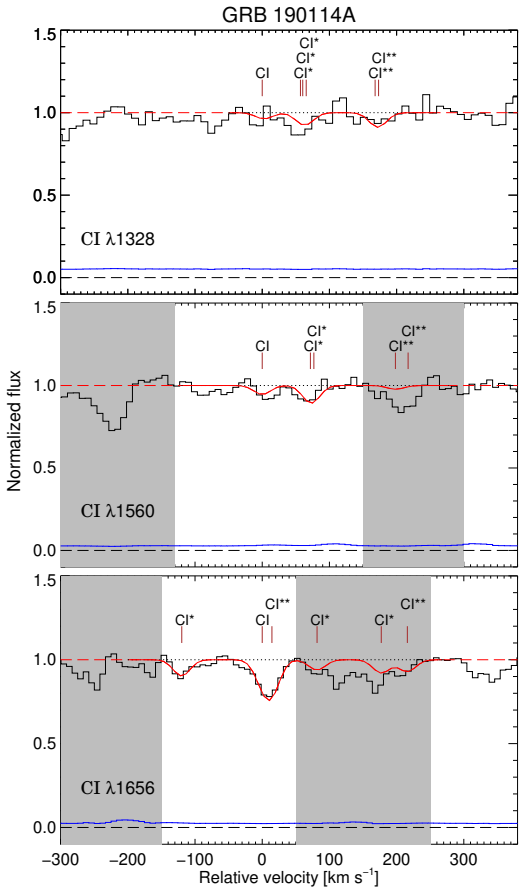

Figure 6.3.6. Same as Fig. 6.3.5 but for GRB 190114A and with a fixed value of $b = 5\,\mathrm{km\,s^{-1}}$, centred on $z = 3.37638$.

this GRB throughout the paper. We also note that the C I equivalent widths and column densities derived for the rest of the GRB C I absorbers studied here are all also consistent with the observed correlation for the quasar absorbers. This linear relation therefore provides a robust way of constraining the total C I column density for non-saturated lines for C I absorption systems observed with low-resolution spectra. The observed scatter of $\sigma = 0.3$ dex is likely dominated by the varying degree of the populations in the excited fine-structure levels relative to the ground-state.

6.3.5 Carbon monoxide

We also searched the afterglow spectra of GRBs 181020A and 190114A for absorption features originating from carbon monoxide (CO). To date, the only detection of CO absorption lines in a GRB afterglow is towards the remarkable burst GRB 080607 (Prochaska et al., 2009). Recently, Bolmer et al. (2019) derived upper limits on the CO column density for all the H_2-bearing GRB-DLAs examined in this study (except for GRBs 181020A and 190114A). We also note that de Ugarte Postigo et al.

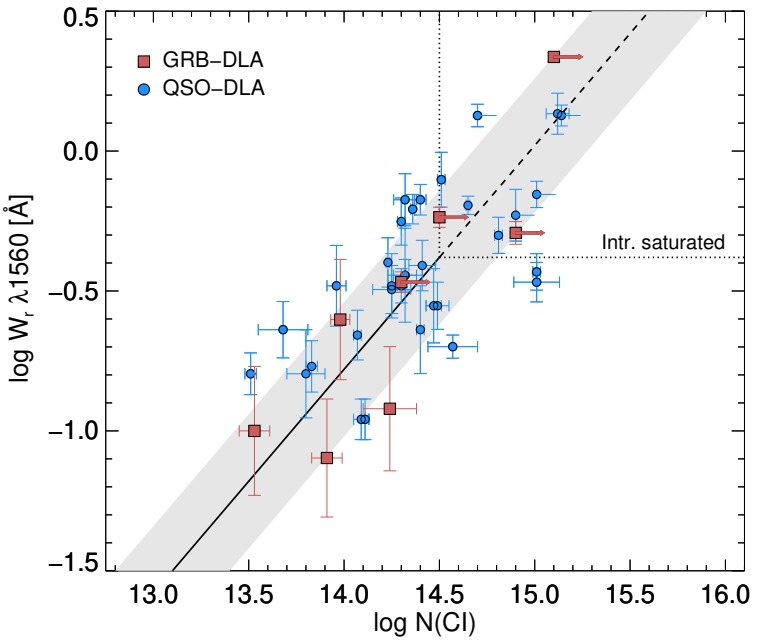

Figure 6.3.7. C I λ 1560 rest-frame equivalent width as a function of total C I column density. Red squares denote GRB C I absorbers from this work. Blue dots show the C I-selected quasar absorbers from Ledoux et al. (2015), for which Noterdaeme et al. (2018) measured the total N(C I) from high-resolution spectroscopy. The black line shows the best linear fit where the $\sigma = 0.3$ dex scatter is shown by the grey-shaded region. The approximate column density (and equivalent width) at which the intrinsic C I lines saturate are marked by the dotted lines.

(2018) searched for CO absorption both in VLT/X-shooter and ALMA spectroscopy of GRB 161023A but were also only able to determine upper limits (this GRB did not show features from H_2 down to deep limits, however). In Figs. 6.3.8 and 6.3.9 we show the region of the spectra where the strongest CO band absorption lines should be located in GRBs 181020A and 190114A, respectively, and a stack of all line complexes (excluding CO λ 1544 in both cases due to blending). We do not detect any evidence of CO in either of the GRB afterglow spectra. To measure the upper limits on N(CO) in GRBs 181020A and 190114A we follow the same approach as Noterdaeme et al. (2018) and compute global (i.e. from the stacked spectra) χ^2 values for a range of column densities, where the 3σ upper limit corresponds to the column density where the χ^2 is 9. This limit is naturally more stringent than inferred locally for each band individually. For both GRBs 181020A and 190114A we derive 3σ upper limits of $\log N(\mathrm{CO}) < 13.3$. The individual and stacked CO line profiles showing the upper limits on N(CO) are overplotted in red in Figs. 6.3.8 and 6.3.9. To be complete, we derive additional limits for GRBs 120119A and 180325A (which were not part of the study of Bolmer et al. 2019). A summary of the resulting upper limits on the abundance of CO for the GRBs studied in this work is provided in Table 6.2.1.

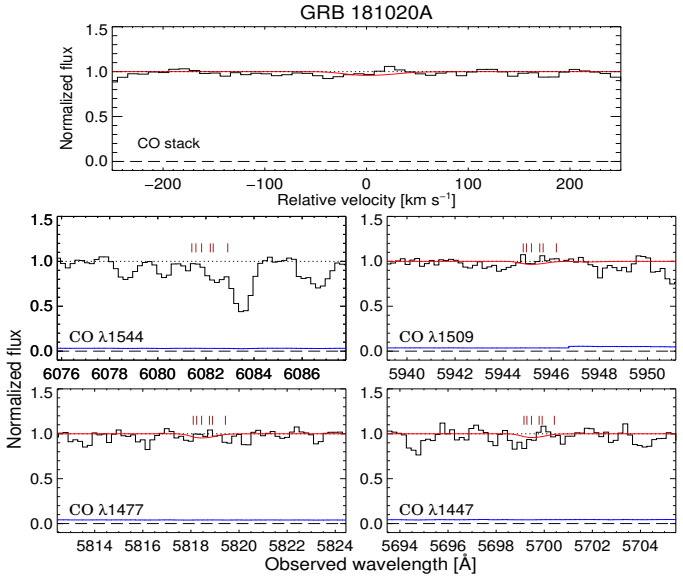

Figure 6.3.8. Normalized VLT/X-shooter VIS arm spectrum of GRB 181020A showing the regions where the strongest CO band absorption lines are expected including a stacked spectrum (excluding CO λ 1544). Again, the black solid lines show the data and the blue lines the associated error. Line profiles showing the derived upper limits on N(CO) are overplotted in red.

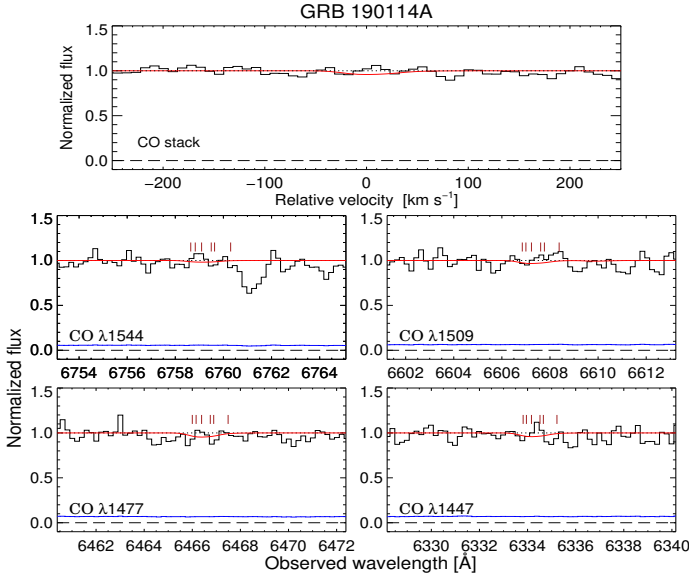

Figure 6.3.9. Same as Fig. 6.3.8 but for GRB 190114A.

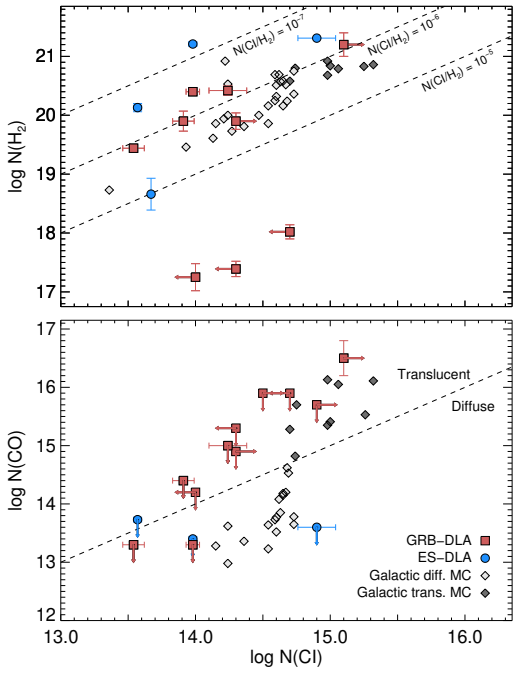

Figure 6.4.1. H_2 (top panel) and CO (bottom panel) vs C I column densities for the GRB molecular gas absorbers studied in this paper. For comparison, we also show a compiled sample of ES-DLAs with a secure detection of H_2 from Guimarães et al. (2012); Noterdaeme et al. (2015b); Balashev et al. (2017); Ranjan et al. (2018), and selected sightlines through diffuse and translucent molecular clouds in the Milky Way (from Burgh et al., 2010). In the top panel, a set of constant C I-to-H_2 abundance ratios are shown for guidance. In the bottom panel, the transition region between diffuse and translucent molecular clouds at $N(\mathrm{C\,I})/N(\mathrm{CO}) = 1$ is shown as well.

6.4 Results

6.4.1 Classification of the molecular gas-phase in GRB hosts

The total set of H I, H_2, C I and CO column densities, the derived gas-phase metallicities, and visual extinctions, A_V, for the GRBs in our sample is provided in Table 6.2.1. All the GRB absorption systems show prominent amounts of neutral atomic hydrogen ($N(\mathrm{H\,I}) > 5\times10^{21}$ cm^{-2}), comparable to the H I content of extremely strong quasar DLAs (ES-DLAs, Noterdaeme et al., 2014, 2015b). This further supports the hypothesis that ES-DLAs probe the neutral gas disc of intervening galaxies in quasar sightlines, similar to GRB-selected absorption systems. We observe a large range of H_2 column densities in the range $N(H_2) = 10^{17.2}$ to $10^{20.5}$ cm^{-2}, which yield integrated molecular fractions, $f_{H_2} = 2N(H_2)/(2N(H_2)+N(\mathrm{H\,I}))$, between $f_{H_2} = 10^{-4.4}$ and $10^{-1.4}$. We caution that in the core of the cloud where H_2 (and C I) is detected, the molecular fraction is likely higher than the integrated value (Balashev et al., 2015) since a fraction of the atomic hydrogen is located in the 'warm' neutral medium (WNM) of the ISM.

To classify the molecular gas-phase observed in GRB hosts, we follow the definition of Burgh et al. (2010). Here, diffuse molecular clouds are defined by having $N(\mathrm{C\,I})/N(\mathrm{CO}) > 1$, where values below are found to trace translucent molecular gas (i.e. the transition between diffuse and dark molecular clouds, see e.g. Snow & McCall 2006). In Fig. 6.4.1 we plot the H_2 measurements and the upper limits on the CO column densities as a function of the total C I column densities for the GRB molecular gas absorbers in our sample. For comparison, we also show a small sample of ES-DLAs

with a secure detection of H_2 (compiled from Guimarães et al., 2012; Noterdaeme et al., 2015b; Balashev et al., 2017; Ranjan et al., 2018), in addition to various diffuse and translucent molecular clouds in Galactic sightlines (from Burgh et al., 2010). We are not able to classify the XS-GRB molecular gas absorption systems studied here based on this classification scheme, but the typical abundance ratios of $N(\mathrm{C\,I})/N(H_2) \approx 10^{-6}$ and the low total $N(\mathrm{C\,I}) < 14.5$ column densities are consistent with originating from diffuse molecular clouds. This is also supported by their CO/H_2 column density ratios and the molecular-hydrogen fractions of the systems (Bolmer et al., 2019). The only exception is the host absorption system of GRB 080607 with a relative abundance ratio of $\log N(CO/H_2) = -4.7 \pm 0.4$, consistent with originating from a translucent molecular cloud (also defined as having $CO/H_2 > 10^{-6}$; Burgh et al. 2010).

We note that in order to observe CO at a detectable level ($\log N(CO) \gtrsim 14$), either an H_2 column density of $\log N(H_2) > 20.5$ is required following the CO to H_2 correlation plot by Sheffer et al. (2008) or a C I column density of $\log N(\mathrm{C\,I}) > 15$ (for diffuse molecular clouds), which would explain the non-detection of CO in the XS-GRB absorbers.

Translucent molecular clouds can also be classified by having $A_V > 1$ mag (Snow & McCall, 2006, see also Sect. 6.4.4). In our sample, only the GRBs 120119A and 180325A (except for GRB 080607) have dust columns consistent with this value. Unfortunately, GRB 120119A is at too low a redshift for the Lyman-Werner bands to enter the observable UV range. For GRB 180325A, the region of the spectrum where the potential Lyman-Werner absorption bands are present is completely suppressed by the high visual extinction (Zafar et al., 2018a; Bolmer et al., 2019).

6.4.2 Detecting neutral atomic carbon in GRB H_2 absorbers

Molecular hydrogen observed in absorption is typically associated with C I in high-redshift QSO-DLA systems (Ge & Bechtold, 1999; Srianand et al., 2005). C I-selected quasar absorbers (Ledoux et al., 2015) have also been shown to always contain H_2 (Noterdaeme et al., 2018). However, C I is not ubiquitous in all H_2-bearing systems. The incidence rate of H_2 in quasar DLAs is of the order $\approx 5-10\%$ (Ledoux et al., 2003; Noterdaeme et al., 2008; Jorgenson et al., 2014; Balashev et al., 2014; Balashev & Noterdaeme, 2018), whereas strong C I absorption features are only found in $\approx 1\%$ of quasar absorbers (Ledoux et al., 2015). In this study, we consistently find that H_2 is always coincident with C I when the Lyman-Werner features are observable (excluding GRBs 120119A and 180325A) in GRB-host absorbers. On the other hand, C I is not detected in all the H_2-bearing GRB-host absorbers (as is the case for GRBs 120327A, 120909A, and 141109A), down to similar limits as derived for the detections.

One explanation could be that H_2-bearing absorbers with low metallicities consequently have less prominent amounts of carbon, below the typical detection threshold. Another possibility is that C I has not been formed significantly in H_2 absorbers with low molecular fractions which consequently provide less shielding, such that the line-of-sight only intersects the outer-most, more diffuse regions of the cloud. To explore the conditions for C I to be detected in the molecular gas-phase further, we examine the molecular-hydrogen fraction, f_{H_2}, of the H_2-bearing GRB absorbers as a function of metallicity in Fig. 6.4.2. For comparison, we overplot the sample of quasar H_2

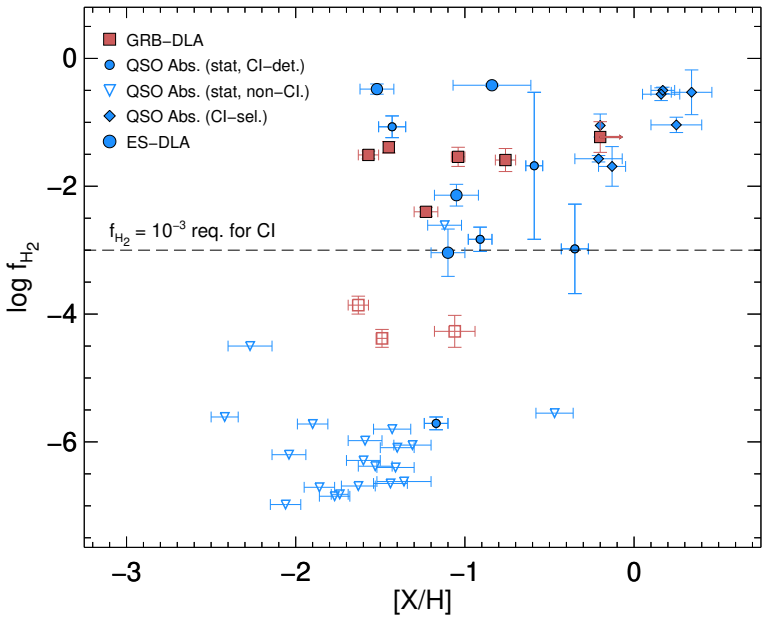

Figure 6.4.2. Molecular-hydrogen fraction as a function of metallicity for the H_2-bearing GRB absorbers (red). Filled squares denote GRBs where C I is also detected, whereas empty squares represent GRBs with H_2 but non-detections of C I. The statistical sample of quasar absorbers from Ledoux et al. (2003) are shown as the small blue symbols where circles denote absorbers with H_2 detections and triangles show the upper limits on the molecular-hydrogen fractions of the absorbers with non-detections of H_2. Filled blue symbols denote quasar absorbers where Srianand et al. (2005) detected C I in absorption, whereas empty blue symbols represent quasar absorbers with non-detections of C I. For comparison, the C I-selected quasar absorbers with measurements of C I, H_2 (Noterdaeme et al., 2018) and metallicities from the literature, are shown as the filled blue diamond symbols. The large blue dots represent the same ES-DLAs as shown in Fig. 6.4.1.

absorbers from Ledoux et al. (2003) for which Srianand et al. (2005) have performed a systematic search for the presence of C I. We also included a sample of C I-selected quasar absorbers with measurements of C I and H_2 (Noterdaeme et al., 2018), and the same sample of ES-DLAs described above. For all the GRB-host absorbers, C I is only detected in systems with molecular fractions above $f_{H_2} > 10^{-3}$. While C I is also only observed in GRB-host absorbers with relative large metallicities ([X/H] $\gtrsim -1.5$), a similar condition appears to be required for the presence of H_2. The presence of C I in GRB H_2 absorbers is, therefore, not specifically related to the metallicity of the systems. From the same samples, we also find that the total column density of C I appears to be linearly correlated with the molecular-hydrogen fraction (see also Noterdaeme et al., 2018). This could indicate that a certain fraction of molecular gas is required to efficiently form and subsequently shield C I. The molecular-hydrogen fraction is therefore likely the primary driver for the presence of C I in H_2-bearing GRB-host absorbers.

6.4.3 The presence of vibrationally-excited H_2

Similar to C I, H_2^* opens a potential route to establish the presence of molecular hydrogen in cases where a direct search for H_2 is not possible. Typical limitations are bursts being at too low redshifts ($z \lesssim 2$) to not cover the wavelength range bluewards of Lyα or significant blending of the Lyman-Werner bands with the Lyα forest in low-resolution spectroscopy (Krühler et al., 2013; Bolmer, 2019). Fully exploiting H_2^* as a molecular gas tracer, however, requires a good understanding of the observable characteristics of the H_2^*-bearing GRB absorbers. In Fig. 6.4.3 we show the positive detections and column densities of H_2^* in GRBs 080607, 120815A, 181020A and 190114A as a function of the H_2 column density and molecular-hydrogen fraction f_{H_2}. Except for GRB 190114A, H_2^* is only detected in GRB absorbers with $\log N(H_2) \gtrsim 20$ and $f_{H_2} > 0.03$. The high S/N afterglow spectrum of GRB 190114A could explain the detection of H_2^* even though the absorber has a ~ 10 times lower H_2 column density and molecular-hydrogen fraction than the other bursts with positive H_2^* detections. We note though that GRBs 121024A and 150403A, both with H_2 column densities and molecular fractions in the same range as GRBs 080607, 120815A, and 181020A, do not show the presence of H_2^* down to $\log N(H_2^*) < 15.7$, which is ~ 5 times less abundant than in the GRB-DLAs 120815A, 181020A, and 190114A.

We additionally examine the dependence on the intrinsic burst luminosity for the detection probability of H_2^*, representing the intensity or amount of photons from the GRB producing the excitation of H_2. We compute the GRB energy output in the observed 15-150 keV *Swift*-BAT band as $E_{\rm BAT} = F_\gamma 4\pi d_L^2 (1+z)^{-1}$ following Lien et al. (2016), where F_γ is the observed BAT fluence in the 15–150 keV band and d_L is the luminosity distance to the bursts at the given redshift. While GRBs 080607 and 181020A are among the most luminous bursts at $z \sim 3$ with $E_{\rm BAT} > 2 \times 10^{53}$ erg (see e.g. Selsing et al., 2019), GRBs 120815A and 190114A are part of the faintest *Swift*-detected population of bursts at their respective redshifts.

This preliminary analysis seems to indicate that the detection probability of H_2^* is likely related to several intrinsic parameters such as GRB luminosity, distance from the bursts to the absorbing molecular gas and the observational difficulty to detect H_2^* with a typical low relative abundance compared to H_2 of $N(H_2^*)/N(H_2) \sim 10^{-4}$. This will be explored further in a follow-up paper (Bolmer et al. in preparation).

6.4.4 The connection between dust and molecular gas

The amount of C I has been observed to be correlated with the visual extinction, A_V, in the line of sight to quasar and GRB absorbers (Ledoux et al., 2015; Ma et al., 2018; Heintz et al., 2019a), suggesting a common origin for the main extinction-derived dust component and C I (see also Heintz et al., 2019b). In Fig. 6.4.4, we compare the measured A_V of the H_2-bearing GRB-host absorbers to the relative molecular gas abundance ratios, in terms of f_{H_2} and $N(\text{C I}/H_2)$. For comparison, the ES-DLAs with positive H_2 detections compiled from the literature are also shown, in addition to Galactic molecular-rich sightlines from the sample of Burgh et al. (2010), divided into populations of translucent or diffuse molecular clouds.

For the GRB-host absorbers, we note that there is tentative evidence for a relation

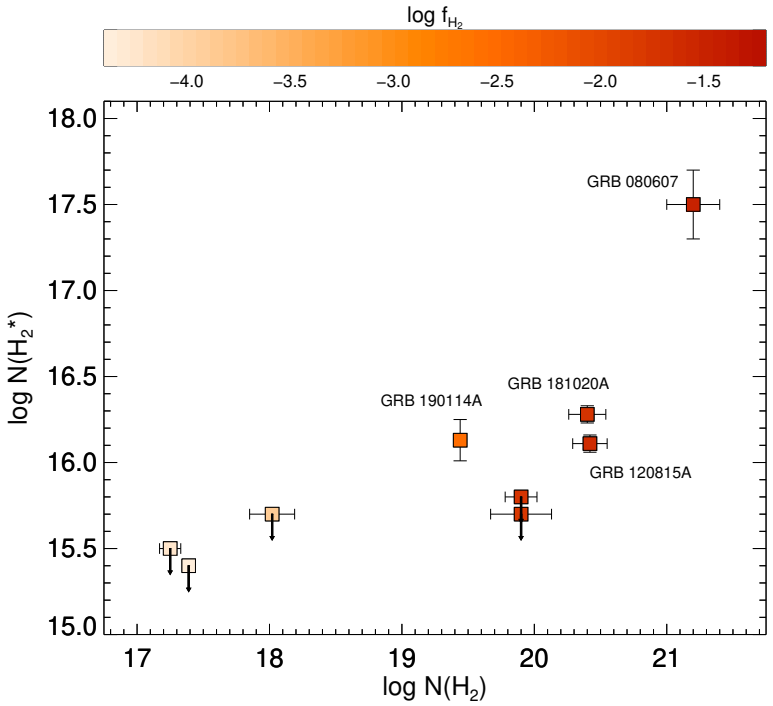

Figure 6.4.3. Vibrationally-excited H_2 (H_2^*) vs column densities of H_2 in the H_2-bearing GRB absorbers, color-coded as a function of the measured molecular fraction f_{H_2}. The four GRB systems with positive detections of H_2^* are marked individually.

between the molecular-hydrogen fraction, f_{H_2}, and A_V. As an example, GRB 080607 shows the largest dust content and highest molecular-hydrogen fraction in our sample. Computing the Kendall-rank correlation coefficient τ for f_{H_2} vs A_V yields $\tau = 0.5$. The significance of the correlation is therefore only 1.7σ. We also note that there is tentative evidence for a relation between the relative C I/H_2 abundance ratio and A_V, with $\tau = 0.6$ at 1.5σ confidence, including only the GRB-host absorber with C I detected in absorption. This analysis is limited by the small number of systems in our sample and the small range of (small) A_V values, however, such that the derived correlations only hint at a possible connection between the amount of dust and the relative molecular gas abundance ratios. We note though, that the relatively steep rise and subsequent flattening of the relative C I-to-H_2 abundance ratio at $A_V = 0.5$ mag is consistent with the expected transition regime where C II is converted to C I (Bolatto et al., 2013).

6.4.5 Kinematics

Direct localization of the absorbing molecular gas and the explosion sites in the GRB host galaxies would provide valuable information of the immediate physical conditions of the absorbing medium. At high redshifts, however, it is challenging to obtain deep

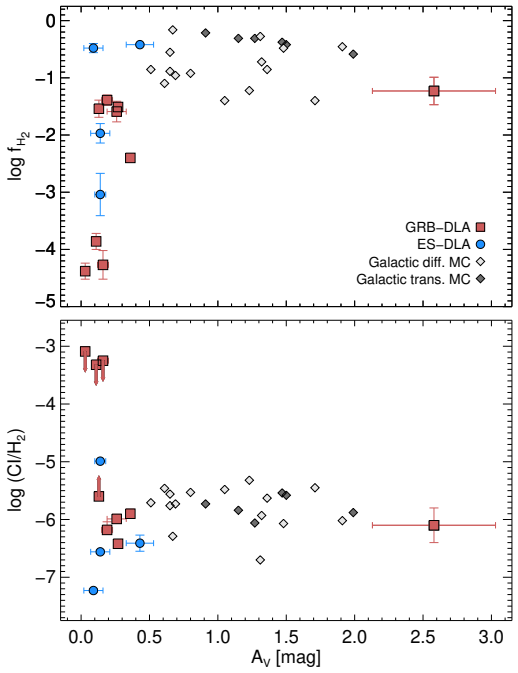

Figure 6.4.4. Molecular-hydrogen fraction and C I/H_2 as a function of visual extinction, A_V. Red squares represent the GRBs from this work. The large blue dots represent the same ES-DLAs as shown in Fig. 6.4.1. Diamond symbols show Galactic sightlines where dark gray-filled (resp. light gray-filled) symbols denote diffuse (resp. translucent) molecular clouds (Burgh et al., 2010).

resolved images, which is required to map the varying galaxy properties accurately (but see e.g. McGuire et al., 2016; Lyman et al., 2017). As an alternative, we can examine the relative velocity of the C I and H_2 absorption line profiles tracing the molecular gas and compare them to the peak optical depth of the other typically observed line complexes originating from distinct gas-phase components of the ISM. Here we assume that each velocity component represents a discrete cloud in the host galaxy, located in the line of sight to the GRB. Specifically, we compare the H_2 and C I absorption components to the line profiles from singly-ionized fine-structure transitions (typically Fe II*), and low-ionization (typically Fe II, Cr II, Mn II, or Si II) and high-ionization (N V) metal lines. The relative velocity of fine-structure lines in GRB afterglow spectra carry information on the absorbing gas UV-pumped by the GRB (typically at distances 0.1 – 2 kpc from the explosion site, e.g. Vreeswijk et al., 2007; D'Elia et al., 2011). The bulk of the metals in the neutral gas-phase of the GRB-host absorption systems is traced by the low-ionization metal lines, whereas the high-ionization lines (specifically N V) have been argued to trace gas in the vicinity of the GRB (within 10 pc; Prochaska et al., 2008b; Heintz et al., 2018b).

We find that in the majority of bursts, the relative velocity of the observed H_2 and C I line profiles are kinematically 'cold', being offset by less than $\delta v \lesssim 20\,\mathrm{km\,s^{-1}}$ from the strongest low- and high-ionization and fine-structure line components. Due to the medium resolution of the data, these low offsets should be treated as being consistent with zero. By association, we argue that the different gas-phase components probed by the various lines suggest that they originate from the same approximate region as the bulk of the neutral gas. The fact that N V is coincident with the bulk of the neutral

absorbing gas in these GRB-host absorption systems is, however, likely due to their high N(H I), which might confine the gas to the central regions of the host galaxy (Heintz et al., 2018b) and is likely related to the GRB event itself.

The two exceptions are GRBs 121024A and 150403A. Friis et al. (2015) showed that for GRB 121024A, the redshift of the Lyman-Werner lines of molecular hydrogen is coincident with the strongest low-ionization metal components, which we also confirm from the C I line profiles. However, the absorption profiles reveal an additional metal line complex at $\delta v \approx -400\,\mathrm{km\,s^{-1}}$ which in turn is coincident with the fine-structure line transitions from Fe II* and Ni II*. The absorbing molecular gas in the GRB host is therefore likely at even greater distances from the explosion site than the gas photoexcited by the GRB (which was found to be at a distance of ≈ 600 pc; Friis et al., 2015). For GRB 150403A, we find that the peak optical depth of C I is coincident with the strongest components from the low-ionization and fine-structure lines, but offset by $\delta v \approx -30\,\mathrm{km\,s^{-1}}$ from N V (see also Heintz et al., 2018b).

6.5 Discussion

We have now established that GRB-host absorbers can be used to probe the diffuse molecular gas-phase in their high-z star-forming galaxies. Additionally, we were able to quantify the defining characteristics of the subset of H_2-rich absorbers showing the presence of C I and H_2^*. This section is aimed at further understanding the physical properties of the molecular gas in high-z GRB absorbers and explore the possible consequence of a severe dust bias in the detection of H_2-bearing GRB absorbers.

6.5.1 Excitation temperature

One of the key physical properties of the cold neutral medium (CNM) is the temperature, which is typically found to be in the range 30 – 100 K for diffuse molecular clouds (Snow & McCall, 2006). For the H_2-bearing GRB-host absorbers we can infer the excitation temperature of the molecular gas from

$$\frac{N(\mathrm{H_2}, j)}{N(\mathrm{H_2}, i)} = \frac{g(\mathrm{H_2}, j)}{g(\mathrm{H_2}, i)} \exp^{-E_{ij}/kT_{ij}}\,, \tag{6.2}$$

where g is the spin statistical weight $g(j) = 2j + 1$, E_{ij} is the energy difference between levels i and j, and T_{ij} is the excitation temperature. The temperature determined from the lowest two rotational levels ($J = 0$ and $J = 1$), T_{01}, is found to be a good representation of the overall kinetic temperature of the thermalized molecular gas (Roy et al., 2006), whereas higher rotational levels typically indicate larger excitation temperatures due to molecule formation and/or UV pumping.

For the GRBs 120815A, 121024A, 150403A, 181020A, and 190114A, where the H_2 column densities in the two lowest rotational states are well constrained, we are able to robustly measure $T_{01} = T_{\mathrm{kin}}$. For the other systems with H_2 detections (i.e. GRBs 120327A, 120909A, and 141109A), the $J = 0$ state is not well constrained by the fit. For these bursts, the derived T_{01} becomes negative, which could suggest that the assumption of equilibrium may not be correct in these cases. To overcome this,

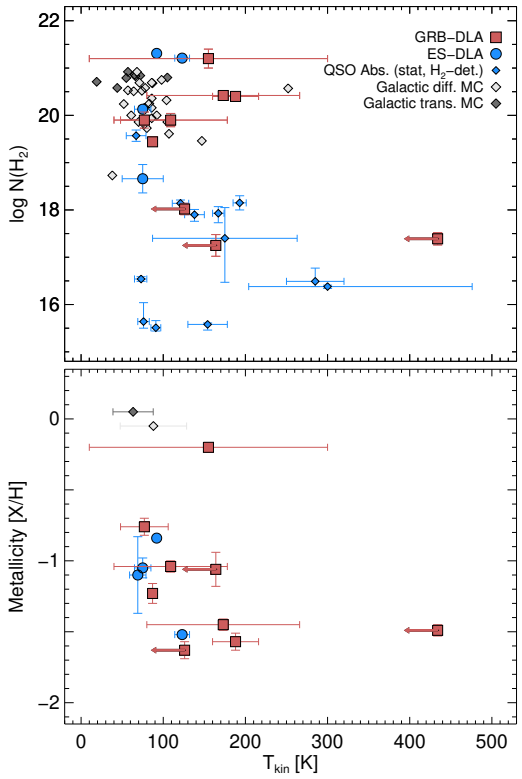

Figure 6.5.1. Measurements of the kinetic temperature from the H_2 rotational excited states as a function of total H_2 column density (top) and metallicity (bottom). Red squares represent the GRBs from this work, where the arrows mark the upper limits on $T_{\rm kin}$ derived from T_{12} (see text). The small blue diamond symbols denote quasar DLAs from the sample studied by Srianand et al. (2005), where large blue dots represent the same ES-DLAs shown in Fig. 6.4.1. The grey-shaded diamond symbols in the top panel again show selected sightlines through diffuse and translucent molecular clouds in the Milky Way (from Burgh et al., 2010). In the bottom panel, only the strongest DLAs with $N(\mathrm{H\,I}) > 10^{21.7}$ cm^{-2} are shown. The grey-shaded diamond symbols here represent the mean $T_{\rm kin}$ for Galactic diffuse and translucent molecular clouds (with error bars denoting the standard deviation), arbitrarily placed at solar metallicities.

we instead compute the excitation temperature from the first two excited states, T_{12}, but only consider those as upper limits for the kinetic temperature since it is typically found that $T_{12} > T_{01}$ (e.g. Srianand et al., 2005). For GRB 080607, Prochaska et al. (2009) estimated an excitation temperature in the range $T_{\rm ex} = 10 - 300$ K. The inferred molecular gas temperatures and upper limits are shown in Fig. 6.5.1 as a function of $N(H_2)$. Here, we also compare the GRB H_2 absorbers to the H_2-bearing quasar absorbers examined by Srianand et al. (2005), the sample of H_2-bearing ES-DLAs and Galactic molecular clouds (Burgh et al., 2010). In general, the H_2-bearing GRB absorbers contain the largest H_2 column densities observed at high redshift, comparable to quasar ES-DLAs and Galactic molecular clouds. We infer kinetic temperatures in the range $T_{\rm kin} \approx 100 - 300$ K, consistent with the majority of H_2-bearing quasar absorbers (Srianand et al., 2005; Balashev et al., 2017). We note that there appears to be tentative evidence for the highest metallicity GRB-host and ES-DLA systems to show lower excitation temperatures at a given H_2 column density (see Fig. 6.5.1), but only at low significance due to the limited data at hand. Computing the Spearman ρ and Kendall-rank τ correlation coefficients for $T_{\rm ex}$ vs [X/H] yield $\rho = -0.67$ and $\tau = -0.49$, such that the correlation significance is 2.01σ (considering only the measurements and excluding limits).

We also examine the higher rotational transitions of H_2 in the afterglow spectra of

GRBs 181020A and 190114A, which might provide clues on the more external layers of the cloud and the incident UV flux. The column densities of the $J \geq 4$ transitions are not well-constrained in either case, so instead of fitting the individual line transitions we produce a synthetic spectrum, including all J transitions up to $J = 7$, to match to the data. For both GRBs, we fix the redshift, the b-parameter and total H_2 column density to the already-determined values and only increase the excitation temperature. We caution that assuming a single b-parameter for the low- and high-J levels might be erroneous (see e.g. Noterdaeme et al., 2007). However, given the intermediate resolution of the spectra we are not able to constrain the higher J levels independently so the results should only be considered as indicative. For GRB 181020A, the spectrum does not show any indication of features arising from $J \geq 4$ transitions below the continuum, suggesting that none of the high-J transitions are significantly populated (consistent with $T_{\rm ex} \lesssim 200$ K). For GRB 190114A, we find that the spectrum is consistent with high-J features arising from a warmer medium, constrained to $T_{\rm ex} \lesssim 300$ K. This would indicate that the intensity of the ambient UV field in the host of GRB 190114A is higher compared to the host of GRB 181020A. It is in principle possible to indirectly measure the ambient UV flux from the fine-structure transition of C II* λ1335 (Wolfe et al., 2003). However, in both the afterglow spectra of GRBs 181020A and 190114A this feature is either saturated or blended with C II λ1334.

6.5.2 The implications of a dust bias for the detection of H_2

With the increased number of known H_2-bearing GRB absorbers, it is clear that the first apparent bias against this subpopulation (Tumlinson et al., 2007; Whalen et al., 2008; Ledoux et al., 2009) is partly alleviated. This is largely owing to the more sensitive, higher-resolution X-shooter spectrograph, with which a large statistical sample of GRBs has been obtained (Selsing et al., 2019). Expanding the discussion from Krühler et al. (2013), we now wish to quantify to what extent the XS-GRB sample is biased against the most metal- and dust-rich H_2-bearing GRB-host absorption systems. Specifically, if there exists a significant dust bias decreasing the H_2 detection probability in these systems.

To do so, we compare the A_V distribution of the statistical sample of XS-GRBs, from which Bolmer et al. (2019) searched for H_2, to an unbiased sample of GRB afterglows (Covino et al., 2013). We normalize the two distributions to the number of bursts with $A_V < 0.2$ mag (which we expect the XS-GRB sample to at least be complete to) and compute the fraction of H_2-bearing GRBs to the number of bursts in the unbiased sample in bins of $A_V = 0.2 - 0.5$, $0.5 - 1.0$, and $1.0 - 2.5$ mag. We find that already at $A_V = 0.2 - 0.5$ mag, the detection probability of the bursts in the XS-GRB sample only constitutes $\sim 25\%$ of the underlying distribution. At $A_V = 0.5 - 1.0$ mag we estimate the fraction of uncovered GRB H_2 absorbers to be $\sim 5\%$, based only on the detection of C I in GRB 120119A which was not part of the statistical H_2 sample so this fraction effectively only serves as an upper limit. Similarly for the $A_V = 1.0 - 2.5$ mag range, we estimate the detection probability to be 2%, based on the single detection of H_2 in GRB 080607 in the unbiased sample of ~ 50 bursts by Covino et al. (2013). Again, the detection probability is likely lower since none of the H_2-bearing XS-GRBs show A_V in this range. This is illustrated in Fig. 6.5.2, where we show the metallicity as a function

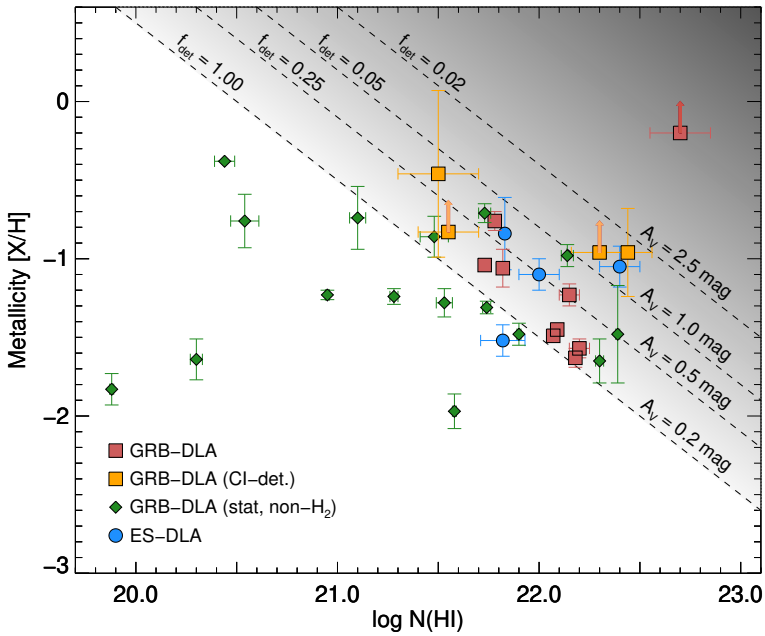

Figure 6.5.2. Gas-phase metallicity as a function of H I column density. Filled red squares represent the GRBs from this work with positive H_2 detections, orange squares denote C I-bearing GRBs (where H_2 could not be constrained) from this work or Heintz et al. (2019a) and the green diamond symbols show the statistical GRB-DLA sample from Bolmer et al. (2019) without H_2 detections. For comparison, the large blue dots show the same ES-DLAs as shown in Fig. 6.4.1. The gray-shaded region and overplotted dashed lines show the expected increase in A_V for a given dust-to-metals ratio, in addition to the estimated detection probability $f_{\rm det}$ of dusty H_2-bearing GRB absorbers (see Sect. 6.5.2 for further details).

of H I column density of the GRB absorbers and compare to the expected dust extinction for a given dust-to-metals ratio (Zafar & Watson, 2013). These estimates do not take into account the increased difficulty of detecting H_2 in faint bursts (either intrinsically or due to overall stronger dust absorption) and also do not include the possibility of steep extinction curves. For example, GRB 140506A (Fynbo et al., 2014; Heintz et al., 2017) would be practically invisible at optical wavelengths if it were located at $z \gtrsim 2$. The dust bias in the observed XS-GRB sample might therefore be even more severe than the simple estimates provided here.

We wish to emphasize though, that if a spectrum of a burst similar to GRB 180325A (with strong C I absorption and $A_V \sim 1.5$ mag) was obtained with higher S/N spectroscopy, the H_2 features might have been revealed as well. Conversely, this further demonstrates the versatility of using C I as an alternative tracer of molecular gas, even in very dust-reddened sightlines. We conclude that the large majority of dusty ($A_V > 0.2$ mag) H_2-bearing GRBs are missed due to a significant dust bias. This confirms the proposal by Ledoux et al. (2009), that GRB-host absorber samples are likely to be biased against dusty and metal-rich sightlines. Only in the cases of rare, extremely

luminous afterglows (such as GRB 080607; Prochaska et al., 2009; Perley et al., 2011) is it possible to detect H_2 in the most dust-obscured afterglows.

6.6 Conclusions

We have presented optical to near-infrared VLT/X-shooter spectra of the afterglows of GRBs 181020A and 190114A at $z = 2.938$ and $z = 3.376$, respectively. Both sightlines are characterized by strong DLAs and substantial amounts of molecular hydrogen with $\log N(\mathrm{H\,I}, \mathrm{H_2}) = 22.20 \pm 0.05,\ 20.40 \pm 0.04$ (GRB 181020A) and $\log N(\mathrm{H\,I}, \mathrm{H_2}) = 22.15 \pm 0.05,\ 19.44 \pm 0.04$ (GRB 190114A). Both GRB-host absorption systems show relatively high molecular fractions of $f_{\mathrm{H_2}} = 0.4 - 3\%$, characteristic of Galactic diffuse molecular gas and consistent with the majority of H_2-bearing quasar absorbers at high-z. These two cases represent only the eighth and ninth unambiguous detection of H_2 in GRB-host absorption systems. We measure gas-phase metallicities of [Zn/H] $= -1.57 \pm 0.06$ and -1.23 ± 0.07, relative depletion abundances of [Zn/Fe] $= 0.67 \pm 0.03$ and 1.06 ± 0.08, and visual extinctions of $A_V = 0.27 \pm 0.02$ mag and 0.36 ± 0.02 mag, for GRB 181020A and GRB 190114A, respectively. While the metallicities of the two systems are relatively low and comparable to typical GRB-host absorbers, their metal column densities, $\log N(\mathrm{H\,I})$ + [Zn/H], are among the highest in the general GRB-host absorber population. They are also both well above the apparent GRB H_2 detection threshold of $\log N(\mathrm{H\,I})$ + [Zn/H] > 20.5 (Bolmer et al., 2019).

In addition to molecular hydrogen, we also detect absorption features from neutral atomic carbon and vibrationally-excited H_2 in both afterglow spectra of GRBs 181020A and 190114A. To complement the analysis of these alternative molecular gas tracers, and to explore the conditions for these rarer absorption features to arise, we systematically searched all the H_2-bearing GRB absorbers from Bolmer et al. (2019) for the presence of C I or H_2^* and measured or provided limits on the respective column densities. We found that C I and H_2^* are efficient tracers of H_2-rich GRB-host absorbers, but also that H_2 does not guarantee the presence of either. First, we explored the conditions required to detect C I in the H_2-bearing GRB absorbers and we found that an apparent threshold of the overall molecular-hydrogen fraction of $f_{\mathrm{H_2}} > 10^{-3}$ is essential. The total C I column density is also found to be linearly connected with $f_{\mathrm{H_2}}$. The defining characteristic for the presence of H_2^* is less clear, likely because it depends on several parameters such as the H_2 abundance, GRB luminosity and distance to the absorbing molecular gas. This somewhat limits the applications of C I and H_2^* as overall efficient molecular gas tracers. On the other hand, identifying absorption features from C I or H_2^* provides indirect evidence of large H_2 abundances, even in the absence of the Lyman-Werner H_2 features (e.g. due to low redshifts, large dust content or low spectral resolution). We also compared the kinematics of the absorption lines from the molecular gas tracers C I and H_2 to the low- and high-ionization and fine-structure absorption features typically observed in GRB-host absorbers. We found that C I and H_2 are in most cases kinematically 'cold', thus likely confined to the same proximate region as the bulk of the metals producing the strongest low- and high-ionization absorption features.

Based on the now nine positive detections of H_2 in GRB-host absorbers, we examined the typical excitation temperatures of the molecular gas, constrained from the

two lowest rotational levels of H_2 ($J = 0, 1$). For the systems in our sample we inferred temperatures in the range $T_{ex} = 100 - 300$ K. Finally, we determined the probability of detecting H_2 in the XS-GRB afterglow sample (Selsing et al., 2019) as a function of A_V. Even in moderately extinguished sightlines with $A_V \gtrsim 0.2$ mag, the number density of GRB H_2 absorbers drops to $\sim 25\%$ compared to an unbiased sample of GRB afterglows. This suggests that while the XS-GRB afterglow survey has been successful in recovering a significant number of H_2-bearing GRB absorbers (Bolmer et al., 2019), the most dust-obscured systems are still missed due to a non-negligible dust bias.

In summary, GRB-host absorbers provide detailed information about the characteristics and physical properties of the diffuse molecular gas-phase in the ISM of star-forming galaxies during the peak of cosmic star-formation. While the absorption features of the molecular gas tracers are typically only detected at UV/optical wavelengths, there are promising prospects of detecting them at sub-mm wavelengths in ALMA spectroscopy as well (de Ugarte Postigo et al., 2018). Connecting the properties inferred from absorption-line analyses to the CO line emission at sub-mm wavelengths would also provide unparalleled insight into the conditions and physical processes fuelling star-formation at high redshift. So far, only a small number of high-z GRB host galaxies have been detected in emission from CO (Michałowski et al., 2018; Arabsalmani et al., 2018a), though without any constraints on the molecular gas properties from absorption. Targeting the CO emission lines of this sample of H_2-bearing GRB-host galaxy absorbers would provide a natural unification of the two approaches. In the near future, identification of the vibrational and ro-vibrational H_2 emission lines will also be possible with the *James Webb Space Telescope* (Kalirai, 2018) at $z \gtrsim 2$ where H_2 can be detected in absorption (Guillard et al., 2015), which so far has only been detected in a single, $z \sim 0.1$ GRB host (Wiersema et al., 2018). This combined analysis of molecular gas in line-of-sight GRB afterglow spectra and integrated host galaxy spectra will also greatly benefit the typically more extensive emission-selected CO galaxy surveys, and significantly improve our understanding of the connection between cold and molecular gas observed in absorption and emission.

Acknowledgements

KEH and PJ acknowledge support by a Project Grant (162948–051) from The Icelandic Research Fund. PN and JKK acknowledge support from the French *Agence Nationale de la Recherche* under contract ANR-17-CE31-0011-01 (Projet "HIH2", PI Noterdaeme) and are grateful to the European Southern Observatory for hospitality and support during a visit to the ESO headquarters in Chile. The Cosmic Dawn Center is funded by the DNRF. AdUP, CCT, DAK and LI acknowledge support from the Spanish research project AYA2017-89384-P, and from the State Agency for Research of the Spanish MCIU through the "Center of Excellence Severo Ochoa" award for the Insituto de Astrofísica de Andalucía (SEV-2017-0709). AdUP and CCT acknowledge support from Ramón y Cajal fellowships (RyC-2012-09975 and RyC-2012-09984). LI acknowledges support from a Juan de la Cierva Incorporación fellowship (IJCI-2016-30940).

Appendix

6.6.1 Gas-phase abundances and dust extinction toward GRBs 181020A and 190114A

Here are shown a subset of the low-ionization metal lines observed in the afterglow spectra of GRB 181020A (Fig. 6.6.1) and GRB 190114A (Fig. 6.6.2). We fitted several other transitions, including single-ionized elements not shown in these plots to constrain the velocity components of the absorption line profiles. However, we here only show few selected lines that best represent the overall velocity structure of the line profiles and focus on the elements used to determine the gas-phase abundance and depletion (e.g. Zn II and Fe II). In Figs. 6.6.3 and 6.6.4 we show the best-fit extinction observed toward GRBs 181020A and 190114A, respectively. Both sightlines can be modelled by a smooth, SMC-like extinction curve and are moderately reddened with $A_V = 0.27 \pm 0.02$ mag and $A_V = 0.36 \pm 0.02$ mag, respectively.

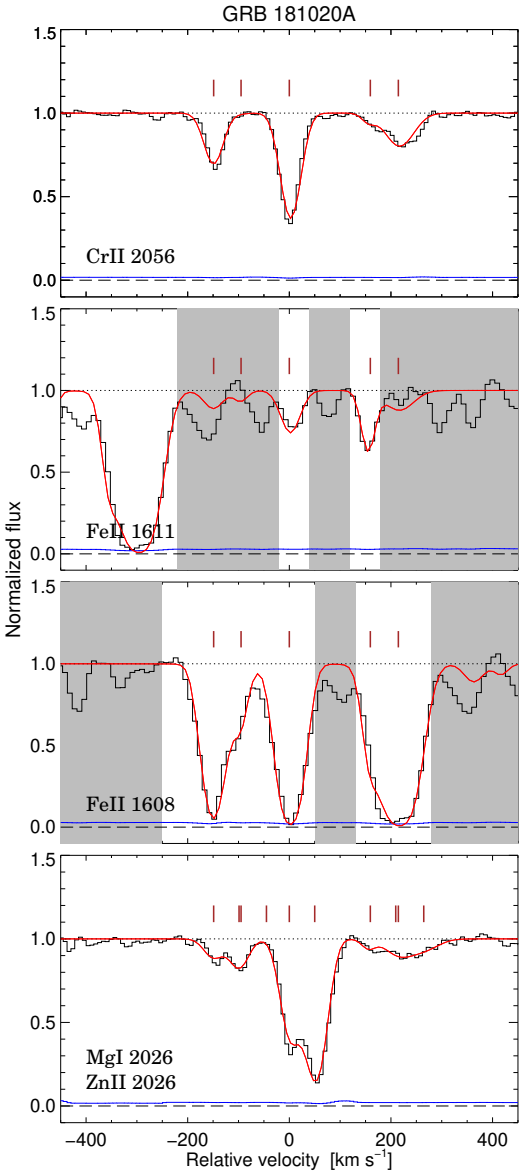

Figure 6.6.1. Normalized VLT/X-shooter spectrum of GRB 181020A in velocity space, centred on the strongest component at $z = 2.9379$. The black solid line shows the spectrum and the associated error is shown in blue. The best-fit Voigt profiles are indicated by the red solid lines. The identified velocity components are marked above each of the absorption profiles. Gray shaded regions were ignored in the fit. These lines are representative of the typical low-ionization metal lines in GRB 181020A, showing most clearly the overall velocity structure.

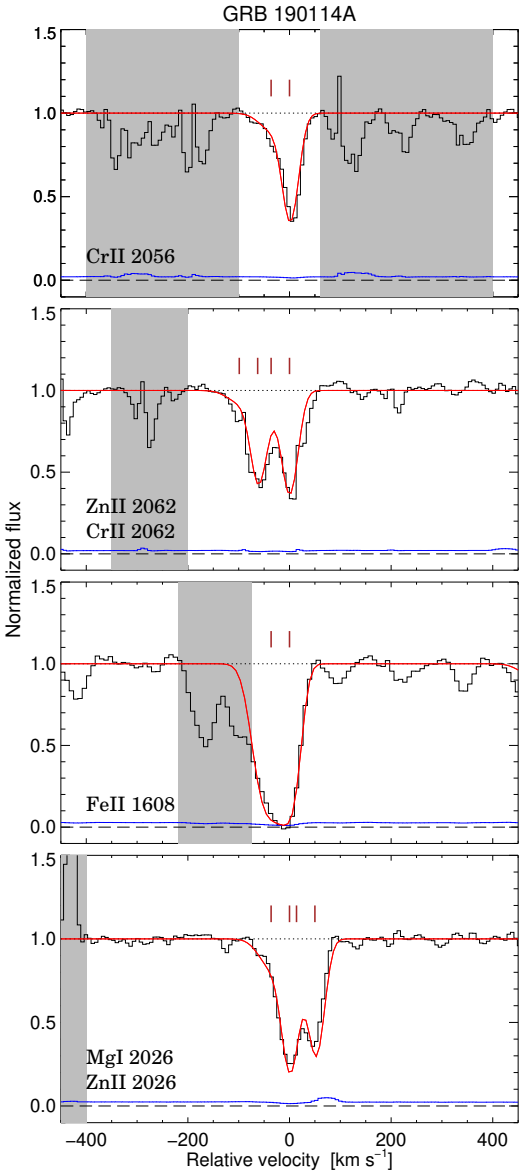

Figure 6.6.2. Same as Fig. 6.6.1 but for GRB 190114A, centred on z = 3.3764.

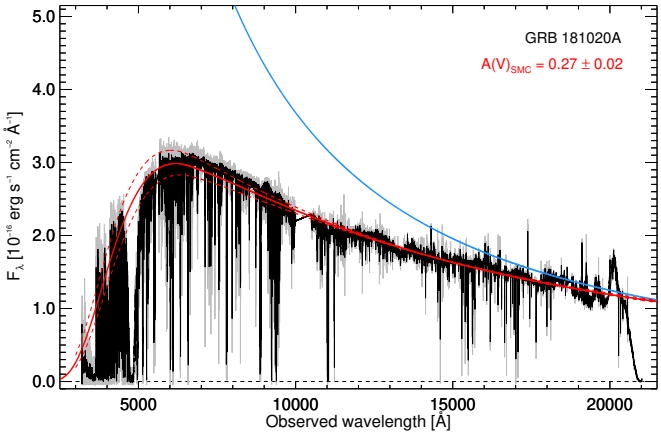

Figure 6.6.3. Extinction curve fit for GRB 181020A. The raw combined VLT/X-shooter spectrum is shown in grey, overplotted with a binned version to enhance the continuum trace. The best-fit SMC-like extinction with $A_V = 0.27 \pm 0.02$ mag is shown by the red solid line, where the error on the fit is shown by the red dashed lines. The best-fit intrinsic spectral slope is overplotted as the solid blue line.

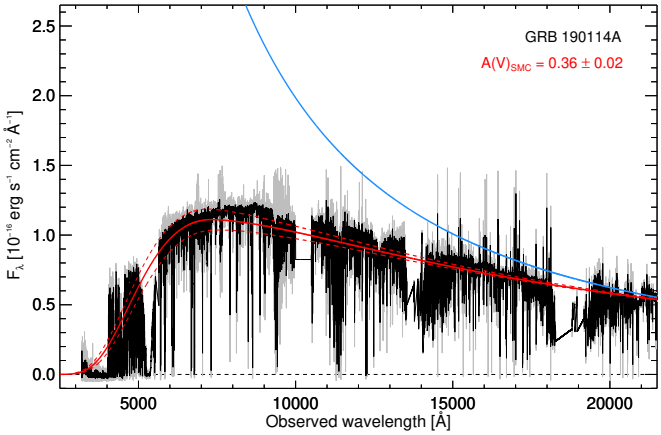

Figure 6.6.4. Same as Fig. 6.6.3 but for GRB 190114A, with a best-fit SMC-like extinction of $A_V = 0.36 \pm 0.02$ mag.

6.6.2 Individual notes on sample XS-GRBs

Here we provide notes on each individual burst studied in this work. Since we extracted information about the gas-phase abundance and dust extinction from the literature for all our sample bursts, we will mainly focus on the C I line measurements. For all cases, we only detect a single absorption component from C I but we caution that at this spectral resolution, the observed line profiles might actually be comprised of several narrow lines. However, the fits to H_2 for most of the GRBs also indicate that only one component from the molecular-gas phase is present in the spectrum. Any intrinsically narrow absorption components contributing significantly to the observed column densities, would also be present at the location of CO but we do not find any evidence of this.

By modelling a set of synthetic spectra with imposed C I lines with varying b-parameters and N(C I), we estimate that the line profiles are intrinsically saturated for $N(\mathrm{C\,I})_{\mathrm{tot}} \gtrsim 14.5$ (for $b \gtrsim 5\,\mathrm{km\,s^{-1}}$). This is also supported by the typical uncertain broadening parameters associated with the GRBs having the largest C I column densities. For the GRB absorbers where the best-fit value for N(C I) is above this limit (GRBs 120119A, 150403A, and 180325A), we therefore only provide the 2σ lower limit on the C I abundances. For the GRB absorption systems with $N(\mathrm{C\,I}) < 14.5$ (GRBs 120815A, 121024A, 181020A, and 190114A) we report the measured value for each of the C I abundances. These are also all consistent with the linear relation found for the quasar C I absorbers in Sect. 6.3 (see Fig. 6.3.7) between $N(\mathrm{C\,I})_{\mathrm{tot}}$ and the rest-frame C I equivalent widths of the same systems. To further verify the robustness of the column density measurements we produce a set of synthetic spectra with varying b-parameters and perform the same fitting routine as detailed in Sect. 6.3.4. We are able to recover the input column densities (for non-saturated lines) within the error for all values of $b \gtrsim 2\,\mathrm{km\,s^{-1}}$.

GRB 120119A at $z = 1.7288$

The spectrum presented here was published by Selsing et al. (2019). The gas-phase abundances listed in Table 6.2.1 derived for this GRB are adopted from Wiseman et al. (2017). They found $\log N(\mathrm{H\,I}) = 22.44 \pm 0.12$, [Zn/H] = -0.96 ± 0.28 and [Zn/Fe] = 1.04 ± 0.35. Following De Cia et al. (2016) we compute a dust-corrected metallicity, [M/H] = [X/H] - δ_X (where δ_X is inferred from the iron-to-zinc depletion), of [M/H] = 0.68 ± 0.30. Both Japelj et al. (2015) and Zafar et al. (2018b) have derived the visual extinction of this GRB and found a consistent value of $A_V \sim 1$ mag. We chose to adopt A_V from the latter study (listed in Table 6.2.1), since they included a full parametrization of the extinction curve in the fit. It was not possible to examine H_2 in this absorption system due to the low redshift.

To fit the neutral atomic carbon abundances for this GRB we ran two iterations; one where b is left as a free parameter and one where we fix the b-parameter to $5\,\mathrm{km\,s^{-1}}$. The fit was only constrained by the C I $\lambda\lambda$ 1560,1656 line transitions since the C I $\lambda\lambda$ 1277,1328 lines were completely blended with telluric absorption features and located in spectral regions with poor S/N. We also masked out one unrelated line in the immediate continuum region of the C I λ 1560 transition, although it does not appear to be blended with the line profiles. We obtain a best-fit b-parameter of $b = 2.9 \pm 0.5\,\mathrm{km\,s^{-1}}$. However, given the S/N of the spectrum we are not able to

Table 6.6.1. Results of the Voigt-profile fitting for GRB 120119A. The column densities for $b = 5\,\mathrm{km\,s^{-1}}$ are reported throughout.

Exc. state (J)	$\log N(\mathrm{C\,I})$ $b = 2.9 \pm 0.5$ ($\mathrm{km\,s^{-1}}$)	$b = 5$ ($\mathrm{km\,s^{-1}}$)
C I	16.85 ± 0.28	15.10 ± 0.51
C I*	16.34 ± 0.66	14.16 ± 0.16
C I**	16.75 ± 0.46	15.13 ± 0.25

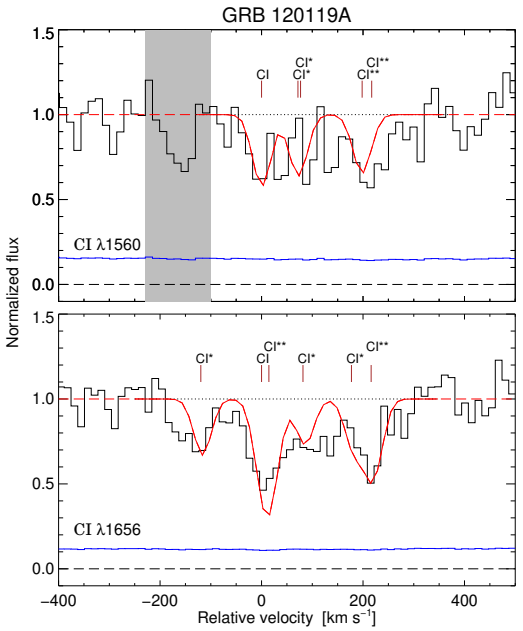

Figure 6.6.5. Normalized VLT/X-shooter spectrum of GRB 120119A in velocity space, centred on the ground-state C I transitions at $z = 1.72912$. The black solid line shows the spectrum and the associated error is shown in blue. The combined best fit Voigt profiles (with fixed $b = 5\,\mathrm{km\,s^{-1}}$) are indicated by the red solid line, with the red dashed line indicating the continuum. The C I ground-state and excited line transitions are marked above each of the absorption profiles. The gray shaded region was ignored in the fit.

distinguish which fit is preferred for $b \lesssim 5\,\mathrm{km\,s^{-1}}$. The derived column densities for both b-parameters are listed in Table 6.6.1. Since the b-parameter cannot be well-constrained we assume $b = 5\,\mathrm{km\,s^{-1}}$ and derive a 2σ lower limit of $\log N(\mathrm{C\,I})_{\mathrm{tot}} \gtrsim 14.9$ for this GRB. This lower limit takes into account both the uncertain line broadening and the intrinsically saturated line profiles. The best fit Voigt profiles are shown overplotted on the normalized VLT/X-shooter spectrum in Fig. 6.6.5 for $b = 5\,\mathrm{km\,s^{-1}}$.

GRB 120327A at $z = 2.8143$

The spectrum presented here was first published by D'Elia et al. (2014), who also reported the presence of H_2 in the spectrum. The neutral and molecular gas-phase abundances listed in Table 6.2.1 derived for this GRB are adopted from Bolmer et al. (2019). They found $\log N(\mathrm{H\,I}) = 22.07 \pm 0.01$, $\log N(\mathrm{H_2}) = 17.39 \pm 0.13$, [Zn/H] =

Table 6.6.2. Results of the Voigt-profile fitting for GRB 120815A.

Exc. state (J)	$\log N$(C I) $b = 2.3 \pm 0.5$ (km s^{-1})	$b = 5$ (km s^{-1})
C I	13.94 ± 0.26	13.35 ± 0.16
C I*	13.62 ± 0.14	13.52 ± 0.11
C I**	13.66 ± 0.22	13.57 ± 0.12

-1.49 ± 0.03 and [Zn/Fe] = 0.27 ± 0.07, resulting in a dust-corrected metallicity of [M/H] = -1.34 ± 0.02. D'Elia et al. (2014) derived an upper limit on the visual extinction along the line of sight to this GRB of $A_V < 0.03$ mag. We find no evidence for C I in this absorption system (see also Heintz et al., 2019a), and derive a 2σ upper limit of $\log N(\mathrm{C\,I})_{\mathrm{tot}} < 14.3$ assuming $b = 2\,\mathrm{km\,s^{-1}}$.

GRB 120815A at $z = 2.3582$

The spectrum presented here was first published by Krühler et al. (2013), who also reported the presence of H_2 and C I in the spectrum. The neutral and molecular gas-phase abundances listed in Table 6.2.1 derived for this GRB are adopted from Bolmer et al. (2019). They found $\log N(\mathrm{H\,I}) = 22.09 \pm 0.01$, $\log N(\mathrm{H_2}) = 20.42 \pm 0.08$, [Zn/H] = -1.45 ± 0.03 and [Zn/Fe] = 1.01 ± 0.05, resulting in a dust-corrected metallicity of [M/H] = -1.23 ± 0.03. We adopt the visual extinction derived by Zafar et al. (2018b) of $A_V = 0.19 \pm 0.04$ mag.

To fit the neutral atomic carbon abundances for this GRB we ran the same two iterations as for GRB 120119A. Since we only detect a single absorption component from the C I λ 1328 line complex, we fixed this in the fit to the C I $\lambda\lambda\lambda$ 1328,1560,1656 line transitions. The C I λ 1277 line was only used to constrain the upper limit on the column density since it is significantly blended with unrelated features. For the line transitions at C I $\lambda\lambda$ 1560,1656 we also masked out regions of the spectrum showing unrelated absorption features, which were excluded as potential additional velocity components based on the identification in the C I λ 1328 line complex. We obtain a best-fit b-parameter of $b = 2.3 \pm 0.5\,\mathrm{km\,s^{-1}}$. The line profiles seem to exclude values of $b \gtrsim 3\,\mathrm{km\,s^{-1}}$, both when considering the line widths and the relative optical depths. We therefore assume the best-fit b value throughout, but provide the derived column density for fixed $b = 5\,\mathrm{km\,s^{-1}}$ in Table 6.6.2. The three fine-structure transitions all show roughly consistent column densities within the errors for both assumed b-parameters. For this GRB we measure a total C I column density of $\log N(\mathrm{C\,I})_{\mathrm{tot}} = 14.24 \pm 0.14$. Since the lines are not intrinsically saturated this estimate should be reliable, which is also supported by the measured C I rest-frame equivalent width following the linear relation from Fig. 6.3.7. The best fit Voigt profiles are shown overplotted on the normalized VLT/X-shooter spectrum in Fig. 6.6.6 for $b = 2.3\,\mathrm{km\,s^{-1}}$.

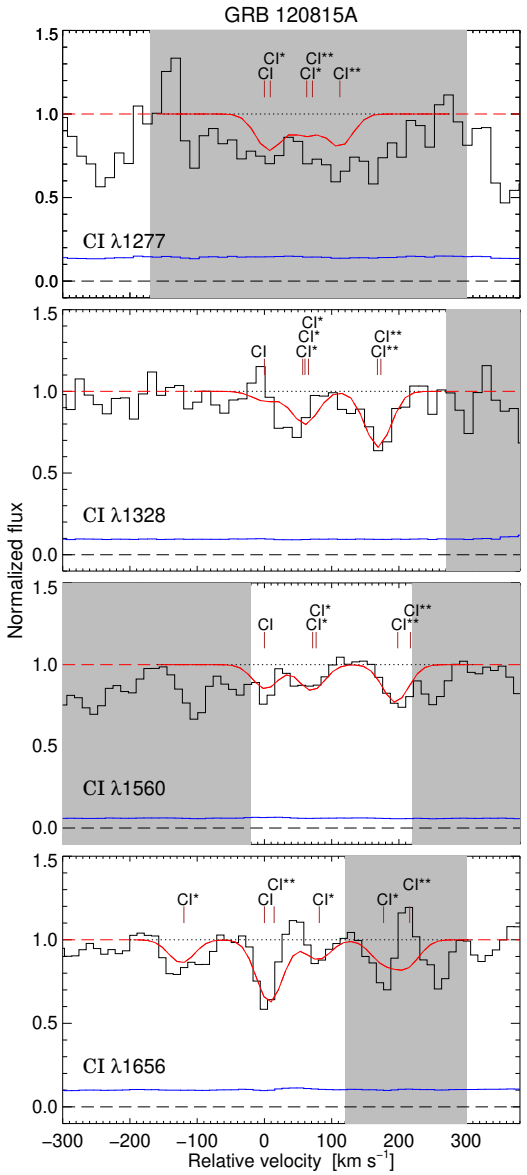

Figure 6.6.6. Same as Fig. 6.6.5 but for GRB 120815A with $b = 2.3 \pm 0.5$, centred on $z = 2.35814$.

GRB 120909A at $z = 3.9290$

The spectrum presented here was published by Selsing et al. (2019). The neutral and molecular gas-phase abundances listed in Table 6.2.1 derived for this GRB are adopted from Bolmer et al. (2019), who also reported the detection of H_2 in the spectrum. They found $\log N(\mathrm{H\,I}) = 21.82 \pm 0.02$, $\log N(\mathrm{H_2}) = 17.25 \pm 0.23$, $[\mathrm{S/H}] = -1.06 \pm 0.12$ and $[\mathrm{S/Fe}] = 0.50 \pm 0.15$, resulting in a dust-corrected metallicity of $[\mathrm{M/H}] = -0.29 \pm 0.10$.

Table 6.6.3. Results of the Voigt-profile fitting for GRB 121024A.

Exc. state	$\log N(\mathrm{C\,I})$ $b = 3.5 \pm 0.5$ ($\mathrm{km\,s^{-1}}$)	$b = 5$ ($\mathrm{km\,s^{-1}}$)
C I	13.61 ± 0.17	13.40 ± 0.15
C I*	13.81 ± 0.10	13.60 ± 0.09
C I**	13.70 ± 0.17	13.23 ± 0.21

Greiner et al. (in prep.) derived a visual extinction in the line of sight to this GRB of $A_V = 0.16 \pm 0.04$ mag (see Bolmer et al., 2019). We find no evidence for C I in this absorption system (see also Heintz et al., 2019a), and derive a 2σ upper limit of $\log N(\mathrm{C\,I})_{\mathrm{tot}} < 14.0$ assuming $b = 2\,\mathrm{km\,s^{-1}}$.

GRB 121024A at $z = 2.3005$

The spectrum presented here was first published by Friis et al. (2015), who also reported the presence of H_2 in the spectrum. The neutral and molecular gas-phase abundances listed in Table 6.2.1 derived for this GRB are adopted from Bolmer et al. (2019). They found $\log N(\mathrm{H\,I}) = 21.78 \pm 0.02$, $\log N(H_2) = 19.90 \pm 0.17$, $[\mathrm{Zn/H}] = -0.76 \pm 0.06$ and $[\mathrm{Zn/Fe}] = 0.77 \pm 0.08$, resulting in a dust-corrected metallicity of $[\mathrm{M/H}] = -0.68 \pm 0.07$. We adopt the visual extinction derived by Zafar et al. (2018b) of $A_V = 0.26 \pm 0.07$ mag.

To fit the neutral atomic carbon abundances for this GRB we again ran the fit leaving b as free parameter or fixed to $b = 5\,\mathrm{km\,s^{-1}}$. We only detect a single absorption component across the four line complexes so we fixed this in the fit and masked out any unrelated or blended features. The fit was mainly constrained by the C I $\lambda\lambda$ 1328,1656 line transitions. The C I $\lambda\lambda$ 1277,1560 lines were only used to constrain the upper limit on the column density since they are significantly blended. We obtain a best-fit b-parameter of $b = 3.5 \pm 0.5\,\mathrm{km\,s^{-1}}$. The line profiles seem to exclude values of $b \gtrsim 5\,\mathrm{km\,s^{-1}}$, both when considering the line widths and the relative optical depths. However, since we are not able to distinguish between the best-fit and fixed b-parameter of $b = 5\,\mathrm{km\,s^{-1}}$, we assume the latter column density throughout. The three fine-structure transitions also all show roughly consistent column densities within the errors for both assumed b-parameters. For this GRB we measure a total C I column density of $\log N(\mathrm{C\,I})_{\mathrm{tot}} = 13.91 \pm 0.08$. Since the lines are not intrinsically saturated this estimate should be reliable, which is also supported by the measured C I rest-frame equivalent width following the linear relation from Fig. 6.3.7. The best fit Voigt profiles are shown overplotted on the normalized VLT/X-shooter spectrum in Fig. 6.6.7 for $b = 5\,\mathrm{km\,s^{-1}}$.

GRB 141109A at $z = 2.9940$

The spectrum presented here was published by Selsing et al. (2019). The neutral and molecular gas-phase abundances listed in Table 6.2.1 derived for this GRB are adopted from Bolmer et al. (2019), who also reported the detection of H_2 in the spectrum. They

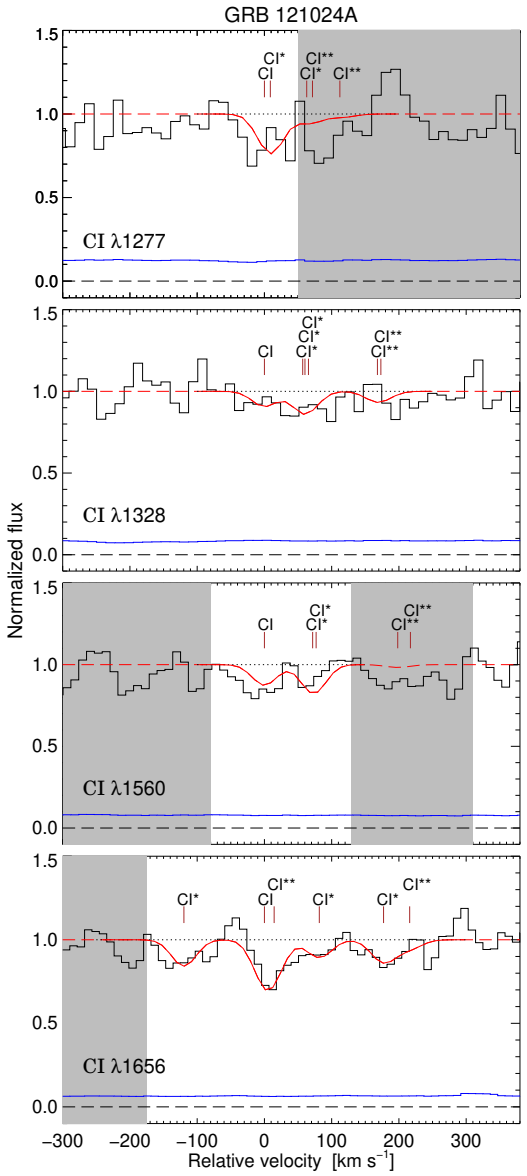

Figure 6.6.7. Same as Fig. 6.6.5 but for GRB 121024A with fixed $b = 5\,\mathrm{km\,s^{-1}}$, centred on $z = 2.30208$.

found $\log N(\mathrm{H\,I}) = 22.18 \pm 0.02$, $\log N(\mathrm{H_2}) = 18.02 \pm 0.12$, [Zn/H] $= -1.63 \pm 0.06$ and [Zn/Fe] $= 0.49 \pm 0.07$, resulting in a dust-corrected metallicity of [M/H] $= -1.37 \pm 0.05$. Heintz et al. (2019a) derived a visual extinction in the line of sight to this GRB of $A_V = 0.11 \pm 0.03$ mag and also found no evidence for C I in this absorption system. We derive a 2σ upper limit of $\log N(\mathrm{C\,I})_{\mathrm{tot}} < 14.7$ assuming $b = 2\,\mathrm{km\,s^{-1}}$.

Table 6.6.4. Results of the Voigt-profile fitting for GRB 150403A.

Exc. state	$\log N$(C I) $b = 5$ (km s^{-1})	$b = 10$ (km s^{-1})
C I	14.12 ± 0.29	13.74 ± 0.13
C I*	14.15 ± 0.15	13.90 ± 0.07
C I**	14.50 ± 0.39	14.08 ± 0.12

GRB 150403A at $z = 2.0571$

The spectrum presented here was published by Selsing et al. (2019). The neutral and molecular gas-phase abundances listed in Table 6.2.1 derived for this GRB are adopted from Bolmer et al. (2019). They found $\log N(\mathrm{H\,I}) = 21.73 \pm 0.02$, $\log N(\mathrm{H_2}) = 19.90 \pm 0.14$, [Zn/H] $= -1.04 \pm 0.04$ and [Zn/Fe] $= 0.63 \pm 0.08$, resulting in a dust-corrected metallicity of [M/H] $= -0.92 \pm 0.05$. We adopt the upper limit on the visual extinction derived by Heintz et al. (2019b) of $A_V < 0.13$ mag.

To fit the neutral atomic carbon abundances for this GRB we only ran iterations with fixed values of $b = 5$ and $b = 10\,\mathrm{km\,s^{-1}}$, since the fit could not converge on a realistic value for b if left as a free parameter. The fit was mainly constrained by the C I $\lambda\lambda$ 1560,1656 line transitions. The C I $\lambda\lambda$ 1277,1328 lines were masked out in the fit since they are significantly blended with tellurics. Their apparent optical depths are, however, still required to be consistent with the derived column densities. For the C I $\lambda\lambda$ 1560,1656 line transitions we also masked out regions of the spectrum showing unrelated absorption features or bad pixels with correlated noise, and therefore only fit for the same components as identified for the C I λ 1656 line complex. The observed line profiles appear to be consistent with both $b = 5$ and $b = 10\,\mathrm{km\,s^{-1}}$, so we adopt $b = 5\,\mathrm{km\,s^{-1}}$ to be consistent with the other bursts. The relative abundances for all the fine-structure transitions of the ground-state are consistent, however, within errors for both b-parameters. For this GRB we derive a 2σ lower limit of $\log N(\mathrm{C\,I})_{\mathrm{tot}} \gtrsim 14.3$. This lower limit takes into account both the uncertain line broadening and the intrinsically saturated line profiles. The best fit Voigt profiles are shown overplotted on the normalized VLT/X-shooter spectrum in Fig. 6.6.8 for $b = 5\,\mathrm{km\,s^{-1}}$.

GRB 180325A at $z = 2.2496$

The spectrum presented here was published by Zafar et al. (2018a), who also reported the detection of C I. The gas-phase abundances and visual extinction listed in Table 6.2.1 derived for this GRB are adopted from their work. They found $\log N(\mathrm{H\,I}) = 22.30 \pm 0.14$, [Zn/H] $= > -0.96$ and $A_V = 1.58 \pm 0.12$ mag from the first epoch VLT/X-shooter observations. It was not possible to search for H_2 in this absorption system due its high visual extinction.

To fit the neutral atomic carbon abundances for this GRB we only ran iterations with fixed b-parameters, since the fit could not converge on a realistic value for b if left

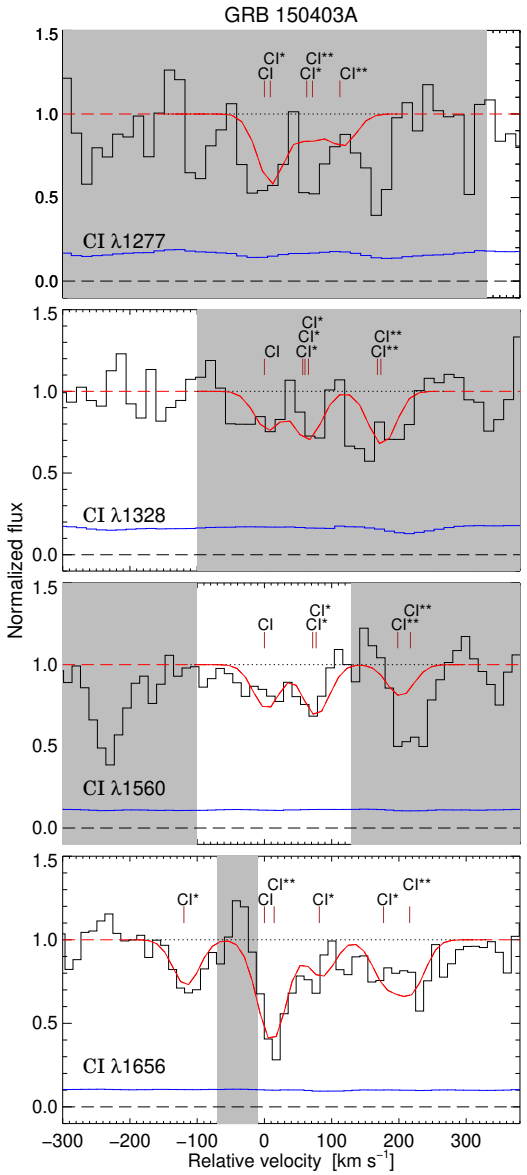

Figure 6.6.8. Same as Fig. 6.6.5 but for GRB 150403A with fixed $b = 5\,\mathrm{km\,s^{-1}}$, centred on $z = 2.05691$.

as a free parameter. The fit was only constrained by the C I $\lambda\lambda$ 1560,1656 line transitions since the C I $\lambda\lambda$ 1277,1328 lines were completely blended with telluric absorption features and in spectral regions with poor S/N. For the C I $\lambda\lambda$ 1560,1656 line transitions we also masked out regions of the spectrum showing unrelated absorption features. The S/N is quite poor in the spectral region around these line complexes as well, so we only perform the fit assuming a single absorption component and with b-parameters fixed to $b = 5$ and $b = 10\,\mathrm{km\,s^{-1}}$, respectively. While the observed line profiles appear to be

Table 6.6.5. Results of the Voigt-profile fitting for GRB 180325A.

Exc. state	$\log N(\mathrm{C\,I})$ $b = 5$ ($\mathrm{km\,s^{-1}}$)	$b = 10$ ($\mathrm{km\,s^{-1}}$)
C I	17.32 ± 0.17	14.50 ± 0.31
C I*	14.98 ± 0.27	14.25 ± 0.11
C I**	14.51 ± 0.30	14.20 ± 0.20

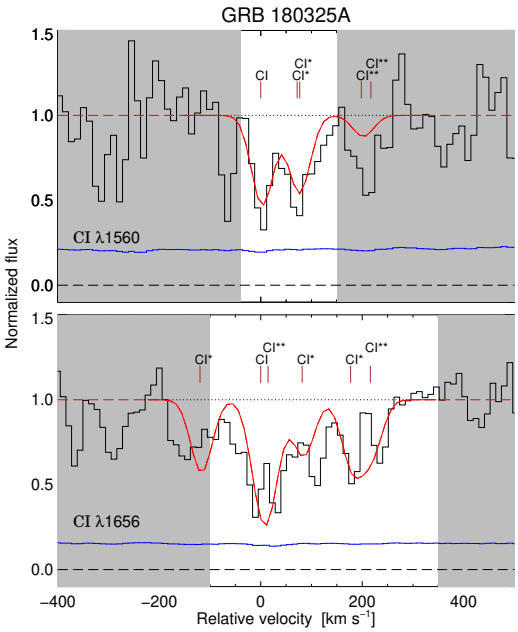

Figure 6.6.9. Same as Fig. 6.6.5 but for GRB 180325A with fixed $b = 10\,\mathrm{km\,s^{-1}}$, centred on $z = 2.24954$.

consistent with both $b = 5$ and $b = 10\,\mathrm{km\,s^{-1}}$, the column densities derived assuming $b = 5\,\mathrm{km\,s^{-1}}$ (especially the ground-state, see Table 6.6.5) are significantly overestimated. We therefore adopt $b = 10\,\mathrm{km\,s^{-1}}$ and derive a 2σ lower limit of $\log N(\mathrm{C\,I})_{\mathrm{tot}} \gtrsim 14.5$ for this GRB. This lower limit takes into account both the uncertain line broadening and the intrinsically saturated line profiles. The best fit Voigt profiles are shown overplotted on the normalized VLT/X-shooter spectrum in Fig. 6.6.9.

Part III

Quasars Concealed by Dusty and Metal-Rich Absorbers

Chapter 7

Selecting dust-reddened quasars

There are at least two ways to gauge the extent of the proposed dust bias in quasar-selected damped Lyman-α absorber (DLA) samples. One is to design a selection that is specifically tailored for the identification of the most dust-reddened systems, that have been missed in current surveys. The focus of this Chapter will be to define a set of selection criteria, specifically targeting quasars at $z \gtrsim 2$ with intervening dusty DLAs based on their photometry that are not identified in classical quasar surveys. In Chapter 8, a prime example of one such system is presented, identified via these new selection criteria.

Another approach to assess the true underlying population of quasars is to define a complete sample. Here, all quasar candidates should be selected uniformly, dependent only on their most basic properties. For such an approach to be effective, this should also include a rejection of the vast majority of local stellar sources, which is typically done in color-space. This might, however, bias the sample against quasars that photometrically resemble stars the most. Ideally, all quasar candidates should be selected regardless of their intrinsic spectral properties within the limiting magnitude of the survey. Such a selection is presented in Chapter 9, based on the astrometric measurements from the *Gaia* mission.

7.1 Photometric data

7.1.1 KiDS and VIKING survey data

The photometric catalag on which the selection presented here is based, was compiled by cross-matching the Kilo-Degree Survey Data Release 3 (KiDS-DR3; de Jong et al., 2017), the VISTA Kilo-Degree INfrared Galaxy Data Release 2 (VIKING-DR2; Edge et al., 2013, 2016) survey, and the *WISE* AllSKY data release (AllWISE; Wright et al., 2010; Cutri, 2013). The KiDS and VIKING are so-called sister surveys in the sense that they aim to cover the same ~ 1500 deg^2 on the sky. The survey areas are divided into two main strips, one in the Northern and one in the Southern Galactic Cap (NGC and SGC). The NGC is centred on $(\alpha, \delta)_{\rm NGC} = (12\ {\rm h},\ 0^{\rm o})$ and the SGC is centred on $(\alpha, \delta)_{\rm SGC} = (0.8\ {\rm h},\ -30^{\rm o})$. The coverage of KiDS-DR3 and VIKING-DR2 is so far only

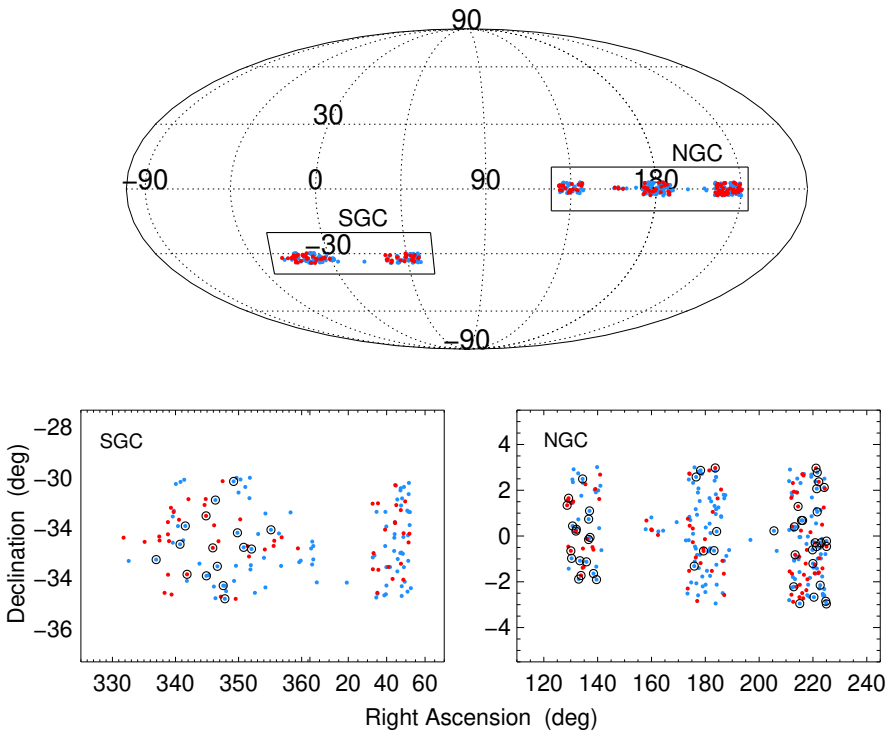

Figure 7.1.1. At the top is shown a Mollweide projection of the positions on the sky of the full list of quasar candidates from the red and blue samples (color-coded accordingly). In the two bottom panels are shown zoom-ins on the two sample regions, the NGC and SGC. The quasar candidates from the red and blue sample are here color-coded as above, where the circles denote quasar candidates for which follow-up spectroscopy was obtained as part of the KV-RQ survey presented here.

a subset of the aimed 1500 deg^2. The current cross-match between the two surveys covers ≈ 340 deg^2 in the NGC and ≈ 225 deg^2 in the SGC (total of ≈ 565 deg^2, see e.g. Fig. 7.1.1).

KiDS covers the optical Sloan *u, g, r* and *i* filters at 3550, 4775, 6230 and 7360 Å, respectively, using the OmegaCAM wide-field imager (Kuijken, 2011) on the VLT Survey Telescope (VST). The VIKING survey covers the near-infrared *Z, Y, J, H* and K_S filters at 8770, 10 200, 12 520, 16 450 and 21 470 Å, respectively, using the VISTA InfraRed CAMera (VIRCAM; Dalton et al., 2006) at the VISTA telescope (Emerson et al., 2006). In the public available KiDS catalog, only fluxes for each source were listed in the relevant filters scaled such that the AB zero point is zero. The conversion from flux, f, into AB magnitudes is therefore $m_{\rm AB} = -2.5\log_{10}(f)$. To obtain the associated errors in the AB magnitude system, σ_m, the errors on the flux, σ_f, can be propagated as $\sigma_m = 2.5\log_{10}(e)\times\sigma_f/f$. The magnitudes for each source are included in the VIKING catalog, but given in the Vega magnitude system. To convert these to

AB magnitudes, the following conversion factors have been applied[1]

$$Z_{\rm AB} = Z_{\rm Vega} + 0.521,\ Y_{\rm AB} = Y_{\rm Vega} + 0.618,\ J_{\rm AB} = J_{\rm Vega} + 0.937,$$
$$H_{\rm AB} = H_{\rm Vega} + 1.384 \text{ and } K_{S,\rm AB} = K_{S,\rm Vega} + 1.839$$

All magnitudes from both the KiDS and VIKING catalog used here are obtained with an aperture size of $2\farcs0$. The KiDS and VIKING surveys are ~ 2 mag deeper than the SDSS and UKIDSS surveys, and are thus an ideal extension to previous searches for faint quasars strongly reddened by dusty DLAs. The AllWISE survey covers the mid-infrared filters W_1, W_2, W_3 and W_4, with effective peak wavelengths at 3.4, 4.6, 12 and 22 μm, respectively. The magnitudes in this catalog is also given in the Vega system, but these are not converted in the final catalog.

7.1.2 Combining the survey catalogs

The final, combined photometric catalog was constructed by B. Milvang-Jensen, by first stitching the 440 (KiDS) and 477 (VIKING) tiles together, to produce a single KiDS+VIKING catalog. For the latter, it was required that the VIKING catalog entry `PRIMARY_SORUCE` = 1 to remove duplicates due to overlapping sky coverage of the individual VIKING tiles. The KiDS and VIKING catalogs were then cross-matched by requiring that; 1) the source should be detected both in KiDS and VIKING, 2) only the closest, best-match counterpart is saved and 3) VIKING sources should be at a maximum distance of $1\farcs0$ from the corresponding KiDS source. The typical separation distance between the optical and near-infared counterparts is $0\farcs12$. The AllWISE catalog was then cross-matched to this combined catalog, including only the best-match counterpart within $2\farcs0$. Only about one-third of the roughly 1.5×10^7 entries in the combined KiDS-VIKING catalog were found to have a counterpart in the AllWISE survey within $2\farcs0$. This is most likely related to the shallower survey depth of the *WISE* mission. A large fraction ($\sim 95\%$) of the sources in the KiDS-VIKING catalog without *WISE* detections also show optical/near-infrared colors consistent with main-sequence stars. These are therefore less likely to be detected by *WISE* due to their weak mid-infrared emission.

7.2 Target selection

The present selection of the candidate quasars is based on a combination of optical to near/mid-infrared photometry. The candidates were required to be detected in (at least) the *g, r, i, J* and K_S filters and in the first three *WISE* bands with a signal-to-noise ratio of at least 3 (i.e., $\mathrm{S/N}_{W1-3} \geq 3$). Furthermore, the candidates should be flagged as point sources in both KiDS and VIKING. In the KiDS catalog a morphology flag is given for each source where `SG2DPHOT` = 1 (for high-confidence stars), 2 (objects with a FWHM less than the typical stellar locus), 4 (stars following their star/galaxy classification) and 0 (for likely galaxies). These values are additive, so a source with `SG2DPHOT` = 5 is a

[1] From the Cambridge Astronomy Survey Unit (CASU): `http://casu.ast.cam.ac.uk/surveys-projects/vista/technical/filter-set`

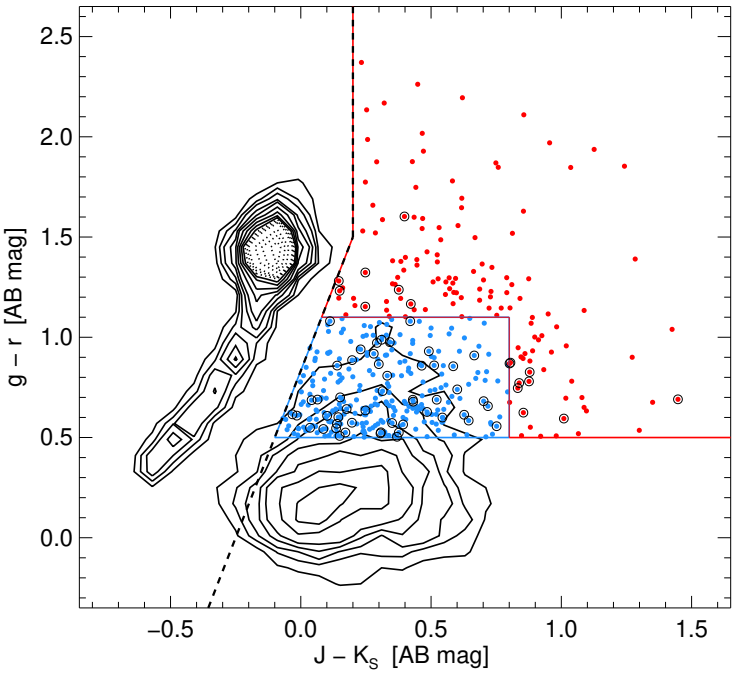

Figure 7.2.1. Optical and near-infrared color-color plot of the point sources brighter than $J < 20$ mag (contours) from the full combined KiDS-VIKING-AllWISE catalog. The high-likelihood quasar candidates from the red and blue samples are shown by the colored dots. The circles again denote quasars for which follow-up spectroscopy was obtained as part of the KV-RQ survey presented here. The red and blue solid lines indicate the selection criteria for the two samples, respectively. The general stellar rejection line is marked by the black dashed line.

high-confidence star which also fulfills their star/galaxy classification. Only sources with `SG2DPHOT` ≥ 1 were included in the final sample. For the VIKING data, it was required that `pGal` < 0.90 (similar to, but more conservative than the `pGal` < 0.95 criterion used by Venemans et al., 2013, 2015, who also gives a detailed discussion of this cut as a star/galaxy separator) and that `mclass` = -1,-2 where `mclass` = 1 (galaxy), 0 (noise), -1 (star), -2 (probably a star), 3 (probably a galaxy) and -9 (saturated). Finally, the candidates should be brighter than $J < 20$ mag to allow for spectroscopic follow-up. The magnitude limit was defined in the near-infared to avoid biasing the sample against sources with heavily reddened optical colors.

7.2.1 Stellar rejection

To increase the quasar selection efficiency it is important exclude the vast population of especially dwarf stars that most resemble quasars at optical wavelengths. Following a similar approach as the 'KX' selection (e.g. Warren et al., 2000; Maddox et al., 2008,

2012) to identify quasars, additional stellar rejection criteria based on the targets $J - K_S$ and $g - r$ colors were imposed (see Fig. 7.2.1). These specific selection criteria were motivated by the similar cuts used in previous searches for dust-reddened quasars (Fynbo et al., 2013a; Krogager et al., 2015, 2016b). Out of the total 11,637 point sources brighter than $J < 20$ mag in the combined catalog, 6601 (56.72%) are located rightwards of the stellar rejection line shown in Fig. 7.2.1. To limit the sample to only include the reddest most sources in the optical, additional color criteria of $g - r > 0.5$ and $r - i > 0.0$ were imposed. This leaves 1256 candidate reddened quasars, which thus constitute $\approx 20\%$ of the full, high-likelihood quasar sample.

7.2.2 Limiting contamination with a red and blue sample

To increase the selection efficiency and further reject contaminating stellar sources, the parent sample was divided into two; a blue and a red sample (again, see Fig. 7.2.1). The blue sample includes all the high-likelihood quasar candidates that have $J - K_S < 0.8$ and $0.5 < g - r < 1.1$. These particular color cuts were imposed to be more inclusive with the *WISE* photometric cuts (described below), since quasars are well-separated from the stellar locus in this region of optical/near-infrared color-color space. The red sample was limited to only contain sources with $J - K_S > 0.8$ or $g - r > 1.1$. In this region, the *WISE* color criteria need to be more conservative to remove the significant population of dwarf stars that overlap with the quasar colors in the optical and near-infared.

7.2.3 High-z identification with *WISE*

To specifically target quasars with intervening DLAs, it is importatnt to constrain the selection to quasars located $z > 2$ such that the Lyα line is observable from the ground. Krogager et al. (2016b) found that most quasars at $z < 2$ can be removed based on their observed mid-infrared $W_2 - W_3$ vs. $W_1 - W_2$ colors. Using a similar, but more conservative, set of mid-infrared photometric color criteria (shown in Fig. 7.2.2) allows a more robust rejection of quasars at $z < 2$, while also being more sensitive to quasars at $z > 3$. Specifically, the *WISE* color cuts were defined as

$$\begin{aligned} &\text{for } W2 - W3 < 2.75 : W1 - W2 < 0.8 \\ &\text{for } W2 - W3 > 2.75 : W1 - W2 < 0.62 \times (W2 - W3) - 0.91 \ . \end{aligned} \tag{7.1}$$

for the blue sample and

$$\begin{aligned} &\text{for } W2 - W3 < 2.75 : W1 - W2 < 1.0 \\ &\text{for } W2 - W3 > 2.75 : W1 - W2 < 0.62 \times (W2 - W3) - 0.71 \ , \end{aligned} \tag{7.2}$$

for the red sample. The lower boundaries of $W_1 - W_2 > 0.6$ (red) and $W1 - W2 > 0.4$ (blue) were imposed to limit contamination from stars and galaxies while still recovering a part of the high-redshift quasars. Since the blue sample only contains a small fraction of contaminating sources, the lower boundary in $W_1 - W_2$ is less conservative such that a higher fraction of $z \gtrsim 3$ quasars are included (Stern et al., 2012).

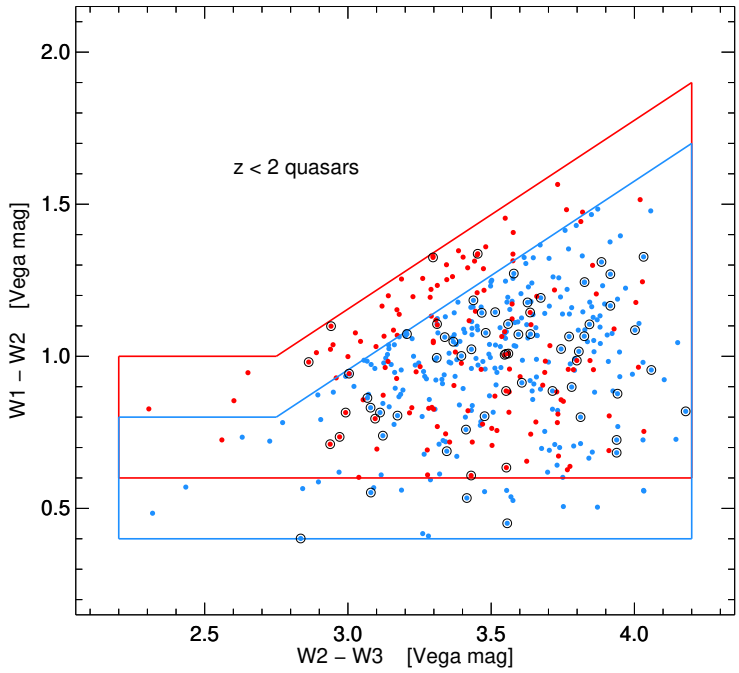

Figure 7.2.2. *WISE* color-color plot of the high-likelihood quasar candidates from the red and blue samples (color-coded accordingly). The circles again denote quasars for which follow-up spectroscopy was obtained as part of the KV-RQ survey presented here. The red and blue solid lines indicate the selection criteria for the two samples, respectively. The exclusion zone for low-redshift quasars in the top-left is highlighted in the figure as well.

7.3 Sample properties

The goal of the red sample is to recover quasars even more reddened by dust in intervening DLAs than those found in the previous searches. The blue sample is mainly constructed to have higher survey efficiency and contain brighter candidates, but still with the potential of revealing a few, but likely less, dust-rich DLAs. In the two constructed catalogs, 139 candidate quasars are in the red sample and 280 are in the blue sample. The SDSS/BOSS quasar surveys cover only the NGC region of the two catalogs, which is also best visible from the Northern hemisphere (e.g. for observations with the Nordic Optical Telescope (NOT)). Before performing follow-up spectroscopy of any of our candidates, sources that had already been observed spectroscopically as part of SDSS or BOSS (DR13) or by us as part of the HAQ (Fynbo et al., 2013a; Krogager et al., 2015) or eHAQ (Krogager et al., 2016b) surveys were removed from the target list. In the blue NGC sample 66 (37%) of the candidates were already observed by SDSS/BOSS (where only 13 of these were at $z < 2$, all showing a substantial amount of reddening). The remaining 53 quasars were all in the target redshift range at $2.0 < z < 3.7$. To be conservative, sources that were classified as galaxies in the SDSS/BOSS were also

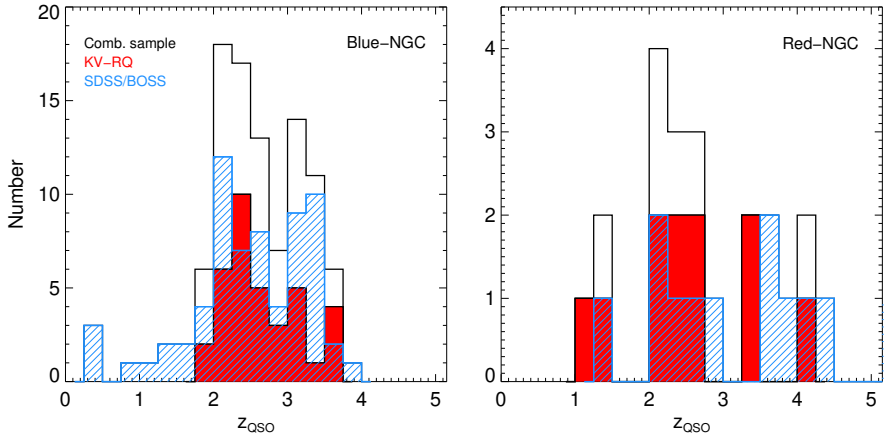

Figure 7.3.1. Quasar redshift distribution of the red and blue NGC samples. The filled red histograms show the z_{QSO} distribution of the quasars identified as part of the KV-RQ survey. The line-filled blue histograms show the candidates from the red and blue samples that had already been observed spectroscopically as part of the SDSS or BOSS (DR13) quasar surveys. The solid black lines show the combined redshift distributions.

removed, but there were only six (3%) such cases. Furthermore, one already observed HAQ (HAQ 1411-0104 at $z = 3.50$) and one source classified as a star in SDSS was removed as well. This leaves 106 candidate dust-reddened quasars in the blue NGC sample. In the red NGC sample only 12 (14%) of the candidates were already observed by SDSS/BOSS (where only two of these were at $z < 2$, both showing a substantial amount of reddening). The remaining 10 quasars were all in the target redshift range at $2.0 < z < 4.3$. Again, sources that were classified as galaxies in the SDSS/BOSS were removed, which were only relevant for seven (8%) such cases in this redder sample. Furthermore, one already observed eHAQ (eHAQ 1136+0027 at $z = 1.12$) and one source classified as a star in SDSS were removed as well. This leaves 65 candidate dust-reddened quasars in the red NGC sample. It is clear that the SDSS/BOSS selection algorithms are much less efficient at identifying the reddest most sources in the optical, as represented by the recovering fraction of the red vs. blue sample.

In Fig. 7.3.1 is shown the redshift distribution of the quasars observed so far as part of the KiDS-VIKING Red Quasar (KV-RQ) survey presented here. It is evident that the KV-RQ survey probes roughly the same redshift distribution as the SDSS/BOSS quasar surveys. We have, however, been able to recover more dust-reddened systems. In addition, 11 new quasars with intervening DLAs have been discovered in the blue sample so far, but unfortunately none in the red sample. One of these quasar DLAs, KV-RQ 1500-0013, will be presented in the next Chapter 8, where the general population of dusty DLAs will also be discussed.

Chapter 8

Characterizing the population of dusty DLAs

This chapter is based on the following article:

A quasar hiding behind two dusty absorbers. Quantifying the selection bias of metal-rich, damped Lyα absorption systems

Published in Astronomy & Astrophysics, vol. 615, id. A43, 14 pp. (2018)

Authors:
K. E. Heintz, J. P. U. Fynbo, C. Ledoux, P. Jakobsson, P. Møller, L. Christensen, S. Geier, J.-K. Krogager & P. Noterdaeme

The cosmic chemical enrichment as measured from damped Lyα absorbers (DLAs) will be underestimated if dusty and metal-rich absorbers have evaded identification. Here we report the discovery and present the spectroscopic observations of a quasar, KV-RQ 1500-0031, at $z = 2.520$ reddened by a likely dusty DLA at $z = 2.428$ and a strong Mg II absorber at $z = 1.603$. This quasar was identified as part of the KiDS-VIKING Red Quasar (KV-RQ) survey, specifically aimed at targeting dusty absorbers which may cause the background quasars to escape the optical selection of e.g. the Sloan Digital Sky Survey (SDSS) quasar sample. For the DLA we find an H I column density of $\log N(\mathrm{H\,I}) = 21.2 \pm 0.1$ and a metallicity of $[\mathrm{X/H}] = -0.90 \pm 0.20$ derived from an empirical relation based on the equivalent width of Si II λ 1526. We observe a total visual extinction of $A_V = 0.16$ mag induced by both absorbers. To put this case into context we compile a sample of 17 additional dusty ($A_V > 0.1$ mag) DLAs toward quasars (QSO-DLAs) from the literature for which we characterize the overall properties, specifically in terms of H I column density, metallicity and dust properties.

From this sample we also estimate a correction factor to the overall DLA metallicity budget as a function of the fractional contribution of dusty QSO-DLAs to the bulk of the known QSO-DLA population. We demonstrate that the dusty QSO-DLAs have high metal column densities ($\log N(\mathrm{H\,I})$ + [X/H]) and are more similar to gamma-ray burst (GRB)-selected DLAs (GRB-DLAs) than regular QSO-DLAs. We evaluate the effect of dust reddening in DLAs as well as illustrate how the induced color excess of the underlying quasars can be significant (up to ~ 1 mag in various optical bands), even for low to moderate extinction values ($A_V \lesssim 0.6$ mag). Finally we discuss the direct and indirect implications of a significant dust bias in both QSO- and GRB-DLA samples.

8.1 Introduction

Cosmic lighthouses such as quasars (QSOs) and gamma-ray bursts (GRBs) are powerful tools to study the chemical enrichment of galaxies through cosmic time (e.g. Pettini et al., 1994, 1997a,b, 1999; Prochaska & Wolfe, 2000; Prochaska et al., 2003, 2007; Fynbo et al., 2006b; Rafelski et al., 2012; Cucchiara et al., 2015). Damped Lyα absorbers (DLAs) can be identified toward these luminous background sources and are defined as having H I column densities of $\log N(\mathrm{H\,I}) > 20.3$. The total gas content of DLAs at high redshift is comparable to the visible stellar mass in spiral galaxies at the present epoch and DLAs are thus believed to be the gas reservoirs from which galaxies at high redshift formed (Wolfe et al., 1986, 2005).

On average, DLAs observed in GRB afterglows (GRB-DLAs) have higher H I column densities (Vreeswijk et al., 2004; Jakobsson et al., 2006b; Fynbo et al., 2009) and metallicities (Savaglio et al., 2003; Savaglio, 2006; Fynbo et al., 2006b; Prochaska et al., 2007; Cucchiara et al., 2015) than DLAs toward quasars (QSO-DLAs). This is expected since QSO-DLAs are cross-section-selected intervening absorbers where the line of sight intersects the galaxy at a random location, whereas GRBs are found to explode in the centremost part or the ultraviolet (UV) brightest regions of the galaxies hosting them (Bloom et al., 2002; Fruchter et al., 2006; Lyman et al., 2017). As a result, QSO-DLAs will also not sample the luminosity function of star-forming galaxies in the same way (Fynbo et al., 2008). However, GRB-DLAs with high H I column densities and high metallicities are observed whereas QSO-DLAs appear to be absent in this upper corner of the Z^1–$N(\mathrm{H\,I})$ plane. Boisse et al. (1998) argued that this apparent threshold could imply a significant dust bias in current, optically selected QSO-DLA samples. This bias, if confirmed, will cause an underestimation of the metallicity, the contribution of neutral gas to the cosmological mass density and the estimated global molecular fraction. The extent to which dusty and therefore also metal-rich QSO-DLAs might be under-represented in optically selected quasar samples due to dust obscuration has been studied extensively in the literature (see e.g. Pei et al., 1991; Fall & Pei, 1993; Vladilo & Péroux, 2005; Smette et al., 2005; Trenti & Stiavelli, 2006; Pontzen & Pettini, 2009) but where some claim it to be negligible, other find it to be significant.

In addition to dust obscuration (simply dimming the underlying quasar) the effect of reddening of otherwise bright quasars will also play an important role in the detection probability of these systems. As an example, Fynbo et al. (2011) discovered a metal-rich

[1] Where Z is the abundance relative to solar defined as $Z \equiv [\mathrm{X/H}] = \log N(\mathrm{X})/N(\mathrm{H}) - \log N(\mathrm{X/H})_\odot$.

DLA on the verge of dropping out of the optical quasar selection of the Sloan Digital Sky Survey (SDSS; Richards et al., 2002, 2004) framework. This initiated the High A_V Quasar (HAQ; Fynbo et al., 2013a; Krogager et al., 2015, 2016b) survey, tailored for the detection of dusty, intervening QSO-DLAs. Two dusty DLAs have so far been identified in this survey, both toward quasars misclassified as stars in the SDSS (Krogager et al., 2016a; Fynbo et al., 2017). The large majority of the sample, however, consists of intrinsically dust-reddened quasars and quasars likely reddened by absorbers at $z < 2$. Some evidence for a dust-bias in optical samples has indeed also been found from radio-selected QSO-DLAs (identifying quasars at radio wavelengths should not be affected by foreground dust, e.g; Ellison et al., 2001, 2008; Akerman et al., 2005; Jorgenson et al., 2006; Ellison & Lopez, 2009), though so-far only from small-number studies, which are therefore not fully conclusive.

After completion of the HAQ survey we redefined our search for the elusive, dusty QSO-DLAs through a new campaign designated the KiDS-VIKING Red Quasar (KV-RQ) survey (see Chap. 7). This survey was built from the Kilo Degree Survey (KiDS; de Jong et al., 2017) and the VISTA Kilo-degree Infrared Galaxy (VIKING; Edge et al., 2013) photometric data, which are roughly two magnitudes deeper than the SDSS and the UKIRT Infrared Deep Sky Survey (UKIDSS) detection limits that the HAQ survey relied on. Furthermore, after the large number of dust-reddened quasars that have now been classified, we were able to increase the efficiency of identifying quasars at $z > 2$ based on optical to near/mid-infrared photometry only and at the same time remove most of the previously observed contaminants (e.g., dwarf stars and compact galaxies).

In this paper we present the third detection of a quasar, for short named KV-RQ 1500-0013, reddened by a dusty and metal-rich DLA and an intervening Mg II absorber identified as part of the KV-RQ survey. Similar to the other two detections in the HAQ survey this source is classified as a star in the SDSS survey, as well as in the Baryon Oscillation Spectroscopic Survey (BOSS) program (Ross et al., 2012; Myers et al., 2015), which nevertheless relies on more complex selection algorithms. It was subsequently selected for spectroscopic follow-up observations by us as it fulfils the specific optical to near/mid-infrared photometric selection criteria defined for the KV-RQ survey (see Chap. 7). With this third detection the substantial number of dusty DLAs that have been reported in the literature, we proceed to evaluate and characterize these elusive DLAs as a population. Specifically, we test how these dusty QSO-DLAs compare to regular QSO-DLAs and GRB-DLAs in terms of H I column density, metallicity (and thus also the metal column density), and dust properties. Moreover, we want to quantify empirically the effect of reddening due to dust on the background quasar. This will allow us to better assess the effect of a dust bias in existing optically selected quasar samples.

The paper is structured as follows. In Section 8.2 we present our new spectroscopic observations of the quasar KV-RQ 1500-0013. In Section 8.3 we report the results of analyzing the quasar and its intervening DLA and Mg II absorber, with special focus on the DLA. Section 8.4 is dedicated to the evaluation and the characteristics of the population of dusty QSO-DLAs as a whole, combining this new observation with previous detections reported in the literature. Here we will also compare this subset of elusive QSO-DLAs to the bulk of known QSO-DLAs and the population of GRB-DLAs. In Section 8.5, we discuss the dust bias induced specifically in optically selected quasar

Table 8.2.1. Log of observations with the GTC

Date	Grism	$\mathcal{R}$	Exp. time (s)	Airmass
04-06-2017	R1000B	500	3×450	1.37
22-06-2017	R2500V	1500	3×1000	1.39
17-07-2017	R2500R	1850	3×1000	1.31

The specific coverage and instrumental resolution of the used grisms can be found at the OSIRIS webpage[a], the naming here following the denotation listed there.

[a] http://www.gtc.iac.es/instruments/osiris/#Longslit_Spectroscopy

samples, by the significant reddening effect these dusty absorbers have on the optical colors of the underlying quasars. Finally in Section 8.6, we summarize and conclude our work with emphasis on the implications of dust bias in DLA samples.

Throughout the paper we assume concordance cosmology with $\Omega_m = 0.315$, $\Omega_\Lambda = 0.685$, and $H_0 = 67.3$ km s^{-1} Mpc^{-1} (Planck Collaboration et al., 2014), the solar abundances of Asplund et al. (2009) and report magnitudes in the AB (Oke & Gunn, 1983) magnitude system.

8.2 Observations

We observed KV-RQ 1500-0013 with the Optical System for Imaging and low to intermediate Resolution Integrated Spectroscopy (OSIRIS) instrument mounted at the Gran Telescopio Canarias (GTC) as part of a larger sample, specifically aimed at targeting candidate quasars reddened by dusty DLAs. The full sample paper describing the selection strategy and sample properties will be released once the full campaign has been completed. The DLA and Mg II absorber were identified after securing longslit spectroscopy with OSIRIS using the R1000B grism covering 3630 – 7500 Å. To better constrain the spectral energy distribution (SED) and the metal line measurements we obtained follow-up observations with the higher resolution R2500V and R2500R grisms, covering the spectral ranges 4500 – 6000 Å and 5575 – 7685 Å, respectively. The log of observations at GTC is provided in Table 8.2.1.

The spectra were reduced using standard procedures for low-resolution spectroscopy in IRAF[2] after the cosmic rays were rejected using the software written by van Dokkum (2001). The spectra were flux calibrated using observations of spectrophotometric standard stars obtained on the same night as the science spectra. Both the spectra and the photometry were corrected for Galactic extinction using the dust maps from Schlafly & Finkbeiner (2011). All wavelengths reported are in vacuum and are corrected to the heliocentric rest frame. To improve the absolute flux calibration and correct for any slit-loss effects we scaled the observed spectra to the *r*-band photometry from KiDS.

[2] IRAF is distributed by the National Optical Astronomy Observatory, which is operated by the Association of Universities for Research in Astronomy (AURA) under a cooperative agreement with the National Science Foundation.

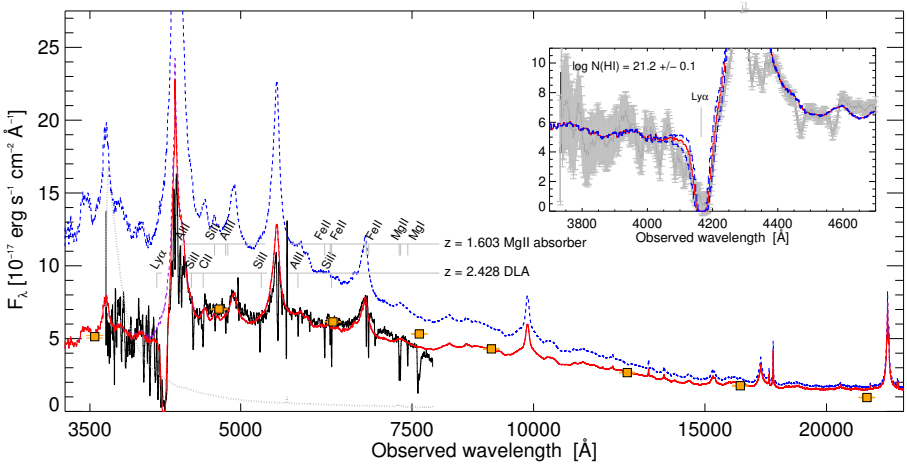

Figure 8.3.1. GTC spectrum taken with the R1000B grism shown as the solid black line together with the optical/near-infrared photometry in the u, g, r, i, Z, Y, J, H, and K_s bands from KiDS and VIKING overplotted as orange squares. The error spectrum is shown as the gray dotted line. In blue is shown a composite quasar template and in red the same composite but reddened by $A_V = 0.16$ mag in the rest frame of the DLA with the model DLA imposed on the template. The purple line shows the reddened template without the DLA. In the inset we zoom in on the spectral region covering the Lyα absorption line of the DLA at $z_{\rm DLA} = 2.4284$ and show the model with the best-fit H I column density and associated error of $\log N({\rm H\,I}) = 21.2 \pm 0.1$ as the red solid and blue dashed lines respectively.

8.3 Results

We present the GTC spectrum taken with the R1000B grism in Fig. 8.3.1 together with the optical/near-infrared photometry from KiDS and VIKING. Overplotted in blue is a composite quasar template (Selsing et al., 2016), where in red we show the same composite but reddened by a visual extinction of $A_V = 0.16$ mag (see below). The advantage of this composite is that it was created from observations of luminous blue quasars observed with the Very Large Telescope (VLT)/X-shooter which provides a broad spectral coverage without any significant host contamination and ensures that the template is constructed from quasars observed in a consistent manner. It is clear that the overall shape of the spectrum is consistent with having a substantial amount of reddening. We identify two intervening absorbers in the spectrum of the quasar at $z = 2.520$, a DLA at a systemic redshift of $z = 2.4284 \pm 0.0004$, and a Mg II absorber at $z = 1.6027 \pm 0.0005$. We will treat the analysis of the two absorbers separately, Sect. 8.3.1 being dedicated to the DLA and Sect. 8.3.2 to the Mg II absorber. In Sect. 8.3.3 we discuss the likely contribution of the two absorbers to the total observed extinction.

8.3.1 The DLA at $z = 2.428$

Neutral hydrogen column density

The Lyα absorption line was detected in the first observation using the R1000B grism, covering the full spectral region of this feature. In the inset in the upper right corner of Fig. 8.3.1 we show a zoom-in of this region. The H I column density was derived by fitting the reddened composite quasar template with a DLA included in the model (using the approximation of Tepper-García, 2006) to the observed spectrum. From the best-fit model we find an H I column density of $\log N(\mathrm{H\,I}) = 21.2 \pm 0.1$ at the redshift $z_{\mathrm{DLA}} = 2.428$. Due to the small discrepancy between the model and the continuum spectrum on the blue side of the Lyα trough, we normalized the region around the absorption line and fit the column density independently. We found the H I column density to be consistent with that derived from the reddened quasar composite with the imposed DLA model.

Even though located close in redshift to the quasar at $z_{\mathrm{QSO}} = 2.520$, we note that this DLA does not belong to the subclass of proximate DLAs (PDLAs), typically defined to be less than 3000 or 5000 km s^{-1} from the quasar emission redshift (Ellison et al., 2002; Russell et al., 2006; Prochaska et al., 2008b), where we measure $\Delta(z_{\mathrm{QSO}} - z_{\mathrm{DLA}}) \approx 8000$ km s^{-1}. Due to the close proximity of PDLAs to the background quasar, they have in general different characteristics to interving DLAs and might be associated with the quasar host galaxy. There are also indications of enhanced ionization in PDLAs causing the overall properties of these to contrast with those of typical intervening DLAs (Møller et al., 1998; Prochaska et al., 2008b; Ellison et al., 2010).

Metallicity

The metal lines associated with the DLA are listed in Table 8.3.1 where we also report the measured redshifts and the rest-frame equivalent widths (W_{rest}) for each of the lines. From the low-ionization absorption features we find the DLA to be located at a systemic redshift of $z = 2.4284 \pm 0.0004$. To determine W_{rest} we fitted the continuum around each of the lines in regions that were free of absorption features and tellurics. We then summed over the absorption profile contained below the normalized flux level. All the observed features are heavily saturated. The medium resolution of the spectra ($\mathcal{R} \approx 160 - 200$ km s^{-1} in the R2500V- and R2500R-grism observations) is too low to allow for a proper Voigt-profile fit to the absorption lines. For example, from high-resolution spectra of GRB afterglows, Prochaska (2006) have shown that strong metal absorption lines usually consists of a number of narrow (≤ 20 km s^{-1}), unsaturated components. We are therefore not able to derive a reliable column density based on Voigt-profile fitting. Furthermore, Si II λ 1808 is blended with Fe II λ 2382 from the Mg II absorber (see Table 8.3.1), which also rules out the possibility of deriving a reliable column density from a single-ion curve-of-growth technique.

To compute the metallicity of the DLA we have to instead rely on the empirical relation by Prochaska et al. (2008a). They found that the gas-phase metallicity, [X/H], is tightly correlated with the rest-frame equivalent width of Si II λ 1526. This correlation is argued to be a representation of the mass-metallicity relation in QSO- and GRB-DLAs, since Si II λ 1526 traces the dynamical motions of the halo gas outside the interstellar

Table 8.3.1. Detected absorption lines and rest-frame equivalent widths of the metal lines associated with the DLA and the Mg II absorber

Transition	$\lambda_{\rm obs}$ (Å)	z	$W_{\rm rest}$ (Å)
DLA			
O I λ 1302	4464.10	2.4282	0.65 ± 0.08
Si II λ 1304	4471.58	2.4282	0.57 ± 0.08
C II λ 1334	4574.82	2.4280	0.81 ± 0.07
Si II λ 1526	5234.08	2.4283	1.06 ± 0.02
C IV λ 1548*	5308.18	2.4286	0.15 ± 0.03
Fe II λ 1608	5515.01	2.4288	0.50 ± 0.02
Al II λ 1670	5728.74	2.4288	0.77 ± 0.10
Si II λ 1808*	6200.71	2.4296	1.82 ± 0.02
Mg II absorber			
Al II λ 1670	4347.65	1.6022	1.70 ± 0.18
Si II λ 1808	4706.66	1.6032	1.26 ± 0.13
Al III λ 1854	4826.14	1.6021	1.20 ± 0.08
Al III λ 1862	4847.12	1.6021	0.84 ± 0.07
Zn II λ 2026	5273.35	1.6027	0.45 ± 0.03
Zn II λ 2062	5368.27	1.6026	0.19 ± 0.02
Fe II λ 2344	6101.29	1.6027	1.97 ± 0.04
Fe II λ 2374	6180.07	1.6027	1.21 ± 0.03
Fe II λ 2382*	6201.48	1.6026	2.30 ± 0.04
Mn II λ 2576	6707.60	1.6030	0.22 ± 0.02
Fe II λ 2586	6732.68	1.6029	1.84 ± 0.02
Mn II λ 2594	6754.18	1.6033	0.21 ± 0.02
Fe II λ 2600	6767.70	1.6028	2.47 ± 0.02
Mn II λ 2606	6783.95	1.6027	0.21 ± 0.02
Mg II λ 2796	7279.00	1.6038	3.14 ± 0.06
Mg II λ 2803	7297.43	1.6037	3.12 ± 0.08
Mg I λ 2852	7426.63	1.6039	1.45 ± 0.03

*Blended.

medium (ISM), thus probing the total mass contained within the galaxy halo. Based on their relation we find [X/H] = -0.90 ± 0.20 for the DLA, where both the errors from the measured rest frame W_{1526} and from the scatter in the relation are included. We caution that since this metallicity estimate is based solely on an empirical relation, the actual metallicity might be different and can only be recovered from higher resolution spectra. Furthermore, the true metallicity could be higher due to the depletion of Si onto dust grains.

8.3.2 A strong Mg II absorber at $z = 1.603$

In addition to the DLA at $z = 2.428$ we identify an intervening Mg II absorber in the quasar spectrum as well. We detected several metal lines associated with the absorber and list them in Table 8.3.1, where again the measured redshifts and the rest-frame equivalent widths for each of the lines are reported. From the low-ionization absorption lines we find a systemic redshift of $z = 1.6027 \pm 0.0005$ of the Mg II absorber. The equivalent widths have been measured in the same way as for the DLA. This Mg II absorber is remarkably strong, where the measured rest-frame equivalent widths of the two components of the Mg II doublet are $W_{2796} = 3.14 \pm 0.06$ Å and $W_{2803} = 3.12 \pm 0.08$ Å, respectively.

Compared to the two samples of Mg II absorbers, one for intervening systems toward quasars and one for absorbers toward GRBs, compiled by Christensen et al. (2017), the strength of W_{2796} is among the 7% strongest Mg II absorbers for any given path length of $\Delta z = 1$. Comparing this system to the extensive sample of DLAs automatically identified in the SDSS survey (Noterdaeme et al., 2012a), we find that only $\approx 15\%$ of the intervening Mg II absorbers have $W_{2796} > 3$ Å, establishing this particular system as a relatively rare Mg II absorber with such strong features imprinted in absorption.

There is indirect evidence for this Mg II absorber being a DLA as well. However, since the Lyα absorption feature is located at ≈ 3150 Å at this redshift, it falls just outside the spectral coverage of the R1000B and R2500U grisms available for OSIRIS at GTC so that we are unable to confirm the high column density of neutral hydrogen. Rao et al. (2006) found from their survey of Mg II absorbers at $z < 1.65$ that systems that are classified as DLAs are confined to the region where the ratio between the rest-frame Mg II and Fe II equivalent widths is $1 \lesssim W_{2796}/W_{2600} \lesssim 2$. We measure a ratio of $W_{2796}/W_{2600} = 1.27 \pm 0.03$ in our case. Furthermore, all of the absorbers from their sample with $W_{2600} > 2$ Å have $\log N(\mathrm{H\,I}) > 20$ and for $W_{2852} > 1$ Å have $\log N(\mathrm{H\,I}) > 20.6$. We measure $W_{2600} = 2.47 \pm 0.02$ Å and $W_{2852} = 1.45 \pm 0.03$ Å, respectively.

8.3.3 Extinction

To derive the amount of extinction in the sightline towards the quasar, KV-RQ 1500-0013, we assume that the composite quasar template of Selsing et al. (2016) is a good representation of the underlying, intrinsic shape of the spectrum. While it is not possible to unambiguously know the exact shape, a large majority of the brightest quasars do, however, appear to have similar spectra which also result in the similarities found between individual composite quasar spectra (Francis et al., 1991; Vanden Berk et al., 2001; Telfer et al., 2002; Glikman et al., 2006; Lusso et al., 2015; Selsing et al., 2016).

Specifically, we fit the model of a composite quasar template with an imposed DLA at the derived redshift to the observed spectrum and photometry. In the majority of sighlines toward QSO- and GRB-DLAs the wavelength dependence on dust extinction is well reproduced by that derived toward individual stars in the Milky Way (MW) and the Small and Large Magellanic Clouds (SMC and LMC; e.g. Schady et al., 2010; Covino et al., 2013; Japelj et al., 2015; Ledoux et al., 2015; Krogager et al., 2015, 2016b). In

these sightlines, the dust model derived by Pei (1992) is parametrized as

$$A_\lambda = A_V \left(\frac{1}{R_V} + 1 \right) \sum_{i=1}^{6} \frac{a_i}{(\lambda/\lambda_i)^{n_i} + (\lambda_i/\lambda)^{n_i} + b_i} \,, \tag{8.1}$$

where the parameters a_i, b_i and n_i are different for each reddening law, and also the total-to-selective extinction ratio, $R_V = 3.08$ (MW), $R_V = 2.93$ (SMC) and $R_V = 3.16$ (LMC). In addition, we also used the steeper extinction curve ($R_V = 2.41$) derived by Zafar et al. (2015) for a sub-sample of intrinsically dust-reddened quasars from the HAQ survey. We fit the observed data to all of the four extinction curves, where the dust can be located at the three different redshifts; $z_{\rm MgII}$, $z_{\rm DLA}$ and $z_{\rm QSO}$. We found a best fit of $A_V = 0.16$ mag assuming the SMC extinction curve, shown in Fig. 8.3.1 as the red lines with (solid) and without (dashed) the DLA imposed on the model. We note, however, that using the steeper extinction curve by Zafar et al. (2015) leads to consistent fits only with a lower best-fit value of A_V as also shown by Krogager et al. (2016b). Since both of the intervening absorbers are good candidates for containing a significant amount of dust (see below), we argue that the dust is unlikely to be intrinsic to the quasar. So, the extinction curve of Zafar et al. (2015) is likely to be not a good assumption in our case and we therefore assume the SMC extinction curve throughout the paper.

We are unable to disentangle the exact location of the dust component. Only in cases where the 2175 Å extinction bump feature is detected is it possible to determine the redshift of the dust imprinting this feature on the observed spectrum (see, e.g., Srianand et al., 2008; Elíasdóttir et al., 2009; Prochaska et al., 2009; Noterdaeme et al., 2009a; Jiang et al., 2011; Kulkarni et al., 2011; Wang et al., 2012; Zafar et al., 2012; Ma et al., 2015; Fynbo et al., 2017, for detections of the 2175 Å extinction bump in the sightlines toward QSO- and GRB-DLAs). Even the strength of the 2175 Å feature can be determined (e.g. Jiang et al., 2010; Ledoux et al., 2015). These authors found that heavy dust depletion is required to produce a pronounced 2175 Å extinction bump and that there also appears to be a tight correlation between the strength of the bump and the amount of extinction.

We do not detect any indication of a bump in our case, thereby excluding the MW and LMC extinction curves, and can therefore not robustly conclude on the location of the dust and the amount of dust located at the different redshifts. The best-fit extinction, however, is consistent with the relatively large metal column density of the DLA system (see e.g. Sect. 8.4.4), where we expect $A_V = 0.13^{+0.13}_{-0.06}$ mag based on the relation from Zafar & Watson (2013), including the scatter. On the other hand, comparing the rest-frame equivalent widths of Fe II λ 1608 from the DLA and Fe II λ 2374 from the Mg II absorber (these two transitions have similar oscillator strengths) indicates that the Mg II system is a factor of two stronger than the DLA in terms of metal content and/or velocity dispersion. We note, however, that for a given amount of dust, stronger reddening effects will be produced at higher redshifts due to the shape of the extinction curve. The observed spectral shape of the quasar is thus more sensitive to dust located in the DLA. Based on the metal lines, however, the Mg II absorber might be the best candidate for hosting the largest amount of dust.

8.4 Properties of dusty QSO-DLAs

With this now third detection of a quasar likely to be reddened by a dusty DLA (though we cannot fully rule out the possibility of a shared dust contribution from, for example, the Mg II absorber) from our surveys, misclassified as a star in SDSS, we will evaluate both the characteristics of these elusive absorbers and the quasar selection methods through which the background quasars are selected. So far only a small population of dusty QSO-DLAs have been analyzed (see e.g. Vladilo et al., 2006, and the references listed in Table 8.4.1). Characterizing this dusty subset of the overall population of QSO-DLAs and understanding the selection bias toward this sub-population are of crucial importance in probing the full underlying population of DLAs (and in general also other types of quasar absorbers) and thus also estimating the true cosmic metallicity distribution.

In addition to the dusty DLA towards KV-RQ 1500-0013, we compiled a sample of similar absorption systems by extracting several dusty QSO-DLAs from the literature where we required the following criteria: *i*) $\log N(\mathrm{H\,I}) > 20.3$ cm^{-2}, *ii*) have (at least) optical magnitudes from the SDSS, *iii*) existing metallicity measurements from any of the mildly depleted elements (preferably Zn, otherwise S) and *iv*) visual extinction larger than $A_V \geq 0.1$ mag. Our final sample consists of 18 dusty QSO-DLAs and is presented in Table 8.4.1. The first criterion is to ensure that the absorber can be classified as a DLA and the second is required so that we can examine the reddening effects on the background QSO (see Sect. 8.5). The third criterion is defined so that we can explore the distribution of these dusty QSO-DLAs in the metallicity versus H I column density plane. Specifically we wish to examine if the apparent upper envelope found for QSO-DLAs by Boisse et al. (1998) is indeed populated by these dusty DLAs, but also to compare this population to GRB-DLAs, which are commonly observed above the apparent $Z - \log N(\mathrm{H\,I})$ threshold for QSO-DLAs. The fourth is defined such that the observed quasar spectrum exhibits significant reddening features due to dust. We note that this limit was actually found to be the upper limit (approximately $E(B-V) < 0.04$) for reddening found in the radio-selected DLA survey by Ellison et al. (2005), but caution that their sample is too small to provide statistically significant results. For the majority of the DLAs, measurements of the dust depletion, [Fe/Zn], are also available.

The compiled sample of dusty QSO-DLAs, together with KV-RQ 1500-0013, contains absorbers with metallicities from 5% up to three times solar metallicity, absorption redshifts spanning $1.6 < z < 3.3$, and visual extinctions between $0.1 < A_V < 0.6$ mag. In Table 8.4.1 we also list the specific selection and surveys from which the background quasars have been selected. One point is remarkable about this sample. Only seven out of the 18 quasars ($\approx 40\%$) with intervening dusty DLAs were selected as part of the SDSS and BOSS quasar surveys (Schneider et al., 2010; Pâris et al., 2014, 2017) following their photometric selection criteria and identification algorithms (Richards et al., 2002, 2004; Ross et al., 2012; Myers et al., 2015). The remaining systems have been selected either from tailored selection criteria designed to target quasars with intervening dusty DLAs (the HAQ, eHAQ and KV-RQ surveys; Krogager et al., 2015, 2016b), or as part of the SDSS/BOSS surveys but only based on radio detections, observed as filler sources or in one case simply as a star classified as part of the SEGUE-2 survey (Yanny et al., 2009).

Table 8.4.1. Properties of the compiled sample of dusty QSO-DLAs

Source	$z_{\rm QSO}$	$z_{\rm DLA}$	A_V (mag)	$\log N$(H I) (cm^{-2})	[X/H]	X	[Fe/X]	Survey	Refs.
J 0000+0048	3.028	2.525	0.23	20.80 ± 0.10	0.46 ± 0.45	Zn	-1.89 ± 0.50	BOSS[a,b]	(1)
J 0016-0012	2.092	1.970	0.11	20.75 ± 0.15	-0.86 ± 0.13	...*	-0.99 ± 0.10	BOSS[a]	(2)
eHAQ 0111+0641	3.214	2.027	0.22	21.50 ± 0.30	-0.60 ± 0.30	Zn	-0.60 ± 0.10	eHAQ[c]	(3,4)
J 0316+0040	2.911	2.180	0.12	21.10 ± 0.20	-1.20 ± 0.22	...*	-0.63 ± 0.20	SEGUE2[d]	(2)
J 0812+3208	2.711	2.626	0.11	21.35 ± 0.15	-0.88 ± 0.11	...*	-0.15 ± 0.05	BOSS[a,e]	(2)
J 0816+1446	3.847	3.287	0.15	22.00 ± 0.10	-1.10 ± 0.10	Zn	-0.48 ± 0.02	BOSS[a]	(5)
J 0840+4942	2.090	1.851	0.13	20.75 ± 0.15	-0.43 ± 0.17	...*	-0.71 ± 0.15	SDSS*[,f]	(2)
Q 0918+1636	3.070	2.583	0.22	20.96 ± 0.05	-0.12 ± 0.05	Zn	-0.91 ± 0.08	BOSS*[,a,b,g]	(6)
J 0927+5823	1.910	1.635	0.38	20.40 ± 0.25	-0.22 ± 0.25	...*	...	BOSS[e]	(2)
J 1135-0010	2.888	2.207	0.11	22.10 ± 0.05	-1.10 ± 0.20	Zn	-0.72 ± 0.10	BOSS*[,a,g,i,j]	(7)
J 1157+6155	2.513	2.460	0.59	21.80 ± 0.20	-0.60 ± 0.38	Zn	-1.02 ± 0.47	SDSS*[,h]	(8,9)
J 1211+0833	2.483	2.117	0.53	21.00 ± 0.20	-0.07 ± 0.21	Zn	-1.74 ± 0.25	BOSS*[,g,j]	(10)
J 1310+5424	1.929	1.801	0.27	21.45 ± 0.15	-0.51 ± 0.15	...*	...	SDSS*[,f,h]	(2)
KV-RQ 1500-0013	2.520	2.428	0.16	21.20 ± 0.10	-0.90 ± 0.20	...*	...	KV-RQ[c]	(14)
J 1709+3258	1.889	1.830	0.17	20.95 ± 0.15	-0.28 ± 0.15	...*	-0.53 ± 0.15	BOSS[k]	(2)
Q 2222+0946	2.927	2.354	0.15	20.55 ± 0.15	-0.46 ± 0.07	Zn	-0.77 ± 0.05	SDSS*[,f,l]	(2,11)
HAQ 2225+0527	2.320	2.130	0.28	20.69 ± 0.05	-0.09 ± 0.05	Zn	-1.22 ± 0.06	HAQ[c]	(12,13)
J 2340-0053	2.084	2.055	0.19	20.35 ± 0.15	-0.59 ± 0.15	...*	-0.53 ± 0.12	BOSS[e]	(2,8)

Notes. Selection flags given in the SDSS database: [a]Known QSO at $z > 2.15$; [b]Additional object observed to reach 40 QSOs deg^{-1} for BOSS outside the standard selection criteria; [c]Red optical to near/mid-infrared selection, classified as star in SDSS/BOSS; [d]Classified as a star in the SEGUE-2 survey; [e]FIRST radio selected; [f]Bright *ugri*-selected quasar; [g]Identified by the neural network and the kernel density estimation (KDE) plus χ^2 algorithms of BOSS; [h]High-redshift *griz*-selected quasar; [i]Identified by the BOSS likelihood method; [j]Selected to be in the uniform BOSS core sample; [k]Filler target; [l]Classified as a blue horizontal branch star as part of the SEGUE target selection. *Quasars selected from the photometric selection criteria and identification algorithms defined specifically for the SDSS/BOSS surveys. *Metallicities from Kaplan et al. (2010) are either based on Si II, Zn II or S II, but the exact ion is not listed in their table 2, and for KV-RQ 1500-0013 the metallicity is derived from an empirical relation based on the equivalent width of Si II λ 1526.

References. (1) Noterdaeme et al. (2017); (2) Kaplan et al. (2010); (3) Krogager et al. (2016b); (4) Fynbo et al. (2017); (5) Guimarães et al. (2012); (6) Fynbo et al. (2011); (7) Noterdaeme et al. (2012b); (8) Ledoux et al. (2015); (9) Wang et al. (2012); (10) Ma et al. (2015); (11) Fynbo et al. (2010); (12) Krogager et al. (2015); (13) Krogager et al. (2016a); (14) This work.

Heintz et al. (2016) estimated that the photometric selection of SDSS/BOSS (excluding objects selected solely on the basis of radio or X-ray detections) was only complete up to approximately 50% for $A_V \geq 0.1$ mag based on a small-scale study of the brightest quasars in the Cosmic Evolution Survey (COSMOS) field. This number is consistent with the fraction of the photometrically selected SDSS/BOSS quasars examined here within the errors dominated by the small-number statistics.

8.4.1 Neutral hydrogen column densities

Even modest amounts of dust will severely affect the detection probability of QSO-DLAs, demonstrated by the case studied here (but see also Krogager et al., 2016a; Fynbo et al., 2017), whereas GRB-DLAs occasionally arise in dusty environments (e.g.

Schady et al., 2010; Zafar et al., 2011a; Krühler et al., 2011, 2013). Furthermore, DLAs with large amounts of dust are expected to have large H I column densities at a fixed metal content due to simple scaling relations between metallicity (and hence also dust), luminosity, mass and H I column density (Møller et al., 2004, 2013; Ledoux et al., 2006; Fynbo et al., 2008; Neeleman et al., 2013; Christensen et al., 2014; Rahmati & Schaye, 2014; Krogager et al., 2017). Recently, Noterdaeme et al. (2014, 2015a,b) showed that high H I column density QSO-DLAs will redden the background QSOs as well, the degree to which being dependent on the redshift and the H I column density of the absorber. This is an additional effect that impedes the detection of these elusive DLAs.

In Fig. 8.4.1 we show a histogram of the H I column densities of the dusty QSO-DLAs from our compiled sample and compare them to the SDSS-DR12 QSO-DLAs (Noterdaeme et al., 2012a) and to the to-date most extensive, compiled sample of GRB-DLAs with H I column density measurements (Tanvir et al., 2018). For the dusty QSO-DLA sample we measure a mean of $\log N(\mathrm{H\,I}) = 21.1$, just below the mean of $\log N(\mathrm{H\,I}) = 21.2$ for the sample of all GRB afterglows and $\log N(\mathrm{H\,I}) = 21.6$ for the subset of GRBs that classify as DLAs with $\log N(\mathrm{H\,I}) > 20.3$. For comparison, the mean H I column density of the SDSS-DR12 QSO-DLAs is $\log N(\mathrm{H\,I}) = 20.7$. When performing a two-sided Kolmogorov-Smirnov test on the dusty QSO-DLA and the GRB-DLA populations we find that the probability that the two samples are drawn from the same parent distribution is $\approx 8 \times 10^{-4}$. The same test yields a probability of $\approx 3 \times 10^{-3}$ that the dusty QSO-DLAs are drawn from the same parent distribution as the regular QSO-DLAs. The H I column density distribution of the dusty QSO-DLAs is thus still more consistent with that of the regular QSO-DLAs.

The lower average (or at least the larger spread) of H I column densities observed toward the majority of QSO-DLAs compared to that of the GRB-DLA population can still mainly be explained by the random sightline to QSOs through the intervening absorber. However, this sample then suggests that the H I frequency distribution, $f_{\mathrm{H\,I}}(N, X)$, should flatten when accounting properly for the dusty QSO-DLAs in the overall DLA population. The potential bias specifically against strong QSO-DLAs ($\log N(\mathrm{H\,I}) > 22$) was already noted by Prochaska et al. (2005) in the early SDSS-DR3 DLA sample and discussed further in Prochaska et al. (2007). They concluded that the H I frequency distribution significantly steepens at $\log N(\mathrm{H\,I}) \approx 21.5$ based on the data. In the more recent data releases of SDSS, however, the steepness of the H I frequency distribution was found to be more moderate and extend to higher column densities (Noterdaeme et al., 2009b, 2012a). Studying absorbers selected from C I (an indication of a high fraction of cold gas), Ledoux et al. (2015) also showed that the H I-distribution is flatter than for regular DLAs, but that these are still predominantly found at low H I column densities and therefore do not contribute to the high end of the H I frequency distribution. We note that the apparent deficit of QSO-DLAs with high H I column densities and high metallicities can also partly be explained by the conversion of H I to H_2 for high $N(\mathrm{H\,I})$ (Schaye, 2001; Krumholz et al., 2009; Noterdaeme et al., 2015a).

8.4.2 Metallicity distribution

DLAs with substantial amounts of dust are expected to also be metal-rich since dust is believed to be produced by the condensation of strongly depleted elements such as iron

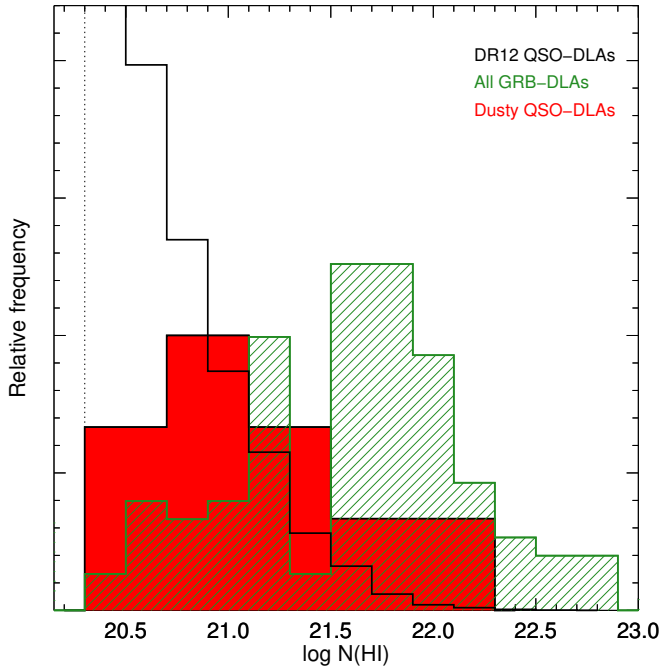

Figure 8.4.1. Histogram of the H I column densities of the GRB-DLA sample (green), the QSO-DLAs from the SDSS-DR12 sample (black), and the dusty QSO-DLAs (light red). The numbers have been rescaled for vizualization purposes.

and chromium and also to a lesser extent carbon, silicon, and magnesium. Empirically, this has been shown by studying dust depletion patterns in large samples of DLAs (Ledoux et al., 2003; De Cia et al., 2013). In Fig. 8.4.2 we plot the metallicities of the dusty QSO-DLAs as a function of redshift (left panel) and H I column density (right panel). For comparison we also show the metallicities from the current most complete list of high-resolution QSO-DLA spectra (mainly selected from the early SDSS-DR3 and DR5) presented in Rafelski et al. (2012, 2014) and the metallicities from the extensive GRB-DLA sample compiled by Cucchiara et al. (2015), except for GRB 130606A where we use the metallicity from Hartoog et al. (2015). While there certainly is some overlap, the dusty QSO-DLAs clearly appear as a distinct population with on average higher metallicities. A similar sample of specifically metal-strong ([X/H] $\gtrsim -1$) QSO-DLAs was studied by Herbert-Fort et al. (2006) and Kaplan et al. (2010), but only a few objects from the latter sample were also dust-rich and met the criterion of $A_V \geq 0.1$ mag to be included in the compiled sample presented here. Compared to these earlier studies, our sample contains absorbers with higher metallicities, H I column densities, and dust content.

In the right panel of Fig. 8.4.2 we also show the upper envelope noted by Boisse et al. (1998) for typical QSO-DLAs, which corresponds to a metal column density of $\log N(\mathrm{H_X}) \equiv \log N(\mathrm{H\,I}) + [\mathrm{X/H}] = 20.5$ (which can be converted to an estimate of

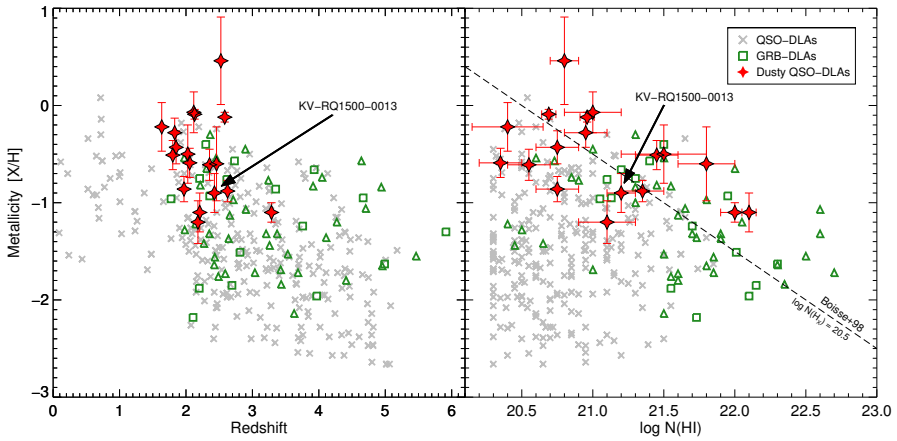

Figure 8.4.2. Metallicity evolution with redshift of the DLA samples (left panel) and as a function of H I column densities, $\log N(\mathrm{H\,I})$, (right panel). The typical QSO-DLAs with metallicities from the literature are shown as gray crosses, the GRB-DLAs as green squares (exact values) and upward triangles (lower limits) and the dusty QSO-DLAs from our sample are shown as red star symbols. The dusty QSO-DLAs reveal a higher average mean metallicity compared to all QSO-DLAs. About two thirds of the dusty QSO-DLAs exceed the apparent demarcation line proposed by Boisse et al. (1998), corresponding to $\log N(\mathrm{H_X}) \equiv \log N(\mathrm{H\,I}) + [\mathrm{X/H}] = 20.5$ cm^{-2}, above which the detection probability of QSO-DLAs is hampered due to dust obscuration of the underlying quasars.

the amount of dust in the absorber, see e.g. Zafar & Watson, 2013) or a zinc column density of $\log N(\mathrm{Zn\,II}) = 13.15$. We find that ten out of the 18 systems in our sample of dusty QSO-DLAs are beyond this proposed limit for significant dust obscuration, with the dusty QSO-DLA towards KV-RQ 1500-0013 just straddling the envelope, having $\log N(\mathrm{H_X}) = 20.30 \pm 0.30$. By computing a Zn II column density of the Mg II absorber at $z = 1.603$ towards KV-RQ 1500-0013 from the equivalent width of Zn II λ 2026 assuming that it is optically thin, we find that $\log N(\mathrm{Zn\,II/cm^{-2}}) = 13.40 \pm 0.03$. We caution, however, that we might underestimate the column density if the line is saturated, but also note that at this resolution the line could be blended with Mg I λ 2026. This suggests that the intervening Mg II absorber towards KV-RQ 1500-0013 actually exceeds this apparent demarcation line noted by Boisse et al. (1998). This implies that a significant fraction of the observed extinction could be caused by the Mg II absorber.

We confirm that the dusty QSO-DLAs which so far have been under-represented in optically selected quasar samples indeed occupy the region of high-Z and high-$N(\mathrm{H\,I})$. A similar conclusion was realized for H_2-bearing DLAs by Noterdaeme et al. (2015a), where it is also discussed how significant amounts of dust are necessary for the conversion of H I to H_2 molecules and not unexpectedly cause the H_2-bearing DLAs to occupy the same region of the $Z - N(\mathrm{H\,I})$ plane.

8.4.3 Correction to the cosmic metallicity distribution

The goal of the dedicated campaigns to search for dusty QSO-DLAs was to quantify the correction to the overall metallicity budget due to the missing sub-population of dusty and metal-rich absorbers in optical quasar surveys. This issue is not straightforward to resolve and is probably the cause of the large discrepancy between earlier studies in the literature (a few per cents to several times the estimated metallicity budget observed from the bulk of known QSO-DLAs has been proposed). To quantify the correction factor using our compiled sample and to provide a potential resolution to this issue we follow a two-step approach. First, we determine the relation between the fraction of dusty QSO-DLAs and the metallicity correction. Then we attempt to bracket this fraction such that we can provide limits on the true, dust-corrected cosmic mean metallicity.

We estimate the potential contribution from this sample of dusty QSO-DLAs to previous measurements of the H I column density weighted mean metallicity, $\langle Z \rangle$, which can be defined as

$$\langle Z \rangle = \log\left(\sum_i 10^{[\mathrm{X/H}]_i} N(\mathrm{H\,I})_i \Big/ \sum_i N(\mathrm{H\,I})_i \right) , \tag{8.2}$$

where i represents each bin of QSO-DLAs (Lanzetta et al., 1995; Prochaska et al., 2003). Specifically, we calculate $\langle Z \rangle$ in the range $z \approx 1.6 - 3.3$ between which the dusty QSO-DLAs are located and compare it to the average value measured for $\langle Z \rangle$ by Rafelski et al. (2012, 2014) for the dust-poor QSO-DLAs in the same redshift range. We also assume that no QSO-DLAs with $A_V > 0.1$ mag are present in the dust-poor sample (no evidence was found for significant reddening in this sub-sample, see Prochaska et al., 2007).

The mean metallicity of our dusty QSO-DLA sample is $[\mathrm{X/H}] = -0.53 \pm 0.43$ (where the uncertainty represents the 1σ scatter) over the entire redshift range (compared to e.g. the sample of metal-strong QSO-DLAs by Kaplan et al., 2010, who find a median of $[\mathrm{X/H}] = -0.67$ at similar redshifts). We then compute the correction factor for a given contribution of dusty QSO-DLAs to the total population of DLAs at $z \approx 1.6 - 3.3$. We define x as the fraction of missed (and likely dusty) QSO-DLAs and derive

$$\langle Z \rangle_{\mathrm{corr}}(\%) = \left(22.109 \times 10^{0.811x - 1.345} - 1 \right) \times 100\% , \tag{8.3}$$

where, for example, $x = 0.1$ corresponds to a missing fraction of DLAs of 10%. For this equation we simply correct the mean metallicity of typical QSO-DLAs in the same redshift range as our sample by adding the mean metallicity of the dusty QSO-DLAs with a weight given by the fraction, x, as $\langle Z \rangle_{\mathrm{corr}} = (1 - x)\langle Z \rangle_{\mathrm{dust-poor}} + x \langle Z \rangle_{\mathrm{dust-rich}}$. This provides an estimate for $\langle Z \rangle_{\mathrm{corr}}(\%)$ which is defined as the increase in the overall metallicity in percentage. We here assume that the regular QSO-DLAs from optical surveys are well represented by the sample of Rafelski et al. (2012, 2014).

Since the DLAs in our sample are not uniformly selected, however, we are not able to estimate the exact fraction and distribution of, for example, metallicity and A_V for the true underlying population. The correction factor is likely underestimated. For example, Pontzen & Pettini (2009) estimated that approximately 7% of QSO-DLAs

(with an upper limit of 17% at 2σ confidence level) are missed from optical samples due to dust obscuration. Their results, however, suggest that the cosmic density of metals measured from optical QSO-DLA surveys could be underestimated by a factor of approximately two. For comparison, we estimate a correction factor of $\approx 20\%$ for the cosmic density of metals assuming that 10% (see Sect. 8.6 for an estimate of this fraction) of the most dusty absorbers are missed in optical QSO-DLA surveys. This indicates that our compiled sample likely does not probe all of the dusty, most metal-rich QSO-DLAs but is just the first representation of the expanded quasar selection criteria.

8.4.4 Dust properties and metal column density

An important piece of information regarding the population of dusty QSO-DLAs is how their dust properties link to the metallicity of the systems. This will further our understanding of how dusty absorbers bias the observed population of QSO-DLAs with respect to metallicity and dust properties at high redshifts. First, we are able to confirm the linear trend between dust depletion and metallicity from our data as has been noted before in the literature (e.g. Pettini et al., 1997a; Ledoux et al., 2003; Akerman et al., 2005; De Cia et al., 2013), but now we can extend the relation out to super-solar metallicities with the recent discovery of the DLA towards J 0000+0048 (Noterdaeme et al., 2017). We also observe a linear relation between the metal column density, $N(\mathrm{H_X})$, and the dust extinction, A_V, similar to previous studies (e.g. Vladilo et al., 2006; Zafar & Watson, 2013) but surprisingly, we do not find any correlation between the inferred dust extinction and the measured dust depletion, [Fe/Zn]. This apparent discrepancy has also been noted for GRB-DLAs (Savaglio & Fall, 2004; Wiseman et al., 2017) and it has been argued that the inconsistency might be due to the fact that iron does not trace most of the dust mass that will otherwise impact the inferred extinction (Zafar & Watson, 2013; Dwek, 2016; Wiseman et al., 2017). Computing the dust-to-gas ratio, $A_V/N(\mathrm{H\,I})$, for each of the absorbers in our sample we find that all, except the two DLAs with the highest H I column densities ($\log N(\mathrm{H\,I}) \approx 22$), have enriched dust properties consistent with that of the Local Group (LG). This contrasts with what has been observed for the bulk of the known QSO-DLA population, with typically much lower dust-to-gas ratios than those observed in the LG (e.g. Vladilo et al., 2008; Khare et al., 2012). A similar result was found from the C I-selected absorber sample by Ledoux et al. (2015), who also detect systems with more evolved dust properties than those of the SMC, the LMC, and even the MW.

From the right panel of Fig. 8.4.2 we can see that, while the dusty QSO-DLAs generally are at higher metallicities than the GRB-DLAs, the distribution of metal column density, $N(\mathrm{H_X})$, for the two populations appears remarkably similar. In Fig. 8.4.3 we show a histogram of the metal column densities for the three DLA populations also shown in Fig. 8.4.2. The populations of dusty QSO-DLAs and GRB-DLAs are clearly distinct from the dust-poor, regular QSO-DLAs, with measured mean values of $\log N(\mathrm{H_X}) = 20.6$, 20.4, and 19.3, respectively. We only considered the GRBs that classify as DLAs having $\log N(\mathrm{H\,I}) > 20.3$ in the analysis. We note that due to the large number of lower limits on the metallicity for GRB-DLAs (we included the lower limits in the figure as their respective values), the actual average value for this population might be higher and comparable to that of the dusty QSO-DLAs. When

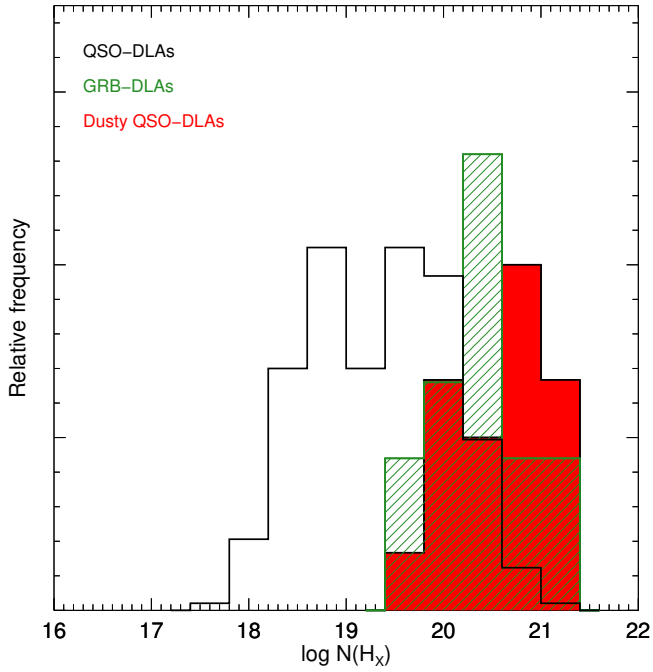

Figure 8.4.3. Histogram of the metal column densities, $\log N(\mathrm{H_X}) \equiv \log N(\mathrm{H\,I}) + [\mathrm{X/H}]$, of the dusty QSO-DLAs (red) compared to the sample of GRB-DLAs (green) and dust-poor QSO-DLAs (black) described in the text. The frequencies have been rescaled for vizualization purposes.

performing a two-sided Kolmogorov-Smirnov test on these two populations, we find that the probability that the two samples are drawn from the same parent distribution is $\approx 4\times10^{-5}$. For comparison, the same test yields a probability of $\approx 2\times10^{-6}$ and $\approx 7\times10^{-7}$ that the dusty QSO-DLAs and the GRB-DLAs are drawn from the same parent distribution as the typical QSO-DLAs, respectively.

8.5 Dust bias in quasar samples

8.5.1 Induced reddening by dusty QSO-DLAs

As already explored by Krogager et al. (2016a) and Fynbo et al. (2017), reddening induced by foreground dusty DLAs will severely decrease the detection probability of the underlying quasars. To assess the effect of dust reddening on the optical colors of the quasars in our sample, we show the distribution of $g-r$, $g-i$, and $r-z$ colors in Fig. 8.5.1. For comparison we also show the same color distribution of all quasars from the SDSS-DR12 quasar sample (DR12Q; Pâris et al., 2017) in the same redshift range as that of the background QSOs from our sample, $z = 1.5-4.0$. Not surprisingly, the majority of the dusty QSO-DLAs have redder colors than the average quasar colors

at all redshifts with a typical color excess of $0.1 - 0.3$ mag. In a few extreme cases the excess is as high as ~ 1 mag. This is a remarkable reddening effect given that the maximum derived extinction for the DLAs in our compiled sample is $A_V \approx 0.6$ mag. GRB-DLAs have been observed with much higher values of extinction ($A_V > 3$ mag, see Prochaska et al., 2009; Krühler et al., 2011), where one would expect a reddening of several magnitudes of the optical colors for DLAs with similar properties toward quasars. To illustrate how the dusty QSO-DLA sample behaves compared to the bulk of the known QSO-DLA population we also show the mean $r - z$ mag color excess (right panel) derived for SDSS-DR5 QSO-DLAs (Vladilo et al., 2008) and the mean $g - i$ mag color excess (middle panel) derived for SDSS-DR7 QSO-DLAs (Khare et al., 2012), which both only slightly lie above the mean derived for the SDSS-DR12 quasars. The compiled sample of dusty QSO-DLAs presented here has a color excess of approximately $r - z = 0.3$ on average compared to the SDSS-DR12 quasar sample.

Evidence for significant reddening effects was found for the C I absorbers presented by Ledoux et al. (2015) as well, revealing that the typical color excess of the C I absorbers was five times that of the early SDSS DLA samples. We also note from the figure that the $r - z$ color of the individual dusty QSO-DLAs is actually the ideal probe of reddening caused by dust. For example, the dusty DLA towards J 0816+1446 with the highest emission redshift of the background quasar (light blue star at $z_{\rm QSO} = 3.85$), has very red $g - r$ and $g - i$ colors primarily due to the high redshifts of the DLA and the quasar, but only have a modest induced reddening in $r - z$ due to its relatively low amount of extinction of $A_V = 0.15$ mag.

To highlight that reddening effects, in addition to simple dimming in the form of dust obscuration, are expected to play a large role in the dust bias as well (as also explored by e.g. Fynbo et al., 2017) we show a histogram of the observed r-band magnitudes of the dusty QSO-DLAs in Fig. 8.5.2. We compare these to the SDSS-DR12 QSO-DLAs (Noterdaeme et al., 2012a) and the total number of quasars from the SDSS-DR12Q survey (Pâris et al., 2017), again at quasar emission redshifts between $z = 1.5 - 4.0$. We find a mean of $r = 18.75$ mag for the quasars with foreground dusty DLAs, roughly two magnitudes brighter than the mean of $r = 20.39$ mag and $r = 20.65$ mag for the full sample of SDSS-DR12 QSO-DLAs and the SDSS-DR12 quasars in the same redshift range, respectively. This indicates that the dominating bias in the SDSS and BOSS quasar samples is not simply obscuration from the DLA since the survey detection limit could detect such systems with up to $1 - 2$ mag extinction. Rather, the reddening effects of dusty DLAs cause the quasars to decieve optical detection or identification techniques, simply due to how these are defined. Expanded selection criteria are thus needed to reveal this missing population as demonstrated by the three bright, dusty QSO-DLAs examined here, identified mainly in the near and mid-infrared.

8.5.2 Selection properties

In Fig. 8.5.3 we show the $g - r$ colors of the dusty QSO-DLAs as a function of $u - g$ (representing the UV excess of quasars compared to stars on which optically selected samples have mainly relied), $r - i$ and $J - K_s$. Overplotted is the SDSS-DR12Q sample again in the same redshift range, $1.5 < z < 4.0$, shown as gray contours. To illustrate the redshift track of unreddened quasars we also show the model colors of the quasar

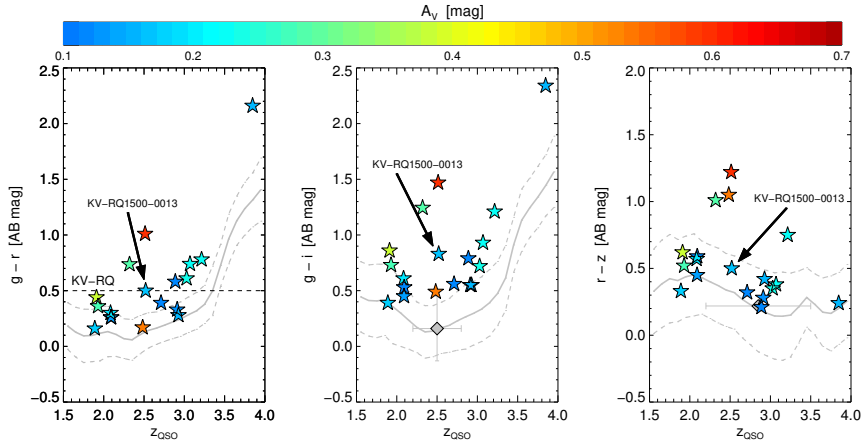

Figure 8.5.1. Optical colors color-coded as a function of visual extinction, A_V, versus quasar emission redshift for the dusty QSO-DLAs presented here and the average quasar colors from the SDSS-DR12Q sample. The solid gray lines denotes the SDSS-DR12Q sample median and the dashed lines show one standard deviation away from the median. The colored symbols show the individual broad-band colors, $g-r$, $g-i$, and $r-z$, of the dusty QSO-DLAs. For comparison, the strongest KV-RQ selection criteria ($g-r>0.5$) is shown in the left panel as the dashed, black line, the mean $g-i$ color excess of DLAs from SDSS-DR7 derived by Khare et al. (2012) is shown in the middle panel, and the mean $r-z$ color excess of DLAs from SDSS-DR5 derived by Vladilo et al. (2008) is shown in the right panel (both as large gray diamonds). The horizontal errors denote the redshift span of the DLAs in each of the two SDSS-based samples. It is clear that the dusty absorbers cause an increased reddening in the optical colors, in general as a function of their extinction.

composite template by Selsing et al. (2016) as a function of redshift. For a simple system where the DLA is at $z_{\rm abs}=2.5$ and the quasar at $z_{\rm QSO}=3.0$, we visualize the reddening vectors for $A_V=0.25, 0.50, 0.75$, and 1.00 mag, assuming the extinction curves of the MW, SMC, and LMC from Pei (1992). The underlying quasars illuminating the dusty QSO-DLAs in our sample have been color-coded following the type of selection from which these were identified. We refer the reader to Table 8.4.1 for the different classifications suggested by the surveys. We find no clear tendency between the quasars that were photometrically selected as part of the SDSS and BOSS surveys, compared to those that were detected in radio or as filler sources. It is clearly demonstrated how in optical color-color space, reddening due to dust and increasing redshifts will make the quasar appear star-like in its optical colors, whereas in the near-infrared the dustiest systems lie the farthest away from the stellar locus.

To test whether the metal column density of the dusty QSO-DLAs is directly related to the detection probability of the underlying quasars, we show our sample in a plot of metallicity as a function of H I column density in Fig. 8.5.4, color-coded following the type of selection the quasars were identified from. The line defined by Boisse et al. (1998) at $\log N({\rm H_X})=20.5$ (or $A_V=0.2$ mag following the relation from Zafar & Watson, 2013) is overplotted here as well. For comparison we also show lines

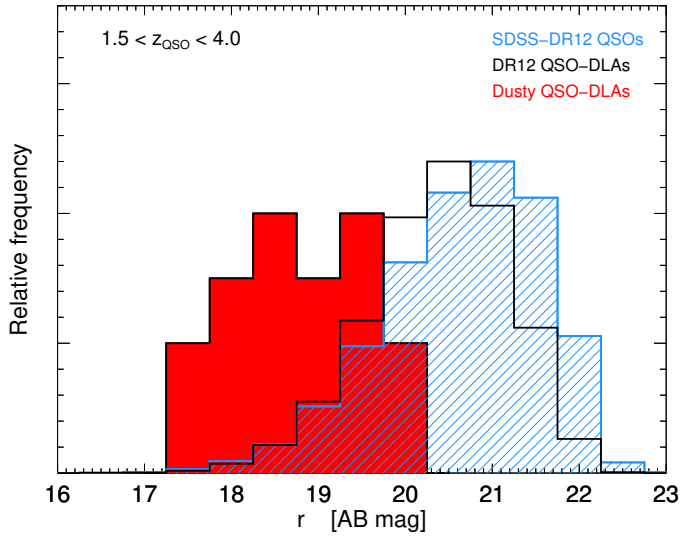

Figure 8.5.2. Histogram of the observed r-band magnitudes of the dusty QSO-DLAs compared to the SDSS-DR12 QSO-DLAs and the total number of quasars from the SDSS-DR12Q survey at redshifts 1.5 – 4.0. The mean r-band magnitude of 18.78 mag for the dusty QSO-DLAs is roughly two magnitudes brighter than the mean of $r = 20.39$ mag and $r = 20.65$ mag for the full sample of SDSS-DR12 QSO-DLAs and quasars, respectively, in the same redshift range.

representing metal column densities of $\log N(\mathrm{H_X}) = 21.0$, 21.5 and 22.0, corresponding to $A_V = 0.63$, 2.00 and 6.31 mag, respectively. Of the ten quasars located above the threshold observed for the regular QSO-DLA population, only five are identified by the photometric selection criteria of the SDSS (two; light blue squares) and BOSS (three; dark blue squares) surveys. The remaining five objects are the two HAQ and eHAQ sources and the three SDSS/BOSS filler or radio quasar detections. Below the line of $\log N(\mathrm{H_X}) = 20.5$ are located five radio-selected or filler sources, two SDSS-selected quasars, and KV-RQ1500-0013.

Thus, we do not find a direct correlation between the metal column density (or dust extinction) and the detection probability of the photometric selection criteria of the SDSS and BOSS surveys. However, we can conclude that the detection probability decreases to $\approx 40\%$ for QSO-DLAs with $A_V \geq 0.1$ mag based on this sample. Furthermore, we demonstrate that the threshold found by Boisse et al. (1998) marking the region of a significant decreasing detection probability is simply a result of the average dust-to-metal ratio of the QSO-DLAs in their sample and the flux limit of the early quasar surveys.

8.5.3 Alleviating the dust bias

It is now clear how even modest amounts of extinction ($0.1 \lesssim A_V \lesssim 0.6$ mag) can induce large optical reddening effects, potentially causing the dust bias. This issue has been studied extensively in the literature (Fall & Pei, 1989; Fall et al., 1989; Pei et al., 1991;

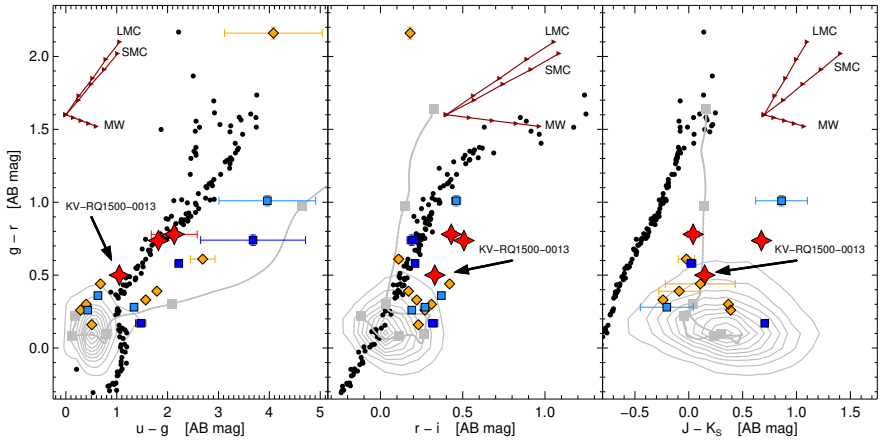

Figure 8.5.3. Effect of dust on optical/near-infrared quasar colors. Only a subset of the dusty QSO-DLAs have near-infrared colors from either 2MASS or UKIDSS. We show where the bulk of the SDSS-DR12 quasar population at $1.5 < z < 4.0$ is located in $g-r$ versus $u-g$, $r-i$, and $J-K_S$ colors as the gray contours. For illustration purposes we model a redshift track of a composite quasar template (gray solid line) in steps of $\Delta z = 0.5$ starting from $z = 1.5$ to $z = 4.0$, each step shown by the gray squares. The black dots denote the colors of standard, main-sequence stars from Hewett et al. (2006). Also shown are reddening vectors for a simple system with a DLA at $z_{\rm abs} = 2.5$ and a quasar at $z_{\rm QSO} = 3.0$, in steps of $A_V = 0.25, 0.50, 0.75$, and 1.00 mag (red arrows). The dusty QSO-DLAs are overplotted and color-coded as a function of how their underlying background quasars were selected. Red star symbols denote the quasars that were misclassified as stars in SDSS but identified in the HAQ and KV-RQ surveys, blue squares show the sources photometrically selected to be quasars in the SDSS (light) and BOSS (dark) surveys, and orange diamonds denote sources that were observed as part of the SDSS and BOSS surveys but were selected as, e.g., filler or radio sources.

Murphy & Liske, 2004; Pontzen & Pettini, 2009; Frank & Péroux, 2010; Murphy & Bernet, 2016), however, there seems to be some tension between the conclusions. While some argue that dust bias is likely to be a minor effect (see e.g. the radio selected samples of Ellison et al., 2001; Jorgenson et al., 2006), others find a significant fraction of absorbers containing dust (e.g. Fall & Pei, 1993; Vladilo & Péroux, 2005). The majority of previous studies have been based on optically selected samples, however, and are therefore more biased as a consequence.

A potential approach to alleviate the dust bias is to select quasars in the near/mid-infrared or based on radio-detections, where the selection techniques are insensitive to reddening. A general approach using the near-infrared UKIDSS survey was carried out by Maddox et al. (2008, 2012) relying on the K-band excess of quasars compared to that of stars (Warren et al., 2000). The effectiveness of this approach is also illustrated in the right panel of Fig. 8.5.3. Instead of defining an unbiased survey, systematically targeting and classifying sources missed by current surveys could potentially also be a way to resolve the issue of dust bias. An example of such an approach was carried out in the designated searches for the missing dusty DLAs (e.g. in the HAQ survey; Fynbo et al.,

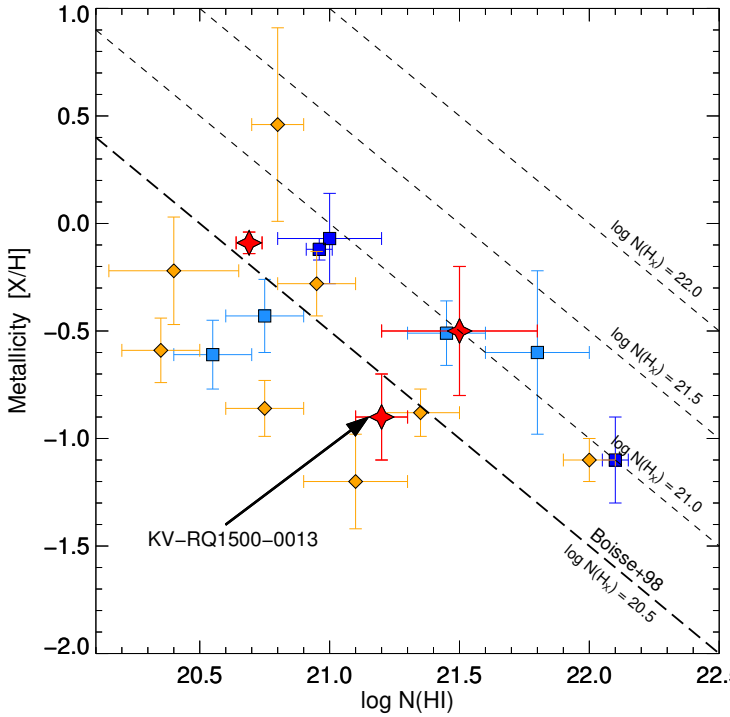

Figure 8.5.4. Metallicity as a function of H I column density of the dusty QSO-DLAs. The colored symbols show the specific selection of the background quasars (see Fig. 8.5.3). Overplotted is again the Boisse et al. (1998) line corresponding to $\log N(\mathrm{H_X}) = 20.5$, shown together with the dashed lines representing metal column densities of $\log N(\mathrm{H_X}) = 21.0$, 21.5, and 22.0, respectively.

2013a; Krogager et al., 2015, 2016b) toward quasars misclassified as stars in SDSS due to their red optical colors. The same method was adopted for the design of the KV-RQ survey from which the dusty QSO-DLA studied here, KV-RQ1500-0013, was identified. More unbiased methods, such as variability (Schmidt et al., 2010; Graham et al., 2014) and purely astrometric selection of quasars (Heintz et al., 2015), also have the capability to select quasars in an unbiased way, at least in terms of colors.

8.6 Discussion and conclusions

In this work we report on the discovery and the spectroscopic observations of the quasar KV-RQ 1500-0013 at $z = 2.520$ with two intervening absorbers. One is a damped Lyα absorber (DLA) at $z = 2.428$, the other is a strong Mg II absorber at $z = 1.603$. The DLA is found to have an H I column density of $\log N(\mathrm{H\,I}) = 21.2 \pm 0.1$ and a relatively high metallicity of approximately [X/H] $= -0.90 \pm 0.20$ (one-seventh of solar). A significant amount of dust with an estimated extinction of $A_V = 0.16$ mag is observed towards

the quasar, found by fitting a composite quasar template to the observed spectra and photometric data. We were not able to locate the redshift of the dust or the individual contributions of the two absorbers to the total observed extinction. The candidate quasar was selected from a designated search for quasars reddened by dusty DLAs, which are misclassified as stars in the SDSS and BOSS surveys, as part of the KiDS-VIKING Red Quasar (KV-RQ) survey (Chap. 7). The quasar KV-RQ 1500-0013 is the third detection of a quasar with an intervening dusty DLA reddened out of the optical selection window of SDSS/BOSS, confirming that dusty and therefore metal-rich foreground galaxies toward quasars are under-represented in current optically selected samples.

We compared the DLA towards KV-RQ 1500-0013 and an additional sample of 17 dusty ($A_V > 0.1$ mag) QSO-DLAs compiled from the literature to the overall population of regular QSO-DLAs (Noterdaeme et al., 2012a; Rafelski et al., 2012, 2014) and to the population of GRB-DLAs (Cucchiara et al., 2015; Tanvir et al., 2018). Typically, GRB-DLAs are observed to have higher H I column densities and metallicities than QSO-DLAs (Savaglio et al., 2003; Savaglio, 2006; Jakobsson et al., 2006b; Fynbo et al., 2006b, 2009; Prochaska et al., 2007; Cucchiara et al., 2015). We have shown here that the apparent deficiency of QSO-DLAs with large H I column densities and metallicities, the sum of which yields the metal column density, can largely be explained by a significant dust bias in optically selected quasar surveys. The detection probability of QSO-DLAs appears to be dependent on the metal column density and extinction. While we do not find a direct correlation between the detection probability and metal column density, we conclude that for $A_V > 0.1$ mag the efficiency of optical selection drops to $\approx 40\%$ based on this sample. We will explore this effect on typical optical selection criteria by modeling the detection probability for a range of redshifts and extinction values in more detail in a future work.

The distribution of metal column density (and thus also extinction) in the dusty QSO-DLA sample was found to have a higher probability of belonging to the same population as GRB-DLAs when compared to the bulk of the known, regular QSO-DLAs. This could indicate that the sightlines toward quasars where dusty DLAs are observed are probing the same internal regions of the foreground galaxies as the environment in which GRBs explode, typically in the most central or brightest part of the galaxies hosting them (Bloom et al., 2002; Fruchter et al., 2006; Lyman et al., 2017). This would also explain the on average larger H I column density of the dusty QSO-DLAs, which is found to be anti-correlated with the impact parameter (Møller & Warren, 1998; Christensen et al., 2007; Fynbo et al., 2008; Monier et al., 2009; Rao et al., 2011; Krogager et al., 2012, 2017; Rahmati & Schaye, 2014; Noterdaeme et al., 2014).

We examined the reddening effect induced by dusty DLAs in the line of sight, compared to the bulk of SDSS-selected quasars and QSO-DLAs. Specifically, we demonstrated that even low extinction (the largest measured extinction in our compiled sample is $A_V \approx 0.6$ mag) can redden the quasar spectrum by as much as ~ 1 mag compared to typical quasar colors at the same redshift. As a result, even low amounts of dust in foreground DLAs will cause a significant fraction of the underlying quasars to evade the optical selection window defined for. for example, the SDSS and BOSS surveys. Preliminary results from the combined KiDS-VIKING photometric catalog, assembled for the KV-RQ survey, reveal that roughly 20% of the brightest quasars ($J < 20$ mag) have colors of $g - r > 0.5$ and $r - i > 0.0$, indicative of significant reddening

(Fynbo et al., 2013a; Krogager et al., 2015, 2016b; Heintz et al., 2016, see also Fig. 8.5.1 and 8.5.3). In this region of color-color space, about 50% of the full sample has been classified as quasars by the SDSS survey. In total we then expect that roughly 10% of all quasars are missed from the selection criteria defined in the SDSS, assuming that all quasars bluer than the colors mentioned here are efficiently identified.

Assuming that the number of intervening DLAs toward these quasars are the same as the non-reddened quasars, then that implies that the SDSS survey fails to identify $\approx 10\%$ of the most dusty DLAs. However, we expect this to be a lower limit since the case studied here and others from the literature are evidence for an additional bias against multiple absorbers in the line of sight toward quasars (Fynbo et al., 2011, 2013b). If such a bias is confirmed, related studies such as the incidence rate of strong Mg II absorbers toward quasars (Evans et al., 2013; Chen et al., 2017; Mathes et al., 2017; Christensen et al., 2017) will be affected as well.

The dusty QSO-DLAs presented here are the first representations of expanded quasar selection criteria. From observations of GRB-DLAs (see, e.g., Figs. 8.4.2 and 8.4.3) we expect even more dusty QSO-DLAs to exist, even though they might be rare. Specifically, none of the dusty QSO-DLAs are observed with $\log N(\mathrm{H_X}) > 21.5$, while a few such cases of GRB-DLAs are present in the samples examined here. While GRB-DLAs certainly are less biased in their selection in terms of obscuration and dust reddening, a bias may still exist in large GRB-selected DLA samples (e.g. Fiore et al., 2007). Such a bias was hinted at in a sample of GRB afterglows obtained with high resolution from observations with the VLT/UVES (Ledoux et al., 2009). This sample showed an on average lower metallicity than existing samples of low- to intermediate-resolution GRB afterglow spectra, which indicates that metal-rich or dust-obscured bursts are missed in the magnitude-limited GRB afterglow samples observed with high-resolution spectrographs. Furthermore, Fynbo et al. (2009) found that afterglows that are undetected in the optical typically have larger X-ray derived hydrogen column densities indicative of a dust bias in this large sample of GRB afterglows. Indeed, there is evidence that bursts with optical non-detections occur in very dusty host galaxies (Perley et al., 2009; Krühler et al., 2011).

We note that in addition to the issues studied in this paper, any dust bias will also affect the galaxy counterparts associated with the dusty QSO-DLAs. Specifically, the more evolved and metal-rich DLAs are thought to represent more massive systems, following mass-metallicity-luminosity relations (Møller et al., 2004, 2013; Fynbo et al., 2008; Krogager et al., 2012, 2017; Christensen et al., 2014; Arabsalmani et al., 2015). This has also been established by dedicated follow-up observations of the most metal-rich QSO-DLAs in SDSS (Fynbo et al., 2010, 2011, 2013b; Krogager et al., 2013, 2017). This implies that the most luminous emission counterparts of QSO-DLAs have evaded selection as well. This sub-population is important to constrain the true luminosity function of DLAs (e.g. Fynbo et al., 1999; Møller et al., 2002).

In the near-future, powerful space missions such as the *James Webb Space Telescope* and *EUCLID* will be a big leap forward in both establishing large surveys of quasars and extending current samples out to large redshifts with observations in the infrared wavelength range. This could potentially allow for an even better understanding of the dust bias in existing surveys, but also as a consequence reveal even dustier and higher redshift DLAs (reaching as far as just after the epoch of reionization) than can be probed

with current telescopes. Ultimately, this will improve the measurement of the cosmic chemical enrichment.

Acknowledgements

We would like to thank the anonymous referee for providing a thorough and constructive report, significantly improving the presentation of this paper. KEH and PJ acknowledge support by a Project Grant (162948–051) from The Icelandic Research Fund. The research leading to these results has received funding from the European Research Council under the European Union's Seventh Framework Program (FP7/2007-2013)/ERC Grant agreement no. EGGS-278202.

Chapter 9

Astrometric selection of quasars

This chapter is based on the following article:

Unidentified quasars among stationary objects from Gaia DR2

Published in Astronomy & Astrophysics, vol. 615, id. L8, 9 pp. (2018)

Authors:
K. E. Heintz, J. P. U. Fynbo, E. Høg, P. Møller, J.-K. Krogager, S. Geier, P. Jakobsson & L. Christensen

Here we apply a technique selecting quasar candidates purely as sources with zero proper motions in the *Gaia* data release 2 (DR2). We demonstrate that this approach is highly efficient toward high Galactic latitudes with $\lesssim 25\%$ contamination from stellar sources. Such a selection technique offers very pure sample completeness, since all cosmological point sources are selected regardless of their intrinsic spectral properties within the limiting magnitude of *Gaia*. We carry out a pilot-study, defining a sample compiled by including all *Gaia*-DR2 sources within one degree of the north Galactic pole (NGP) selected to have proper motions consistent with zero within 2σ uncertainty. By cross-matching the sample to the optical Sloan Digital Sky Survey (SDSS) and the mid-infrared (MIR) AllWISE photometric catalogues, we investigate the colours of each of our sources. We determine the efficiency of our selection by comparison with previously spectroscopically confirmed quasars. The majority of the zero-proper-motion sources selected here have optical to MIR colours consistent with known quasars. The remaining population may be contaminating stellar sources, but some may also be quasars with colours similar to stars. Spectroscopic follow-up of the zero-proper-motion sources is needed to unveil such a hitherto hidden quasar population. This approach has the potential to allow substantial progress on many important questions concerning quasars, such as determining the fraction of dust-obscured quasars, the fraction of broad

absorption line (BAL) quasars, and the metallicity distribution of damped Lyman-α absorbers. This technique could also potentially reveal new types of quasars or even new classes of cosmological point sources.

9.1 Introduction

There is great interest in building unbiased catalogues of quasars for use in answering a range of important astrophysical questions. Further constraints on these objects are needed to further our understanding of the quasar phenomenon itself and the growth and occurrence of supermassive black holes through cosmic time. Quasars are also used as probes of intervening material, and have been shown to play a role in re-ionisation of both hydrogen and helium, and effect the ultraviolet (UV) background levels throughout the universe (Hewett & Foltz, 1994; Weymann et al., 1981). Most current quasar surveys, however, rely on their specific intrinsic properties, such as strong UV emission (Schneider et al., 2010), distinct near-infrared (NIR) and mid-infrared (MIR) colours (Maddox et al., 2012; Secrest et al., 2015), X-ray output (Brusa et al., 2010) or prominent radio emission (Ivezić et al., 2002).

In this *Letter* we apply an astrometric approach, identifying quasars as apparently stationary sources on the sky, based purely on the astrometric measurement from the *Gaia* mission (Heintz et al., 2015), and present a pilot study. Such a technique was already proposed by Koo et al. (1986) but has so far not been widely applied. Our goal here is to quantify the efficiency and completeness of this selection technique. Identifying quasars based only on their zero proper motions has the potential to open a route of selecting quasars in an unbiased way, and might even lead to the discovery of new types of quasars or other types of extragalactic point sources.

9.2 Astrometric selection of quasars

The *Gaia* data release 2 (DR2; Gaia Collaboration et al., 2018) catalogue consists of more than 1.3×10^9 sources down to $G \approx 21$ mag, for which the five-parameter astrometric solution (positions, parallaxes, and proper motions) has been determined (Lindegren et al., 2018). The Gaia G filter is very broad, covering the spectral range from 400 to 1000 nm, and therefore quasars in a wide range of redshifts should be included in the catalogue.

We extract all sources within a radius of one degree from the north Galactic pole (NGP) centred on $(\alpha, \delta) = 12^{\rm h}\,51^{\rm m}\,26^{\rm s}.0\ +27^{\rm o}\,07^{\rm m}\,42^{\rm s}.0$ from the *Gaia* DR2 catalogue (see Fig. 9.2.1). We then limit our search to sources with $18 < G < 20$ mag, for which the associated uncertainty is up to 1.2 mas yr^{-1} in the respective proper motion components. This is motivated by our pre-study (Heintz et al., 2015) in which we (based on pre-launch simulations of the Gaia data) found that the expected contamination of apparently stationary stars is lower than $\approx 20\%$ at the Galactic poles, but increases significantly when observing closer to the Galactic plane or at magnitudes brighter than $G < 18$ mag. This criterion also rejects the faintest *Gaia* sources ($G > 20$ mag), which still have significant errors on their measured proper motions. We then select all point sources

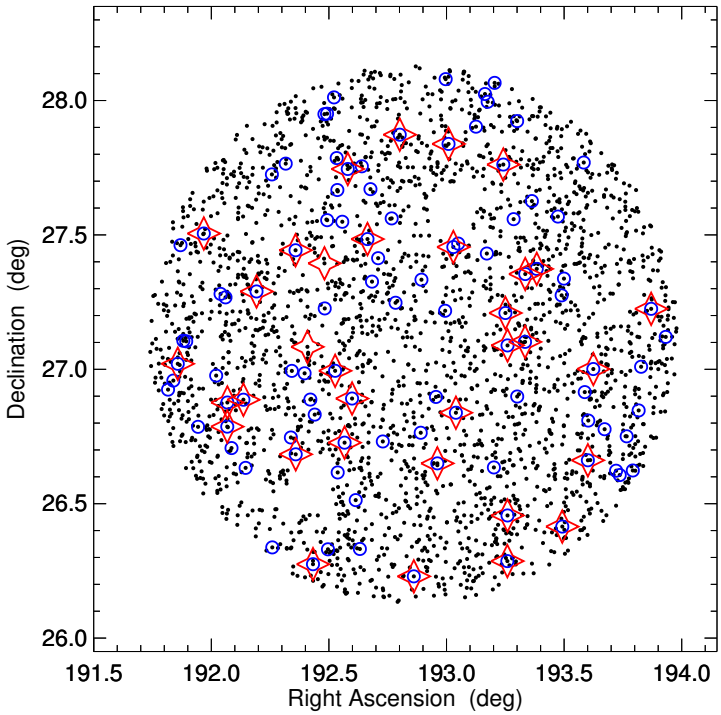

Figure 9.2.1. Location on the sky of all point-like *Gaia* sources with proper motions and $18 < G < 20$ mag (black dots) within one degree of the NGP. The subset of these with proper motions consistent with zero within 2σ are shown by the blue circles and those that are already spectroscopically confirmed quasars are shown by the red star symbols.

with total proper motions, $\mu = \sqrt{\mu_{\rm RA}^2 + \mu_{\rm Dec}^2}$, consistent with zero at the 2σ confidence level (i.e. $\mathrm{S/N}_\mu = \mu/\mu_{\rm err} < 2$). Finally, we identify the counterpart to each source in the Sloan Digital Sky Survey (SDSS) and require that all *Gaia* sources have morphologies consistent with being point sources (`class` = 6 in the SDSS) to limit our search to quasars only (i.e. excluding Seyferts and potential contaminating extended galaxies). This results in about 2% of the sample being removed due to extended morphology. Matching the *Gaia* sample to the SDSS with a matching radius of less than 1 arcsec also allows us to investigate the properties of our sample in optical colour-colour space.

In total, we find that there are 2,634 point sources observed by *Gaia*, all with measured proper motions and $18 < G < 20$ mag, within one degree of the NGP, of which 100 sources ($\approx 4\%$) have proper motions consistent with zero (within 2σ). These are marked with blue circles in Fig. 9.2.1. Cross-matching our extracted catalogue with the SDSS data release 14 quasar sample (SDSS-DR14Q, Pâris et al., 2017) and the NASA/IPAC Extragalactic Database (NED), we find that 34 quasars are already spectroscopically confirmed within the same magnitude limit and region on the sky, of which 32 ($\approx 95\%$) also have $\mathrm{S/N}_\mu = \mu/\mu_{\rm err} < 2$. This number is expected based on

Table 9.3.1. Point sources within one degree of the NGP with proper motions consistent with zero (within 2σ) and $18 < G < 20$ mag.

Source	R.A.	Decl.	u	g	r	i	z	$W1-W2$	$z_{\rm QSO}$
GQ125420+274609	12:54:20.0	+27:46:09.6	23.2	21.4	20.0	19.1	18.7	-	-
GQ125302+261711	12:53:02.1	+26:17:11.2	20.0	19.4	19.6	19.5	19.2	0.86	2.32
GQ125358+262453	12:53:58.1	+26:24:53.7	20.9	20.1	19.8	19.9	19.8	0.91	3.10
GQ125302+262722	12:53:02.2	+26:27:22.5	19.7	19.5	19.1	19.0	19.1	1.21	1.26
GQ125456+263623	12:54:56.8	+26:36:23.8	23.2	20.8	19.6	19.0	18.8	-0.09	-

Notes. Right ascension and declination are from the *Gaia* DR2 catalogue. Optical magnitudes are in the AB system and are from the SDSS photometric data. The MIR $W1-W2$ colours are from the AllWISE catalogue and are in the Vega system. Spectroscopic redshifts are based on the already identified quasars in the SDSS-DR14 quasar survey (Pâris et al., 2017) or the NED database (specifically from Crampton et al., 1987). Photometric redshifts (marked by a "P") are from Richards et al. (2009). This is part of the full table that can be viewed in the Appendix at the end of this Chapter.

the statistics of the 2σ cut. For the remaining two, the measured proper motions are 2.76 ± 1.09 and 1.22 ± 0.58 mas yr^{-1}. We also discover two spectroscopically confirmed stars, observed as part of the SDSS-APOGEE survey (Alam et al., 2015). An extract of the full sample of *Gaia* sources with zero proper motions is presented in Table 9.3.1. We also examine the additional requirement that the sources have parallaxes consistent with zero within 3σ, but only five sources (GQs 1255+2707, 1248+2658, 1247+2655, 1247+2706, and 1251+2804) were outside this criterion so we chose to include them for completeness.

9.3 Selection efficiency and completeness

We now investigate the location of the *Gaia* sources with zero proper motions in optical colour-colour space. By doing so, we can examine whether these candidate quasars have, for example, UV excess typical of unobscured, low-z quasars (e.g. Sandage, 1965; Schmidt & Green, 1983). About 70% of the zero proper motion sources have blue ($u-g<1$) colours (see Fig. 9.3.1). For quasars at $z \gtrsim 2.2$, the Lyman-α emission line will move out of the u-band, such that the quasars appear redder in $u-g$ colour space. At red $g-r$ colours ($g-r>1$), the zero-proper-motion sources have optical colours consistent with M or G dwarf stars. While some of these are likely to be stellar contaminations, removing these candidates will also exclude dust-reddened quasars and broad absorption line (BAL) quasars from the sample, which are found to have very red optical colours and to be systematically missing in most existing quasar samples (Fynbo et al., 2013a; Krogager et al., 2015, 2016b; Ross et al., 2015; Krawczyk et al., 2015).

To assess the efficiency of our selection, we cross-match our sample of *Gaia* sources with zero proper motions to the all-sky MIR survey based on the *WISE* satellite (AllWISE; Wright et al., 2010). Mid-infrared selection of quasars is efficient at separating stars and galaxies from quasars and is not affected by dust extinction, while also being sensitive to high-redshift quasars. Of the 100 *Gaia* point sources with zero proper

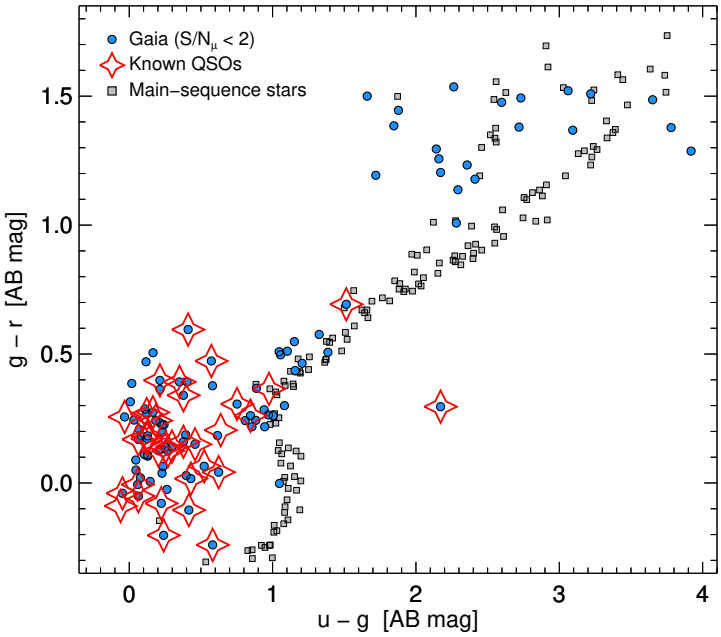

Figure 9.3.1. Optical colour-colour plots of the *WISE*-detected Gaia point sources with proper motions and $18 < G < 20$ mag (black dots) within one degree of the NGP. *Gaia* point sources with zero proper motions are represented by the blue dots and the spectroscopically confirmed quasars are shown by the red star symbols. Typical stellar colours are shown as grey dots.

motions, we identify 76 of the counterparts in the AllWISE catalogue within 1 arcsec. This cross-match might introduce a bias excluding quasars with weak IR emission. Stellar contaminants will also have weak IR emission however, and we find that of the 24 sources excluded in this approach, roughly half have a significant UV excess, whereas the other half have optical colours consistent with the main sequence stellar track. In Fig. 9.3.2, we show the zero proper motion *Gaia* sources in mid-infrared colour-colour space. Overplotted are contours of the SDSS-DR14Q sample for which *WISE* photometry exists. A simple colour criterion of $W1 - W2 > 0.8$ has been found to be robust in identifying quasars at most redshifts (Stern et al., 2012). In our sample of zero proper motion sources with *WISE* photometry, 55 (70%) have $W1 - W2 > 0.8$ (of which 29 are already identified quasars) and have WISE colours consistent with the full SDSS-DR14Q sample. We consider the remaining 26 sources as high-likelihood quasars. All these have also been photometrically identified as quasars by (Richards et al., 2009), and we list their estimated photometric redshifts in Table 9.3.1 as well, marked by a "P". We note, however, that at $W1 - W2 < 0.8$, two spectroscopically confirmed quasars have also been observed, one being a high-z quasar with optical colours consistent with known quasars in this redshift range and the other being a typical UV-excess quasar. These have MIR colours more consistent with typical stellar colours, as also illustrated in Fig. 9.3.2. We therefore consider the sources with zero proper

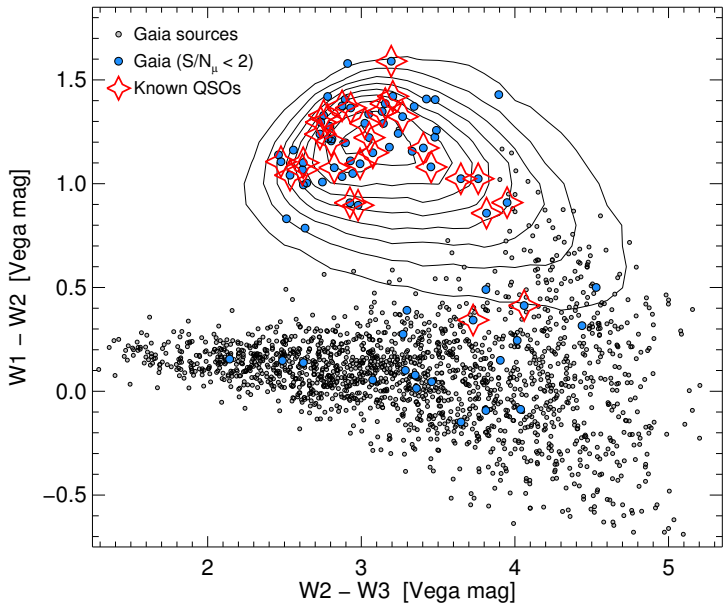

Figure 9.3.2. *WISE* colour-colour plot of all *Gaia* point sources (black dots), the subset with zero proper motions (blue dots), and spectroscopically confirmed quasars (red star symbols) within one degree of the NGP. Overplotted are contour levels linearly spaced in ten steps from 0 – 100% of the full SDSS-DR14 quasar sample with MIR counterparts in the AllWISE catalogue.

motions and $W1 - W2 < 0.8$ as possible contaminants (excluding the two already known quasars). We then infer a conservative selection efficiency of $N_{\rm QSO}/N_{\rm star} \gtrsim 75\%$. This is a lower limit due to the population of quasars with blue $W1 - W2$ colours that also populates our sample.

We present our main result in Fig. 9.3.3 where we show the full sample of *Gaia* sources with $18 < G < 20$ mag and within one degree of the NGP for which a counterpart in the AllWISE catalogue could be identified. It is clear from the figure that the majority of point sources selected on the basis of zero proper motions occupy a distinct region in S/N$_\mu$ – *WISE* colour parameter space. This demonstrates that selecting quasars as stationary sources on the sky is definitely feasible and has a high efficiency of $\gtrsim 75\%$. The completeness is close to 100% within the defined magnitude limit, since all cosmological objects are selected without any prior assumptions on the spectral energy distributions.

9.4 Discussion and conclusions

Here we have demonstrated the possibility to select quasars as stationary objects in the *Gaia* DR2 data set. When observing fields well away from the Galactic stellar disk (here the NGP) the contamination from stars is very modest (below 25%) when targeting the

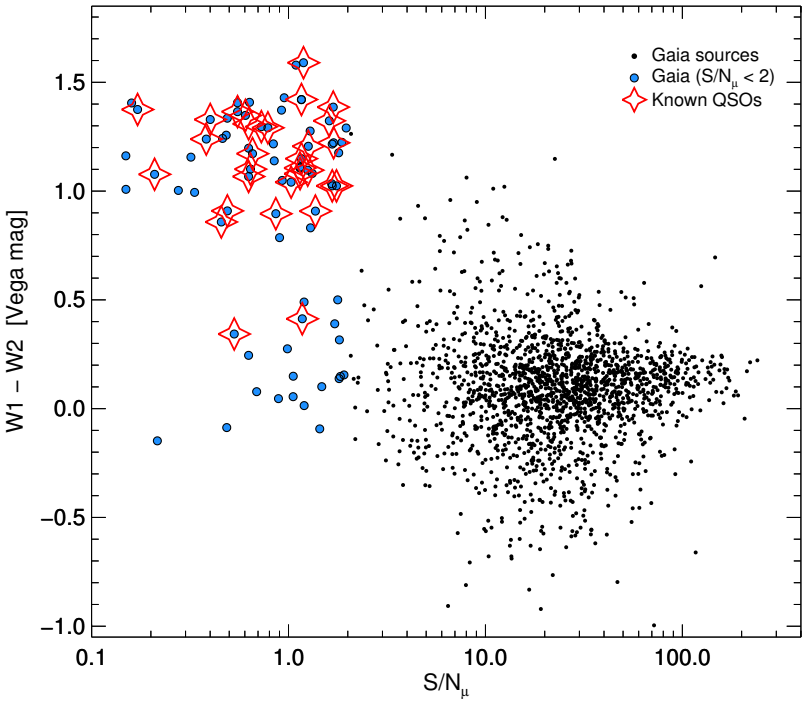

Figure 9.3.3. W1-W2 colour as a function of S/N$_\mu$ of the *WISE*-detected Gaia point sources with proper motions and $18 < G < 20$ mag (black dots) within one degree of the NGP. *Gaia* point sources with zero proper motions are represented by blue dots and spectroscopically confirmed quasars are shown with red star symbols.

most relevant magnitudes (here $18 < G < 20$). Therefore, astrometric selection offers both a complete and clean selection of quasars.

This technique offers the possibility to take major steps ahead on some very interesting problems relating to the quasar phenomenon. We mention a few examples here. First, obtaining a more complete picture of dust obscuration in quasar hosts will be possible with a sample of quasars selected using proper motions. Second, the redshift dependence of the frequency of BAL quasars can be determined. Third, using a purely astrometrically selected sample of quasars, we can get an independent gauge of the metallicity distribution of intervening galaxies, in particular the damped Lyman-α absorbers. Fourth, the identification of quasars via zero proper motion also provides unbiased measurements of number densities of various absorbers, such as C IV, Mg II, and H I. Such a sample will still be subject to a flux limit, but this is easier to model than the combined effect of a flux limit and the effect of dust reddening on the quasar-selection efficiency in optical quasar surveys. We also note that the *Gaia* DR2 data have been applied to find new gravitationally lensed quasars (Krone-Martins et al., 2018).

An interesting case is the confirmed quasar SDSS J125209.59+265018.4 (GQ125209 +265018 in Table 9.3.1). In Fig. 9.3.1, this is located as the object on the stellar track

at $u - g = 1.5$. In Fig. 9.3.2, it is one of the two sources with blue WISE colours at $W1 - W2 < 0.8$. This illustrates well the capability of the selection of quasars from astrometry to find quasars that are otherwise difficult to photometrically identify.

When the full *Gaia* data are released, the errors on the proper motions will decrease and it will therefore be easier to disentangle objects that are truly stationary (quasars) from stars with low proper motions. This will also make it possible to search for stationary sources at even fainter magnitudes. Also, since Gaia astrometry exists for most of the sky, this proper motion criteria could help reduce the contamination in other quasar surveys. Since Gaia covers the full sky, the selection can also be carried out for a large sample of sources; however, with the caveat that the contamination from apparently stationary stars increases significantly closer to the Galactic plane. We can also estimate the expected contamination of, for example, the WISE $W1 - W2$ colour selection, where it can be seen from Fig. 9.3.3 that 15% of the sources with $W1 - W2 > 0.8$ have significant proper motions at more than 5σ.

Acknowledgements

We would like to thank the referee for a clear and constructive report. KEH and PJ acknowledge support by a Project Grant (162948–051) from The Icelandic Research Fund. The Cosmic Dawn Center is funded by the DNRF. LC is supported by DFF – 4090-00079.

Appendix A – Full table

Table 9.4.1. Point sources within one degree of the NGP with proper motions consistent with zero (within 2σ) and $18 < G < 20$ mag.

Source	R.A.	Decl.	u	g	r	i	z	$W1-W2$	$z_{\rm QSO}$
GQ125420+274609	12:54:20.0	+27:46:09.6	23.2	21.4	20.0	19.1	18.7	-	-
GQ125302+261711	12:53:02.1	+26:17:11.2	20.0	19.4	19.6	19.5	19.2	0.86	2.32
GQ125358+262453	12:53:58.1	+26:24:53.7	20.9	20.1	19.8	19.9	19.8	0.91	3.10
GQ125302+262722	12:53:02.2	+26:27:22.5	19.7	19.5	19.1	19.0	19.1	1.21	1.26
GQ125456+263623	12:54:56.8	+26:36:23.8	23.2	20.8	19.6	19.0	18.8	-0.09	-
GQ125510+263724	12:55:10.1	+26:37:25.0	21.0	20.2	19.9	19.9	19.8	-	-
GQ125424+263941	12:54:24.3	+26:39:41.8	19.3	19.1	19.2	19.0	19.1	1.59	1.60
GQ125453+263721	12:54:53.0	+26:37:21.8	20.9	19.8	19.5	19.4	19.2	-	-
GQ125503+264502	12:55:03.8	+26:45:02.7	21.3	20.2	19.6	19.4	19.2	-	-
GQ125441+264637	12:54:41.3	+26:46:37.8	20.9	19.7	19.3	19.0	19.0	-	-
GQ125424+264833	12:54:24.6	+26:48:33.8	20.1	19.9	19.7	19.6	19.7	1.22	1.47P
GQ125516+265049	12:55:16.1	+26:50:49.0	25.0	21.1	19.8	19.2	18.9	-	-
GQ125518+270034	12:55:18.6	+27:00:34.3	23.9	21.2	19.7	18.2	17.5	0.16	-
GQ125543+270714	12:55:43.7	+27:07:14.1	23.8	21.0	19.7	18.2	17.5	0.14	star
GQ125126+261346	12:51:26.6	+26:13:46.9	19.6	19.7	19.4	19.3	19.4	1.11	1.43
GQ124943+261629	12:49:43.8	+26:16:29.7	18.9	18.9	18.7	18.5	18.5	0.34	1.84
GQ124959+261949	12:49:59.0	+26:19:49.3	21.1	20.2	19.9	19.7	19.7	-	-
GQ125031+261953	12:50:31.6	+26:19:53.7	19.6	19.4	19.3	19.4	19.4	1.00	0.88P
GQ125027+263048	12:50:27.3	+26:30:48.1	20.7	19.5	19.0	18.8	18.7	-	-
GQ125248+263805	12:52:48.3	+26:38:05.6	24.8	21.6	20.1	19.0	18.3	0.08	-
GQ125150+263900	12:51:50.7	+26:39:00.1	17.7	17.6	17.4	17.2	17.1	0.90	1.91
GQ125133+264550	12:51:33.7	+26:45:50.4	20.0	19.9	19.4	19.4	19.5	1.42	1.28P
GQ125209+265018	12:52:09.6	+26:50:18.5	21.9	20.4	19.7	19.5	19.3	0.41	3.44
GQ124902+262014	12:49:02.2	+26:20:14.7	22.6	20.8	19.7	19.1	18.8	-	-
GQ125008+263658	12:50:09.0	+26:36:58.6	19.7	19.3	19.3	19.2	19.2	1.05	0.68P
GQ124835+263759	12:48:35.0	+26:37:59.8	20.1	20.1	19.9	19.8	19.9	1.28	1.15P
GQ124820+264225	12:48:20.6	+26:42:25.1	20.4	19.4	19.4	19.4	19.6	-	-
GQ124926+264101	12:49:26.1	+26:41:01.4	19.7	19.3	19.2	19.2	19.2	1.10	0.67
GQ124921+264446	12:49:21.2	+26:44:46.8	19.9	19.9	19.6	19.6	18.9	0.99	0.31P
GQ125054+264353	12:50:55.0	+26:43:53.6	20.1	19.8	19.6	19.2	19.2	1.22	1.59P
GQ125015+264337	12:50:16.0	+26:43:37.6	18.5	18.4	18.4	18.2	18.3	1.38	1.79
GQ125149+265349	12:51:49.2	+26:53:50.0	23.1	21.0	19.8	19.3	19.1	0.50	star
GQ124945+264953	12:49:45.5	+26:49:53.3	25.0	21.2	19.8	19.1	18.8	0.25	-
GQ124941+265314	12:49:41.0	+26:53:14.8	20.5	19.9	19.7	19.7	19.6	-	2.46P
GQ125023+265328	12:50:23.6	+26:53:28.7	19.8	19.4	19.0	18.9	18.9	1.08	1.49
GQ124935+265906	12:49:35.2	+26:59:06.4	25.0	21.4	19.9	19.1	18.7	0.15	-
GQ125006+265939	12:50:06.3	+26:59:39.9	19.9	19.8	19.5	19.7	19.7	1.20	0.97

Table 9.4.1. *Continued.*

Source	R.A.	Decl.	u	g	r	i	z	$W1-W2$	$z_{\rm QSO}$
GQ125421+265454	12:54:21.0	+26:54:54.7	20.2	20.0	19.6	19.6	19.6	1.16	1.30P
GQ125429+270003	12:54:29.8	+27:00:03.8	19.7	19.5	19.4	19.1	19.2	1.10	1.64
GQ125312+265355	12:53:12.1	+26:53:55.7	24.6	21.5	20.0	18.9	18.4	-	-
GQ125302+270519	12:53:02.3	+27:05:19.9	22.6	20.4	20.1	20.0	20.0	1.02	2.99
GQ125320+270607	12:53:20.1	+27:06:07.4	20.1	19.7	19.1	18.8	18.9	1.32	1.15
GQ125528+271330	12:55:28.8	+27:13:30.1	20.0	19.8	19.5	19.7	19.7	1.30	1.03
GQ125357+271630	12:53:57.5	+27:16:30.6	22.2	19.9	18.9	18.5	18.3	-	-
GQ125359+272014	12:53:59.8	+27:20:14.8	20.6	20.3	20.3	19.9	20.4	1.58	0.08P
GQ125158+271304	12:51:58.6	+27:13:04.1	21.6	20.2	19.7	19.5	19.6	-	-
GQ125300+271234	12:53:00.1	+27:12:34.2	19.5	19.2	19.1	19.0	19.0	1.42	1.48
GQ125241+272550	12:52:41.1	+27:25:50.8	21.4	21.2	20.7	20.1	19.9	1.22	0.22P
GQ125134+272000	12:51:34.4	+27:20:00.2	20.9	19.9	19.7	19.7	19.7	-	-
GQ125107+271451	12:51:08.0	+27:14:51.5	20.2	19.8	19.4	19.2	18.8	0.79	0.38P
GQ125206+272717	12:52:07.0	+27:27:17.5	18.7	18.6	18.6	18.4	18.5	1.22	1.68
GQ125211+272803	12:52:11.9	+27:28:03.8	20.7	20.6	20.4	20.0	20.1	1.41	1.87P
GQ125332+272225	12:53:32.1	+27:22:25.1	19.6	19.3	19.2	18.9	18.8	1.39	1.63
GQ125320+272116	12:53:20.3	+27:21:16.0	18.0	17.8	18.0	17.9	17.8	1.04	0.51
GQ125353+273405	12:53:53.7	+27:34:05.9	21.4	20.3	19.8	19.5	19.5	0.39	-
GQ125308+273331	12:53:08.5	+27:33:31.2	23.8	21.6	20.4	19.2	18.5	-0.09	-
GQ125327+273733	12:53:27.1	+27:37:33.1	19.9	19.9	19.8	19.6	19.4	1.08	1.96P
GQ125257+274542	12:52:58.0	+27:45:42.5	19.0	18.7	18.6	18.5	18.4	1.32	2.00
GQ124816+264712	12:48:16.3	+26:47:12.3	18.1	18.1	18.2	17.9	17.8	1.35	1.86
GQ124746+264709	12:47:46.5	+26:47:09.8	21.2	20.2	20.0	19.8	19.7	-	-
GQ124816+265235	12:48:16.4	+26:52:35.3	20.1	19.5	19.4	19.4	19.3	-	2.51
GQ124832+265312	12:48:32.8	+26:53:12.7	18.2	17.8	17.9	17.7	17.8	1.11	0.59
GQ124804+265836	12:48:05.0	+26:58:36.1	24.8	22.2	20.7	19.1	18.3	0.15	-
GQ124715+265528	12:47:15.9	+26:55:28.1	22.4	20.1	18.9	18.6	18.3	-	-
GQ124721+265728	12:47:21.3	+26:57:28.9	21.3	20.2	19.7	19.5	19.4	-	-
GQ124725+270114	12:47:25.8	+27:01:14.1	19.8	19.3	19.2	19.2	19.0	1.07	0.80
GQ124731+270622	12:47:31.5	+27:06:22.2	20.9	20.0	19.8	19.7	19.8	-	-
GQ124734+270615	12:47:34.4	+27:06:15.2	23.7	21.8	20.3	19.0	18.3	0.05	-
GQ124922+265938	12:49:22.2	+26:59:38.9	21.3	20.1	19.7	19.5	19.5	-	-
GQ124955+271335	12:49:55.7	+27:13:35.3	19.5	19.4	19.3	19.2	19.2	1.37	1.47P
GQ124846+271722	12:48:46.1	+27:17:22.7	19.8	19.4	19.1	18.8	18.7	1.29	1.51
GQ124814+271603	12:48:14.5	+27:16:03.6	22.8	20.4	19.2	18.6	18.3	-0.15	-
GQ124809+271650	12:48:09.4	+27:16:50.1	20.2	20.0	19.7	19.8	19.7	1.16	0.95P
GQ124925+272634	12:49:26.0	+27:26:34.5	18.7	18.5	18.3	18.4	18.5	1.37	1.16
GQ124728+272742	12:47:28.6	+27:27:42.5	21.2	20.7	20.3	19.9	19.9	-	0.46P
GQ124752+273018	12:47:52.3	+27:30:18.9	20.4	20.0	19.9	19.9	19.8	0.91	0.91
GQ125043+271934	12:50:44.0	+27:19:34.3	20.3	20.2	20.1	20.2	20.0	0.83	0.93P
GQ125050+272448	12:50:50.2	+27:24:48.4	24.6	21.5	20.1	18.7	17.9	0.06	-
GQ125039+272904	12:50:39.4	+27:29:04.4	20.7	20.1	19.6	19.1	18.9	1.15	1.89

Table 9.4.1. *Continued.*

Source	R.A.	Decl.	u	g	r	i	z	$W1-W2$	z_{QSO}
GQ125104+273341	12:51:04.1	+27:33:41.2	20.2	20.2	19.8	19.8	20.1	1.24	1.15P
GQ124958+273317	12:49:58.2	+27:33:17.5	20.0	19.8	19.8	19.7	19.6	1.26	1.72P
GQ125013+273256	12:50:13.7	+27:32:56.4	19.9	19.8	19.6	19.5	19.7	1.14	1.15P
GQ125008+274001	12:50:08.6	+27:40:01.5	21.1	20.1	19.9	19.7	19.8	0.32	-
GQ125042+274012	12:50:42.4	+27:40:13.0	20.2	20.0	19.7	19.6	19.6	1.41	1.48P
GQ125033+274519	12:50:33.6	+27:45:19.1	20.0	19.8	19.7	19.6	19.7	1.41	1.48P
GQ125019+274443	12:50:19.2	+27:44:43.1	20.5	19.7	19.4	19.1	18.7	1.02	2.67
GQ125007+274709	12:50:07.9	+27:47:09.4	23.6	21.4	19.8	18.7	18.0	0.28	-
GQ125202+275018	12:52:02.1	+27:50:18.6	19.3	18.8	18.7	18.7	18.5	1.17	2.48
GQ125312+275524	12:53:12.1	+27:55:24.6	19.7	19.5	19.3	19.3	19.2	1.18	1.00P
GQ125230+275410	12:52:30.1	+27:54:10.0	19.4	19.3	19.0	19.1	19.1	1.03	1.04P
GQ125241+275942	12:52:42.0	+27:59:42.7	24.0	21.8	20.6	19.1	18.3	0.10	-
GQ125239+280127	12:52:39.2	+28:01:27.2	19.6	19.6	19.5	19.4	19.2	1.29	2.04P
GQ125249+280356	12:52:49.1	+28:03:56.4	19.4	19.3	19.2	19.4	19.2	1.01	0.93P
GQ125112+275222	12:51:12.3	+27:52:22.4	19.0	18.8	18.5	18.5	18.6	1.24	1.04
GQ125159+280446	12:51:59.1	+28:04:46.3	23.1	21.4	19.9	18.8	18.2	0.01	-
GQ124901+274330	12:49:01.8	+27:43:30.2	21.1	20.2	19.8	19.7	19.5	-	-
GQ124915+274554	12:49:15.9	+27:45:54.8	19.6	19.3	19.3	19.2	18.9	1.43	2.16P
GQ124955+275657	12:49:55.4	+27:56:57.7	21.2	19.9	19.3	19.0	18.9	0.49	-
GQ124958+275703	12:49:58.1	+27:57:03.7	19.8	19.6	19.4	19.1	19.0	1.34	1.91P
GQ125005+280041	12:50:05.2	+28:00:41.9	21.0	20.2	20.0	19.8	19.7	-	-

Notes. Right ascension and declination are from the *Gaia* DR2 catalogue. Optical magnitudes are in the AB system and are from the SDSS photometric data. The mid-infrared *W1*-*W2* colours are from the AllWISE catalogue and are in the Vega system. Spectroscopic redshifts are based on the already identified quasars in the SDSS-DR14 quasar survey (Pâris et al., 2017) or the NED database (specifically from Crampton et al., 1987). Photometric redshifts (marked by a "P") are from Richards et al. (2009).

Appendix B – Thumbnail images of all sources

Thumbnails of all point sources within one degree of the NGP with proper motions consistent with zero (within 2σ) and $18 < G < 20$ mag. East is up and north is to the right.

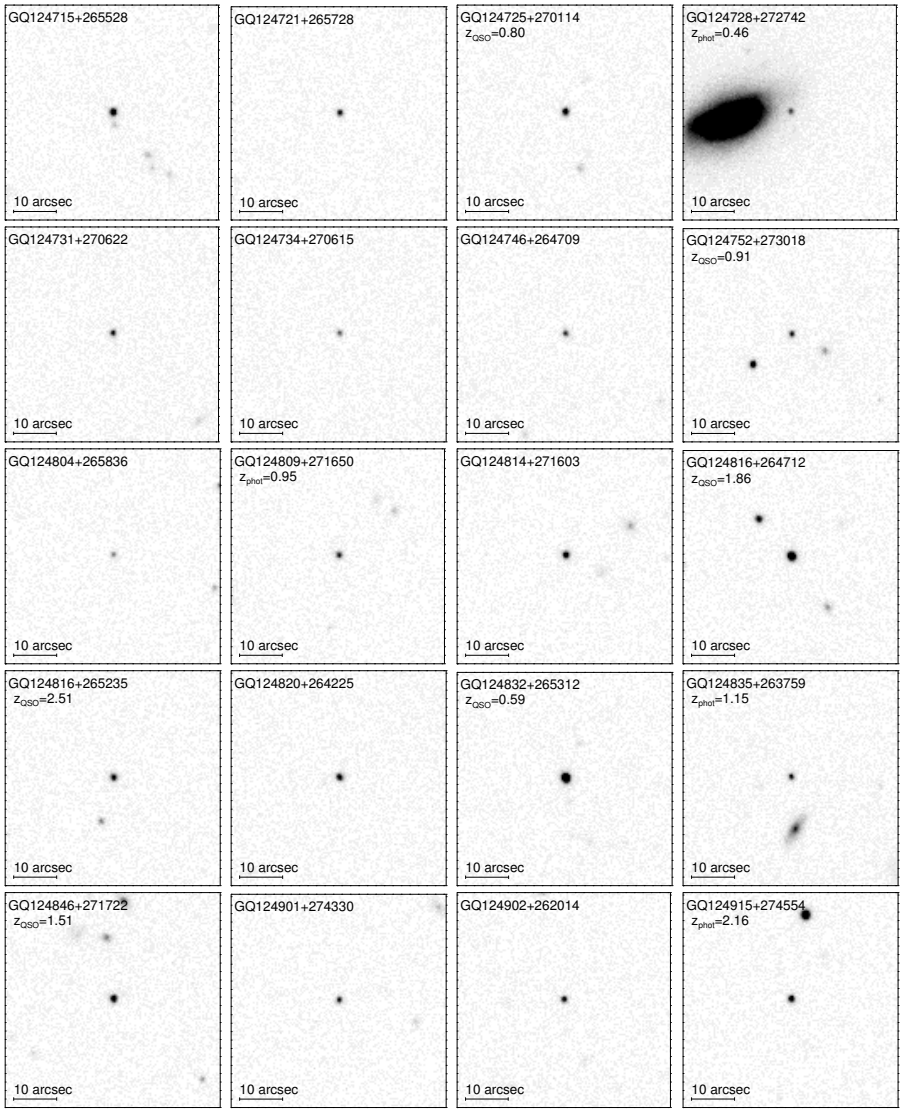

Figure 9.4.1. 50×50 arcsec^2 thumbnails around each stationary source.

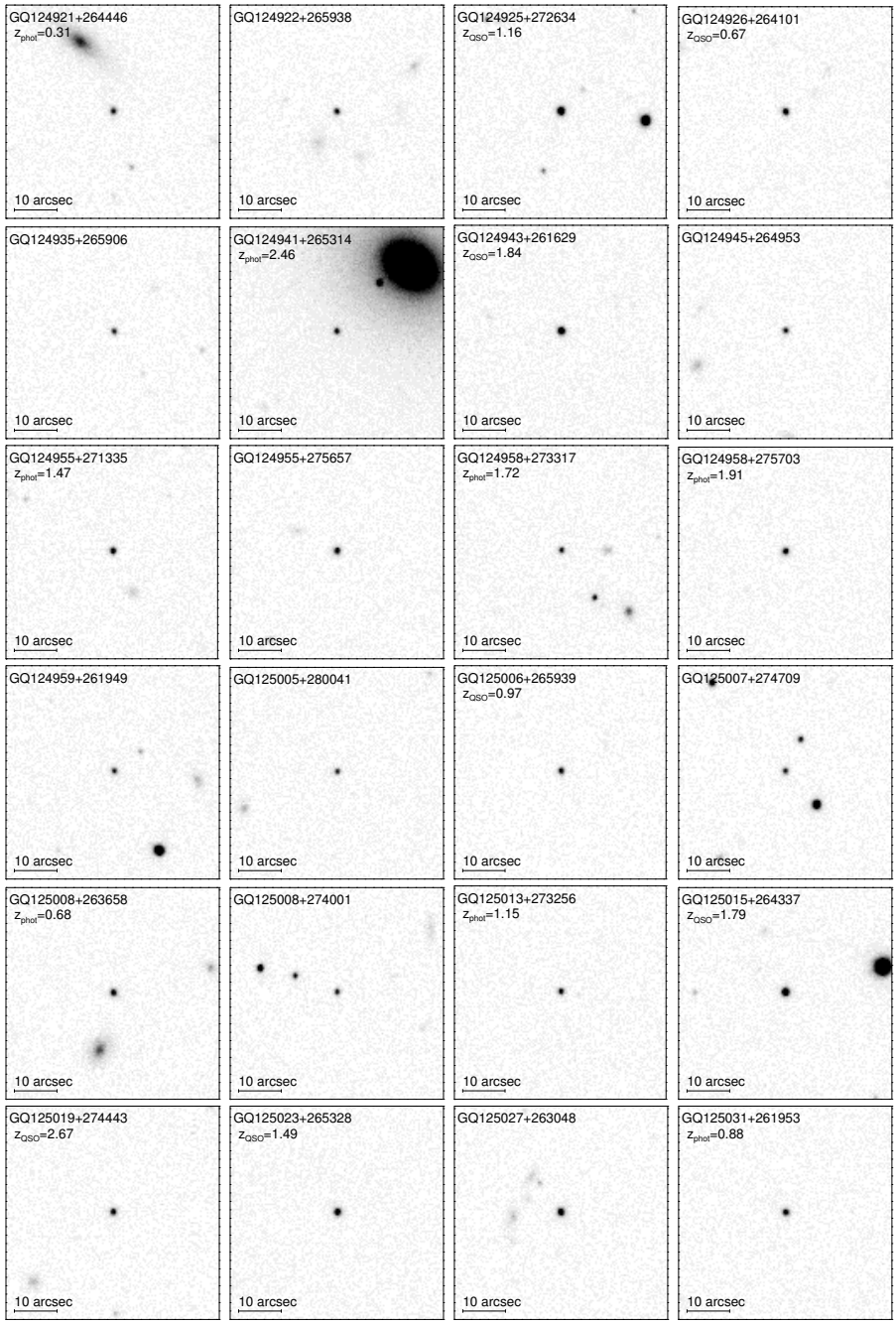

Figure 9.4.1. *Continued.*

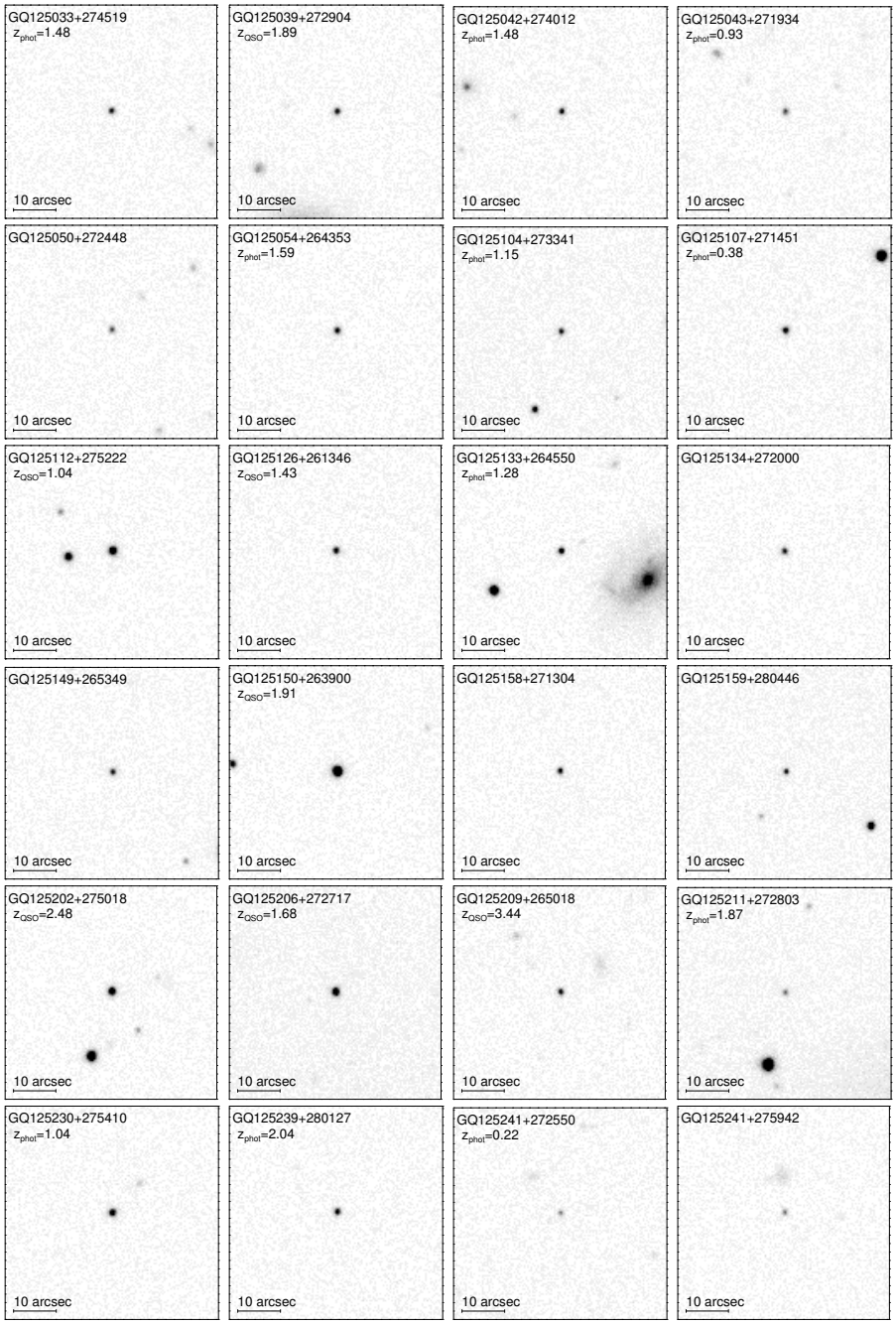

Figure 9.4.1. *Continued.*

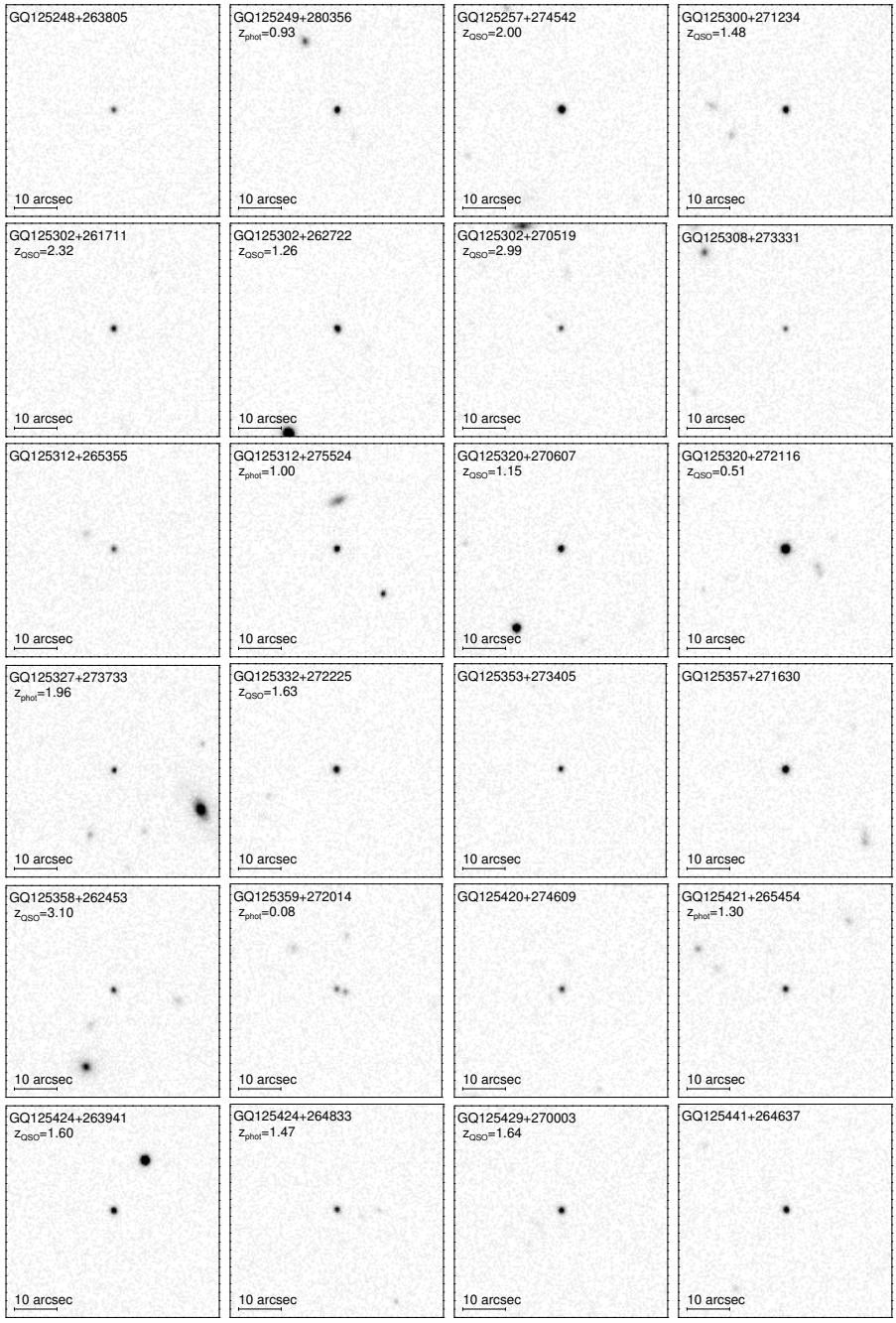

Figure 9.4.1. *Continued.*

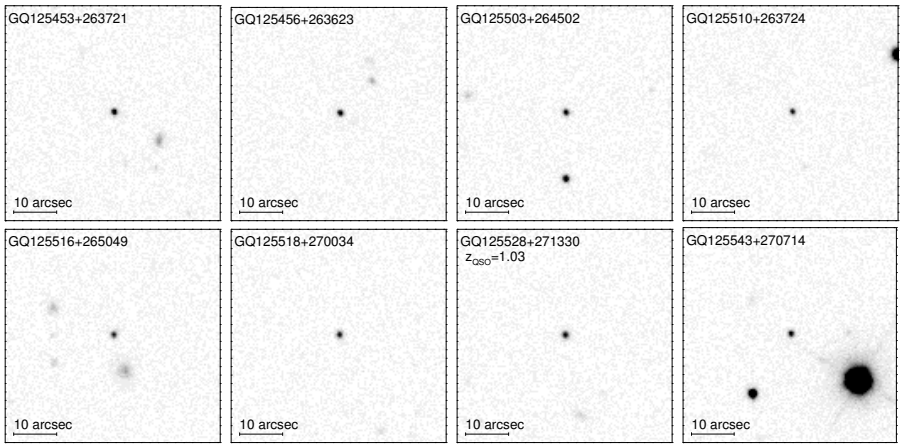

Figure 9.4.1. *Continued.*

Chapter 10

Summary and Outlook

Here I will provide a summary of the work done in this thesis and some near-future prospects that would be natural directions to continue in, based on both personal and general knowledge that has been obtained as part of this work.

In the first part of this thesis I studied the gas, dust and metals in the circumburst regions of GRBs. In Chapter 2, I presented the analysis of a single burst, GRB 140506A at $z = 0.889$, and the very peculiar dust extinction curve observed in the first VLT/X-shooter afterglow spectrum of this GRB. Based on late-time follow-up observations of the host galaxy, it was possible to exclude an extreme 2175 Å extinction bump as the origin of the steep extinction. Instead, we showed that the shape of the afterglow was more likely a combination of a steep extinction curve along the GRB line of sight and contamination by the host galaxy light at short wavelengths. We also derived the properties of the host galaxy and found that it was consistent with other known GRB hosts at similar redshifts and showed no sign of a steep extinction curve component, similar to that observed in the afterglow spectrum. In Chapter 3, I presented a study of the high-ionization metal lines in a large sample of GRB absorbers observed as part of the VLT/X-shooter GRB afterglow legacy survey (Selsing et al., 2019). In this work, we proposed a scenario where N v is produced by recombination of atoms in the nearby gas after the nitrogen atoms had been completely ionized and stripped of their electrons by the intense flux from the GRB and following afterglow. We then explored the kinematics of the high-ionization lines compared to those observed in the singly-ionized neutral gas and found that N v is likely confined to the same cloud component as the bulk of the neutral gas for large H I column densities of $N(\mathrm{H\,I}) > 10^{21.5}\,\mathrm{cm}^{-2}$. The strongest evidence for N v to originate in the circumburst came from the tentative correlation with the X-ray derived equivalent hydrogen column density, $N_{\mathrm{H,X}}$, that have been claimed to originate within ~ 10 pc from the GRB explosition site (Watson et al., 2013).

In both of the studies outlined above, the evidence for the observed tracers of gas, dust and metals to originate in the circumburst region of the GRB is primarily based on indirect observations. One way to test (or exclude) if for example the N v absorption line is produced by the GRB would be to obtain time-resolved afterglow spectra of GRB absorbers where this feature is present. The time-variability (if any) of the N v abundance would then hint at the origin of this absorption feature. Another powerful

way to study the GRB progenitors and the gas in the immediate region of the GRB explosion site would be through spatially resolved spectroscopic observations of the host galaxies of low-redshift GRBs using sensitive integral field unit (IFU) instruments. Especially the new sensitive Multi-Unit Spectrograph Explorer (MUSE) on the VLT will revolutionize our understanding of GRB host galaxies and their spatially resolved environments.

In the work presented in the second part of this thesis in Chapters 4 through 6, we demonstrated how GRBs can be used as probes of the molecular gas-phase in the ISM of high-redshift galaxies. In particular, we surveyed neutral atomic-carbon C I, which is used as a tracer for molecular hydrogen H_2, in a large sample of GRB afterglow spectra. We found that there is a significant excess of cold gas in GRB host absorption systems, with a detection probability of $\sim 25\%$ for C I, compared to $\sim 1\%$ in quasar absorbers (Ledoux et al., 2015). Moreover, we found that a larger H I column density and metallicity is required for GRB absorbers to show C I and H_2 than what is typically observed in quasar absorbers, likely related to enhanced star-formation and more intense interstellar UV radiation fields in the GRB host absorption systems. We also showed that the 2175 Å dust extinction feature is only detected in the most dust-reddened and C I-rich absorption systems and likely produced from carriers located in the same C I-bearing molecular cloud. We then characterized the physical properties of the diffuse molecular gas-phase in the ISM of H_2-bearing GRB host galaxy absorption systems and examined the defining characteristics for these systems to simultanously probe other molecular gas tracers such as C I and vibrationally-excited H_2 (H_2^*). A large H_2 abundance and molecular gas fraction is found to be essential for GRB host absorbers to also show the presence of C I and H_2^*, limiting their overall efficiency of tracing diffuse molecular gas. However, both C I and H_2^* could open a potential route to identify molecular clouds even in low-redshift, highly dust-obscured GRB afterglows observed with low-resolution spectroscopy.

Now that a large sample of GRB and quasar absorption systems with molecular gas has been detected at high-z, the next natural step is to examine how the properties of the cold and molecular gas derived from absorption and emission are connected. One way to do this is by targeting the CO emission of these systems and compare it to the molecular gas tracers observed in absorption (Neeleman et al., 2016). I have also recently applied for a similar project to search for CO emission in a sample of H_2-rich GRB host galaxy absorbers using the Atacama Large Millimeter/submillimeter Array (ALMA). These studies would allow us to couple the wealth of information on the molecular gas derived in absorption to that observed in emission. Moreover, based on preliminary results (Heintz & Watson, in preparation), it appears that it is actually possible to use GRB and quasar absorbers to obtain a direct calibration of the C I (and CO) luminosity to the molecular gas mass of high-z galaxies, which would be extremely beneficial to the extensive samples of emission-selected galaxies for which molecular line emission has been detected.

The focus of the final part of this thesis was to understand and explore the possible effects quasar selection bias had on the census of neutral gas and metals in high-z absorption-selected galaxies. One way to gauge this effect is to design selection criteria that are tailored to identify dusty and metal-rich absorbers that have otherwise been

missed in typical quasar surveys. In Chapter 7, I presented such a selection that were found to be very efficient in identifying $z > 2$ dust-reddened quasars. In the work done for Chapter 8, we characterize one of the foreground dusty damped Lyman-α absorbers (DLAs) found in one such sightline. The DLA was found to have $\sim 10\%$ solar metallicity and visual extinction of $A_V = 0.16$ mag, demonstrating that even absorption systems with modest metal and dust content can cause the background quasar to drop out of typical optical selection criteria. We then compiled a sample of DLAs with similar dust content and showed that this missing population of quasar DLAs better resemble absorption systems observed in GRB sightlines. The tension in the chemical enrichment as a function of redshift of the GRB absorbers and the typical quasar DLA population would therefore be relieved if these dusty quasar DLAs are properly taken into account. Another way to assess the full underlying quasar population would be to define a new, less biased way of identifying quasars. In the work presented in Chapter 9, we demonstrated that it is possible to efficiently select quasars at high Galactic latitudes based on their zero proper motion on the sky using the astrometric data from the *Gaia* satellite. Specifically, we found that the relative number of quasars to stars within one degree of the North Galactic Pole was $\sim 75\%$ based on the photometry of the zero-proper-motion sources.

Now that we have demonstrated that there is indeed a dust bias against the most metal-rich DLAs, the next crucial step is to quantify this effect more robustly. In the recent work by Krogager et al. (2019), we found that the dust bias arises as an effect of the magnitude and colour criteria utilized in the Sloan Digital Sky Survey (SDSS) quasar target selection. As a consequence, DLAs identified as part of this survey would underestimate the mass density of neutral hydrogen by 10 to 50%, and the mass density in metals by at least 30% at $z \sim 3$. For the *Gaia*-selection of quasars, the next step would be to obtain spectroscopy of a complete sample of zero-proper-motion sources to quantify the efficiency directly. We currently have one accepted proposal at the Nordic Optical Telescope to observe such a sample. This way of identifying quasars, based solely on zero proper motion and unbiased by any assumptions on spectral energy distributions, might also lead to the discovery of new types of quasars or new classes of extragalactic point sources.

Publications

Number of refereed first-author articles: 10, citations: 42.
Number of refereed articles: 31, citations: 1327.
Last updated on: July 16, 2019.

Refereed publications

1. *The effect of dust bias on the census of neutral gas and metals in the high-redshift Universe due to SDSS-II quasar colour selection*,
Krogager, J.-K., Fynbo, J. P. U., Møller, P., Noterdaeme, P., **Heintz, K. E.**, & Pettini, M., Monthly Notices of the Royal Astronomical Society, vol 486, issue 3, 21 pp. (2019)

2. *On the dust properties of high-redshift molecular clouds and the connection to the 2175 Å extinction bump*,
Heintz, K. E., Zafar, T., De Cia, A., Vergani, S. D., Jakobsson, P., Fynbo, J. P. U., Watson, D., Japelj, J., Møller, P., Covino, S., Kaper, L., & Andersen, A. C., Monthly Notices of the Royal Astronomical Society, vol. 486, issue 2, 12 pp. (2019)

3. *Gaia-assisted selection of a quasar reddened by dust in an extremely strong damped Lyman-α absorber at $z = 2.226$*,
Geier, S. J., **Heintz, K. E.**, Fynbo, J. P. U., Ledoux, C., Christensen, L., Jakobsson, P., Krogager, J.-K., Milvang-Jensen, B., Møller, P., & Noterdaeme, P., Astronomy & Astrophysics, vol. 625, id. L9, 5 pp. (2019)

4. *The fraction of ionizing radiation from massive stars that escapes to the intergalactic medium*,
Tanvir, N. R., Fynbo, J. P. U., de Ugarte Postigo, A., Japelj, J., Wiersema, K., Malesani, D., Perley, D. A., Levan, A. J., Selsing, J., Cenko, S. B., Kann, D. A., Milvang-Jensen, B., Berger, E., Cano, Z., Chornock, R., Covino, S., Cucchiara, A., D'Elia, V., Gargiulo, A., Goldoni, P., Gomboc, A., **Heintz, K. E.**, Hjorth, J., Izzo, L., Jakobsson, P., Kaper, L., Krühler, T., Laskar, T., Myers, M., Piranomonte, S., Pugliese, G., Rossi, A., Sánchez-Ramírez, R., Schulze, S., Sparre, M., Stanway, E. R., Tagliaferri, G., Thöne, C. C., Vergani, S., Vreeswijk, P. M., Wijers, R. A. M. J., Watson, D., & Xu, D., Monthly Notices of the Royal Astronomical Society, vol. 483, issue 4, 29 pp. (2019)

5. *The X-shooter GRB afterglow legacy sample (XS-GRB)*,
Selsing, J., Malesani, D., Goldoni, P., Fynbo, J. P. U., Krühler, T., Antonelli, L. A., Arabsalmani, M., Bolmer, J., Cano, Z., Christensen, L., Covino, S., D'Avanzo, P., D'Elia, V., De Cia, A., de Ugarte Postigo, A., Flores, H., Friis, M., Gomboc, A., Greiner, J., Groot, P., Hammer, F., Hartoog, O. E., **Heintz, K. E.**, Hjorth, J., Jakobsson, P., Japelj, J., Kann, D. A., Kaper, L., Ledoux, C., Leloudas, G., Levan, A. J., Maiorano, E., Melandri, A., Milvang-Jensen, B., Palazzi, E., Palmerio, J. T., Perley, D. A., Pian, E., Piranomonte, S., Pugliese, G., Sánchez-Ramírez, R., Savaglio, S., Schady, P., Schulze, S., Sollerman, J., Sparre, M., Tagliaferri, G., Tanvir, N. R., Thöne, C. C., Vergani, S. D., Vreeswijk, P., Watson, D., Wiersema, K., Wijers, R., Xu, D. & Zafar, T., Astronomy & Astrophysics, vol. 623, id. A92, 42 pp. (2019)

6. *Evidence for diffuse molecular gas and dust in the hearts of gamma-ray burst host galaxies. Unveiling the nature of high-redshift damped Lyman-α systems*,
Bolmer, J., Ledoux, C., Wiseman, P., De Cia, A., Selsing, J., Schady, P., Greiner, J., Savaglio, S., Burgess, J. M., D'Elia, V., Fynbo, J. P. U., Goldoni, P., Hartmann, D. H., **Heintz, K. E.**, Jakobsson, P., Japelj, J., Kaper, L., Tanvir, N. R., Vreeswijk, P. M. & Zafar, T., Astronomy & Astrophysics, vol. 623, id. A43, 45 pp. (2019)

7. *The intergalactic magnetic field probed by a giant radio galaxy*,
O'Sullivan, S. P., Machalski, J., Van Eck, C. L., Heald, G., Brüggen, M., Fynbo, J. P. U. **Heintz, K. E.**, Lara-Lopez, M. A., Vacca, V., Hardcastle, M. J., Shimwell, T. W., Tasse, C., Vazza, F., Andernach, H., Birkinshaw, M., Haverkorn, M., Horellou, C., Williams, W. L., Harwood, J. J., Brunetti, G., Anderson, J. M., Mao, S. A., Nikiel-Wroczyński, B., Takahashi, K., Carretti, E., Vernstrom, T., van Weeren, R. J., Orrú, E., Morabito, L. K., & Callingham, J. R., Astronomy & Astrophysics, vol. 622, id. A16, 12 pp. (2019)

8. *Signatures of a jet cocoon in early spectra of a supernova associated with a γ-ray burst*,
Izzo, L., de Ugarte Postigo, A., Maeda, K., Thöne, C. C., Kann, D. A., Della Valle, M., Sagues Carracedo, A., Michałowski, M. J., Schady, P., Schmidl, S., Selsing, J., Starling, R. L. C., Suzuki, A., Bensch, K., Bolmer, J., Campana, S., Cano, Z., Covino, S., Fynbo, J. P. U., Hartmann, D. H., **Heintz, K. E.**, Hjorth, J., Japelj, J., Kamiński, K., Kaper, L., Kouveliotou, C., Krużyński, M., Kwiatkowski, T., Leloudas, G., Levan, A. J., Malesani, D. B., Michałowski, T., Piranomonte, S., Pugliese, G., Rossi, A., Sánchez-Ramírez, R., Schulze, S., Steeghs, D., Tanvir, N. R., Ulaczyk, K., Vergani, S. D., & Wiersema, K., Nature, vol. 565, issue 7739, 4 pp. (2019)

9. *Cold gas in the early Universe. Survey for neutral atomic-carbon in GRB host galaxies at $1 < z < 6$ from optical afterglow spectroscopy*,
Heintz, K. E., Ledoux, C., Fynbo, J. P. U., Jakobsson, P., Noterdaeme, P., Krogager, J.-K., Bolmer, J., Møller, P., Vergani, S. D., Watson, D., Zafar, T., De Cia, A., Tanvir, N. R., Malesani, D. B., Japelj, J., Covino, S., & Kaper, L., Astronomy & Astrophysics, vol. 621, id. A20, 13 pp. (2019)

10. *X-shooter and ALMA spectroscopy of GRB 161023A. A study of metals and molecules in the line of sight towards a luminous GRB*,
de Ugarte Postigo, A., Thöne, C. C., Bolmer, J., Schulze, S., Martín, S., Kann, D. A., D'Elia, V., Selsing, J., Martin-Carrillo, A., Perley, D. A., Kim, S., Izzo, L., Sánchez-Ramírez, R., Guidorzi, C., Klotz, A., Wiersema, K., Bauer, F. E., Bensch, K., Campana, S., Cano, Z., Covino, S., Coward, D., De Cia, A., de Gregorio-Monsalvo, I., De Pasquale, M., Fynbo, J. P. U., Greiner, J., Gomboc, A., Hanlon, L., Hansen, M., Hartmann, D. H., **Heintz, K. E.**, Jakobsson, P., Kobayashi, S., Malesani, D. B., Martone, R., Meintjes, P. J., Michałowski, M. J., Mundell, C. G., Murphy, D., Oates, S., Salmon, L., van Soelen, B., Tanvir, N. R., Turpin, D., Xu, D., & Zafar, T., Astronomy & Astrophysics, vol. 620, id. A119, 23 pp. (2018)

11. *X-shooting GRBs at high redshift: probing dust production history*,
Zafar, T., Møller, P., Watson, D., Lattanzio, J., Hopkins, A. M., Karakas, A., Fynbo, J. P. U., Tanvir, N. R., Selsing, J., Jakobsson, P., **Heintz, K. E.**, Kann, D. A., Groves, B., Kulkarni, V., Covino, S., D'Elia, V., Japelj, J., Corre, D., & Vergani S., Monthly Notices of the Royal Astronomical Society, vol. 480, issue 1, 10 pp. (2018)

12. *The properties of GRB 120923A at a spectroscopic redshift of* $z \approx 7.8$,
Tanvir, N. R., Laskar, T., Levan, A. J., Perley, D. A., Zabl, J., Fynbo, J. P. U., Rhoads, J., Cenko, S. B., Greiner, J., Wiersema, K., Hjorth, J., Cucchiara, A., Berger, E., Bremer, M. N., Cano, Z., Cobb, B. E., Covino, S., D'Elia, V., Fong, W., Fruchter, A. S., Goldoni, P., Hammer, F., **Heintz, K. E.**, Jakobsson, P., Kann, D. A., Kaper, L., Klose, S., Knust, F., Krühler, T., Malesani, D., Misra, K., Nicuesa Guelbenzu, A., Pugliese, G., Sánchez-Ramírez, R., Schulze, S., Stanway, E. R., de Ugarte Postigo, A., Watson, D., Wijers, R. A. M. J., & Xu, D., The Astrophysical Journal, vol. 865, id. 107, 16 pp. (2018)

13. *Highly ionized metals as probes of the circumburst gas in the natal regions of gamma-ray bursts*,
Heintz, K. E., Watson, D., Jakobsson, P., Fynbo, J. P. U., Bolmer, J., Arabsalmani, M., Cano, Z., Covino, S., D'Elia, V., Gomboc, A., Japelj, J., Kaper, L., Krogager, J.-K., Pugliese, G., Sánchez-Ramírez, R., Selsing, J., Sparre, M., Tanvir, N. R., Thöne, C. C., de Ugarte Postigo, A., & Vergani, S. D., Monthly Notices of the Royal Astronomical Society, vol. 479, issue 3, 21 pp. (2018)

14. *ALMA observations of a metal-rich damped Ly*α *absorber at* $z = 2.5832$*: evidence for strong galactic winds in a galaxy group*,
Fynbo, J. P. U., **Heintz, K. E.**, Neeleman, M., Christensen, L., Dessauges-Zavadsky, M., Kanekar N., Møller, P., Prochaska, J. X., Rhodin, N. H. P., & Zwaan, M., Monthly Notices of the Royal Astronomical Society, vol. 479, issue 2, 6 pp. (2018)

15. *VLT/X-shooter GRBs: Individual extinction curves of star-forming regions*,
Zafar, T., Watson, D., Møller, P., Selsing, J., Fynbo, J. P. U., Schady, P., Wiersema, K., Levan, A. J., **Heintz, K. E.**, de Ugarte Postigo, A., D'Elia, V., Jakobsson, P.,

Bolmer, J., Japelj, J., Covino, S., Gomboc, A., & Cano, Z., Monthly Notices of the Royal Astronomical Society, vol. 479, issue 2, 12 pp. (2018)

16. *The host galaxy of the short GRB 111117A at z = 2.211. Impact on the short GRB redshift distribution and progenitor channels*,
Selsing, J., Krühler, T., Malesani, D., D'Avanzo, P., Schulze, S., Vergani, S. D., Palmerio, J., Japelj, J., Milvang-Jensen, B., Watson, D., Jakobsson, P., Bolmer, J., Cano, Z., Covino, S., D'Elia, V., de Ugarte Postigo, A., Fynbo, J. P. U., Gomboc, A., **Heintz, K. E.**, Kaper, L., Levan, A. J., Piranomonte, S., Pugliese, G., Sánchez-Ramírez, R., Sparre, M., Tanvir, N. R., Thöne, C. C., & Wiersema, K., Astronomy & Astrophysics, vol. 616, id. A48, 11 pp. (2018)

17. *Unidentified quasars among stationary objects from Gaia DR2*,
Heintz, K. E., Fynbo, J. P. U., Høg, E., Møller, P., Krogager, J.-K., Geier, S., Jakobsson, P., & Christensen, L., Astronomy & Astrophysics, vol. 615, id. L8, 9 pp. (2018)

18. *A quasar hiding behind two dusty absorbers. Quantifying the selection bias of metal-rich, damped Lyα absorption systems*,
Heintz, K. E., Fynbo, J. P. U., Ledoux, C., Jakobsson, P., Møller, P., Christensen, L., Geier, S., Krogager, J.-K., & Noterdaeme, P., Astronomy & Astrophysics, vol. 615, id. A43, 14 pp. (2018)

19. *The 2175 Å Extinction Feature in the Optical Afterglow Spectrum of GRB 180325A at z = 2.25*,
Zafar, T., **Heintz, K. E.**, Fynbo, J. P. U., Malesani, D., Bolmer, J., Ledoux, C., Arabsalmani, M., Kaper, L., Campana, S., Starling, R. L. C., Selsing, J., Kann, D. A., de Ugarte Postigo, A., Schweyer, T., Christensen, L., Møller, P., Japelj, J., Perley, D., Tanvir, N. R., D'Avanzo, P., Hartmann, D. H., Hjorth, J., Covino, S., Sbarufatti, B., Jakobsson, P., Izzo, L., Salvaterra, R., D'Elia, V., & Xu, D., The Astrophysical Journal Letters, vol. 860, id. L21, 7 pp. (2018)

20. *The luminous, massive and solar metallicity galaxy hosting the Swift γ-ray burst GRB 160804A at z = 0.737*,
Heintz, K. E., Malesani, D., Wiersema, K., Jakobsson, P., Fynbo, J. P. U., Savaglio, S., Cano, Z., D'Elia, V., Gomboc, A., Hammer, F., Kaper, L., Milvang-Jensen, B., Møller, P., Piranomonte, S., Selsing, J., Rhodin, N. H. P., Tanvir, N. R., Thöne, C. C., de Ugarte Postigo, A., Vergani, S. D., & Watson, D., Monthly Notices of the Royal Astronomical Society, vol. 474, issue 2, 12 pp. (2018)

21. *Mass and metallicity scaling relations of high-redshift star-forming galaxies selected by GRBs*,
Arabsalmani, M., Møller, P., Perley, D. A., Freudling, W., Fynbo, J. P. U., Le Floc'h, E., Zwaan, M. A., Schulze, S., Tanvir, N. R., Christensen, L., Levan, A. J., Jakobsson, P., Malesani, D., Cano, Z., Covino, S., D'Elia, V., Goldoni, P., Gomboc, A., **Heintz, K. E.**, Sparre, M., de Ugarte Postigo, A., & Vergani, S. D., Monthly Notices of the Royal Astronomical Society, vol. 473, issue 3, 13 pp. (2018)

22. *Solving the conundrum of intervening strong Mg* II *absorbers towards gamma-ray bursts and quasars*,
Christensen, L., Vergani, S. D., Schulze, S., Annau, N., Selsing, J., Fynbo, J. P. U., de Ugarte Postigo, A., Cañameras, R., Lopez, S., Passi, D., Cortés-Zuleta, P., Ellison, S. L., D'Odorico, V., Becker, G., Berg, T. A. M., Cano, Z., Covino, S., Cupani, G., D'Elia, V., Goldoni, P., Gomboc, A., Hammer, F., **Heintz, K. E.**, Jakobsson, P., Japelj, J., Kaper, L., Malesani, D., Møller, P., Petitjean, P., Pugliese, V., Sánchez-Ramírez, R., Tanvir, N. R., Thöne, C. C., Vestergaard, M., Wiersema, K., & Worseck, G., Astronomy & Astrophysics, vol. 608, id. A84, 10 pp. (2017)

23. *A kilonova as the electromagnetic counterpart to a gravitational-wave source*,
Smartt, S. J., et al. (2017); co-author #59 (out of 121), Nature, vol. 551, issue 7678, 51 pp. (2017)

24. *Multi-messenger Observations of a Binary Neutron Star Merger*,
LIGO/VIRGO & follow-up collaboration; co-author as part of ePESSTO, The Astrophysical Journal Letters, vol. 848, id. L12, 59 pp. (2017)

25. *The High A_V Quasar survey: A $z = 2.027$ metal-rich damped Lyman-α absorber towards a red quasar at $z = 3.21$*,
Fynbo, J. P. U., Krogager, J.-K., **Heintz, K. E.**, Geier, S., Møller, P., Noterdaeme, P., Christensen, L., Ledoux, C., & Jakobsson, P., Astronomy & Astrophysics, vol. 606, id. A13, 6 pp. (2017)

26. *GRB 161219B / SN 2016jca: A low-redshift gamma-ray burst supernova powered by radioactive heating*,
Cano, Z., Izzo, L., de Ugarte Postigo, A., Thöne, C. C., Krühler, T., **Heintz, K. E.**, Malesani, D., Geier, S., Fuentes, C., Chen, T.-W., Covino, S., D'Elia, V., Fynbo, J. P. U., Goldoni, P., Gomboc, A., Hjorth, J., Jakobsson, P., Kann, D. A., Milvang-Jensen, B., Pugliese, G., Sánchez-Ramírez, R., Schulze, S., Sollerman, J., Tanvir, N. R., & Wiersema, K., Astronomy & Astrophysics, vol. 605, id. A107, 21 pp. (2017)

27. *Steep extinction towards GRB 140506A reconciled from host galaxy observations: Evidence that steep reddening laws are local*,
Heintz, K. E., Fynbo, J. P. U., Jakobsson, P., Krühler, T., Christensen, L., Watson, D., Ledoux, C., Noterdaeme, P., Perley, D. A., Rhodin, H., Selsing, J., Schulze, S., Tanvir, N. R., Møller, P., Goldoni, P., Xu, D., & Milvang-Jensen, B., Astronomy & Astrophysics, vol. 601, id. A83, 10 pp. (2017)

28. *The Extended High A(V) Quasar Survey: Searching for Dusty Absorbers Toward Mid-infrared Selected Quasars*,
Krogager, J.-K., Fynbo, J. P. U., **Heintz, K. E.**, Geier, S., Ledoux, C., Møller, P., Noterdaeme, P., Venemans, B., & Vestergaard, M., The Astrophysical Journal, vol. 832, id. 49, 21 pp. (2016)

29. *Determining the fraction of reddened quasars in COSMOS with multiple selection techniques from X-ray to radio wavelengths*,
Heintz, K. E., Fynbo, J. P. U., Møller, P., Milvang-Jensen, B., Zabl, J., Maddox,

N., Krogager, J.-K., Geier, S., Vestergaard, M., Noterdaeme, P., & Ledoux, C., Astronomy & Astrophysics, vol. 595, id. A13, 22 pp. (2016)

30. *Serendipitous Discovery of a Projected Pair of QSOs Separated by 4.5 arcsec on the Sky*,
Heintz, K. E., Fynbo, J. P. U., Krogager, J.-K., Vestergaard, M., Møller, P., Arabsalmani, M., Geier, S., Noterdaeme, P., Ledoux, C., Saturni, F. G., & Venemans, B., The Astronomical Journal, vol. 152, id. 13, 4 pp. (2016)

31. *A study of purely astrometric selection of extragalactic point sources with Gaia*, **Heintz, K. E**., Fynbo, J. P. U., & Høg, E., Astronomy & Astrophysics, vol. 578, id. A91, 4 pp. (2015)

Papers in progress

1. *Silicon and iron dust in gamma-ray burst host galaxy absorbers*,
Zafar et al. (2019), submitted to MNRAS.
2. *Short GRB 160821B: a reverse shock, a refreshed shock, and a well-sampled kilonova*, Lamb et al. (2019), submitted to ApJ.
3. *The spectral evolution of AT 2018dyb and the presence of metal lines in tidal disruption events*, Leloudas et al. (2019), submitted to ApJ.
4. *Exploring galaxy dark matter halos across redshifts with strong quasar absorbers*, Christensen et al. (2019), submitted to MNRAS.
5. *Strontium identified in the merger of two neutron stars*,
Watson et al. (2019), submitted to *Nature*.

GRB coordinate network circulars (GCNs)

1. *GRB 190613B: Optical observations from NOT*,
de Ugarte Postigo, A., Malesani, D. B., **Heintz, K. E.**, and Moran, S., GCN circular # 24825 (2019).
2. *GRB 190531B: VLT optical upper limit*,
Japelj, J., Rossi, A., Malesani, D. B., **Heintz, K. E.**, Pugliese, G., and Kaper, L., GCN circular # 24711 (2019).
3. *GRB 190530A: NOT photometry and spectroscopy*,
Heintz, K. E., Fynbo, J. P. U., de Ugarte Postigo, A., Malesani, D. B., Selsing, J., Milvang-Jensen, B., and Moran, S., GCN circular # 24686 (2019).
4. *LIGO/Virgo S190408an: GROND Observations of MASTER OT J154209.55-431742.2*,
Chen, T.-W., Schweyer, T., Rossi, A., **Heintz, K. E.**, Gromadzki, M., Bolmer, J., and Schady, P., GCN circular # 24097 (2019).
5. *GRB 190219A: NOT optical afterglow candidate*,
Xu, D., **Heintz, K. E.**, Malesani, D. B., Zhu, Z. P., Galindo, P., and Viuho, J., GCN circular # 23911 (2019).

6. *GRB 190211A: NOT optical observations*,
Heintz, K. E., Xu, D., Malesani, D. B., and Moran, S., GCN circular # 23890 (2019).

7. *GRB 190114C: X-shooter observations of a highly extinguished afterglow*,
Kann, D. A., Thöne, C. C., Selsing, J., Izzo, L., de Ugarte Postigo, A., Pugliese, G., Sbarufatti, B., **Heintz, K. E.**, D'Elia, V., Covino, S., Wiersema, K., Perley, D. A., Vergani, S., Fynbo, J. P. U., Watson, D., Tanvir, N. R., Hartmann, D., Xu, D., Schulze, S., and Bolmer, J., GCN circular # 23710 (2019).

8. *GRB 190114A: NOT optical observations*,
Selsing, J., de Ugarte Postigo, A., and **Heintz, K. E.**, GCN circular # 23697 (2019).

9. *GRB 190114C: NOT optical counterpart and redshift*,
Selsing, J., Fynbo, J. P. U., **Heintz, K. E.**, and Watson, D., GCN circular # 23695 (2019).

10. *GRB 190106A: VLT/X-shooter redshift confirmation*,
Schady, P., Xu, D., **Heintz, K. E.**, Tanvir, N. R., Malesani D. B., Kann, D. A., Sánchez-Ramírez, R., and Wiersema, K., GCN circular # 23632 (2019).

11. *GRB 181213A: NOT optical observations*,
Heintz, K. E., Malesani, D. B., Fynbo, J. P. U., de Ugarte Postigo, A., Balaguer-Nuñez, L., Carbajo, J., Galindo, F., and Perez, C., GCN circular # 23537 (2018).

12. *GRB 181201A: VLT/FORS2 tentative spectroscopic redshift*,
Izzo, L., de Ugarte Postigo, A., Kann, D. A., Malesani, D. B., **Heintz, K. E.**, Tanvir, N. R., D'Elia, V., Wiersema, K., Kouveliotou, C., and Levan, A. J., GCN circular # 23488 (2018).

13. *GRB 181201A: NOT optical observations*,
Heintz, K. E., Malesani, D. B., and Moran-Kelly, S., GCN circular # 23478 (2018).

14. *GRB 181110A: VLT/X-shooter redshift*,
Perley, D. A., Malesani, D. B., Fynbo, J. P. U., **Heintz, K. E.**, Kann, D. A., D'Elia, V., Izzo, L., and Tanvir, N. R., GCN circular # 23421 (2018).

15. *GRB 181020A: VLT/X-shooter spectroscopy and redshift*,
Fynbo, J. P. U., de Ugarte Postigo, A., D'Elia, V., Tanvir, N. R., Pugliese, G., Kann, D. A., Malesani, D. B., and **Heintz, K. E.**, GCN circular # 23356 (2018).

16. *GRB 181010A: VLT/X-shooter redshift*,
Vielfaure, J.-B., Japelj, J., Malesani, D. B., D'Elia, V., Fynbo, J. P. U., Tanvir, N. R., Vergani, S. D., Rossi, A., Vreeswijk, P., Izzo, L., Kann, D. A., Milvang-Jensen, B., Xu, D., and **Heintz, K. E.**, GCN circular # 23315 (2018).

17. *GRB 180914B: VLT/X-shooter spectroscopic redshift*,
D'Avanzo, P., **Heintz, K. E.**, de Ugarte Postigo, A., Levan, A. J., Izzo, L., Malesani, D. B., Kann, D. A., and Tanvir, N. R., GCN circular # 23246 (2018).

18. *GRB 180904A: NOT optical observations, candidate host galaxy*,
Malesani, D., **Heintz, K. E.**, and Dyrbye, S., GCN circular # 23195 (2018).

19. *GRB 180728A: Classification of the associated SN 2018fip*,
Selsing, J., Izzo, L., Rossi, A., Malesani, D. B., **Heintz, K. E.**, de Ugarte Postigo, A., Schady, P., Starling, R. L. C., Sollerman, J., Leloudas, G., Cano, Z., Fynbo, J. P. U., Della Valle, M., Pian, E., Kann, D. A., Perley, D. A., Palazzi, E., Klose, S., Hjorth, J., Covino, S., D'Elia, V., Tanvir, N. R., Levan, A. J., Hartmann, D., and Kouveliotou C., GCN circular # 23181 (2018).

20. *GRB 180728A: Discovery of the associated supernova*,
Izzo, L., Rossi, A., Malesani, D. B., **Heintz, K. E.**, Selsing, J., Schady, P., Starling, R. L. C., Sollerman, J., Leloudas, G., Cano, Z., Fynbo, J. P. U., Della Valle, M., Pian, E., Kann, D. A., Perley, D. A., Palazzi, E., Klose, S., Hjorth, J., Covino, S., D'Elia, V., Tanvir, N. R., Levan, A. J., Hartmann, D., and Kouveliotou C., GCN circular # 23142 (2018).

21. *GRB 180809B: VLT optical upper limits*,
Japelj, J., Malesani, D. B., Selsing, J., Tanvir, N. R., Kann, D. A., D'Elia, V., Pugliese, G., **Heintz, K. E.**, Fynbo, J. P. U., Levan, A. J., and Schady, P., GCN circular # 23114 (2018).

22. *GRB 180728A: No evidence of SN in early VLT/X-shooter spectra*,
Heintz, K. E., Izzo, L., Rossi, A., de Ugarte Postigo, A., Malesani, D. B., Perley, D. A., Thöne, C. C., Fynbo, J. P. U., Milvang-Jensen, B., Kann, D. A., Tanvir, N. R., Levan, A. J., Schulze, S., and Pugliese, G., GCN circular # 23067 (2018).

23. *GRB 180720B: VLT/X-shooter redshift*,
Vreeswijk, P. M., Kann, D. A., **Heintz, K. E.**, de Ugarte Postigo, A., Milvang-Jensen, B., Malesani, D. B., Covino, S., Levan, A. J., and Pugliese, G., GCN circular # 22996 (2018).

24. *GRB 180624A: NOT optical counterpart*,
Selsing, J., **Heintz, K. E.**, Fynbo, J. P. U., Malesani, D., Lehtinen, J. J., and Willamo, T., GCN circular # 22867 (2018).

25. *GRB 180620B: VLT/X-shooter redshift*,
Izzo, L., Arabsalmani, M., Malesani, D. B., Wiersema, K., Pugliese, G., Vergani, S. D., de Ugarte Postigo, A., **Heintz, K. E.**, Kann, D. A., Schady, P., Tanvir, N. R., Fynbo, J. P. U., Thöne, C. C., and Bolmer, J., GCN circular # 22823 (2018).

26. *GRB 180614A: NOT optical upper limits*,
Heintz, K. E., Fynbo, J. P. U., Malesani, D., Lehtinen, J. J., Willamo, T., and Galindo, P., GCN circular # 22784 (2018).

27. *GRB 180512A: NOT upper limits*,
Heintz, K. E., Malesani, D., Siltala, L., and Rodrigues, P. M., GCN circular # 22713 (2018).

28. *GRB 180418A: NOT optical observations*,
Malesani, D., **Heintz, K. E.**, Stone, M., and Stone, J., GCN circular # 22660 (2018).

29. *GRB 180329B: NOT optical afterglow detection*,
Perley, D. A., **Heintz, K. E.**, and Malesani, D., GCN circular # 22562 (2018).

30. *GRB 180325A: VLT/X-shooter spectroscopic observations*,
D'Avanzo, P., Bolmer, J., D'Elia, V., Fynbo, J. P. U., **Heintz, K. E.**, Izzo, L., Japelj, J., Kann, D. A., Malesani, D., Selsing, J., Tanvir, N. R., Zafar, T., Campana, S., de Ugarte Postigo, A., Hjorth, J., Kaper, L., Melandri, A., and Smette, A., GCN circular # 22555 (2018).

31. *GRB 180325A: NOT redshift*,
Heintz, K. E., Fynbo, J. P. U., and Malesani, D., GCN circular # 22535 (2018).

32. *GRB 180314A: VLT/X-shooter redshift*,
Sbarufatti, B., Bolmer, J., de Ugarte Postigo, A., Fynbo, J. P. U., Selsing, J., **Heintz, K. E.**, Malesani, D., Tanvir, N. R., Levan, A. J., Smette, A., Wiersema, K., and Covino, S., GCN circular # 22484 (2018).

33. *GRB 180205A: VLT/X-shooter redshift*,
Tanvir, N. R., **Heintz, K. E.**, Selsing, J., Japelj, J., Bolmer, J., Kann, D. A., Xu, D., de Ugarte Postigo, A., Malesani, D., Fynbo, J. P. U., and Pugliese, G., GCN circular # 22384 (2018).

34. *GRB 180115A: NOT detection of optical counterpart*,
Cano, Z., **Heintz, K. E.**, de Ugarte Postigo, A., Marquez, I., and Cazzoli, S., GCN circular # 22345 (2018).

35. *GRB 180102A: NOT optical observations*,
Malesani, D., **Heintz, K. E.**, Sagues Carracedo, A., and Dideriksen, A. K., GCN circular # 22298 (2018).

36. *GRB 171222A: Redshift from 10.4m GTC/OSIRIS*,
de Ugarte Postigo, A.,Izzo, L., Kann, D. A., Thöne, C. C., Perley, D. A., Malesani, D., **Heintz, K. E.**, and Garcia, D., GCN circular # 22272 (2017).

37. *GRB 171222A: NOT optical afterglow*,
Perley, D. A., Malesani, D., **Heintz, K. E.**, de Ugarte Postigo, A., and Lehiten, J. J., GCN circular # 22269 (2017).

38. *GRB 171010A: VLT spectroscopic identification of the associated SN 2017htp*,
de Ugarte Postigo, A., Selsing, J., Malesani, D., Xu, D., Izzo, L., **Heintz, K. E.**, Kann, D. A., Leloudas, G., Schulze, S., Tanvir, N. R., Covino, S., D'Avanzo, P., Fynbo, J. P. U., Hartmann, D., Hjorth, J., Kouveliotou, C., Kaper, L., Levan, A. J., Melandri, A., Møller, P., Pugliese, G., Sbarufatti, B., Schady, P., and Schmidl, S., GCN circular # 22096 (2017).

39. *GRB 171027A: VLT optical upper limits*,
Malesani, D., Tanvir, N. R., Schady, P., de Ugarte Postigo, A., **Heintz, K. E.**, and Pugliese, G., GCN circular # 22060 (2017).

40. *GRB 171020A: NOT spectroscopic redshift*,
Malesani, D., Fynbo, J. P. U., **Heintz, K. E.**, Stone, M., and Karhunen, K., GCN circular # 22039 (2017).

41. *GRB 171010A: ePESSTO NTT spectroscopic redshift*,
Kankare, E., O'Neill, D., Izzo, L., D'Elia, V., Vergani, S. D., Malesani, D., **Heintz, K. E.**, Schady, P., Melandri, A., D'Avanzo, P., Campana, S., Covino, S.,

Magee, M., Chen, T.-W., Galbany, L., Inserra, C., Maguire, K., Smartt, S., Yaron, O., Young, D., and Manulis, I., GCN circular # 22002 (2017).

42. *GRB 171010A: NOT optical observations*,
Malesani, D., **Heintz, K. E.**, Calissendorff, P., and Losada, I. R., GCN circular # 22000 (2017).

43. *GRB 170921A: NOT optical observations*,
Malesani, D., **Heintz, K. E.**, Tanvir, N. R., Kann, D. A., Pursimo, T., and Dyrbye, S., GCN circular # 21909 (2017).

44. *GRB 170903A: Host galaxy redshift from OSIRIS/GTC*,
de Ugarte Postigo, A., Izzo, L., Thöne, C. C., Kann, D. A., **Heintz, K. E.**, Castro-Rodrigues, N., and Marante, A., GCN circular # 21799 (2017).

45. *GRB 170728B: NOT optical afterglow confirmation*,
Heintz, K. E., Tanvir, N. R., Perley, D A., and Rasmussen, R. T., GCN circular # 21374 (2017)

46. *GRB 170607A: NOT optical afterglow detection*,
Heintz, K. E., de Ugarte Postigo, A., and Claesen, J., GCN circular # 21217 (2017)

47. *GRB 170519A: NOT optical observations*,
de Ugarte Postigo, A., Xu, D., Malesani, D., **Heintz, K. E.**, Gandolfi, D., and Telting, J., GCN circular # 21120 (2017)

48. *GRB 170405A: NOT optical observations*,
Malesani, D., **Heintz, K. E.** and Pursimo, T., GCN circular # 20988 (2017)

49. *GRB 170205A: NOT upper limits*,
Heintz, K. E., Malesani, D., Tanvir, N. R., de Ugarte Postigo, A., Korn, A. J. and Losada, I. R., GCN circular # 20638 (2017)

50. *GRB 170205A: NOT afterglow observations*,
Krühler, T., Xu, D., **Heintz, K. E.** and Fedorets, G., GCN circular # 20612 (2017)

51. *GRB 170127B: NOT r-band upper limits*,
Cano, Z., **Heintz, K. E.**, Malesani, D., and Tronsgaard, R., GCN circular # 20549 (2017)

52. *GRB 170113A: VLT/X-shooter redshift*,
Xu, D., **Heintz, K. E.**, Malesani, D., and Fynbo, J. P. U., GCN circular # 20458 (2017)

53. *GRB 161129A: NOT optical observations and candidate host galaxy*,
Heintz, K. E., Malesani, D., Cano, Z., de Ugarte Postigo, A., Fedorets, G., Tronsgaard Rasmussen, R., Djupvik, A. A., Losada, I. R., Svardh, I., Clasen, J. and Armas Perez, S., GCN circular # 20244 (2016)

54. *GRB 161117A: VLT/X-shooter spectroscopy and redshift*,
Malesani, D., Krühler, T., **Heintz, K. E.** and Fynbo, J. P. U., GCN circular # 20180 (2016)

55. *GRB 161108A: NOT redshift*,
de Ugarte Postigo, A., Malesani, D., Perley, D. A., Fynbo, J. P. U., **Heintz, K. E.**,

Somero, A., Gafton, E., Damsted, S., Erfanianfar, G., Finoguenov, A., Gibson, C., Kiefer, F., Kirkpatrick, C., Lumme, M., Oja, V., Rantakyla, J., Salmenpera, I. and Seppala, M., GCN circular # 20150 (2016)

56. *GRB 161014A: VLT/X-shooter redshift confirmation*,
Selsing, J., **Heintz, K. E.**, Malesani, D., Xu, D., de Ugarte Postigo, A., Tanvir, N. R., Wiersema, K. and Fynbo, J. P. U., GCN circular # 20061 (2016)

57. *GRB 161014A: NOT optical observations*,
Heintz, K. E., Xu, D., Malesani, D., Poretti, E., Telting, J., de Ugarte Postigo, A. and Fynbo, J. P. U., GCN circular # 20044 (2016)

58. *GRB 161007A: NOT optical observations*,
Heintz, K. E., Malesani, D., de Ugarte Postigo, A., Pursimo, T., Kruehler, T., Telting, J. and Fynbo, J. P. U., GCN circular # 20020 (2016)

59. *GRB 160804A: VLT/X-shooter redshift*,
Xu, D., **Heintz, K. E.**, Malesani, D., Wiersema, K., and Fynbo, J. P. U., GCN circular # 19773 (2016)

60. *GRB 150314A: NOT optical observations*,
Xu, D., de Ugarte Postigo, A., Geier, S., **Heintz, K. E.**, Fynbo, J. P. U., Malesani, D., and Jakobsson, P., GCN circular # 17582 (2015)

Astronomer's telegrams (ATels)

1. *GRB 180728A: No evidence of SN in early VLT/X-shooter spectra*,
Heintz, K. E., Izzo, L., Rossi, A., de Ugarte Postigo, A., Malesani, D. B., Perley, D. A., Thöne, C. C., Fynbo, J. P. U., Milvang-Jensen, B., Kann, D. A., Tanvir, N. R., Levan, A. J., Schulze, S., and Pugliese, G., ATel # 11898 (2018).

2. *ePESSTO spectroscopic classification of optical transients*,
Malesani, D., **Heintz, K. E.**, Leloudas, G., D'Avanzo, P., Barbarino, C., Chen, T. W., Kostrzewa-Rutkowska, Z., Congiu, E., Gromadzki, M., Inserra, C., Kankare, E., Maguire, K., Smartt, S. J., Yaron, O., Young, D., Manulis, I., Tonry, J., Denneau, L., Heinze, A., Weiland, H., Stalder, B., Rest, A., Smith, K. W., McBrien, O., Wright, D. E., Chambers, K. C., Flewelling, H., Huber, M., Lowe, T., Magnier, E., Schultz, A., Waters, C., Wainscoat, R. J., and Wilman, M., ATel # 11564 (2018).

3. *ePESSTO spectroscopic classification of optical transients*,
Malesani, D., **Heintz, K. E.**, Leloudas, G., D'Avanzo, P., Barbarino, C., Chen, T. W., Kostrzewa-Rutkowska, Z., Gromadzki, M., Onori, F., Inserra, C., Kankare, E., Maguire, K., Smartt, S. J., Yaron, O., Young, D., Smith, K. W., Wright, D. E., Chambers, K. C., Flewelling, H., Huber, M., Lowe, T., Magnier, E., Schultz, A., Waters, C., Wainscoat, R. J., and Wilman, M., ATel # 11560 (2018).

4. *ePESSTO spectroscopic classification of optical transients*,
Heintz, K. E., Malesani, D., D'Avanzo, P., Leloudas, G., Barbarino, C., Chen, T. W., Kostrzewa-Rutkowska, Z., Inserra, C., Kankare, E., Maguire, K., Smartt, S. J., Yaron, O., Young, D., and Manulis, I., ATel # 11556 (2018).

5. *ePESSTO spectroscopic classification of optical transients*,
Heintz, K. E., Malesani, D., D'Avanzo, P., Leloudas, G., Barbarino, C., Chen, T. W., Kostrzewa-Rutkowska, Z., Inserra, C., Kankare, E., Maguire, K., Smartt, S. J., Yaron, O., Young, D., Tonry, J., Denneau, L., Heinze, A., Weiland, H., Stalder, B., Rest, A., Smith, K. W., McBrien, O., Young, D. R., Wright, D. E., and Wyrzykowski, L., ATel # 11554 (2018).

6. *ePESSTO spectroscopic classification of optical transients*,
Malesani, D., Rubin, A., Leloudas, G., **Heintz, K. E.**, Dennefeld, M., Galbany, L., Benetti, S., Taubenberger, S., Inserra, C., Kankare, E., Maguire, K., Smartt, S. J., Yaron, O., and Young, D., ATel # 11524 (2018).

7. *ePESSTO spectroscopic classification of optical transients*,
Rubin, A., Malesani, D., **Heintz, K. E.**, Dennefeld, M., Galbany, L., Gromadzki, M., Benetti, S., Inserra, C., Kankare, E., Maguire, K., Smartt, S. J., Yaron, O., and Young, D., ATel # 11519 (2018).

8. *ePESSTO spectroscopic classification of optical transients*,
Malesani, D., Rubin, A., Leloudas, G., **Heintz, K. E.**, Anderson, J., Maguire, K., Inserra, C., Kankare, E., Smartt, S. J., Yaron, O., Young, D., Tonry, J., Denneau, L., Heinze, A., Weiland, H., Stalder, B., Rest, A., Smith, K. W., McBrien, O., Wright, D. E., Chambers, K. C., Flewelling, H., Huber, M., Lowe, T., Magnier, E., Schultz, A., Waters, C., Wainscoat, R. J., and Wilman, M., ATel # 11509 (2018).

Bibliography

Abbott, B. P., Abbott, R., Abbott, T. D., et al. 2017a, Physical Review Letters, 119, 161101

—. 2017b, ApJ, 848, L12

Akerman, C. J., Ellison, S. L., Pettini, M., & Steidel, C. C. 2005, A&A, 440, 499

Alam, S., Albareti, F. D., Allende Prieto, C., et al. 2015, ApJS, 219, 12

Amanullah, R., Goobar, A., Johansson, J., et al. 2014, ApJ, 788, L21

Appenzeller, I., Fricke, K., Fürtig, W., et al. 1998, The Messenger, 94, 1

Arabsalmani, M., Møller, P., Fynbo, J. P. U., et al. 2015, MNRAS, 446, 990

Arabsalmani, M., Le Floc'h, E., Dannerbauer, H., et al. 2018a, MNRAS, 476, 2332

Arabsalmani, M., Møller, P., Perley, D. A., et al. 2018b, MNRAS, 473, 3312

Arcodia, R., Campana, S., & Salvaterra, R. 2016, A&A, 590, A82

Arnouts, S., Cristiani, S., Moscardini, L., et al. 1999, MNRAS, 310, 540

Asplund, M., Grevesse, N., Sauval, A. J., & Scott, P. 2009, ARA&A, 47, 481

Atwood, W. B., Abdo, A. A., Ackermann, M., et al. 2009, ApJ, 697, 1071

Bañados, E., Venemans, B. P., Mazzucchelli, C., et al. 2018, Nature, 553, 473

Balashev, S. A., Klimenko, V. V., Ivanchik, A. V., et al. 2014, MNRAS, 440, 225

Balashev, S. A., & Noterdaeme, P. 2018, MNRAS, 478, L7

Balashev, S. A., Noterdaeme, P., Klimenko, V. V., et al. 2015, A&A, 575, L8

Balashev, S. A., Petitjean, P., Ivanchik, A. V., et al. 2011, MNRAS, 418, 357

Balashev, S. A., Noterdaeme, P., Rahmani, H., et al. 2017, MNRAS, 470, 2890

Barthelmy, S. D., Barbier, L. M., Cummings, J. R., et al. 2005, Space Sci. Rev., 120, 143

Barthelmy, S. D., Evans, P. A., Gehrels, N., et al. 2007, GRB Coordinates Network, 6692

Beardmore, A. P., Barthelmy, S. D., Chester, M. M., et al. 2012, GRB Coordinates Network, Circular Service, No. 12859, #1 (2012), 12859

Behar, E., Dado, S., Dar, A., & Laor, A. 2011, ApJ, 734, 26

Berg, T. A. M., Ellison, S. L., Prochaska, J. X., Venn, K. A., & Dessauges-Zavadsky, M. 2015, MNRAS, 452, 4326

Berger, E. 2014, ARA&A, 52, 43

Berger, E., Fong, W., & Chornock, R. 2013, ApJ, 774, L23

Bissaldi, E., Briggs, M. S., Piron, F., Takahashi, H., & Uehara, T. 2009, GRB Coordinates Network, 9972

Bissaldi, E., Racusin, J. L., Longo, F., et al. 2014, GRB Coordinates Network, Circular Service, No. 16969, #1 (2014), 16969

Black, J. H., Hartmann, L. W., Raymond, J. C., & Dupree, A. K. 1980, ApJ, 239, 502
Blanco, A., Fonti, S., & Orofino, V. 1996, ApJ, 462, 1020
Blandford, R. D., & Znajek, R. L. 1977, MNRAS, 179, 433
Bloom, J. S., Kulkarni, S. R., & Djorgovski, S. G. 2002, AJ, 123, 1111
Boisse, P., Le Brun, V., Bergeron, J., & Deharveng, J.-M. 1998, A&A, 333, 841
Bolatto, A. D., Wolfire, M., & Leroy, A. K. 2013, ARA&A, 51, 207
Bolmer, J. 2019, Dissertation, Technische Universität München, München
Bolmer, J., Greiner, J., Krühler, T., et al. 2018, A&A, 609, A62
Bolmer, J., Ledoux, C., Wiseman, P., et al. 2019, A&A, 623, A43
Bregman, J. N., & Harrington, J. P. 1986, ApJ, 309, 833
Brusa, M., Civano, F., Comastri, A., et al. 2010, ApJ, 716, 348
Bruzual, G., & Charlot, S. 2003, MNRAS, 344, 1000
Buchner, J., Schulze, S., & Bauer, F. E. 2017, MNRAS, 464, 4545
Burgh, E. B., France, K., & Jenkins, E. B. 2010, ApJ, 708, 334
Calzetti, D., Armus, L., Bohlin, R. C., et al. 2000, ApJ, 533, 682
Cameron, E. 2011, PASA, 28, 128
Cami, J., & Cox, N. L. J., eds. 2014, IAU Symposium, Vol. 297, The Diffuse Interstellar Bands
Campana, S., Salvaterra, R., Ferrara, A., & Pallottini, A. 2015, A&A, 575, A43
Campana, S., Thöne, C. C., de Ugarte Postigo, A., et al. 2010, MNRAS, 402, 2429
Cano, Z., Wang, S.-Q., Dai, Z.-G., & Wu, X.-F. 2017, Advances in Astronomy, 2017, 8929054
Cardelli, J. A., Clayton, G. C., & Mathis, J. S. 1989, ApJ, 345, 245
Carilli, C. L., & Walter, F. 2013, ARA&A, 51, 105
Castro-Tirado, A. J., Møller, P., García-Segura, G., et al. 2010, A&A, 517, A61
Chabrier, G. 2003, PASP, 115, 763
Chen, H.-W., Perley, D. A., Pollack, L. K., et al. 2009, ApJ, 691, 152
Chen, S.-F. S., Simcoe, R. A., Torrey, P., et al. 2017, ApJ, 850, 188
Christensen, L., Hjorth, J., & Gorosabel, J. 2004, A&A, 425, 913
Christensen, L., Møller, P., Fynbo, J. P. U., & Zafar, T. 2014, MNRAS, 445, 225
Christensen, L., Wisotzki, L., Roth, M. M., et al. 2007, A&A, 468, 587
Christensen, L., Vergani, S. D., Schulze, S., et al. 2017, A&A, 608, A84
Cooper, T. J., Simcoe, R. A., Cooksey, K. L., et al. 2019, arXiv e-prints, arXiv:1901.05980
Corre, D., Buat, V., Basa, S., et al. 2018, A&A, 617, A141
Cortzen, I., Garrett, J., Magdis, G., et al. 2019, MNRAS, 482, 1618
Covino, S., Melandri, A., Salvaterra, R., et al. 2013, MNRAS, 432, 1231
Crampton, D., Cowley, A. P., & Hartwick, F. D. A. 1987, ApJ, 314, 129
Croom, S. M., Smith, R. J., Boyle, B. J., et al. 2004, MNRAS, 349, 1397
Cucchiara, A., Fumagalli, M., Rafelski, M., et al. 2015, ApJ, 804, 51
Cucchiara, A., Levan, A. J., Fox, D. B., et al. 2011, ApJ, 736, 7
Curran, P. A., van der Horst, A. J., Beardmore, A. P., et al. 2007, A&A, 467, 1049
Cutri, R. M. e. 2013, VizieR Online Data Catalog, 2328
Dalton, G. B., Caldwell, M., Ward, A. K., et al. 2006, in Proc. SPIE, Vol. 6269, Society of Photo-Optical Instrumentation Engineers (SPIE) Conference Series, 62690X
D'Avanzo, P. 2015, Journal of High Energy Astrophysics, 7, 73

D'Avanzo, P., Barthelmy, S. D., Bernardini, M. G., et al. 2014, GRB Coordinates Network, Circular Service, No. 17037, #1 (2014), 17037
D'Avanzo, P., Barthelmy, S. D., Burrows, D. N., et al. 2016, GRB Coordinates Network, Circular Service, No. 18979, #1 (2016), 18979
D'Avanzo, P., Bolmer, J., D'Elia, V., et al. 2018, GRB Coordinates Network, Circular Service, No. 22555, #1 (2018/March-0), 22555
De Cia, A., Ledoux, C., Mattsson, L., et al. 2016, A&A, 596, A97
De Cia, A., Ledoux, C., Petitjean, P., & Savaglio, S. 2018, A&A, 611, A76
De Cia, A., Ledoux, C., Savaglio, S., Schady, P., & Vreeswijk, P. M. 2013, A&A, 560, A88
De Cia, A., Ledoux, C., Fox, A. J., et al. 2012, A&A, 545, A64
de Jong, J. T. A., Verdoes Kleijn, G. A., Erben, T., et al. 2017, A&A, 604, A134
de Ugarte Postigo, A., Malesani, D., & Xu, D. 2015, GRB Coordinates Network, Circular Service, No. 18426, #1 (2015), 18426
de Ugarte Postigo, A., Tanvir, N. R., Xu, D., & Fynbo, J. 2019, GRB Coordinates Network, Circular Service, No. 23680, #1 (2019), 23680
de Ugarte Postigo, A., Thöne, C. C., Bolmer, J., et al. 2018, A&A, 620, A119
D'Elia, V., Campana, S., Covino, S., et al. 2011, MNRAS, 418, 680
D'Elia, V., Fiore, F., Meurs, E. J. A., et al. 2007, A&A, 467, 629
D'Elia, V., Fiore, F., Perna, R., et al. 2009a, ApJ, 694, 332
—. 2009b, A&A, 503, 437
D'Elia, V., Fynbo, J. P. U., Covino, S., et al. 2010, A&A, 523, A36
D'Elia, V., Fynbo, J. P. U., Goldoni, P., et al. 2014, A&A, 564, A38
Della Valle, M., Chincarini, G., Panagia, N., et al. 2006, Nature, 444, 1050
Draine, B. 1989, in IAU Symposium, Vol. 135, Interstellar Dust, ed. L. J. Allamandola & A. G. G. M. Tielens, 313
Draine, B. T. 1990, in Astronomical Society of the Pacific Conference Series, Vol. 12, The Evolution of the Interstellar Medium, ed. L. Blitz, 193–205
Draine, B. T. 2000, ApJ, 532, 273
—. 2003, ARA&A, 41, 241
Draine, B. T., & Hao, L. 2002, ApJ, 569, 780
Draine, B. T., & Lee, H. M. 1984, ApJ, 285, 89
Draine, B. T., & Li, A. 2007, ApJ, 657, 810
Dwek, E. 2016, ApJ, 825, 136
Dyson, J. E. 1977, A&A, 59, 161
Edge, A., Sutherland, W., Kuijken, K., et al. 2013, The Messenger, 154, 32
Edge, A., Sutherland, W., & Viking Team. 2016, VizieR Online Data Catalog, 2343
Eitan, A., & Behar, E. 2013, ApJ, 774, 29
Elias-Rosa, N., Benetti, S., Cappellaro, E., et al. 2006, MNRAS, 369, 1880
Elias-Rosa, N., Benetti, S., Turatto, M., et al. 2008, MNRAS, 384, 107
Elíasdóttir, Á., Fynbo, J. P. U., Hjorth, J., et al. 2009, ApJ, 697, 1725
Ellison, S. L., Hall, P. B., & Lira, P. 2005, AJ, 130, 1345
Ellison, S. L., & Lopez, S. 2009, MNRAS, 397, 467
Ellison, S. L., Prochaska, J. X., Hennawi, J., et al. 2010, MNRAS, 406, 1435
Ellison, S. L., Yan, L., Hook, I. M., et al. 2001, A&A, 379, 393
—. 2002, A&A, 383, 91

Ellison, S. L., York, B. A., Pettini, M., & Kanekar, N. 2008, MNRAS, 388, 1349
Emerson, J., McPherson, A., & Sutherland, W. 2006, The Messenger, 126, 41
Evans, J. L., Churchill, C. W., Murphy, M. T., Nielsen, N. M., & Klimek, E. S. 2013, ApJ, 768, 3
Evans, P. A., Beardmore, A. P., Page, K. L., et al. 2009, MNRAS, 397, 1177
Fall, S. M., & Pei, Y. C. 1989, ApJ, 337, 7
—. 1993, ApJ, 402, 479
Fall, S. M., Pei, Y. C., & McMahon, R. G. 1989, ApJ, 341, L5
Fan, X., Strauss, M. A., Becker, R. H., et al. 2006, AJ, 132, 117
Fiore, F., Guetta, D., Piranomonte, S., D'Elia, V., & Antonelli, L. A. 2007, A&A, 470, 515
Fitzpatrick, E. L., & Massa, D. 1986, ApJ, 307, 286
—. 1990, ApJS, 72, 163
—. 2007, ApJ, 663, 320
Folatelli, G., Phillips, M. M., Burns, C. R., et al. 2010, AJ, 139, 120
Fox, A. J., Ledoux, C., Petitjean, P., & Srianand, R. 2007a, A&A, 473, 791
Fox, A. J., Ledoux, C., Vreeswijk, P. M., Smette, A., & Jaunsen, A. O. 2008, A&A, 491, 189
Fox, A. J., Petitjean, P., Ledoux, C., & Srianand, R. 2007b, A&A, 465, 171
Fox, A. J., Prochaska, J. X., Ledoux, C., et al. 2009, A&A, 503, 731
Francis, P. J., Hewett, P. C., Foltz, C. B., et al. 1991, ApJ, 373, 465
Frank, S., & Péroux, C. 2010, MNRAS, 406, 2235
Friis, M., De Cia, A., Krühler, T., et al. 2015, MNRAS, 451, 167
Fruchter, A., Krolik, J. H., & Rhoads, J. E. 2001, ApJ, 563, 597
Fruchter, A. S., Levan, A. J., Strolger, L., et al. 2006, Nature, 441, 463
Fynbo, J. P. U., de Ugarte Postigo, A., D'Elia, V., et al. 2018, GRB Coordinates Network, Circular Service, No. 23356, #1 (2018), 23356
Fynbo, J. P. U., Krogager, J.-K., Venemans, B., et al. 2013a, ApJS, 204, 6
Fynbo, J. P. U., Prochaska, J. X., Sommer-Larsen, J., Dessauges-Zavadsky, M., & Møller, P. 2008, ApJ, 683, 321
Fynbo, J. P. U., Watson, D., Thöne, C. C., et al. 2006a, Nature, 444, 1047
Fynbo, J. P. U., Starling, R. L. C., Ledoux, C., et al. 2006b, A&A, 451, L47
Fynbo, J. P. U., Jakobsson, P., Prochaska, J. X., et al. 2009, ApJS, 185, 526
Fynbo, J. P. U., Laursen, P., Ledoux, C., et al. 2010, MNRAS, 408, 2128
Fynbo, J. P. U., Ledoux, C., Noterdaeme, P., et al. 2011, MNRAS, 413, 2481
Fynbo, J. P. U., Geier, S. J., Christensen, L., et al. 2013b, MNRAS, 436, 361
Fynbo, J. P. U., Krühler, T., Leighly, K., et al. 2014, A&A, 572, A12
Fynbo, J. P. U., Krogager, J.-K., Heintz, K. E., et al. 2017, A&A, 606, A13
Fynbo, J. U., Møller, P., & Warren, S. J. 1999, MNRAS, 305, 849
Fynbo, J. U., Jensen, B. L., Gorosabel, J., et al. 2001, A&A, 369, 373
Gaia Collaboration, Brown, A. G. A., Vallenari, A., et al. 2018, ArXiv e-prints, arXiv:1804.09365
Galama, T. J., & Wijers, R. A. M. J. 2001, ApJ, 549, L209
Galama, T. J., Vreeswijk, P. M., van Paradijs, J., et al. 1998, Nature, 395, 670
Ge, J., & Bechtold, J. 1999, in Astronomical Society of the Pacific Conference Series, Vol. 156, Highly Redshifted Radio Lines, ed. C. L. Carilli, S. J. E. Radford, K. M.

Menten, & G. I. Langston, 121
Gehrels, N., Ramirez-Ruiz, E., & Fox, D. B. 2009, ARA&A, 47, 567
Gehrels, N., Chincarini, G., Giommi, P., et al. 2004, ApJ, 611, 1005
Gehrels, N., Norris, J. P., Barthelmy, S. D., et al. 2006, Nature, 444, 1044
Geier, S. J., Heintz, K. E., Fynbo, J. P. U., et al. 2019, A&A, 625, L9
Glikman, E., Helfand, D. J., & White, R. L. 2006, ApJ, 640, 579
Glover, S. C. O., & Clark, P. C. 2016, MNRAS, 456, 3596
Goldoni, P., Royer, F., François, P., et al. 2006, in Proc. SPIE, Vol. 6269, Society of Photo-Optical Instrumentation Engineers (SPIE) Conference Series, 62692K
Goldstein, A., Veres, P., Burns, E., et al. 2017, ApJ, 848, L14
Gompertz, B. P., Burrows, D. N., Cenko, S. B., et al. 2014, GRB Coordinates Network, 16214
Goobar, A. 2008, ApJ, 686, L103
Gordon, K. D., Clayton, G. C., Misselt, K. A., Landolt, A. U., & Wolff, M. J. 2003, ApJ, 594, 279
Goshu, B. S. 2017, American Journal of Astronomy and Astrophysics, 5, 42
Graham, M. J., Djorgovski, S. G., Drake, A. J., et al. 2014, MNRAS, 439, 703
Greiner, J., Bornemann, W., Clemens, C., et al. 2008, PASP, 120, 405
Greiner, J., Krühler, T., Klose, S., et al. 2011, A&A, 526, A30
Greiner, J., Fox, D. B., Schady, P., et al. 2015, ApJ, 809, 76
Guillard, P., Boulanger, F., Lehnert, M. D., Appleton, P. N., & Pineau des Forêts, G. 2015, in SF2A-2015: Proceedings of the Annual meeting of the French Society of Astronomy and Astrophysics, 81–85
Guimarães, R., Noterdaeme, P., Petitjean, P., et al. 2012, AJ, 143, 147
Hartoog, O. E., Malesani, D., Wiersema, K., et al. 2012, GRB Coordinates Network, Circular Service, No. 13730, #1 (2012), 13730
Hartoog, O. E., Malesani, D., Fynbo, J. P. U., et al. 2015, A&A, 580, A139
Heintz, K. E., Fynbo, J. P. U., & Høg, E. 2015, A&A, 578, A91
Heintz, K. E., Fynbo, J. P. U., Møller, P., et al. 2016, A&A, 595, A13
Heintz, K. E., Fynbo, J. P. U., Jakobsson, P., et al. 2017, A&A, 601, A83
Heintz, K. E., Fynbo, J. P. U., Ledoux, C., et al. 2018a, A&A, 615, A43
Heintz, K. E., Watson, D., Jakobsson, P., et al. 2018b, MNRAS, 479, 3456
Heintz, K. E., Ledoux, C., Fynbo, J. P. U., et al. 2019a, A&A, 621, A20
Heintz, K. E., Zafar, T., De Cia, A., et al. 2019b, MNRAS, 486, 2063
Henning, T., & Salama, F. 1998, Science, 282, 2204
Herbert-Fort, S., Prochaska, J. X., Dessauges-Zavadsky, M., et al. 2006, PASP, 118, 1077
Hewett, P. C., & Foltz, C. B. 1994, PASP, 106, 113
Hewett, P. C., Warren, S. J., Leggett, S. K., & Hodgkin, S. T. 2006, MNRAS, 367, 454
Hjorth, J., Melandri, A., Malesani, D., Kruehler, T., & Xu, D. 2013, GRB Coordinates Network, Circular Service, No. 14365, #1 (2013), 14365
Hjorth, J., Sollerman, J., Møller, P., et al. 2003, Nature, 423, 847
Hopkins, P. F., & Lee, H. 2016, MNRAS, 456, 4174
Hunt, L. K., Palazzi, E., Michałowski, M. J., et al. 2014, A&A, 565, A112
Hutton, S., Ferreras, I., Wu, K., et al. 2014, MNRAS, 440, 150
Ilbert, O., Arnouts, S., McCracken, H. J., et al. 2006, A&A, 457, 841

Immler, S., Barthelmy, S. D., Baumgartner, W. H., et al. 2012, GRB Coordinates Network, Circular Service, No. 13727, #1 (2012), 13727
Ivezić, Ž., Menou, K., Knapp, G. R., et al. 2002, AJ, 124, 2364
Izzo, L., de Ugarte Postigo, A., Maeda, K., et al. 2019, arXiv e-prints, arXiv:1901.05500
Jakobsson, P., Hjorth, J., Fynbo, J. P. U., et al. 2004, ApJ, 617, L21
Jakobsson, P., Björnsson, G., Fynbo, J. P. U., et al. 2005, MNRAS, 362, 245
Jakobsson, P., Levan, A., Fynbo, J. P. U., et al. 2006a, A&A, 447, 897
Jakobsson, P., Fynbo, J. P. U., Ledoux, C., et al. 2006b, A&A, 460, L13
Japelj, J., Covino, S., Gomboc, A., et al. 2015, A&A, 579, A74
Japelj, J., Vergani, S. D., Salvaterra, R., et al. 2016, A&A, 590, A129
Jenkins, E. B. 1987, in Astrophysics and Space Science Library, Vol. 134, Interstellar Processes, ed. D. J. Hollenbach & H. A. Thronson, Jr., 533–559
Jenkins, E. B. 2009, ApJ, 700, 1299
Jiang, P., Ge, J., Prochaska, J. X., et al. 2010, ApJ, 720, 328
Jiang, P., Ge, J., Zhou, H., Wang, J., & Wang, T. 2011, ApJ, 732, 110
Johansson, J., Goobar, A., Kasliwal, M. M., et al. 2017, MNRAS, 466, 3442
Jorgenson, R. A., Murphy, M. T., Thompson, R., & Carswell, R. F. 2014, MNRAS, 443, 2783
Jorgenson, R. A., Wolfe, A. M., & Prochaska, J. X. 2010, ApJ, 722, 460
Jorgenson, R. A., Wolfe, A. M., Prochaska, J. X., et al. 2006, ApJ, 646, 730
Kalirai, J. 2018, Contemporary Physics, 59, 251
Kann, D. A., Klose, S., Zhang, B., et al. 2010, ApJ, 720, 1513
Kaplan, K. F., Prochaska, J. X., Herbert-Fort, S., Ellison, S. L., & Dessauges-Zavadsky, M. 2010, PASP, 122, 619
Kawai, N., Kosugi, G., Aoki, K., et al. 2006, Nature, 440, 184
Kennicutt, R. C., & Evans, N. J. 2012, ARA&A, 50, 531
Kennicutt, Jr., R. C. 1998, ARA&A, 36, 189
Kewley, L. J., & Dopita, M. A. 2002, ApJS, 142, 35
Kewley, L. J., & Ellison, S. L. 2008, ApJ, 681, 1183
Khare, P., vanden Berk, D., York, D. G., Lundgren, B., & Kulkarni, V. P. 2012, MNRAS, 419, 1028
Kistler, M. D., Yüksel, H., Beacom, J. F., Hopkins, A. M., & Wyithe, J. S. B. 2009, ApJ, 705, L104
Koo, D. C., Kron, R. G., & Cudworth, K. M. 1986, PASP, 98, 285
Kouveliotou, C., Meegan, C. A., Fishman, G. J., et al. 1993, ApJ, 413, L101
Krawczyk, C. M., Richards, G. T., Gallagher, S. C., et al. 2015, AJ, 149, 203
Krisciunas, K., Prieto, J. L., Garnavich, P. M., et al. 2006, AJ, 131, 1639
Krogager, J.-K. 2018, arXiv e-prints, arXiv:1803.01187
Krogager, J.-K., Fynbo, J. P. U., Møller, P., et al. 2012, MNRAS, 424, L1
Krogager, J.-K., Fynbo, J. P. U., Møller, P., et al. 2019, MNRAS, 486, 4377
Krogager, J.-K., Fynbo, J. P. U., Noterdaeme, P., et al. 2016a, MNRAS, 455, 2698
Krogager, J.-K., Møller, P., Fynbo, J. P. U., & Noterdaeme, P. 2017, MNRAS, 469, 2959
Krogager, J.-K., Fynbo, J. P. U., Ledoux, C., et al. 2013, MNRAS, 433, 3091
Krogager, J.-K., Geier, S., Fynbo, J. P. U., et al. 2015, ApJS, 217, 5
Krogager, J.-K., Fynbo, J. P. U., Heintz, K. E., et al. 2016b, ApJ, 832, 49

Krone-Martins, A., Delchambre, L., Wertz, O., et al. 2018, ArXiv e-prints, arXiv:1804.11051
Krongold, Y., & Prochaska, J. X. 2013, ApJ, 774, 115
Krühler, T., Fynbo, J. P. U., Milvang-Jensen, B., Tanvir, N., & Jakobsson, P. 2012, GRB Coordinates Network, Circular Service, No. 13134, #1 (2012), 13134
Krühler, T., Küpcü Yoldaş, A., Greiner, J., et al. 2008, ApJ, 685, 376
Krühler, T., Greiner, J., Schady, P., et al. 2011, A&A, 534, A108
Krühler, T., Fynbo, J. P. U., Geier, S., et al. 2012, A&A, 546, A8
Krühler, T., Ledoux, C., Fynbo, J. P. U., et al. 2013, A&A, 557, A18
Krühler, T., Malesani, D., Fynbo, J. P. U., et al. 2015, A&A, 581, A125
Krumholz, M. R., Ellison, S. L., Prochaska, J. X., & Tumlinson, J. 2009, ApJ, 701, L12
Kuijken, K. 2011, The Messenger, 146, 8
Kulkarni, S. R., Djorgovski, S. G., Ramaprakash, A. N., et al. 1998, Nature, 393, 35
Kulkarni, V. P., & Fall, S. M. 2002, ApJ, 580, 732
Kulkarni, V. P., Torres-Garcia, L. M., Som, D., et al. 2011, ApJ, 726, 14
Lanzetta, K. M., Wolfe, A. M., & Turnshek, D. A. 1995, ApJ, 440, 435
Lanzetta, K. M., Wolfe, A. M., Turnshek, D. A., et al. 1991, ApJS, 77, 1
Laporte, S. J., Kennea, J. A., Klingler, N. J., et al. 2019, GRB Coordinates Network, Circular Service, No. 23677, #1 (2019), 23677
Ledoux, C., Noterdaeme, P., Petitjean, P., & Srianand, R. 2015, A&A, 580, A8
Ledoux, C., Petitjean, P., Bergeron, J., Wampler, E. J., & Srianand, R. 1998, A&A, 337, 51
Ledoux, C., Petitjean, P., Fynbo, J. P. U., Møller, P., & Srianand, R. 2006, A&A, 457, 71
Ledoux, C., Petitjean, P., & Srianand, R. 2003, MNRAS, 346, 209
Ledoux, C., Vreeswijk, P. M., Smette, A., et al. 2009, A&A, 506, 661
Léger, A., Verstraete, L., D'Hendecourt, L., et al. 1989, in IAU Symposium, Vol. 135, Interstellar Dust, ed. L. J. Allamandola & A. G. G. M. Tielens, 173
Lehner, N., Zech, W. F., Howk, J. C., & Savage, B. D. 2011, ApJ, 727, 46
Leighly, K. M., Terndrup, D. M., Baron, E., et al. 2014, ApJ, 788, 123
Li, A., & Draine, B. T. 2001, ApJ, 554, 778
Li, A., & Greenberg, J. M. 1997, A&A, 323, 566
Li, L.-X. 2008, MNRAS, 388, 1487
Liang, C., & Kravtsov, A. 2017, arXiv e-prints, arXiv:1710.09852
Lien, A., Sakamoto, T., Barthelmy, S. D., et al. 2016, ApJ, 829, 7
Lien, A. Y., Barthelmy, S. D., D'Elia, V., et al. 2015, GRB Coordinates Network, Circular Service, No. 17665, #1 (2015), 17665
Lien, A. Y., Baumgartner, W. H., Burrows, D. N., et al. 2013, GRB Coordinates Network, Circular Service, No. 14361, #1 (2013), 14361
Lindegren, L., Hernandez, J., Bombrun, A., et al. 2018, ArXiv e-prints, arXiv:1804.09366
Lodders, K., Palme, H., & Gail, H.-P. 2009, Landolt Börnstein, 712
Lusso, E., Worseck, G., Hennawi, J. F., et al. 2015, MNRAS, 449, 4204
Lyman, J. D., Levan, A. J., Tanvir, N. R., et al. 2017, MNRAS, arXiv:1701.05925
Ma, J., Ge, J., Zhao, Y., et al. 2017, MNRAS, 472, 2196
Ma, J., Caucal, P., Noterdaeme, P., et al. 2015, MNRAS, 454, 1751

Ma, J., Ge, J., Prochaska, J. X., et al. 2018, MNRAS, 474, 4870
MacFadyen, A. I., & Woosley, S. E. 1999, ApJ, 524, 262
Madau, P., & Dickinson, M. 2014, ARA&A, 52, 415
Maddox, N., Hewett, P. C., Péroux, C., Nestor, D. B., & Wisotzki, L. 2012, MNRAS, 424, 2876
Maddox, N., Hewett, P. C., Warren, S. J., & Croom, S. M. 2008, MNRAS, 386, 1605
Magdis, G. E., Daddi, E., Béthermin, M., et al. 2012, ApJ, 760, 6
Malesani, D., Fynbo, J. P. U., Christensen, L., et al. 2009a, GRB Coordinates Network, 9761
Malesani, D., Schulze, S., de Ugarte Postigo, A., et al. 2012, GRB Coordinates Network, Circular Service, No. 13649, #1 (2012), 13649
Malesani, D., Goldoni, P., Fynbo, J. P. U., et al. 2009b, GRB Coordinates Network, 9942
Maller, A. H., Prochaska, J. X., Somerville, R. S., & Primack, J. R. 2003, MNRAS, 343, 268
Mangano, V., Cummings, J. R., Cusumano, G., et al. 2008, GRB Coordinates Network, 7847
Markwardt, C. B., Barthelmy, S. D., Chester, M. M., et al. 2009, GRB Coordinates Network, 9754
Mathes, N. L., Churchill, C. W., & Murphy, M. T. 2017, ArXiv 1701.05624, arXiv:1701.05624
Matthews, T. A., & Sandage, A. R. 1963, ApJ, 138, 30
McGuire, J. T. W., Tanvir, N. R., Levan, A. J., et al. 2016, ApJ, 825, 135
McKee, C. F., & Ostriker, E. C. 2007, ARA&A, 45, 565
Meegan, C., Lichti, G., Bhat, P. N., et al. 2009, ApJ, 702, 791
Meegan, C. A., Fishman, G. J., Wilson, R. B., et al. 1992, Nature, 355, 143
Melandri, A., Barthelmy, S. D., D'Avanzo, P., et al. 2015, GRB Coordinates Network, Circular Service, No. 18425, #1 (2015), 18425
Mereghetti, S., Gotz, D., Ferrigno, C., Fotopoulou, S., & Borkowski, J. 2016, GRB Coordinates Network, Circular Service, No. 20103, #1 (2016), 20103
Mészáros, P. 2006, Reports on Progress in Physics, 69, 2259
Metzger, B. D., & Berger, E. 2012, ApJ, 746, 48
Michałowski, M. J., Karska, A., Rizzo, J. R., et al. 2018, A&A, 617, A143
Mishra, A., & Li, A. 2017, ApJ, 850, 138
Modigliani, A., Goldoni, P., Royer, F., et al. 2010, in Proc. SPIE, Vol. 7737, Observatory Operations: Strategies, Processes, and Systems III, 773728
Modjaz, M., Liu, Y. Q., Bianco, F. B., & Graur, O. 2016, ApJ, 832, 108
Møller, P., Fynbo, J. P. U., & Fall, S. M. 2004, A&A, 422, L33
Møller, P., Fynbo, J. P. U., Ledoux, C., & Nilsson, K. K. 2013, MNRAS, 430, 2680
Møller, P., & Warren, S. J. 1998, MNRAS, 299, 661
Møller, P., Warren, S. J., & Fynbo, J. U. 1998, A&A, 330, 19
Møller, P., Fynbo, J. P. U., Hjorth, J., et al. 2002, A&A, 396, L21
Monier, E. M., Turnshek, D. A., & Rao, S. 2009, MNRAS, 397, 943
Mortlock, D. J., Warren, S. J., Venemans, B. P., et al. 2011, Nature, 474, 616
Moss, M. J., D'Ai, A., D'Elia, V., et al. 2018, GRB Coordinates Network, Circular Service, No. 23349, #1 (2018), 23349

Murphy, M. T., & Bernet, M. L. 2016, MNRAS, 455, 1043
Murphy, M. T., & Liske, J. 2004, MNRAS, 354, L31
Myers, A. D., Palanque-Delabrouille, N., Prakash, A., et al. 2015, ApJS, 221, 27
Narayan, R., Paczynski, B., & Piran, T. 1992, ApJ, 395, L83
Narayanan, D., Conroy, C., Davé, R., Johnson, B. D., & Popping, G. 2018, ApJ, 869, 70
Neeleman, M., Wolfe, A. M., Prochaska, J. X., & Rafelski, M. 2013, ApJ, 769, 54
Neeleman, M., Prochaska, J. X., Zwaan, M. A., et al. 2016, ApJ, 820, L39
Nobili, S., & Goobar, A. 2008, A&A, 487, 19
Noll, S., Pierini, D., Cimatti, A., et al. 2009, A&A, 499, 69
Noterdaeme, P., Ledoux, C., Petitjean, P., & Srianand, R. 2008, A&A, 481, 327
Noterdaeme, P., Ledoux, C., Srianand, R., Petitjean, P., & Lopez, S. 2009a, A&A, 503, 765
Noterdaeme, P., Ledoux, C., Zou, S., et al. 2018, A&A, 612, A58
Noterdaeme, P., Petitjean, P., Ledoux, C., & Srianand, R. 2009b, A&A, 505, 1087
Noterdaeme, P., Petitjean, P., Pâris, I., et al. 2014, A&A, 566, A24
Noterdaeme, P., Petitjean, P., & Srianand, R. 2015a, A&A, 578, L5
Noterdaeme, P., Petitjean, P., Srianand, R., Ledoux, C., & Le Petit, F. 2007, A&A, 469, 425
Noterdaeme, P., Srianand, R., Rahmani, H., et al. 2015b, A&A, 577, A24
Noterdaeme, P., Petitjean, P., Carithers, W. C., et al. 2012a, A&A, 547, L1
Noterdaeme, P., Laursen, P., Petitjean, P., et al. 2012b, A&A, 540, A63
Noterdaeme, P., Krogager, J.-K., Balashev, S., et al. 2017, A&A, 597, A82
Nysewander, M., Fruchter, A. S., & Pe'er, A. 2009, ApJ, 701, 824
Oesch, P. A., Brammer, G., van Dokkum, P. G., et al. 2016, ApJ, 819, 129
Oke, J. B. 1974, ApJS, 27, 21
Oke, J. B., & Gunn, J. E. 1983, ApJ, 266, 713
Osterbrock, D. E. 1989, Astrophysics of gaseous nebulae and active galactic nuclei (University Science Books)
Pagani, C., Barthelmy, S. D., Gehrels, N., et al. 2012a, GRB Coordinates Network, Circular Service, No. 13645, #1 (2012), 13645
Pagani, C., Barthelmy, S. D., Baumgartner, W. H., et al. 2012b, GRB Coordinates Network, Circular Service, No. 13886, #1 (2012), 13886
Page, K. L., Barthelmy, S. D., Beardmore, A. P., et al. 2006, GRB Coordinates Network, 5823
Palmerio, J. T., Vergani, S. D., Salvaterra, R., et al. 2019, A&A, 623, A26
Pâris, I., Petitjean, P., Aubourg, É., et al. 2014, A&A, 563, A54
Pâris, I., Petitjean, P., Ross, N. P., et al. 2017, A&A, 597, A79
Pâris, I., Petitjean, P., Aubourg, É., et al. 2018, A&A, 613, A51
Pei, Y. C. 1992, ApJ, 395, 130
Pei, Y. C., Fall, S. M., & Bechtold, J. 1991, ApJ, 378, 6
Pei, Y. C., Fall, S. M., & Hauser, M. G. 1999, ApJ, 522, 604
Perley, D. A., Bloom, J. S., Butler, N. R., et al. 2008, ApJ, 672, 449
Perley, D. A., Cenko, S. B., Bloom, J. S., et al. 2009, AJ, 138, 1690
Perley, D. A., Morgan, A. N., Updike, A., et al. 2011, AJ, 141, 36
Perley, D. A., Levan, A. J., Tanvir, N. R., et al. 2013, ApJ, 778, 128
Perley, D. A., Krühler, T., Schulze, S., et al. 2016a, ApJ, 817, 7

Perley, D. A., Tanvir, N. R., Hjorth, J., et al. 2016b, ApJ, 817, 8
Perna, R., Lazzati, D., & Fiore, F. 2003, ApJ, 585, 775
Péroux, C., McMahon, R. G., Storrie-Lombardi, L. J., & Irwin, M. J. 2003, MNRAS, 346, 1103
Petitjean, P., Ledoux, C., Noterdaeme, P., & Srianand, R. 2006, A&A, 456, L9
Pettini, M., Ellison, S. L., Steidel, C. C., & Bowen, D. V. 1999, ApJ, 510, 576
Pettini, M., King, D. L., Smith, L. J., & Hunstead, R. W. 1997a, ApJ, 478, 536
Pettini, M., & Pagel, B. E. J. 2004, MNRAS, 348, L59
Pettini, M., Smith, L. J., Hunstead, R. W., & King, D. L. 1994, ApJ, 426, 79
Pettini, M., Smith, L. J., King, D. L., & Hunstead, R. W. 1997b, ApJ, 486, 665
Pettini, M., Zych, B. J., Steidel, C. C., & Chaffee, F. H. 2008, MNRAS, 385, 2011
Pian, E., D'Avanzo, P., Benetti, S., et al. 2017, Nature, 551, 67
Pilyugin, L. S. 2001, A&A, 369, 594
Pilyugin, L. S., & Thuan, T. X. 2005, ApJ, 631, 231
Piran, T. 2004, Reviews of Modern Physics, 76, 1143
Planck Collaboration, Ade, P. A. R., Aghanim, N., et al. 2014, A&A, 571, A16
—. 2016, A&A, 594, A13
Pontzen, A., & Pettini, M. 2009, MNRAS, 393, 557
Poudel, S., Kulkarni, V. P., Morrison, S., et al. 2018, MNRAS, 473, 3559
Prochaska, J. X. 1999, ApJ, 511, L71
—. 2006, ApJ, 650, 272
Prochaska, J. X., Chen, H.-W., & Bloom, J. S. 2006, ApJ, 648, 95
Prochaska, J. X., Chen, H.-W., Dessauges-Zavadsky, M., & Bloom, J. S. 2007, ApJ, 666, 267
Prochaska, J. X., Chen, H.-W., Wolfe, A. M., Dessauges-Zavadsky, M., & Bloom, J. S. 2008a, ApJ, 672, 59
Prochaska, J. X., Dessauges-Zavadsky, M., Ramirez-Ruiz, E., & Chen, H.-W. 2008b, ApJ, 685, 344
Prochaska, J. X., Gawiser, E., Wolfe, A. M., Castro, S., & Djorgovski, S. G. 2003, ApJ, 595, L9
Prochaska, J. X., & Herbert-Fort, S. 2004, PASP, 116, 622
Prochaska, J. X., Herbert-Fort, S., & Wolfe, A. M. 2005, ApJ, 635, 123
Prochaska, J. X., & Wolfe, A. M. 1997, ApJ, 487, 73
—. 1998, ApJ, 507, 113
—. 2000, ApJ, 533, L5
Prochaska, J. X., Sheffer, Y., Perley, D. A., et al. 2009, ApJ, 691, L27
Pugliese, G., Covino, S., Kruehler, T., Xu, D., & Tanvir, N. R. 2016, GRB Coordinates Network, Circular Service, No. 18982, #1 (2016), 18982
Pugliese, V., Xu, D., Tanvir, N. R., et al. 2015, GRB Coordinates Network, Circular Service, No. 17672, #1 (2015), 17672
Rafelski, M., Neeleman, M., Fumagalli, M., Wolfe, A. M., & Prochaska, J. X. 2014, ApJ, 782, L29
Rafelski, M., Wolfe, A. M., Prochaska, J. X., Neeleman, M., & Mendez, A. J. 2012, ApJ, 755, 89
Rahmati, A., & Schaye, J. 2014, MNRAS, 438, 529
Ramírez-Tannus, M. C., Cox, N. L. J., Kaper, L., & de Koter, A. 2018, ArXiv

(1808.10226), arXiv:1808.10226
Ranjan, A., Noterdaeme, P., Krogager, J.-K., et al. 2018, A&A, 618, A184
Rao, S. M., Belfort-Mihalyi, M., Turnshek, D. A., et al. 2011, MNRAS, 416, 1215
Rao, S. M., & Turnshek, D. A. 2000, ApJS, 130, 1
Rao, S. M., Turnshek, D. A., & Nestor, D. B. 2006, ApJ, 636, 610
Rauch, M. 1998, ARA&A, 36, 267
Richards, G. T., Fan, X., Newberg, H. J., et al. 2002, AJ, 123, 2945
Richards, G. T., Nichol, R. C., Gray, A. G., et al. 2004, ApJS, 155, 257
Richards, G. T., Myers, A. D., Gray, A. G., et al. 2009, ApJS, 180, 67
Robertson, B. E., & Ellis, R. S. 2012, ApJ, 744, 95
Ross, N. P., Myers, A. D., Sheldon, E. S., et al. 2012, ApJS, 199, 3
Ross, N. P., Hamann, F., Zakamska, N. L., et al. 2015, MNRAS, 453, 3932
Rossi, A., Klose, S., Ferrero, P., et al. 2012, A&A, 545, A77
Roy, N., Chengalur, J. N., & Srianand, R. 2006, MNRAS, 365, L1
Russell, D. M., Ellison, S. L., & Benn, C. R. 2006, MNRAS, 367, 412
Salpeter, E. E. 1964, ApJ, 140, 796
Salvaterra, R. 2015, Journal of High Energy Astrophysics, 7, 35
Salvaterra, R., Della Valle, M., Campana, S., et al. 2009, Nature, 461, 1258
Sánchez-Ramírez, R., Ellison, S. L., Prochaska, J. X., et al. 2016, MNRAS, 456, 4488
Sandage, A. 1965, ApJ, 141, 1560
Sari, R., Piran, T., & Narayan, R. 1998, ApJ, 497, L17
Savage, B. D., & Sembach, K. R. 1996, ARA&A, 34, 279
Savage, B. D., Sembach, K. R., & Lu, L. 1997, AJ, 113, 2158
Savaglio, S. 2006, New Journal of Physics, 8, 195
Savaglio, S., & Fall, S. M. 2004, ApJ, 614, 293
Savaglio, S., Fall, S. M., & Fiore, F. 2003, ApJ, 585, 638
Saxton, C. J., Barthelmy, S. D., Beardmore, A. P., et al. 2011, GRB Coordinates Network, 12423
Sbarufatti, B., Barthelmy, S. D., Burrows, D. N., et al. 2008, GRB Coordinates Network, 7828
Sbarufatti, B., Barthelmy, S. D., Gehrels, N., et al. 2012, GRB Coordinates Network, Circular Service, No. 13123, #1 (2012), 13123
Schady, P., Savaglio, S., Krühler, T., Greiner, J., & Rau, A. 2011, A&A, 525, A113
Schady, P., Page, M. J., Oates, S. R., et al. 2010, MNRAS, 401, 2773
Schady, P., Dwelly, T., Page, M. J., et al. 2012, A&A, 537, A15
Schaye, J. 2001, ApJ, 562, L95
Schlafly, E. F., & Finkbeiner, D. P. 2011, ApJ, 737, 103
Schlegel, D. J., Finkbeiner, D. P., & Davis, M. 1998, ApJ, 500, 525
Schmidt, K. B., Marshall, P. J., Rix, H.-W., et al. 2010, ApJ, 714, 1194
Schmidt, M. 1963, Nature, 197, 1040
Schmidt, M., & Green, R. F. 1983, ApJ, 269, 352
Schneider, D. P., Richards, G. T., Hall, P. B., et al. 2010, AJ, 139, 2360
Schulze, S., Chapman, R., Hjorth, J., et al. 2015, ApJ, 808, 73
Secrest, N. J., Dudik, R. P., Dorland, B. N., et al. 2015, ApJS, 221, 12
Selsing, J., Fynbo, J. P. U., Christensen, L., & Krogager, J.-K. 2016, A&A, 585, A87
Selsing, J., Malesani, D., Goldoni, P., et al. 2019, A&A, 623, A92

Sembach, K. R., Wakker, B. P., Savage, B. D., et al. 2003, ApJS, 146, 165
Sheffer, Y., Prochaska, J. X., Draine, B. T., Perley, D. A., & Bloom, J. S. 2009, ApJ, 701, L63
Sheffer, Y., Rogers, M., Federman, S. R., et al. 2008, ApJ, 687, 1075
Smartt, S. J., Chen, T.-W., Jerkstrand, A., et al. 2017, Nature, 551, 75
Smette, A., Wisotzki, L., Ledoux, C., et al. 2005, in IAU Colloq. 199: Probing Galaxies through Quasar Absorption Lines, ed. P. Williams, C.-G. Shu, & B. Menard, 475–477
Snow, T. P., & McCall, B. J. 2006, ARA&A, 44, 367
Soderberg, A. M., Chakraborti, S., Pignata, G., et al. 2010, Nature, 463, 513
Sollerman, J., Östlin, G., Fynbo, J. P. U., et al. 2005, New Astronomy, 11, 103
Solomon, P. M., & Vanden Bout, P. A. 2005, ARA&A, 43, 677
Sparre, M., Hartoog, O. E., Krühler, T., et al. 2014, ApJ, 785, 150
Srianand, R., Gupta, N., Petitjean, P., Noterdaeme, P., & Saikia, D. J. 2008, MNRAS, 391, L69
Srianand, R., Petitjean, P., Ledoux, C., Ferland, G., & Shaw, G. 2005, MNRAS, 362, 549
Stanek, K. Z., Matheson, T., Garnavich, P. M., et al. 2003, ApJ, 591, L17
Stark, D. P. 2016, ARA&A, 54, 761
Starling, R. L. C., Willingale, R., Tanvir, N. R., et al. 2013, MNRAS, 431, 3159
Stecher, T. P., & Donn, B. 1965, ApJ, 142, 1681
Stern, D., Assef, R. J., Benford, D. J., et al. 2012, ApJ, 753, 30
Storey, P. J., & Zeippen, C. J. 2000, MNRAS, 312, 813
Storrie-Lombardi, L. J., & Wolfe, A. M. 2000, ApJ, 543, 552
Svensson, K. M., Levan, A. J., Tanvir, N. R., Fruchter, A. S., & Strolger, L.-G. 2010, MNRAS, 405, 57
Tanvir, N. R., Fynbo, J. P. U., Melandri, A., et al. 2012a, GRB Coordinates Network, Circular Service, No. 13890, #1 (2012), 13890
Tanvir, N. R., Kruehler, T., De Cia, A., et al. 2016, GRB Coordinates Network, Circular Service, No. 20104, #1 (2016), 20104
Tanvir, N. R., Levan, A. J., Fruchter, A. S., et al. 2013, Nature, 500, 547
Tanvir, N. R., Fox, D. B., Levan, A. J., et al. 2009, Nature, 461, 1254
Tanvir, N. R., Levan, A. J., Fruchter, A. S., et al. 2012b, ApJ, 754, 46
Tanvir, N. R., Laskar, T., Levan, A. J., et al. 2018, ApJ, 865, 107
Tanvir, N. R., Fynbo, J. P. U., de Ugarte Postigo, A., et al. 2019, MNRAS, 483, 5380
Telfer, R. C., Zheng, W., Kriss, G. A., & Davidsen, A. F. 2002, ApJ, 565, 773
Tepper-García, T. 2006, MNRAS, 369, 2025
Thöne, C. C. 2008, PhD thesis, Dark Cosmology Centre, Niels Bohr Institute Faculty of Science, University of Copenhagen
Thöne, C. C., Fynbo, J. P. U., Goldoni, P., et al. 2013, MNRAS, 428, 3590
Tody, D. 1993, in Astronomical Society of the Pacific Conference Series, Vol. 52, Astronomical Data Analysis Software and Systems II, ed. R. J. Hanisch, R. J. V. Brissenden, & J. Barnes, 173
Trenti, M., & Stiavelli, M. 2006, ApJ, 651, 51
Treyer, M., Schiminovich, D., Johnson, B., et al. 2007, ApJS, 173, 256
Troja, E., D'Ai, A., D'Elia, V., et al. 2018, GRB Coordinates Network, Circular Service, No. 22532, #1 (2018/March-0), 22532

Tumlinson, J., Prochaska, J. X., Chen, H.-W., Dessauges-Zavadsky, M., & Bloom, J. S. 2007, ApJ, 668, 667
Ukwatta, T. N., Barthelmy, S. D., Gehrels, N., et al. 2013, GRB Coordinates Network, Circular Service, No. 14781, #1 (2013), 14781
Ukwatta, T. N., Barthelmy, S. D., Baumgartner, W. H., et al. 2015, GRB Coordinates Network, Circular Service, No. 18499, #1 (2015), 18499
van der Horst, A. J., Kouveliotou, C., Gehrels, N., et al. 2009, ApJ, 699, 1087
van Dokkum, P. G. 2001, PASP, 113, 1420
Vanden Berk, D. E., Richards, G. T., Bauer, A., et al. 2001, AJ, 122, 549
Venemans, B. P., Findlay, J. R., Sutherland, W. J., et al. 2013, ApJ, 779, 24
Venemans, B. P., Verdoes Kleijn, G. A., Mwebaze, J., et al. 2015, MNRAS, 453, 2259
Vergani, S. D., Salvaterra, R., Japelj, J., et al. 2015, A&A, 581, A102
Vergani, S. D., Palmerio, J., Salvaterra, R., et al. 2017, A&A, 599, A120
Vernet, J., Dekker, H., D'Odorico, S., et al. 2011, A&A, 536, A105
Vladilo, G., Centurión, M., Levshakov, S. A., et al. 2006, A&A, 454, 151
Vladilo, G., & Péroux, C. 2005, A&A, 444, 461
Vladilo, G., Prochaska, J. X., & Wolfe, A. M. 2008, A&A, 478, 701
Vreeswijk, P. M., Kaufer, A., Spyromilio, J., et al. 2010, in Proc. SPIE, Vol. 7737, Observatory Operations: Strategies, Processes, and Systems III, 77370M
Vreeswijk, P. M., Ellison, S. L., Ledoux, C., et al. 2004, A&A, 419, 927
Vreeswijk, P. M., Ledoux, C., Smette, A., et al. 2007, A&A, 468, 83
—. 2011, A&A, 532, C3
Wakker, B. P., Savage, B. D., Fox, A. J., Benjamin, R. A., & Shapiro, P. R. 2012, ApJ, 749, 157
Wang, J.-G., Zhou, H.-Y., Ge, J., et al. 2012, ApJ, 760, 42
Warren, S. J., Hewett, P. C., & Foltz, C. B. 2000, MNRAS, 312, 827
Watson, D. 2009, in Astronomical Society of the Pacific Conference Series, Vol. 414, Cosmic Dust - Near and Far, ed. T. Henning, E. Grün, & J. Steinacker, 277
Watson, D., Hjorth, J., Fynbo, J. P. U., et al. 2007, ApJ, 660, L101
Watson, D., & Jakobsson, P. 2012, ApJ, 754, 89
Watson, D., Reeves, J. N., Osborne, J., et al. 2002, A&A, 393, L1
Watson, D., Fynbo, J. P. U., Ledoux, C., et al. 2006, ApJ, 652, 1011
Watson, D., Zafar, T., Andersen, A. C., et al. 2013, ApJ, 768, 23
Waxman, E., & Draine, B. T. 2000, ApJ, 537, 796
Weingartner, J. C., & Draine, B. T. 2001, ApJ, 548, 296
Weymann, R. J., Carswell, R. F., & Smith, M. G. 1981, ARA&A, 19, 41
Whalen, D., Prochaska, J. X., Heger, A., & Tumlinson, J. 2008, ApJ, 682, 1114
Wiersema, K., Flores, H., D'Elia, V., et al. 2011, GRB Coordinates Network, 12431
Wiersema, K., Togi, A., Watson, D., et al. 2018, MNRAS, 481, 1126
Wijers, R. A. M. J., Bloom, J. S., Bagla, J. S., & Natarajan, P. 1998, MNRAS, 294, L13
Willingale, R., Starling, R. L. C., Beardmore, A. P., Tanvir, N. R., & O'Brien, P. T. 2013, MNRAS, 431, 394
Winkler, C., Courvoisier, T. J.-L., Di Cocco, G., et al. 2003, A&A, 411, L1
Wiseman, P., Schady, P., Bolmer, J., et al. 2017, A&A, 599, A24
Wolf, C., & Podsiadlowski, P. 2007, MNRAS, 375, 1049
Wolfe, A. M., Gawiser, E., & Prochaska, J. X. 2005, ARA&A, 43, 861

Wolfe, A. M., Lanzetta, K. M., Foltz, C. B., & Chaffee, F. H. 1995, ApJ, 454, 698
Wolfe, A. M., & Prochaska, J. X. 2000, ApJ, 545, 591
Wolfe, A. M., Prochaska, J. X., & Gawiser, E. 2003, ApJ, 593, 215
Wolfe, A. M., Turnshek, D. A., Smith, H. E., & Cohen, R. D. 1986, ApJS, 61, 249
Woosley, S. E. 1993, ApJ, 405, 273
Woosley, S. E., & Bloom, J. S. 2006, ARA&A, 44, 507
Woosley, S. E., Eastman, R. G., & Schmidt, B. P. 1999, ApJ, 516, 788
Wright, E. L., Eisenhardt, P. R. M., Mainzer, A. K., et al. 2010, AJ, 140, 1868
Xiang, F. Y., Li, A., & Zhong, J. X. 2011, ApJ, 733, 91
Xu, D., Levan, A. J., Fynbo, J. P. U., et al. 2014a, GRB Coordinates Network, Circular Service, No. 16983, #1 (2014), 16983
Xu, D., Tanvir, N. R., Malesani, D., & Fynbo, J. 2015, GRB Coordinates Network, Circular Service, No. 18505, #1 (2015), 18505
Xu, D., Vreeswijk, P. M., Fynbo, J. P. U., et al. 2014b, GRB Coordinates Network, Circular Service, No. 17040, #1 (2014), 17040
Xu, D., Malesani, D., Schulze, S., et al. 2013, GRB Coordinates Network, Circular Service, No. 14816, #1 (2013), 14816
Yanny, B., Rockosi, C., Newberg, H. J., et al. 2009, AJ, 137, 4377
York, D. G., Adelman, J., Anderson, Jr., J. E., et al. 2000, AJ, 120, 1579
Zafar, T., & Møller, P. 2019, MNRAS, 482, 2731
Zafar, T., & Watson, D. 2013, A&A, 560, A26
Zafar, T., Watson, D., Fynbo, J. P. U., et al. 2011a, A&A, 532, A143
Zafar, T., Watson, D. J., Tanvir, N. R., et al. 2011b, ApJ, 735, 2
Zafar, T., Watson, D., Elíasdóttir, Á., et al. 2012, ApJ, 753, 82
Zafar, T., Møller, P., Watson, D., et al. 2015, A&A, 584, A100
Zafar, T., Heintz, K. E., Fynbo, J. P. U., et al. 2018a, ApJ, 860, L21
Zafar, T., Watson, D., Møller, P., et al. 2018b, MNRAS, 479, 1542
Zafar, T., Møller, P., Watson, D., et al. 2018c, MNRAS, 480, 108
Zeimann, G. R., Ciardullo, R., Gronwall, C., et al. 2015, ApJ, 814, 162
Zhang, B. 2007, ChJAA, 7, 1
Zitrin, A., Labbé, I., Belli, S., et al. 2015, ApJ, 810, L12
Zou, S., Petitjean, P., Noterdaeme, P., et al. 2018, A&A, 616, A158
Zwaan, M. A., van der Hulst, J. M., Briggs, F. H., Verheijen, M. A. W., & Ryan-Weber, E. V. 2005, MNRAS, 364, 1467